LEVERAGING MANIFOLD THEORY FOR TRAJECTORY DESIGN - A FOCUS ON FUTURISTIC CISLUNAR MISSIONS

A Dissertation

by

SANDEEP K. SINGH

Submitted to the Graduate and Professional School of
Texas A&M University
in partial fulfillment of the requirements for the degree of

DOCTOR OF PHILOSOPHY

Chair of Committee,	John L. Junkins
Co-Chair,	Manoranjan Majji
Committee Members,	Srinivas R. Vadali
	Nicholas Suntzeff
Head of Department,	Ivett A. Leyva

May 2022

Major Subject: Aerospace Engineering

ABSTRACT

Optimal control methods for designing trajectories have been studied extensively by astrodynamicists. *Direct* and *indirect* methods provide separate approaches to arrive at the optimal solution, each having their associated advantages and challenges. Among the realm of optimized transfer trajectories, fuel-optimal trajectories are typically most sought and characterized by sequential thrust and coast arcs.

On the other hand, it is well known that a simplified dynamical model like the CR3BP analyzed in a rotating coordinate system, reveal fixed points known as Lagrange points. These spatial points can be orbited, with researchers categorizing periodic orbits around them starting from the simple planar Lyapunov orbits and continuing to the more enigmatic butterfly orbits. Studying linearized dynamics using eigenanalysis in the vicinity of a point on these periodic orbits lead to interesting departures spatially manifesting into the invariant manifolds.

This thesis delves into the novel idea of merging aspects of invariant manifold theory and indirect optimal control methods to provide efficient computation of feasible transfer trajectories. The marriage of these ideas provide the possibility of alleviating the challenges of an end-to end optimization using indirect methods for a long mission by utilizing the pre-computed and analyzed manifolds for insertion points of a long terminal coast arc. In addition to this, realistic and accurate mission scenarios require consideration of a high-fidelity dynamical model as well as shadow constraints. A methodology to use the "manifold analogues" in such cases has been discussed and utilized in this thesis along with modelling of eclipses during optimization, providing mission designers a basis for efficient and accurate/mission-ready trajectory design. This overcomes the shortcomings in state of the art software packages such as MYSTIC and COPERNICUS.

DEDICATION

To my mother and father for always motivating me to strive for excellence.

To my beloved partner Sonali for the much needed emotional support.

To my siblings, friends and extended family.

ACKNOWLEDGMENTS

I would like to express my sincere gratitude to Texas A&M University for providing me the opportunity of being a student here. I would also like to thank the Department of Aerospace Engineering for the opportunity to write a doctoral thesis.

To my advisor and committee chair, Professor John L. Junkins, I am eternally grateful for the opportunity to pursue my doctoral studies under your guidance. It's hard to not tear up writing this, as I distinctly remember the administrative challenges surrounding my arrival. Your words of support and encouragement helped me immensely through that time and even though we hadn't met, it gave me a reassuring feeling about my choice at a critical juncture in life. None of this would have been possible without your continued support and motivation. It has been a journey that has equipped me with stories to last a lifetime. I came in with the dream of studying astrodynamics but I am leaving with much more than just knowledge.

To my committee members, my co-chair Professor Manoranjan Majji and Professor(s) Srinivas R. Vadali and Nicholas Suntzeff, I am grateful for your assistance, guidance and words of encouragement throughout my time as a doctoral student and especially after the preliminary examination. Thank you for analyzing my strengths and encouraging me to embrace and work on my weaknesses.

To Professor Ehsan Taheri, the significance of you being a part of this journey is hard to express in words. Apart from the technical discussions and collaborations, you have been a friend. Thank you for always being available to chat and helping me see the lighter side of the life of a doctoral student. Your advice at critical junctures have been instrumental in making this happen. We have come a long way from our first interaction, when I was having a hard time locating the Jack K Williams Administration building on campus and you walked out to receive me. I hope our collaborations will continue long into the future.

To my internship mentor(s) Brian Anderson and Professor Robyn Woollands, thank you so much for giving me the opportunity to fulfill a childhood dream of working at NASA. I am grateful

for your mentor-ship and guidance in helping me make the most of such a rare opportunity.

To Dr. Alok Das, for posing the challenge of identifying *selenocentric* quasi-stable orbits for imaging missions which kick-started my research efforts. Thank you for the opportunity to work on the D2S2 mission. I believe it is the most rewarding experience to see your research bear fruit in terms of application to a real mission. A big thank you to the D2S2 Flight Dynamics Working Group, in particular, Eric Anderson from AFRL, Travis Swenson from Aerospace Corporation, John Carrico from SEE and Jon Upham from Blue Canyon Technologies. I am grateful for the numerous weekly meetings as I learnt a lot from them and gained precious exposure that gave me confidence in my ability and work.

To everyone else who has ever lent a helping hand in-terms of emotional, technical or motivational support, *dhanyawaad*. To all my friends and the 'volleyball group', thanks for the games and all the memories. *Good Game, Well Played!*

CONTRIBUTORS AND FUNDING SOURCES

Contributors

This work was supported by a dissertation committee consisting of Professor John L. Junkins (advisor and committee chair), Professor(s) Manoranjan Majji (committee co-chair) and Srinivas R. Vadali of the Department of Aerospace Engineering and Professor Nicholas Suntzeff of the Department of Physics & Astronomy.

The work on constructing invariant manifold analogues described in Chapter 4 was done in collaboration with Dr. Brian Anderson from Jet Propulsion Laboratory, California Institute of Technology.

All other work conducted for the thesis (or) dissertation was completed by the student independently.

Funding Sources

Graduate study was supported by an assistantship from the Department of Aerospace Engineering, Texas A&M University and summer internships (2019 & 2020) at Jet Propulsion Laboratory, California Institute of Technology was supported under contract with National Aeronautics and Space Administration, United States of America (80NM0018D0004).

NOMENCLATURE

GTO	Geostationary Transfer Orbit
sGTO	super Geostationary Transfer Orbit
TPBVP	Two Point Boundary Value Problem
OCP	Optimal Control Problem
NRHO	Near Rectilinear Halo Orbit
BCP	Bicircular Problem
CR3BP	Circular Restricted Three Body Problem
HFM	High Fidelity Model
MT	Minimum Time
MF	Minimum Fuel
EMEJ2000	Earth Mean Equator J2000
ECI	Earth Centered Inertial
IC	Initial Condition
FC	Final Condition
ΔV	Increase in specific spacecraft momentum
L_{i}	Lagrange Points or Libration Points
TOF	Time of Flight
TLI	Trans-lunar Injection
LOI	Lunar Orbit Insertion
AoP	Argument of Periapse
LTO	Lunar Transfer Orbit
WSB	Weak Stability Boundary

HOCP	Hybrid Optimal Control Problem
MEE	Modified Equinoctial Elements
PMP	Pontryagin's Minimum Principle
FFS	Finite Fourier Series
NLP	Non-linear Programming
RAAN	Right Ascension of Ascending Node

TABLE OF CONTENTS

Page

[1]Part of this section is reprinted with permission from "Eclipse-conscious transfer to lunar gateway using ephemeris-driven terminal coast arcs" by Singh, S., Junkins, J., Anderson, B., Taheri, E., 2021, Journal of Guidance, Control and Dynamics, 44(11), 1972-1988, Copyright ©2021 by the American Institute of Aeronautics and Astronautics, Inc.

[2]Separate parts of this section are reprinted with permissions from:
"Eclipse-conscious transfer to lunar gateway using ephemeris-driven terminal coast arcs" by Singh, S., Junkins, J., Anderson, B., Taheri, E., 2021, Journal of Guidance, Control and Dynamics, 44(11), 1972-1988, Copyright ©2021 by the American Institute of Aeronautics and Astronautics, Inc.;
"Exploiting manifolds of L1 halo orbits for end-to-end Earth–Moon low-thrust trajectory design" by Singh, S. K., Anderson, B. D., Taheri, E., Junkins, J. L., 2021, Acta Astronautica, 183, 255-272, Copyright ©2021 IAA. Published by Elsevier Ltd. All rights reserved.

[3]Parts of this chapter have been reprinted with permission from "Eclipse-conscious transfer to lunar gateway using ephemeris-driven terminal coast arcs" by Singh, S., Junkins, J., Anderson, B., Taheri, E., 2021, Journal of Guid-

ance, Control and Dynamics, 44(11), 1972-1988, Copyright ©2021 by the American Institute of Aeronautics and Astronautics, Inc.

[4]Parts of this chapter have been reprinted with permissions from:
"Eclipse-conscious transfer to lunar gateway using ephemeris-driven terminal coast arcs" by Singh, S., Junkins, J., Anderson, B., Taheri, E., 2021, Journal of Guidance, Control and Dynamics, 44(11), 1972-1988, Copyright ©2021 by the American Institute of Aeronautics and Astronautics, Inc. ;
"Exploiting manifolds of L1 halo orbits for end-to-end Earth–Moon low-thrust trajectory design" by Singh, S. K., Anderson, B. D., Taheri, E., Junkins, J. L., 2021, Acta Astronautica, 183, 255-272, Copyright ©IAA. Published by Elsevier Ltd.
"Low-Thrust Transfers to Southern L_2 Near-Rectilinear Halo Orbits Facilitated by Invariant Manifolds by Singh, S. K., Anderson, B. D., Taheri, E., Junkins, J. L. (2021). Journal of Optimization Theory and Applications, 191(2), 517-544. Copyright ©2021, The Author(s), under exclusive licence to Springer Science Business Media, LLC, part of Springer Nature.

LIST OF FIGURES

FIGURE Page

LIST OF TABLES

TABLE Page

1. INTRODUCTION AND LITERATURE REVIEW

1.1 The Moon - Our Nearest Neighbor

Many theories regarding the origin of the Earth's Moon have been put forward. The leading theory, however, is that a smaller body (approximately Mars sized) collided with the Earth roughly 4.5 billion years ago. The debris from this collision attributed to both the Earth and the impacting body accumulated to form our sole natural satellite. The newly formed Moon was in a molten state but "eventually" within 100 million years, the molten magma cooled down and crystallized with the less-dense rocks floating upwards and eventually formed the lunar crust. It is theorized that the early Moon developed a global magnetic field via a mechanism similar to most terrestrial planets. Ever since the early days of rampant volcanic activity, the Moon has remained lifeless and largely unchanged. Additionally, the sparse atmosphere is not capable of impeding impacts from asteroids, meteoroids and even comets, therefore leading to a surface riddled with craters. Over the billions of years since its formation, the surface has fragmented into particles ranging from huge boulders to just powder.

The Earth's Moon had somewhat of a turbulent beginning. Nevertheless, the influence it exerts on us is remarkable and underrated at the same time. For instance, the lunar gravitational pull directly affects life on the Earth in a significant way and is responsible for the current length of day, seasons and tides [3]. According to computer models, early Earth had a six-hour day almost 4.5 billion years ago but since then with the help of the Moon, the Earth has been slowing down resulting in longer days. Over time, the Moon's gravitational pull on the Earth led to a transfer of "spin" energy launching the Moon into higher and higher orbits. Therefore, the distance between the two bodies has kept on increasing but the rotation rates have decreased over time [4]. The more distant Moon revolves around the Earth every 27 days while it's spin rate is much slower than the Earth's $\approx$ 27.3 days. This $\approx$ 1:1 resonance of the Moon's orbit and attitude motion leads to Earth observation always looking at the same side of the Moon (nearside). Additionally, the Moon's

gravitational pull is also responsible for maintaining the 23.5 ° tilt of the Earth's North Pole with respect to the Ecliptic normal which consistently provides the various seasons observed on the Earth [5]. Furthermore, the Moon's gravity has a differential effect on the pull it exerts on the near and far side of the Earth, resulting in tides in the oceans. The Sun's gravity is also important, maintaining the Earth in a stable heliocentric orbit but the differential effect of its gravity is much smaller, therefore contributing to only ≈ one-third of the tides on the Earth. Figure 1.1 depicts the mechanism behind occurrence of high and low tides due to the lunar gravity.

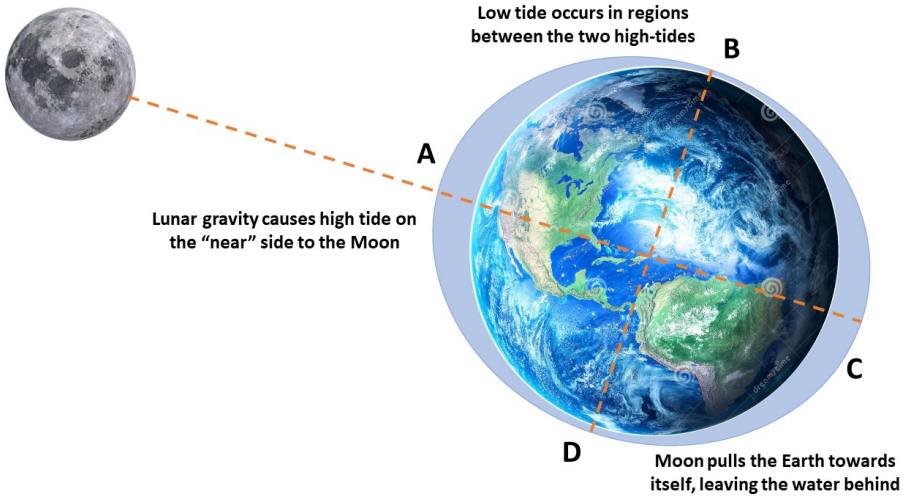

Figure 1.1: Lunar tides on the Earth

Therefore, without the Moon, life on Earth probably would not have existed at all. For instance, the length of the day on Earth would reduce from 24 hours to 6 hours. The tilt of the Earth's rotation axis which currently wobbles slightly (≈ 3 °) around its nominal over a 41,000 year cycle due to the existence of the Moon. Without the Moon, the "n" body effects of the planetary giants would vary the tilt between 0° – 80°. Additionally, as discussed above, without the tug from the Moon, the tides on Earth would have been much smaller only due to the effect of the Sun.

1.2 The Rich History of Lunar Exploration

Being our nearest neighbor in the solar system, the Moon has always been a source of fascination for mankind. In particular, researchers across the globe have recognised the Moon as being of great scientific significance. This has been evidenced in the various attempts by humans to access the Moon by robotic as well as manned missions. Historically, the first physical exploration of the Moon began with *Luna 2* (1959), a space probe from the Soviet Union as it made an impact on the lunar surface on September 14, 1959 [1]. This was revolutionary since, before this, the Moon had only been observed via telescopes. Due to the space race, during the cold war, engineering arguably saw a kind of unprecedented progress that is since yet to be seen. NASA's Apollo Space Program was the only program to successfully land humans on the Moon. There were six lunar landings by humans during the Apollo program, with the first in 1969 when two American astronauts historically placed scientific instruments and returned lunar samples back to the Earth. This was a landmark achievement and led to a better understanding of our only natural satellite [6, 7, 8, 9].

The cold-war inspired "space-race" between the Soviet Union and the United States of America was focused on reaching the Moon. A number of scientific and technological firsts were achieved during this time-period. For instance, the first photographs of the far side of the Moon was captured in 1959 by the Soviet Union and the United States became the first country to successfully land humans on the Moon in 1969. Although this was a time of prominent achievements, the road was not without a fair share of failures. Some startling and lesser known facts regarding the failed attempts underscore the enormity of the task at hand. *Luna 1* (January 1959), attributed to be the first artificial object to flyby the Moon ultimately also became the first object to enter a heliocentric orbit but it was in essence designed as an impact probe which was successfully achieved by it successor *Luna 2* (see Figure 1.2) [1]. While *Luna 3* (October 1959) was the last of the first generation of Luna spacecraft which imaged the lunar far-side, the second generation spacecraft (*Luna 4 - 14*) were much more heavy landers and orbiters and encountered numerous failures. Eventually, *Luna 9* (January 1966) became the first soft-landing on the lunar surface while Luna-

10 (March 1966) became the first successful lunar orbiter. The third generation Luna spacecraft (*Luna 15 - 24*) were even heavier (≈ 5700 kg) and designed for sample-return, rover and orbiter missions. *Luna 16* (September 1970) became the first robotic mission to return a lunar sample [10, 11] whereas, *Luna 17*(November 1970) was the first mission to put a rover on the Moon.

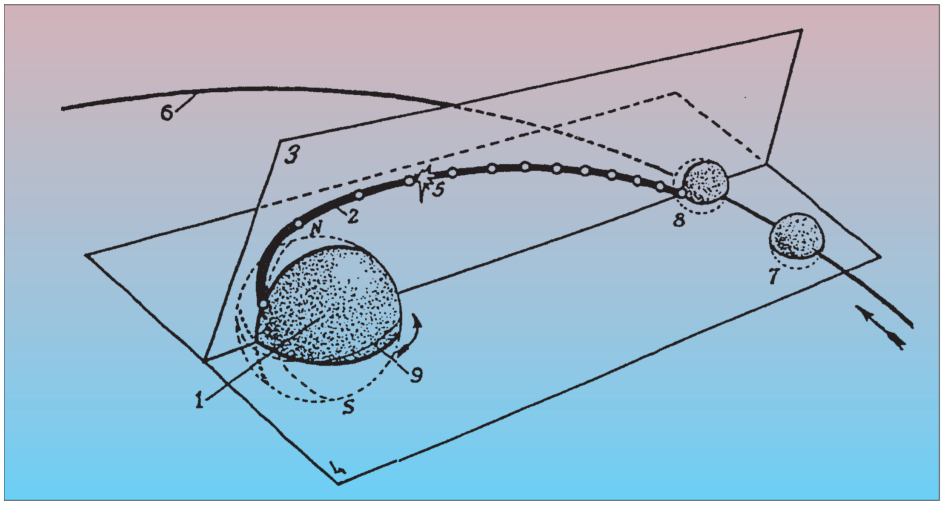

Figure 1.2: Luna 2 Mission Profile [1]

In parallel with the soviet activities, the United States of America carried out numerous unmanned missions in our quest to reach the Moon. The ≈ 330 kg Rangers (1962-65) were designed as impact probes to deliver images of the Moon before crash. Unfortunately, Ranger-4 met with a crash on the lunar far side and was for a long time the only known artificial object there until the Chang'e 4 mission [12] (May 2018) of China recently landed and deployed a rover on the far-side. Coinciding with the Ranger missions were five lunar orbiters that successfully mapped the lunar equatorial region in a quest to identify landing sites for the soon to follow Apollo missions. In 1968, Apollo 8 became the first mission to successfully orbit the Moon while the historic Apollo 11 mission followed in 1969, establishing the first human presence on the Moon. In 1971, Apollo 15 placed the first manned rover on the Moon.

Figure 1.3 depicts the Apollo 11 mission profile in detail. The Saturn V rocket put the space-

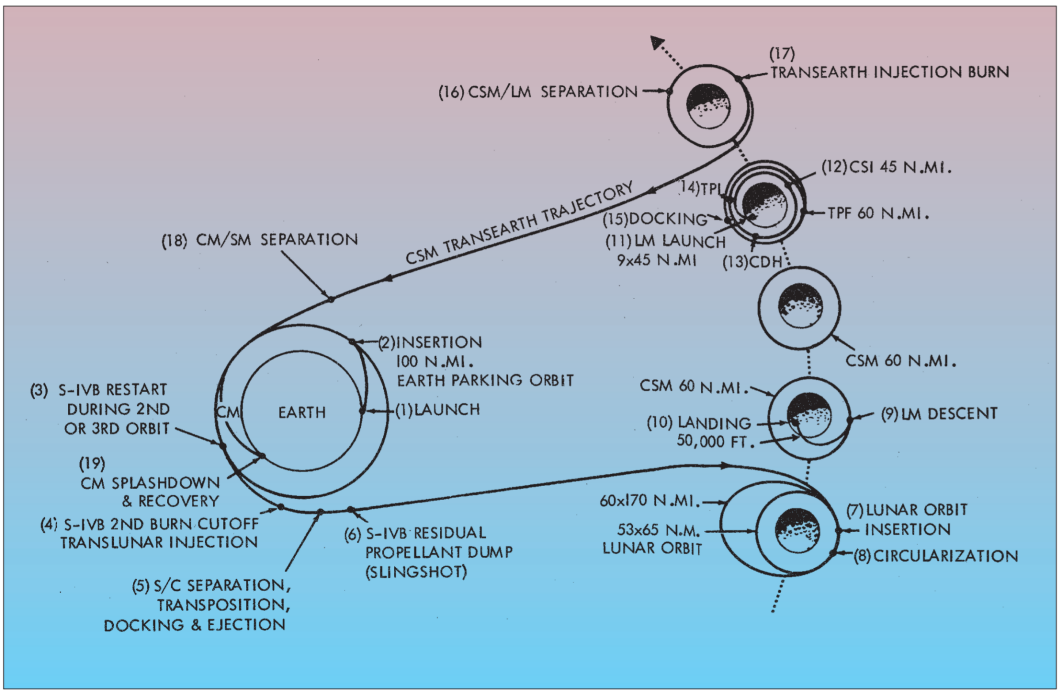

Figure 1.3: The Apollo Mission Profile [1]

craft initially in a 160 km Low Earth Orbit (LEO). An impulsive Trans-Lunar Injection (TLI) burn was carried out sending the spacecraft on it's way to the Moon and the journey was completed in $\approx$ 70 hrs. In order to get captured, a Lunar Orbit Insertion (LOI) maneuver was carried out to insert the spacecraft into an elliptical selenocentric orbit (270 km $\times$ 100 km). A second maneuver to circularize the orbit followed eventually sending the spacecraft in a 100 km circular orbit. The Lunar Module (LM) was decoupled and another maneuver changed its orbit to a low periselene elliptical orbit (15 km $\times$ 100 km). Eventually, a powered descent took the LM to the lunar surface. Apollo 8 and 10-13 were designed for "free-return" trajectories i.e., the TLI leg orbital energy would not allow the spacecraft to escape the Earth-Moon system in case of any motor malfunction. The amazing rescue mission of Apollo 13 would not have been possible if not for the "free-return" trajectory design. Essentially, the Apollo class of trajectories used a direct transfer strategy with multiple impulsive burns using a chemical high-thrust engine. This led to the transfer time having an upper bound of four days but at the cost of high ΔV (velocity increase provided to spacecraft) requirements.

After a "lull" period following the Apollo 17 mission (December 7 - 19, 1972), the 90's saw a renewed interest in the Moon from space agencies across the globe. The trajectories flown by these uncrewed missions were more state-of the art and required less ΔV as compared to the previous 'direct' trajectories. The underlying concept used in designing these trajectories was to search for alternatives to 'direct' transfers. In essence, novel concepts like using multiple staging orbits, employing lunar swing-bys as well as cooperating with mother nature (underlying physics) to reduce costs required for a lunar capture i.e., move towards near-ballistic capture trajectories. As expected these transfers typically had a significantly longer transit time but were more fuel-efficient. Some examples of mission profiles from this time-frame include, the Japanese Hiten mission [2] in 1993 (6 months Time of Flight (TOF), 196 kg) [see Figure 1.4], the US Clementine mission launched in 1994 (3 weeks TOF, 1690 kg) and finally the most significant mission of the 90s, the Lunar Prospector Mission launched in 1998 (105 hrs., 300 kg).

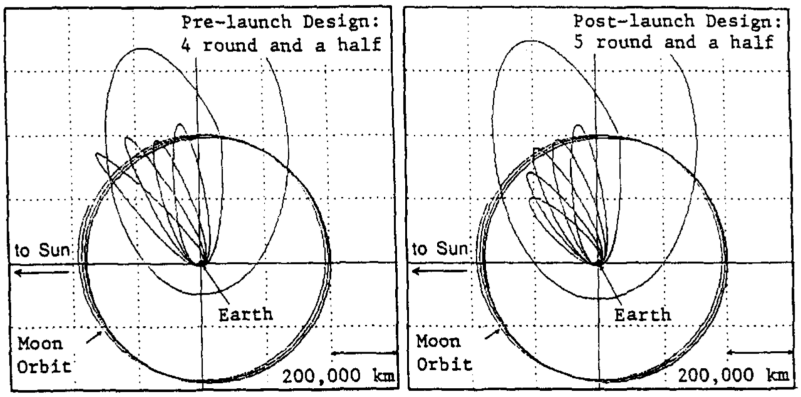

Figure 1.4: The Japanese Hiten Mission Profile (Pre-Launch & Post-Launch) [2]

Initially, the main Hiten spacecraft was planned to be inserted into a highly elliptical geocentric orbit with an apogee of 476,000 km which would swing past the Moon but due to a ΔV deficit of 50 m/s the launch vehicle could only manage an insertion orbit apogee of 290,000 km. On the first lunar swing-by, Hiten launched an orbiter called *Hagoromo* whose transmitter malfunctioned but its orbit confirmed via Earth observations. Belbruno and Miller [13] from the Jet Propulsion

Laboratory later devised a 'ballistic' capture trajectory that would enable the main Hiten probe to also enter a lunar orbit. A version of the solution was later used inserting the probe into a temporary lunar orbit. Later on, the probe would become the first mission to demonstrate the aerobraking technique.

1.3 About Trajectory Design Methods for Lunar Missions

Designing trajectories in any force field typically involves solving an optimization problem that determines a control sequence which when applied drives the spacecraft from an initial state to a desired final state. In the context of spacecraft trajectory design problems, there is often an obvious trade-off between fuel consumption and time-of flight. Two of the most popular high-level approaches to achieve an Earth-Moon transfer are discussed below.

1.3.1 Direct Trajectories

The 'direct' trajectories were primarily used by the initial missions to the Moon, some of which were described in the preceding sections. The trajectory flown was very basic, with a general scenario including a spacecraft in an initial geocentric 'parking orbit'. Using single/multiple impulsive maneuvers, the apogee of the parking orbit is raised to the Moon's orbit around the Earth or even beyond. Such maneuvers are termed as TLI maneuvers and uses the spacecraft engine or the launch vehicle upper-stage engine to provide the necessary impulse.

Consider a spacecraft in an initial geocentric parking orbit of altitude 300 km (see Figure 1.5).

Assuming a circular orbit, the spacecraft orbital velocity is 7.7 km/s in this orbit. Let us also assume that the Moon is in a circular orbit around the Earth with a radius of R = 384400 km. The geocentric transfer arc therefore should have a perigee of 300 km and an apogee of 384400 km. Using these numbers and assuming a keplerian transfer arc, the spacecraft has a perigee velocity of 10.83 km/s. Therefore, the departure impulse (δv_d) required to leave the parking orbit and fly the transfer arc is 10.83 - 7.7 = 3.13 km/s. Similarly, spacecraft velocity on the transfer arc at apogee is 0.19 km/s which is easily computed by employing Kepler's second law i.e., conservation of angular momentum. Also, since the Moon is moving in it's orbit at the speed of 1.03 km/s, a

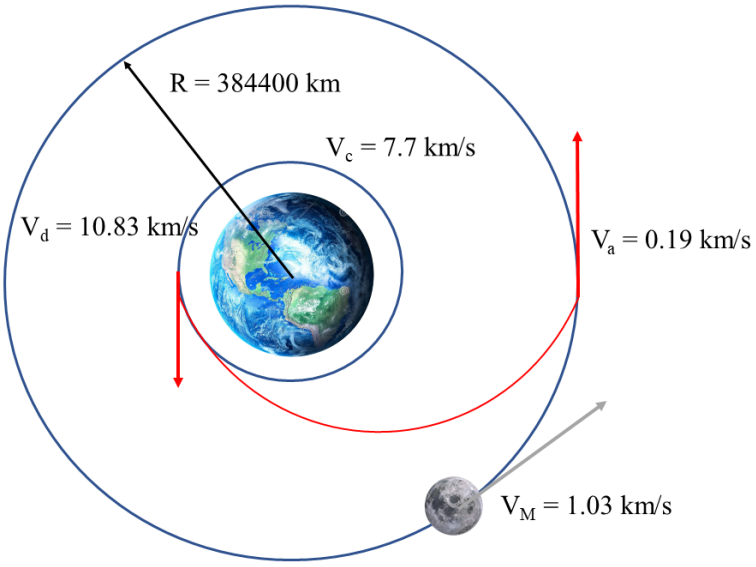

Figure 1.5: A simple Hohmann direct lunar transfer scenario.

second arrival impulse (δv_a) is required for capture to occur with the magnitude being 1.03 - 0.19 = 0.84 km/s.

The transfer scenario discussed above is a Hohmann transfer and is the most optimal in terms of total ΔV (a measure of fuel consumption via the Tsiolkovsky Rocket Equation) requirements for a circle-to-circle planar orbit transfer. For this case, the Hohmann transfer arc has an apogee equal to the Earth-Moon distance. Now, in case of a mission scenario where more weight is on minimizing the time of flight rather than fuel consumption, an apogee higher than the Earth-Moon distance could be chosen. Although it would incur a larger ΔV cost. A direct transfer of this kind, typically takes 2-5 days. Note that both the departure and arrival impulses could be distributed over multiple arcs (Figure 1.6) in which case another important question arises, 'How many impulses is optimal?'. Taheri and Junkins have recently studied this problem in detail for the general 3D orbit transfer case and answered the question succinctly in their paper [14].

Figure 1.6: Sequential Raising of Apogee using multiple impulses

1.3.2 Indirect Trajectories

The cost associated with launching and injecting a spacecraft into a desired orbit is a strong function of the mass of the spacecraft. Additionally, a large fraction of the spacecraft mass is composed of the mass of propellant on-board in order to execute the various ΔV maneuvers. Therefore, an easy way to reduce mission costs is to reduce this ΔV requirement. There are a couple of obvious ways to achieve this,

- piggy-back ride along with a primary payload
- cooperate with underlying physics to gain/lose energy

Let us discuss these scenarios in more detail.

1.3.2.1 Piggy-Back Rides

In the recent past, launch vehicles have demonstrated the capability to execute launches of multiple auxiliary payloads along with a primary spacecraft. For instance, the Ariane V has a specially designed structure known as the Ariane Structure for Auxiliary Payloads (ASAP) [15] enabling piggy-back rides for micro- and nano-satellites. Another example is the historic and

record-breaking launch by the Indian Space Research Organisation (ISRO) when it injected 104 satellites in a single rideshare launch using the Polar Satellite Launch Vehicle (PSLV) - C37 [16, 17]. This record was later broken by SpaceX which launched 143 satellites into orbit using a single launch.

A limitation of the piggy-back launches is that the companion satellites are sought primarily for the Geostationary Transfer Orbit (GTO), restricting the initial parking orbit for such spacecraft/satellite. While, this may look like another constraint to our end-to end trajectory design problem, it is more favorable in most situations than meets the eye. Essentially, the energy of a GTO is usually higher than any low Earth parking orbit which directly translates into savings on any required TLI maneuvers.

A class of direct transfers are known as short transfers from the GTO. Essentially, this class of transfers are possible for cases when the angle between the line of nodes of the GTO as well as the lunar orbit is small. In such cases, mid-course corrections en-route to the Moon are enough to successfully make the transfer. A special case of such direct transfers is when the capture occurs at the instance when the Moon is at the orbit nodal point. In this special case, no plane change maneuver in terms of matching the Right Ascension of Ascending Node (RAAN) is required. Figure 1.7 depicts an example scenario where the difference in RAAN i.e., $\Delta\Omega$ is small between the GTO and the Moon's orbit.

On the flip-side, if $\Delta\Omega$ is large, a large plane change is necessary in order for the spacecraft to be captured by the Moon. These large plane change maneuvers are very costly but the ΔV required to bring about the change is smaller when the spacecraft is slower. Therefore, the obvious choice for scheduling the maneuvers is when the spacecraft is farthest from the central body i.e., at the apogee. Conservation of angular momentum also means that higher the apogee, lower the spacecraft velocity. Usually, the apogee is raised much higher than the Earth-Moon distance and then the plane change maneuver occurs as the spacecraft reaches apogee (on the LTO leg) such that it can get captured by the Moon on the return-leg. This long transfer, also known as a bi-elliptic transfer significantly reduces the plane-change cost considerably. Owning to the 'no free lunch'

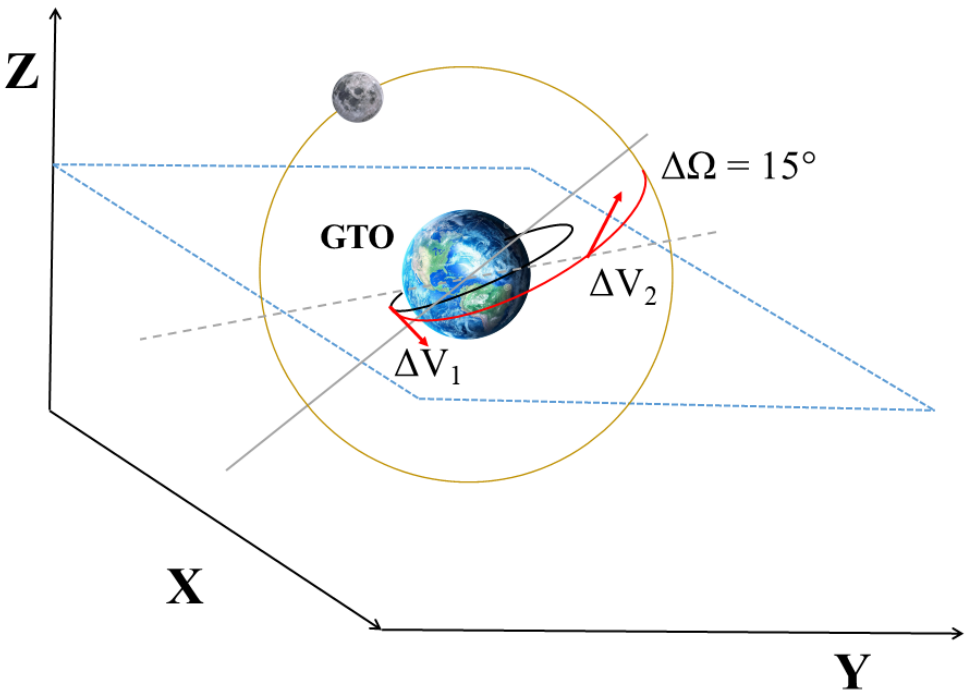

Figure 1.7: Short Transfers from GTO - Example

theorem, this translates into a much higher transfer time ≈ 50 days as compared to the 2-5 days for a direct transfer. Figure 1.8 depicts an example scenario.

It is important to note here that, the spacecraft now arrives at the Moon near perigee on the second arc of the bi-elliptic transfer. Therefore, spacecraft velocity is now higher than the direct transfer scenario where capture occurs at apogee of the LTO. Since the relative velocity with respect to the Moon is not lower, the ΔV needed for lunar insertion is also lower. Of course, the location of the periselene in the arrival orbit is not arbitrary and depends on the arrival geometry. Additional maneuvers would be required to position the periselene at a desired location, for instance, over the lunar south pole.

1.3.2.2 Weak Stability Boundary Transfers

In the preceding section, it was identified that an important procedure to reduce the ΔV further was to cooperate with the underlying physics in order to make the spacecraft gain or lose energy

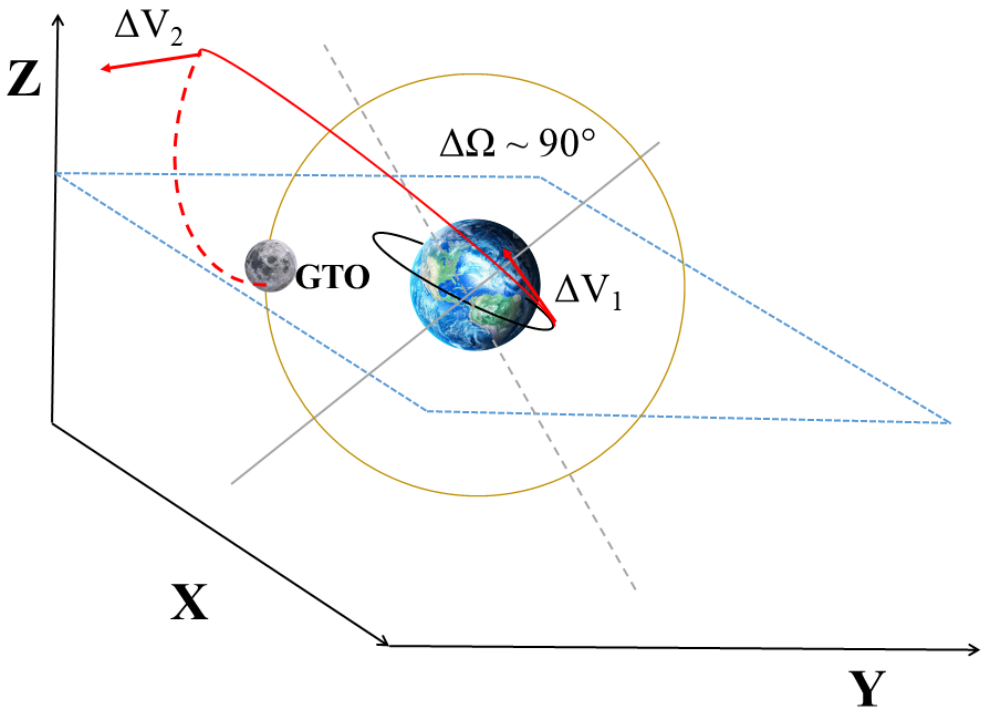

Figure 1.8: Long Transfers from GTO - Example

for a very small fuel cost. *Surprisingly, mother nature gives us ample opportunities to make this happen, we only need to look.* Based on this idea, Belbruno in 1987 [18] was the first to introduce the notion of Weak Stability Boundary (WSB) trajectories.

Lowering the TLI ΔV would probably mean inability to reach the Moon, therefore the only knob available for optimization is the Lunar Orbit Injection maneuver. This could be possible by arriving at the Moon with a very low relative velocity. A bi-elliptic transfer was shown in the previous section to be a simple yet effective way to perform this increment in the Trans-lunar Orbit energy level. The notion that energy could be 'stolen' from other bodies such as the Sun and the Moon in the context of Earth-Moon transfers opens a whole new realm of transfer possibilities. For instance, we saw in the case of a bi-elliptic transfer, a burn is required at the apogee of the first leg in order to execute the plane-change maneuver. *Can this maneuver be achieved by using the perturbation from Sun's gravity rather than an engine burn?*

In order to make this happen, the spacecraft must first be taken to a WSB region. This re-

gion is defined to have the same order of magnitude for the 'primary' or governing force and the perturbation to be used to effect the maneuver. For instance, in the context of a spacecraft being transferred from the Earth to the Moon, a region where the Earth's and the Sun's gravity forces on the spacecraft have the same order of magnitude. Artificial maneuvers in these regions are extremely effective and can lead to a drastic change in lunar arrival conditions. Actually, these regions occur near the Lagrangian Points. This might seem like a coincidence but the correlation will become clear in subsequent discussions.

A similar concept was discussed in Jules Verne's science fiction classic *From the Earth to the Moon* where the spacecraft 'Columbiad' is in a selenocentric orbit with apogee close to the Earth-Moon L_1 Lagrangian point. In the novel, a small ΔV provided to the spacecraft around L_1 was sufficient to send the spacecraft on it's way back to the Earth. A non-fictional example was the Japanese Hiten mission which was destined to fail and did not have enough fuel leftover for a classical transfer and had to use a WSB trajectory in order to undergo a ballistic capture by the Moon in an elliptical orbit, thereby salvaging the mission. Using the Hiten mission trajectory as a case study, the spacecraft was required to cross the Sun-Earth WSB at a distance of approximately 1.4 million km from the Earth. For context, the Earth-Moon distance is 384,400 km.

Consider the two orbits shown in Figure 1.9. The motion is described in an Earth-centered rotating frame with the Sun always along the X-axis (horizontal).

The red arrows show the direction of the Sun's gravity gradient. The gradient becomes stronger as we move further away from the central body (Earth in this case). Assuming the sense of motion is counter-clockwise i.e., the orbits are prograde, it is immediately obvious that the Sun's gravity retards the current motion and therefore leads to a decrease in orbital energy in quadrant 1 (Q1). On the other hand, in the other elliptical orbit shown in the figure, the gradient is in direction of motion and therefore promotes it. This adds energy to the spacecraft and can be used to increase the orbital energy. This perturbing effect when integrated over time leads to an increase in the perigee of the orbit which can eventually equal the Earth-Moon distance. Thus, co-operating with the nature of underlying forces in the rotating system helps achieve orbit perigee radius close to

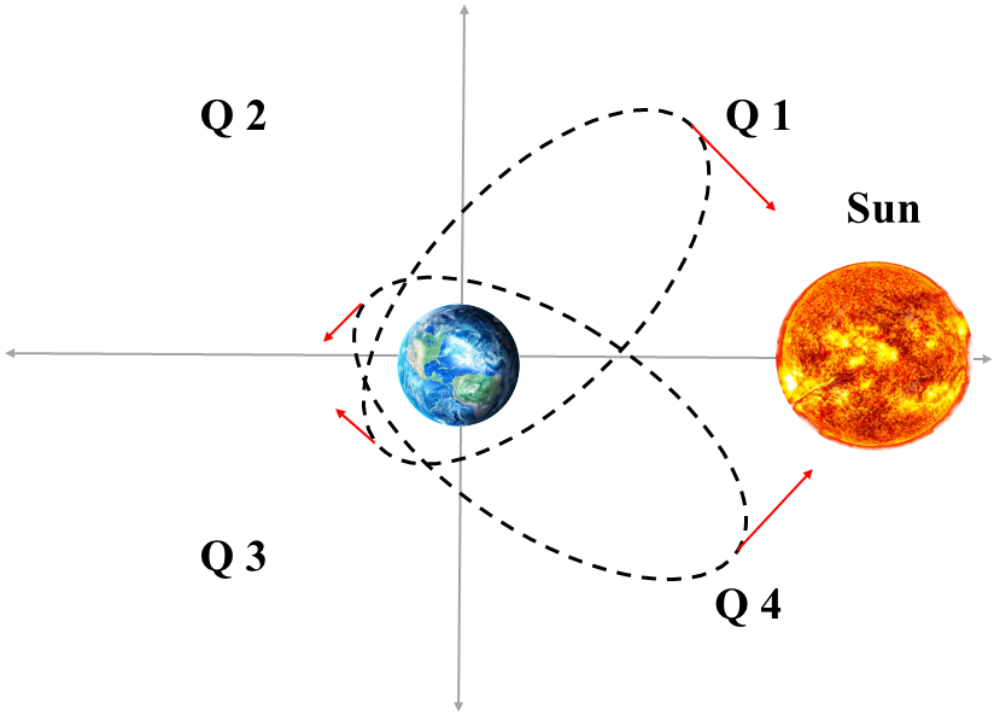

Figure 1.9: Gravity Gradient Field Lines due to the Sun

the desired numerical value for little effort.

In a similar fashion, the Earth-Moon dynamical system provides opportunities for a WSB trajectory in order to reduce arrival ΔV. In order to get captured, the energy of the spacecraft on the aforementioned trans-lunar trajectory must be close to the Moon's orbital energy. This would require using the Earth's gravity to lower the orbital energy of relative to the Moon so that the spacecraft is unable to escape from it. A ballistic capture can only occur if the spacecraft is been afforded just the right amount of energy. Note that, post-capture the aposelene of the spacecraft's orbit must be reduced immediately since motion around L_1 is chaotic and the Earth/Sun perturbations are just as adept to disturb the well-crafted energy balance which led to capture and could again send the spacecraft into a higher energy escape orbit. Therefore, the weak capture orbit must be tweaked and the spacecraft should immediately start descending into the Moon's gravity well.

Figure 1.10 depicts a representative WSB transfer for lunar-capture. Note that the trajectory depicted is a quadrant II type trajectory. A quadrant IV trajectory is also possible as discussed

before, the geometry would just be rotated 180 °. By definition a WSB region is defined as a state-space domain where chaotic dynamics can occur. Thus, WSB can only be defined in systems that are governed by non-linear dynamics. In fact, Belbruno and Carrico [19] state that WSB regions are basically generalizations of Lagrange Points. We will discuss Lagrange Points in detail in the succeeding sections. For more details on the definition of WSB regions, the readers are referred to [20, 21].

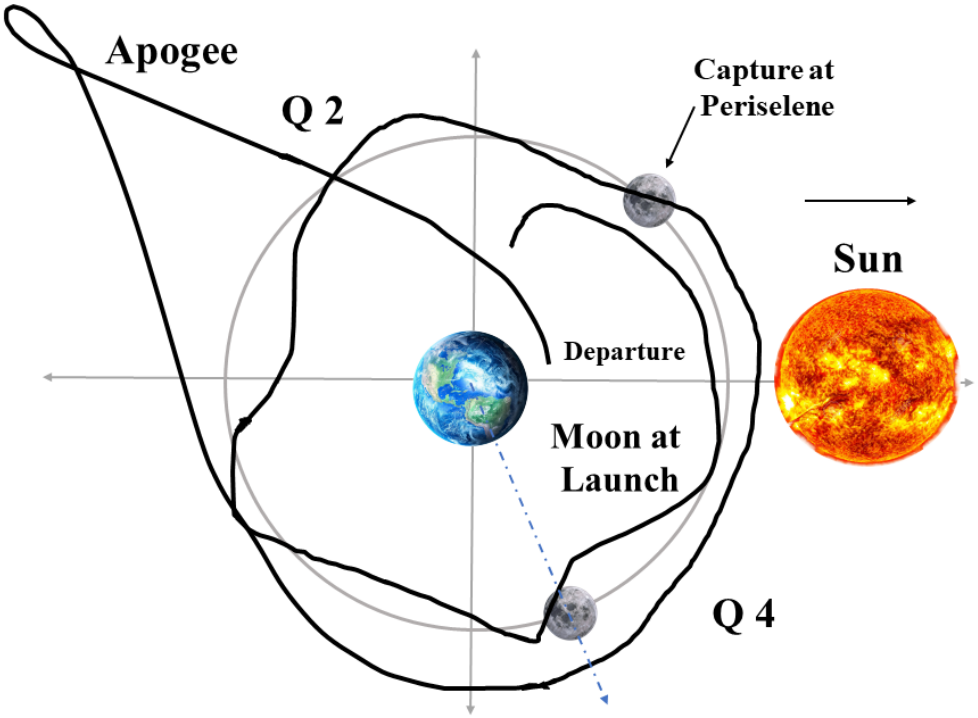

Figure 1.10: A representative quadrant II Earth-Moon transfer

In the earlier days, it was extremely difficult to compute WSB transfers efficiently. The sensitive dynamics in the region of interest made it hard for conventional search methods to numerically converge. Eventually, researchers found solace in rather employing backward propagation methods where the targeting would start from the lunar WSB, and the Equations of Motion (EOMs) integrated backwards to gauge the sensitivity of tiny variations in the lunar capture state and how it mapped in terms of trajectories coming back to the Earth at the desired state [22, 23]. It was later

discovered that backward propagation was successful because the trajectories emanating from the WSB region were essentially following invariant manifolds associated to the WSB. Additionally it was conjectured and later verified that the WSB was in fact composed of many intersections of invariant manifolds [24].

A detailed discussion on invariant manifolds, periodic orbits, Lagrangian points will be presented in the subsequent chapters but it is important to recognize that WSBs give us an indication of the fact that these manifolds can actually enable many transfers in terms of effectiveness or optimality.

1.4 Low-Thrust Trajectory Optimization Techniques

A major goal of researchers from the space domain today is to reduce the cost of accessing and utilising space for the benefit of mankind. The main objective is to keep pushing to new frontiers and ultimately expanding the reach of humans into space. Novel mission architectures and state of the art design tools have become a primary requirement in order to achieve this. The shift from chemical propulsion (CP) systems on-board spacecraft to the more efficient electric propulsion (EP) system has revolutionized space mission design and enabled us to push our horizons.

In this context, scientists and researchers have recognized the use of concurrent engineering principles to compute high-level trade-off analysis i.e., performing an exhaustive search of possible options and assessing them against multiple criteria. This is extremely effective in the preliminary design of any mission which would be later refined. Figure 1.11 compares traditional engineering principles which is sequential to concurrent engineering which exhibits overlap between the various phases. However, feasibility in terms of run-time is highly correlated with mission complexity. Complexity can be defined in terms of low-thrust systems, gravity assist maneuvers (single/multiple), discontinuous control, path constraints, eclipses etc. Mission designers need to solve for the optimal steering law, and/or sequence of swing-bys that accomplishes the mission goals in the best possible fashion while satisfying subsystem constraints and operational restrictions. The designed trajectory affects propellant expenditures, time of flight, operational time all of which greatly impacts mission feasibility. As a consequence, any concurrent optimization methodology

runs into the issue of high run-time. Therefore, state-of the art methods being researched today focus on intelligent ways to reduce human and machine hours without compromising on robustness and flexibility of the algorithms as well as with little to no compromise on fidelity of the underlying dynamical system.

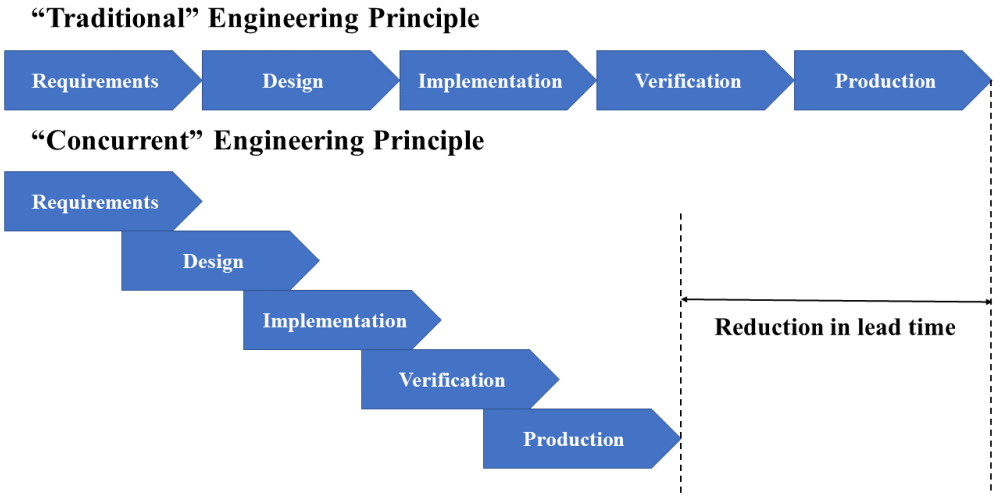

Figure 1.11: Traditional vs. Concurrent Engineering Principles

The optimization of spacecraft trajectories equipped with chemical propulsion engine is a well-known and well-studied problem in literature [25, 26, 27, 28, 29]. On the other hand, optimization of trajectories flown by spacecraft equipped with low-thrust engine like a Solar Electric Propulsion (SEP) engine is extremely challenging. Solar sail, ion thruster and tether propulsion are some of the other low-thrust propulsion technologies being researched for use in space missions. The obvious question here that needs answering is - *What makes low-thrust trajectory design so much more challenging than impulsive trajectory design?*

For optimizing CP trajectories, the design space is much smaller as compared to their EP counterparts. CP design space is restricted to number, magnitude and direction of impulses (see Figure 1.12). On the flip side, EP trajectory optimization requires computation of a continu-

ous/discontinuous steering law that describes the control throughout the entire transfer while satisfying subsystem constraints and operational constraints. In addition to the complicated design space, the underlying dynamics which is non-linear and non-convex makes it even more challenging. CP has a brute force element to it which can cancel out perturbations integrated over time between maneuvers with one big ΔV maneuver to stay on path. Low-thrust EP engines are unable to perform such big maneuvers and requires the control to continuously fight perturbations while also satisfying the boundary conditions. Finally, the existence of multiple local extremals further complicates the procedure [30]. Finally, mission designers might be interested in determining sequence and optimal number of gravity assist flybys or to embed subsystem design as a concurrent engineering problem. Thus, a search over wide design spaces as well as complex combinatorial problems are demanded.

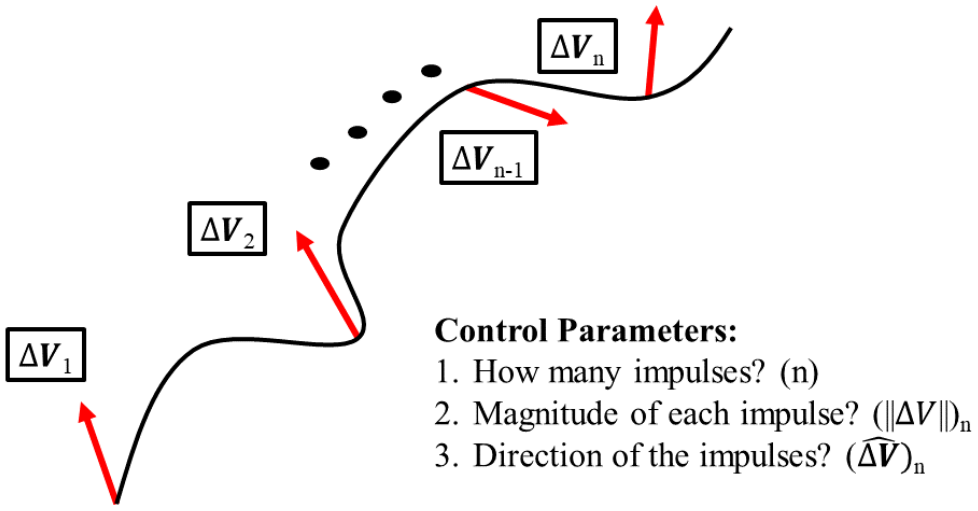

Figure 1.12: Chemical Propulsion Trajectory Design Space

The optimization of low-thrust trajectories have been classically formulated as an Optimal Control Problem (OCP) with continuous spacecraft dynamics and with design variables and parameters. In terms of the control authority, EP systems have two distinct working modes i.e., thrusting and coasting. Thrusting represents the mode when the spacecraft engine is 'ON' and

propellant is being expended. On the other hand, when the spacecraft is coasting, the engine is turned 'OFF' with no propellant being expended. In case a concurrent engineering design was sought, a Hybrid Optimal Control Problem (HOCP) would need to be formulated where decision-making and mission-planning would be modelled as discrete variables. General frameworks for HOCPs with mathematical formulation is discussed in detail in [31, 32]. Particular frameworks in the context of space mission design problems are discussed in [33, 34].

The available literature on devising robust numerical and analytical techniques based on classical OCP formulation to solve low-thrust trajectory optimization problems portrays it as a well-studied problem. Betts' work [35] was one of the first attempts at categorizing the various methods with a focus on numerical techniques, direct and indirect methods with boundary and path constraints. An extension of Betts' paper was authored by Ross and D'Souza [34] which included new approaches based on HOCP for mission design. Rao [36] included the state-of the art methods and tools for optimal trajectory generation. In 2012, Conway [37] discussed the advantages and shortcomings of current methods and evaluated them to find the best numerical approach. Since, the focus of the work described in this dissertation is an embedded indirect method which is capable of including embedded constraints that enforce additional discontinuities in the optimal control profile, indirect methods are discussed in greater detail, although brief discussions on direct methods are also provided.

1.4.1 Mathematical Modelling of the Dynamical System

The first step towards formulating and solving an optimal control problem is to accurately describe the underlying dynamics that govern motion of the body using a mathematical model. This includes derivation of a set of differential equations which describes the evolution of the system states with control variables embedded in the equations which provide the degrees of freedom in the system. In the context of spacecraft trajectory optimization, a subset of the state space (position and velocity of the spacecraft) defines the trajectory with the governing differential equations termed as the EOMs. The impact of a judicious choice of elements to describe the motion impacts the speed, robustness and accuracy of any developed algorithms.

1.4.1.1 State Space Representation

The motion of a spacecraft, typically assumed to be a point mass, can be described in three dimensions by using six independent parameters or generalized coordinates. The various existing element sets can be broadly classified as those based on position and velocity (e.g., Cartesian, Polar, Spherical etc.) and slow variables based on variation of the orbital elements (e.g., Classical, Equinoctal, Modified Equinoctal etc.) [38, 39, 40, 41]. A brief overview is presented below,

- *Cartesian State Space:* The most common and most widely used set for describing the motion of spacecraft. The state space elements represent the position and velocity of the spacecraft typically projected on an inertial Cartesian frame.

$$\mathbf{x}_{\text{CSS}} = \{x, y, z, v_x, v_y, v_z\} \tag{1.1}$$

- *Polar State Space:* Primarily used for planar representation of simplified dynamics. The state space elements are,

$$\mathbf{x}_{\text{PSS}} = \{r, \theta, v, \psi\}, \tag{1.2}$$

  where r is the distance from origin (central body), θ is the right ascension (polar) angle, v is the magnitude of velocity in an inertial frame and ψ is the flight path angle. A Spherical State Space is the 3D version of the Polar State Space with the additional states: ϕ depicting declination and A_z depicting Azimuth. The state-space is represented as,

$$\mathbf{x}_{\text{SSS}} = \{r, \theta, \phi, v, \psi, A_z\}, \tag{1.3}$$

- *Classical Orbital Elements:* Another representation of the state space comes from integration constants appearing out of integration of the EOMs depicting keplerian motion. The classical orbital elements are represented by,

$$\mathbf{x}_{\text{COE}} = \{a, e, i, \Omega, \omega, M\}, \tag{1.4}$$

where a is semi-major axis, e is eccentricity, i is inclination, Ω is the Right Ascension of Ascending Node (RAAN), ω is the Argument of Periapse (AOP) and M is the Mean Anomaly. Note that instead of M, the True Anomaly ν or the Eccentric Anomaly E are also valid choices for the sixth element.

- *Modified Equinoctal Elements:* Finally, another mdoel that completely defines the state of the spacecraft is the Modified Equinoctal Elements (MEE) [42] and is represented by,

$$\mathbf{x}_{\text{MEE}} = \{p, f, g, h, k, L\}, \tag{1.5}$$

where p is the semi-latus rectum, L is the true longitude, (f, g) represent projection of the eccentricity vector onto an inertial frame while (h, k) are related to inclination.

The CSS representation, as mentioned before, is the most basic and most widely used in spacecraft trajectory optimization. The primary advantages associated with CSS is that it is easy to impose constraints like flyby distance as well as to model multi-body gravitational perturbations. Additionally, the resulting EOMs are singularity free. A strong disadvantage of CSS is that for multi-revolution motion large oscillations are observed in the Cartesian states compromising the robustness of any algorithms using CSS. The PSS state space are excellent for near-planar motion which could be a good option for interplanetary transfers, since they are approximately planar.

The COE are typically used in multi-revolution planeto-centric trajectories as they lead to a much faster integration of EOMs as compared to CSS. Moreover, it is intuitive and physically each element helps in describing the geometry of the trajectory. The first five elements are slowly evolving as compared to CSS which have all rapidly evolving elements. Unfortunately, the element set is riddled with singularities which can complicate numerical propagation of EOMs. For instance, at zero inclination ($i = 0$) RAAN loses its meaning whereas at zero eccentricity ($e = 0$) AOP is undefined. This limits the use of COEs in their classical form since a lot of orbits of interest like the GEO are equatorial and circular ($i = 0$, $e = 0$). As the elements approach these values during propagation, there is a large oscillation in some elements and numerical propagation cannot

continue in the vicinity of these singularities [43].

A lot of the issues with COEs are circumvented by the MEEs. Thus, they are also slow variables and present a much better option for representing planeto-centric trajectories. They are non-singular $\forall\ (e, i)$ and therefore have increased robustness. However, unlike COEs the MEEs have a less intuitive physical meaning. Both the COE and MEE are efficient sets for representing transfers with free final true longitude/mean anomaly but neither are attractive for problems with large perturbing forces such as the re-entry problem.

Thus, there are plenty of choices available for a suitable state-space representation. The ultimate choice is highly dependent on the specific mission or on the mission designer's experience. Note that, other forms of state representations may also be used for spacecraft trajectory optimization as described in [39]. These alternate forms are also well presented in a survey by Hintz [38]. Additionally, the spacecraft's mass evolution, m, is required to fully describe the dynamics of the system. It is used to compute the acceleration $\mathbf{a}_{\mathrm{T}}$ produced by the which is in turn dependent on the maximum thrust force $T_{\max}$ produced by the low-thrust propulsion subsystem, and it varies with respect to time as propellant mass is consumed.

1.4.1.2 Continuous Control Representation

A low-thrust engine is controlled by continuously varying the direction and magnitude of the acceleration produced by the engine. The engine acceleration, $\mathbf{a}_{\mathrm{T}}$, is expressed as a function of the thrust generated, current spacecraft mass and control variables as follows:

$$\mathbf{a}_{\mathrm{T}} = \frac{T_{\max}}{m}\,\sigma\,\hat{\mathbf{u}}(t). \tag{1.6}$$

In the above expression, $\hat{\mathbf{u}}(t)$ is a unit vector that can be represented the direction cosines describing the direction of the thrust pointing vector with respect to any convenient orthogonal set. Alternatively, the two thrust steering angles namely, azimuth and declination can be used to define the thrust vector. This leads to a reduction in the control space dimension from three to two and avoid any path constraints on the components of $\hat{\mathbf{u}}(t)$.

Thus, a varied selection of control variables are possible. During preliminary design, mission designers may use heuristic control laws, where the thrust direction is prescribed as a function of some parameters. Heuristic control laws generally yield sub-optimal trajectories, but the results are deemed acceptable for preliminary design. Some popular choices are discussed below,

- *Blended Control:* The optimal thrust steering that maximize the variation of a set of orbital elements independently, $\mathbf{u}_{\mathrm{x}}(\mathbf{x}) \in \mathbb{R}^n$ and computed as a function of the spacecraft position. The complete control law is devised from these individual steering laws to simultaneously modify all elements of the state vector by using a weighted sum. It can be expressed as,

$$\mathbf{u}^*(\mathbf{x}, t) = \sum W_x(t)\, \mathbf{u}_{\mathrm{x}}(\mathbf{x}) \tag{1.7}$$

  where W_x are the unknown weights to be determined. This approach is commonly used with COEs or MEEs in a planeto-centric setting where rendezvous with a particular state is not necessarily a boundary condition.

- *Pontryagin's Minimum Principle (PMP):* This is based on Calculus of Variation development using a pre-defined cost functional and uses Lagrange multipliers (λ) to augment other constraints to the functional. For more details and derivations from first principle, the reader is referred to these excellent references [44, 45, 46]. First order necessary conditions are derived which result in the following expression for the optimal thrust steering direction of a spacecraft in order to minimise time-of flight,

$$\mathbf{u}^*(\lambda, t) = -\frac{M^T(x)\lambda(t)}{\|M^T(x)\lambda(t)\|} \tag{1.8}$$

  where $M(x)$ is a state-dependent matrix whose elements are governed by the choice of state space representation and $\lambda(t)$ denotes the Lagrange multipliers to incorporate the path costs. While this approach along with the rest of the necessary conditions, gives locally optimal solutions and effective for use with COEs and MEEs, formulation is not always straightforward

when a new constraint is added or when the objective function is updated. The direction of the thrust vector was named "primer vector" by Lawden [25].

- *Lyapunov Control (LC):* : A scalar Lyapunov function defined as an energy-like (i.e., a positive-definite) function of the state and defined as, $V(\Delta\mathbf{x}(t), W_x) \in \mathbb{R}$ where $\Delta\mathbf{x} = \mathbf{x}(t) - \mathbf{x}_f$ with $\mathbf{x}_f$ being the target state.

  W_x is a positive definite matrix that can be represented using a set of unknown parameters which can be assigned or determined as part of the solution. The Lyapunov function must satisfy the following,

$$\dot{V}(W_x) = \vec{\boldsymbol{\nabla}}_x V(\Delta\mathbf{x}, W_x) f(\mathbf{x}, \mathbf{u}) \leq 0 \tag{1.9}$$

  Finally, the Lyapunov optimal thrust steering law is obtained by minimizing the variation of $\dot{V}$ with respect to $\mathbf{u}$. This is mathematically expressed as,

$$\mathbf{u}^* = arg \min_u \vec{\boldsymbol{\nabla}}_x V(\Delta\mathbf{x}, W_x) f(\mathbf{x}, \mathbf{u}). \tag{1.10}$$

  It must be noted that this control law drives the spacecraft to the desired final condition without explicit inclusion of the final boundary conditions in the problem.

- *Other Control Functions:* Some other control functions, associated with direct methods, but not discussed in detail here include *Shape Based* approaches and *Finite Fourier Series* (FFS) based control where in the former, the state is represented using a predefined form with parameters embedded in the trajectory definition and need to be determined. On the other hand, the latter has a FFS representation of the control law where the coefficients need to be determined to solve for control.

1.4.1.3 Discrete Controls

Discrete controls capture switching of controls between bounds of allowable control or change engine operating modes. The switch is modeled using a binary control input $\zeta \in \{0, 1\}$. For instance, $\zeta = 0$ signifies coast of spacecraft whereas $\zeta = 1$ signifies thrusting segments. Additionally, other decisions regarding changing between engine operating modes (combination of maximum thrust and specific impulse (I_{sp})) can also be covered using this approach. In this dissertation, it is demonstrated that this method is also effective, when used in a Composite Smoothing Control (CSC) [47] setting, in making decisions regarding control authority based on operational constraints like spacecraft coasting while flying through an eclipse. Typically, the switching is captured using a switching function (e.g., tangent hyperbolic [48, 49, 50, 51], logarithmic [52, 50] etc.) and a smoothing parameter (ρ) is embedded in the switching function to control function smoothness and perform continuation to gradually approach the sharply switching discontinuous control.

1.4.1.4 Representation of the Dynamics

Propagating or integrating the state equations of motion along with the differential equation defining mass flow rate is essential. For any numerical optimization technique to work, numerous such propagation are required. This becomes especially time-consuming in case the fidelity of the EOMs is high. While the achieved control is accurate and robust to perturbations since most of the perturbing effects are already considered in the optimization process, the numerical run-times are infeasible for a preliminary design problem where quick trade-off solutions are sought.

Consider a spacecraft moving under the influence of gravitational attraction from N-bodies, acceleration from a low-thrust engine and other perturbing effects from space environment (see Figure 1.13).

The dynamics typically defines the N-body system also known as the Perturbed Restricted N-Body Problem (PRNBP). The EOMs with respect to an inertial Cartesian frame are mathematically expressed as,

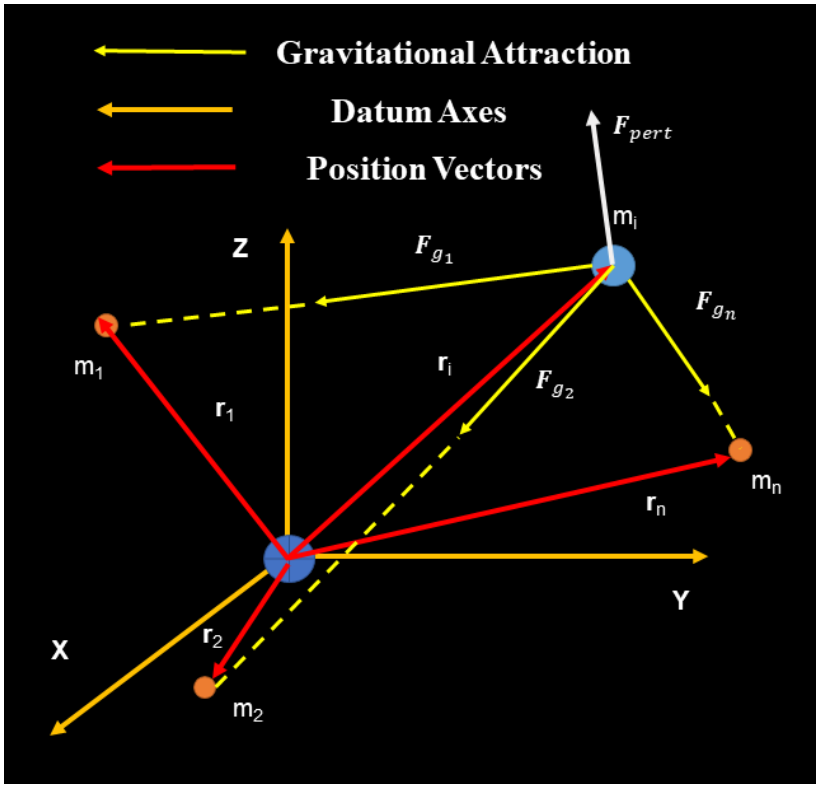

Figure 1.13: The 'N-body' Problem Schematic

$$\dot{\mathbf{v}} = -\sum_{i=1}^{n} \frac{\mu_i(\mathbf{r} - \mathbf{r}_i)}{|(\mathbf{r} - \mathbf{r}_i)|^3} + \mathbf{a}_T + \mathbf{a}_P, \quad \dot{\mathbf{r}} = \mathbf{v}, \quad \dot{m} = \dot{m}(\mathbf{x}, \mathbf{u}, t). \tag{1.11}$$

In this equation, μ_i and $\mathbf{r}_i$ depict the gravitational constant and the position vector of the i^{th} body and $\dot{m}$ represents the propellant consumption rate. Note that $\mathbf{a}_T$ is the acceleration due to the propulsion system thrusting whereas, $\mathbf{a}_P$ include any perturbations experienced by the spacecraft other than the gravitational perturbations. Also note that, the EOMs can be formulated using other state-space representations like COEs, MEEs etc. using Lagrange's Planetary Equations [53, 41].

As discussed above, for preliminary mission design, a simplified or surrogate model is sought. Firstly, the number of gravitational attracting bodies can be reduced to an acceptable number. This decision is made by studying the relative perturbing acceleration on the spacecraft by each body in our Solar System. As an example, gravitational perturbing acceleration on a spacecraft in a 500 km geocentric orbit due to other Solar System Bodies (SSBs) in decreasing order are listed in Table

1.1.

Table 1.1: Gravitational Perturbation due to SSBs on a 500 km Earth satellite.

SSB	**Acceleration** (km/s^2)
Two-Body	0.89
Spherical Harmonics	10^{-3}
Sun	6×10^{-4}
Moon	3.3×10^{-6}
Jupiter	3.2×10^{-8}
Venus	1.9×10^{-8}
Saturn	2.3×10^{-9}
Mars	7.1×10^{-10}
Mercury	2.6×10^{-10}
Uranus	8×10^{-11}
Neptune	3.6×10^{-11}
Pluto	10^{-12}

Based on the numbers it is clear that modeling a transfer between Earth Orbits, the primary effects are the Two-Body effects as well as gravitational anomalies of the Earth modelled using Spherical Harmonics. Based on the radial distance to a body whose gravity field is represented by spherical harmonics, it is possible to use radial adaptation [54] to select the degree required to model acceleration to a pre-defined tolerance. The Sun is the most dominant third body for near-earth orbits followed by the Moon. On the other hand, a transfer that takes place further away from the Earth and closer to the Moon might necessitate inclusion of the Moon as a third body before the Sun. PR3BP and R2BP are some simplified models that are regularly used in the cases discussed above. On the other hand, for interplanetary trajectories, patched conics technique is popular where the entire trajectory is split into different segments and patched together at the boundary. The segments are modelled using R2BP i.e., trajectory changes from heliocentric to planetocentric as the spacecraft moves into a particular planet's sphere of influence. Additionally, analytical solutions, asymptotic analysis and averaging techniques are also employed to speed up the solution process even further.

1.4.2 Objective Functions

The objective function or the performance index represents the cost or benefits of the mission depending on whether the problem is a minimization or a maximization problem respectively. In most trajectory optimization problems the objective functions can be broadly classified into two types of objectives, pertaining to spacecraft guidance and control, one where it is a function of the control effort and the other when it is a function of the time of operation or time required to accomplish the mission objectives. While the former is related to the spacecraft thrust acceleration levels or propellant mass consumed, $J = m(t_0) - m(t_f)$, the latter can be represented by a simple Mayer form $J = t_f - t_0$ i.e., the time of flight. More generally, the performance index can be a general function of the state and control variables, and furthermore multiple optimization goals can be considered. Depending on the number of objectives being considered, the problem can be identified as single-objective or multiple-objective optimization problem.

For a single-objective optimization problem, in essence, the goal is to look for a solution in the feasible set which provides an extremal value for the scalar objective function. From a mathematical stand-point a solution $(\mathbf{x}^*, \mathbf{u}^*)$ is optimal for a minimization problem, if it satisfies,

$$J^*(\mathbf{x}^*, \mathbf{u}^*) \leq J(\mathbf{x}, \mathbf{u}). \tag{1.12}$$

Single objective optimization problems are obviously easier to solve than their multi-objective counterparts where the aim is to find an extremal control which maximizes/minimizes a vector function formed by multiple conflicting criteria like, $J = [J_1, J_2, ..., J_n]$. The solution consists of a $n - 1$ dimensional hyper-surface known as the Pareto-optimal set, or Pareto front [55].

A feasible solution $(\mathbf{x}^*, \mathbf{u}^*)$ is defined to be weak Pareto-optimal if there is no other feasible solution $(\mathbf{x}, \mathbf{u})$ which simultaneously improves upon all the objectives in the vector objective function. This is mathematically represented as,

$$J_i^*(\mathbf{x}^*, \mathbf{u}^*) \leq J_i(\mathbf{x}, \mathbf{u}) \ \ \forall \ \ i \in [1, 2, ...n]. \tag{1.13}$$

Although multi-objective optimization problems are much harder to solve and are significantly more computationally intensive, preliminary mission design greatly benefits from the trade-offs provided by multi-objective optimization. In reality, most trajectory optimization problems are in-fact multi-objective, even if not formally cast as a multi-objective optimization problem. A relevant example can be described by the scenario where a spacecraft is travelling from the Earth to the Moon and it is required that the spacecraft utilises a minimum amount of fuel, flies through the least number of eclipses, minimises the maximum eclipse duration and also minimises time. It is obvious that one or more of these objectives are conflicting and therefore a Pareto-front depicts the trade-offs in the set of feasible solution space. Figure 1.14 depicts a scenario where trade-offs between propellant mass consumed and time of flight is captured as a Pareto-front. Note that spacecraft flying design A is fast but uses up more propellant whereas, design C is the slowest but provides larger propellant savings.

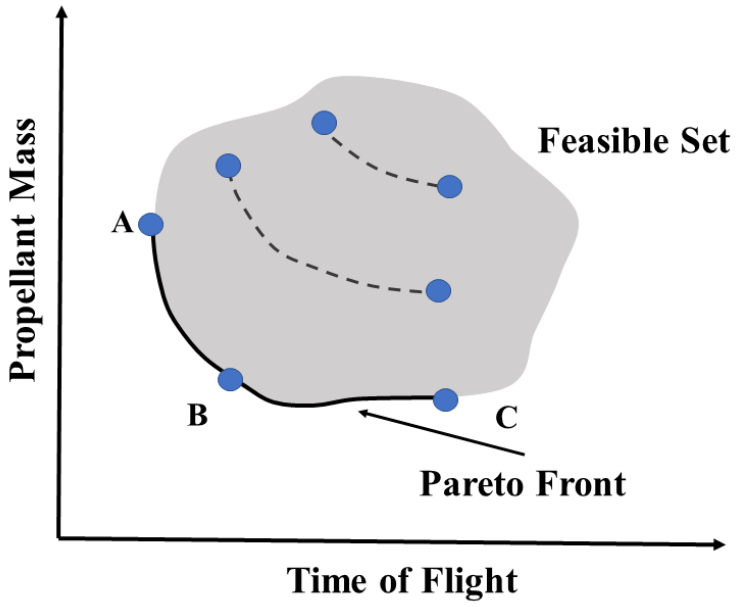

Figure 1.14: Pareto-Front Schematic : Spacecraft Trajectory Optimization Problem

It is immediately obvious that a feasible set solution space of the kind depicted in Figure 1.14

would be of tremendous help for preliminary mission design and are highly sought after. An actual mission is rarely flown as a purely fuel- or time- optimal trajectory and such trade-offs are really important.

1.4.3 Optimal Control Problem: Solution Approaches

After discussing state-space representation using various element sets, control representation, dynamics representation and objective functions, it is required that we figure out appropriate methods to solve the problem we have been striving to construct. The chosen solution method impacts the flexibility, robustness and automation of the method. Typically, low-thrust trajectory optimization methods are formulated as continuous optimal control problems. Solutions to these continuous problems are sometimes used as a first guess for the more complicated hybrid optimal control problems associated with final mission trajectory design.

Analytical and numerical approaches are available and have been researched to solve these optimal control problems. Analytical expressions, although highly desirable are very difficult to obtain without simplifying assumptions, frequently to the point where the problem is morphed into something that is very far from reality. On the other hand, numerical approaches are being constantly researched and can be classified into three sub-categories: indirect approach, direct approach and dynamic programming. These are discussed briefly for the sake of brevity below,

- *Indirect Approach:* Indirect approaches are based on analytically derived first-order necessary conditions. Solution to a Two-point Boundary Value Problem (TPBVP) is derived from the PMP necessary conditions and can be achieved by various numerical methods [56]. States and co-states need to be solved for, simultaneously, to generate an optimal trajectory which obeys the Euler-Lagrange equation. The minimum principle helps obtain control as an explicit or implicit function of states and co-states. An additional set of boundary constraints called the transversality conditions [44] must be satisfied for special cases of the boundary conditions.

- *Direct Approach:* A direct approach focuses on transcribing the continuous optimal control

problem into a Non-Linear Programming (NLP) problem. Transcription essentially means discretizing the state and control variables in time and the NLP determines unknown decision variables that satisfy a set of non-linear algebraic constraints. The optimal solution needs to also satisfy the first order necessary conditions i.e., the Karush-Kuhn-Tucker (KKT) conditions [57, 58]. NLP is numerically solved using various well-known methods.

- *Dynamic Programming:* Dynamic programming method is based on Bellman's principle of optimality. It can be used for both discrete and continuous time systems. The continuous time equivalent led to the Hamilton-Jacobi-Bellman (HJB) equation and the solution process requires initially solving a set of partial differential equations. Discretization is typically required to approximate the solution of the HJB equation.

Single shooting is the most common technique employed for solving direct and indirect problems. For indirect approach, the trajectory is usually integrated forward in time from t_0 to t_f using an initial guess for the adjoint variables i.e., the Lagrange multipliers or the so called co-states as they are unknowns of the problem. Boundary conditions or constraints are imposed on the trajectory at t_f and once the algorithm converges to a set of co-states, a locally optimal trajectory and control are found by propagating from the converged solution for the entire duration i.e, t_f. While this sounds relatively straightforward in terms of problem formulation, multi-rev trajectories are hard to optimize using single shooting and local extrema frequently exist. Techniques such as pseudo arc-length continuation [59] and homotopy [60, 61] methods alleviate the convergence issues in many cases. Moreover, challenges associated with discontinuous controls and unreachable boundary conditions arise frequently and both heuristic insights and robust algorithms are needed to make reliable progress.

To alleviate convergence issues, multiple shooting techniques are employed. In this method the time interval $[t_0, t_f]$ is broken up into N+1 sub intervals. The trajectory is then integrated over each sub-interval $[t_i, t_{i+1}]$. Initial co-states at each sub-interval are the unknowns and need to be determined. Additionally, continuity is ensured by enforcing additional conditions at sub-interval interfaces. Qualitatively, multiple-shooting reduces sensitivity at the expense of increasing

dimensionality.

For collocation [62], the states (and co-states) are discretized over a predefined time-grid, such that the state and co-state differential equations are evaluated at prescribed time-points (nodes). The errors should be zero at each node, so the system-governing equations are transformed into discrete defect constraints. The state and co-state variables are usually modelled as orthogonal polynomials and the coefficients are the unknowns which can be solved for by enforcing the nodal co-location constraints. Local and global collocation methods are two choices depending on the choice of quadrature and orthogonal polynomials to approximate the differential equations.

1.4.4 Existing Tools

Several preliminaries required for formulating and solving low-thrust optimization problems have been explained in the previous sections. In order to put in context the importance of the work which will be presented in the later sections, it is important to consider a survey of existing tools and identify the gaps that need to be filled. In this section, existing state-of the art tools are tabulated with main characteristics and limitations highlighted. Table 1.2 depicts tools that implement indirect methods of low-thrust trajectory optimization. Note that in the following tables, IT : Interplanetary, PC: Planetocentric, G: General , PR-NBP: Perturbed N-body Problem, PR-TBP: Perturbed Two-body Problem, AVG: Averaging.

Table 1.2: Some state-of the art tools using Indirect Method for Trajectory Optimization.

Name	**Ref**	**Proprietor**	**Approach**	**Dynamics**	**Transfers**
VARITOP	[63]	JPL	Single Shooting	PR-TBP	IT
SAIL	[64]	JPL	Single Shooting	PR-TBP	IT
ITOP	[65]	Aerospace Corp.	Single Shooting	PR-TBP	PC
MIPELEC	[66]	CNES	Single Shooting	PR-TBP + AVG	PC
-	[67]	Meng et al.	Multiple Shooting	PR-TBP	PC
-	[68]	Olympio	Gradient Method	PR-NBP	G

The main advantage of using indirect methods is that the solution is assured to satisfy the first

order necessary conditions for optimality. Additionally, the approach itself might provide insights into the physical characteristics of the problem. The main drawback is the need to find analytical derivations of the co-state and control differential equations, which can be difficult if the dynamical model being considered for the OCP is complicated. Numerical solution requires an appropriate guess for the initial co-states which is not intuitive. Moreover, the domain of convergence is usually small but can be somewhat alleviated by appropriate normalizations. Finally, when inequality path constraints are included, the formulation and numerical solution becomes even more challenging.

On the flip side, direct methods do not require analytical derivatives to establish auxiliary equations. The direct methods are often easier to initialize with a larger domain of convergence. Although, the required initial estimates may be hard to guess for multi-rev trajectories with numerous thrust and coast arcs. Therefore, they might not converge to the optimal solution if the assumed form of the control sequence is incorrect but they frequently provide at-least a sub-optimal solution unlike indirect methods. Another important advantage is that these methods handle general constraints effectively due to the nature of the approach. Table 1.3 depicts some of the more frequently used state-of the art trajectory design tools based on direct methods.

Table 1.3: Some state-of the art tools using Direct Method for Trajectory Optimization.

Name	**Ref**	**Proprietor**	**Approach**	**Dynamics**	**Transfers**
ASTOP	[69]	Space Flight Solutions	Single Shooting	PR-NBP	IT
COPERNICUS	[70]	JSC	Multiple Shooting	PR-NBP	G
GMAT	[71]	NASA	Collocation	PR-NBP	G
MALTO	[72]	JPL	Multiple Shooting	Kepler Model	IT
MANTRA	[73]	ESA	Multiple Shooting	PR-NBP	G
STK	[74]	AGI	Collocation	-	G

In this dissertation, efficient trajectory design of cislunar trajectories leveraging invariant manifolds as long terminal coast arcs is primarily sought. The low-thrust trajectory optimization problem is formulated using the MEE set of coordinates, owing to better performance for multi-rev trajectories. Moreover, the problem is formulated using the indirect method and the resulting

TPBVP is solved using numerical techniques. The methodology developed herein are widely applicable across different underlying dynamical models which have been elucidated by the case studies presented in the results section.

The dissertation delves into the literature of computing invariant manifolds in the CR3BP system for various periodic orbits but then builds on the existing literature by providing a methodology to approximate the manifold trajectories in a more complex ephemeris driven dynamical system by computing manifold "analogues". Patch-conditions are heuristically selected and an optimal control problem is formulated and solved to merge onto the manifolds via the pre-computed patch points. Due to the contribution of approximating manifolds in a higher fidelity system, the overarching methodology is robust and efficient. Moreover, a cascading hybrid optimization algorithm has also been presented which embeds the shadow constraints into the indirect formulation and converges to eclipse conscious, optimal trajectories, a feature lacking in most state-of the art tools. It is hereby noted that the heuristic selection of patch-states can be replaced by a more systematic optimization problem which finds a globally optimal patch state on the bundle of manifold trajectories. This approach is a part of future investigations and as such is beyond the scope of this dissertation.

To briefly outline the remainder of this dissertation, Chapter 2 discusses the various simplified dynamical systems along with the periodic orbits that exist around their equilibrium points as well as existence of invariant manifold bundles. Chapter 3 discusses the computation methodology of invariant manifolds and highlights in detail the advantages of leveraging them in the trajectory design process by performing a case study on the double pendulum system. It also discusses the methodology of computing manifold "analogues" in a high fidelity system followed by the heuristic methods for identifying patch states. Chapter 4 discusses various numerical techniques crucial to solving multi-rev low-thrust transfer trajectory design problem like homotopy methods and arc-length continuation while also discussing an embedded indirect formulation of time-optimal and fuel-optimal trajectory design problems conscious of spacecraft eclipses. Finally, all the developed novel methodologies are applied to three distinct problems in the cislunar domain which encom-

pass the various choices of ‘origin-target’ orbits as well as dynamical systems and are presented in Chapter 5.

2. SIMPLIFIED MODELS, PERIODIC ORBITS AND INVARIANT MANIFOLDS

In the previous chapter, we talked about the various dynamical system simplifications that would lead to more robust algorithms which are amenable to numerical treatment. In this chapter, we will discuss some prominent simplifications of a high-fidelity model ('N-Body System') and use them to study equilibrium points that exist in such a system, periodic orbits around these equilibrium points and introduce manifold theory by looking at methods for computation of these space trajectories.

Instead of considering a dynamical system comprising of N gravitationally interacting bodies, which is a complicated system, we first consider a simplified system which is higher fidelity than a two-body Keplerian system. Let us consider a three-body system. The system is defined as [75, 76], "Three particles move in space under their mutual gravitational attraction; given their initial conditions, determine their subsequent motion." This problem has been of interest for many mathematicians and physicists since the mid 1600s. The attempts at solving this problem began with none other than Newton himself [77] while he studied the *inequalities* in lunar motion.

In the 1740s the problem was formulated as the search for solutions of a system of ordinary differential equations by the works of Euler, Clairaut and d'Alembert. Much developed by Lagrange, Laplace and their followers. Lagrange won the 1776 Paris Prize for his study of the libration points and their stability. The mathematical theory entered a new era at the end of the 19th century with the works of Poincaré (1890) and since the 1950s with the development of computers. The general three-body problem involves 18 first order differential equations which through use of conservation equations and calculus, can be reduced to 6. Closed form analytical solutions like for the two-body problem is not possible due to a lack of conserved quantities to simplify the system further. In fact, Poincaré provided rigorous proof that the n-body problem, for n>2, is not analytically integrable. However, many restricted cases have been studied with different simplifications to understand the motion of a spacecraft in such a system for these limited cases.

2.1 The Circular Restricted Three Body Problem (CR3BP)

The CR3BP system is defined as consisting of two large masses that orbit their common barycenter in circular orbits. A third body, significantly smaller than the other two, is introduced in the system and the motion of this body with negligible size and mass, as it is acted upon by the gravitational force from the two massive bodies needs to be defined. Although, the definition itself 'restricts' the physics significantly which to the naked eye would seem is almost to the point of impracticality, there are many systems in our solar system to which these assumptions apply well. To a good first approximation, the trajectories of the Apollo command module can be designed based on this assumption. This is largely due to the fact that most planets, including the Earth, are in a near-circular heliocentric orbit and the Moon is also in a near-circular orbit around the Earth. While the deviations from the defined CR3BP behaviour is not negligible, the relative ease of getting solutions in this simplified model together with the truth that the approximation is good enough to provide important insights into system-behavior, makes it's study important and significant.

Consider a mechanical system with three gravitationally interacting masses m_1, m_2 and m. Assume that $m << m_1, m_2$ such that m has a negligible effect on the motion of m_1 and m_2. Generally, the motion is solved in three dimensions but typically since the motion in z is fairly trivial, it will be omitted from the initial discussion. The two masses m_1 and m_2 are assumed to move according to Keplerian motion along a circular orbit of radius R. The distances of the two masses m_1 and m_2 from their barycenter can be defined as,

$$r_1 = \frac{R * m_2}{(m_1 + m_2)} \text{ and } r_2 = \frac{R * m_1}{(m_1 + m_2)} \text{ respectively,} \tag{2.1}$$

where R is the distance between m_1 and m_2 (Assume $m_1 > m_2$ and m_1 is the primary while m_2 is the secondary). Figure 2.1 depicts the Circular Restricted Three Body system. The above relations also give,

$$\frac{r_1}{r_2} = \frac{m_2}{m_1}. \tag{2.2}$$

R is constant due to the circular assumption and therefore the masses orbit the barycenter at the same constant angular velocity $\tilde{\omega}$. For proper scaling using normalization, assume that $R = r_1 + r_2 = 1$. This is typically done as it results in a scaling that is easier to analyze and deduce results rather than dealing with the large distance scale in astronomical units that are typical of the three body problem. We define a new parameter $\mu = \frac{m_2}{m_1+m_2}$. Since $R = r_1 + r_2 = 1$, the coordinates of $M_1 = (-r_1, 0) = (-\frac{R*m_2}{m_1+m_2}, 0) = (-\mu, 0)$ and that of $M_2 = (r_2, 0) = (1 - r_1, 0) = (1 - \mu, 0)$.

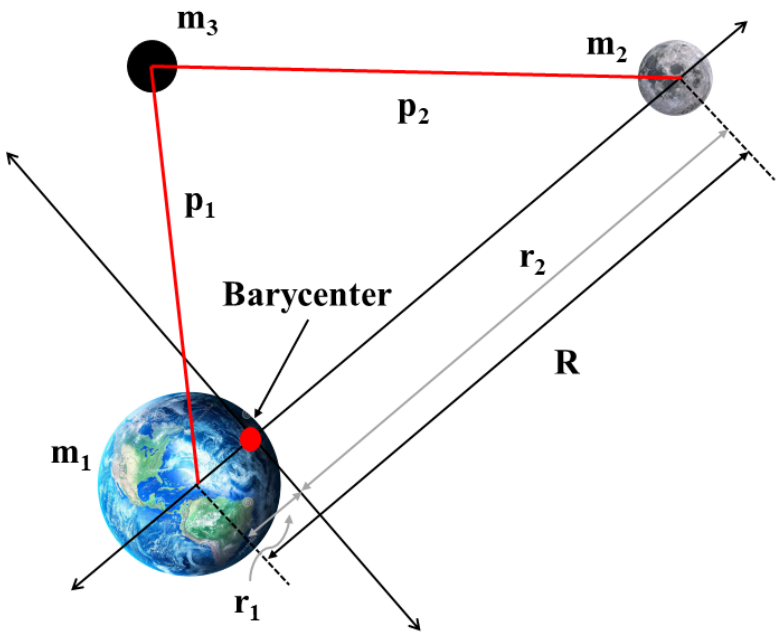

Figure 2.1: Circular Restricted Three Body Problem : System Schematic

2.1.1 Equations of Motion

In this section, the governing EOMs for the mass m are derived from first principles. The method used to derive the EOMs is Lagrangian Mechanics [78]. The Kinetic Energy of m in an inertial frame centered at the barycenter is,

$$T = \frac{1}{2} m_3 (\dot{x}^2 + \dot{y}^2). \tag{2.3}$$

The Potential Energy in this system is purely gravitational and is mathematically represented as,

$$V = -\frac{Gm_3m_1}{p_1} - \frac{Gm_3m_2}{p_2}, \tag{2.4}$$

where the radial distance are $p_1 = \sqrt{(x-x_1)^2 + (y-y_1)^2}$ and $p_2 = \sqrt{(x-x_2)^2 + (y-y_2)^2}$ and represent the distance between m and the primary and secondary bodies in the system respectively. Let us consider motion in a barycentric rotating frame where the primary and secondary masses are stationary. We will reap the rewards of this transformation later. Defining the rotational coordinates in terms of the inertial coordinates, angular velocity and time, we have,

$$x'(t) = x\cos\tilde{\omega}t - y\sin\tilde{\omega}t \tag{2.5}$$

$$y'(t) = y\cos\tilde{\omega}t + x\sin\tilde{\omega}t, \tag{2.6}$$

where as previously defined $\tilde{\omega}$ is the system angular velocity. The Lagrangian $L = T - V$ expressed in rotating coordinates is,

$$L = \frac{1}{2}m_3(\dot{x}^2 + \dot{y}^2 + 2x\tilde{\omega}\dot{y} - 2y\tilde{\omega}\dot{x} + \tilde{\omega}^2(x^2 + y^2)) - \frac{Gm_3m_1}{p_1} - \frac{Gm_3m_2}{p_2}. \tag{2.7}$$

Note that the primed coordinates have been eliminated in favor of un-primed quantities. Now, Lagrange's equation is stated mathematically as,

$$\frac{d}{dt}\Big(\frac{\partial L}{\partial \dot{q}_j}\Big) - \frac{\partial L}{\partial q_j} \tag{2.8}$$

where $q'_j s$ are generalized coordinates (x and y in this case). Using Lagrange's equation [78] on the derived Lagrangian for the system in rotating coordinates gives the EOMs in rotating coordinates as,

$$\ddot{x} = 2\tilde{\omega}\dot{y} + x\tilde{\omega}^2 - \frac{Gm_1(x - x_1)}{p_1^3} - \frac{Gm_2(x - x_2)}{p_2^3} \tag{2.9}$$

$$\ddot{y} = -2\tilde{\omega}\dot{x} + y\tilde{\omega}^2 - \frac{Gm_1(y - y_1)}{p_1^3} - \frac{Gm_2(y - y_2)}{p_2^3}. \tag{2.10}$$

Analogous to the classical two-body problem, the EOMs described above is that the equations are independent of the mass of the third body whose motion it describes i.e., m. Invoking Kepler's third law for m_1 and m_2, given that $\frac{m}{m_1}$ and $\frac{m}{m_2}$ are negligible, we have,

$$\tilde{\omega}^2 = \frac{G(m_1 + m_2)}{(r_1 + r_2)^3}. \tag{2.11}$$

Since, $r_1 + r_2 = 1$, we can simplify this expression by eliminating G in favor of $\tilde{\omega}$,

$$G = \frac{\tilde{\omega}^2}{(m_1 + m_2)}. \tag{2.12}$$

Plugging this in the EOMs and noting from before that $\mu = \frac{m_2}{m_1 + m_2}$, we have,

$$\ddot{x} = 2\tilde{\omega}\dot{y} + x\tilde{\omega}^2 - \frac{\tilde{\omega}^2(1 - \mu)(x - x_1)}{p_1^3} - \frac{\tilde{\omega}^2\mu(x - x_2)}{p_2^3} \tag{2.13}$$

$$\ddot{y} = -2\tilde{\omega}\dot{x} + y\tilde{\omega}^2 - \frac{\tilde{\omega}^2(1 - \mu)(y - y_1)}{p_1^3} - \frac{\tilde{\omega}^2\mu(y - y_2)}{p_2^3}. \tag{2.14}$$

$(\dot{\cdot}) = \frac{d}{dt}$ for Equations (2.13) and (2.14). Let the time variable be expressed as $t = \frac{1}{\tilde{\omega}}\tau$. This scaling leads to the following set of equations,

$$\tilde{\omega}^2\ddot{x} = 2\tilde{\omega}^2\dot{y} + x\tilde{\omega}^2 - \frac{\tilde{\omega}^2(1 - \mu)(x - x_1)}{p_1^3} - \frac{\tilde{\omega}^2\mu(x - x_2)}{p_2^3} \tag{2.15}$$

$$\tilde{\omega}^2\ddot{y} = -2\tilde{\omega}^2\dot{x} + y\tilde{\omega}^2 - \frac{\tilde{\omega}^2(1 - \mu)(y - y_1)}{p_1^3} - \frac{\tilde{\omega}^2\mu(y - y_2)}{p_2^3}. \tag{2.16}$$

Now, it is understood that $(\cdot)$ has been re-defined to mean $\frac{d}{d\tau}$ in Equations (2.15)-(2.16) and hereafter in this section. All terms contain $\tilde{\omega}$ in these equations and can be cancelled out from both sides giving us the following scaled set of non-dimensional EOMs,

$$\ddot{x} = 2\dot{y} + x - \frac{(1-\mu)(x-x_1)}{p_1^3} - \frac{\mu(x-x_2)}{p_2^3} \tag{2.17}$$

$$\ddot{y} = -2\dot{x} + y - \frac{(1-\mu)(y-y_1)}{p_1^3} - \frac{\mu(y-y_2)}{p_2^3}. \tag{2.18}$$

Since the position of the primary and secondary masses is stationary with respect to the barycentric co-rotating frame, their position can be defined arbitrarily and for making the EOMs well structured, they are assumed to lie on the x-axis of this rotating coordinate system. Using the definition of μ and expressions for x_1 and x_2 derived before in terms of μ, we finally have the usable set of EOMs,

$$\ddot{x} = 2\dot{y} + x - \frac{(1-\mu)(x+\mu)}{p_1^3} - \frac{\mu(x-1+\mu)}{p_2^3} \tag{2.19}$$

$$\ddot{y} = -2\dot{x} + y - \frac{(1-\mu)y}{p_1^3} - \frac{\mu y}{p_2^3}. \tag{2.20}$$

These equations show that acceleration of the mass m in the CR3BP depends on three separate terms, coriolis, centrifugal and gravitational. The coriolis force acts in a direction perpendicular to the rotational axis and the velocity of m in the rotating frame and is proportional to the object's speed in the rotating frame. The centrifugal force acts outward in the radial direction. Table 2.1 depicts μ for some primary-secondary pairs in our solar system.

2.1.2 Lagrange Points

With the derived EOMs, the next logical step is to derive as much insights as possible into the behavior of the CR3BP dynamical system. As standalone differential equations, the first observation is that the motion in the plane containing the bodies m_1 and m_2 is coupled on the x-y

Table 2.1: μ for some Primary-Secondary pairs in our Solar System.

System	m_1 (kg)	m_2 (kg)	μ
Sun-Earth	1.9891×10^{30}	5.9736×10^{24}	3.0039×10^{-7}
Earth-Moon	5.9736×10^{24}	7.3477×10^{22}	1.2151×10^{-2}
Sun-Jupiter	1.9891×10^{30}	1.4143×10^{27}	7.1904×10^{-4}
Sun-Saturn	1.9891×10^{30}	5.846×10^{26}	2.8571×10^{-4}
Saturn-Titan	5.846×10^{26}	1.3452×10^{23}	2.366×10^{-4}

directions. The motion nevertheless remains unintuitive and heuristic insights just from the EOMs are impossible to derive. Simulations using random initial conditions for the three masses and random ratios between the masses lead to chaotic behaviour in most cases unless these parameters are meticulously chosen.

Euler and Lagrange proved the existence of five distinct equilibrium points for the mass m in the CR3BP system. The existence of these points arises out of a balance between the gravitational attraction from the larger bodies and the centrifugal forces observed in the co-rotating coordinate frame. These equilibrium points are known as Lagrange Points [79]. In order to solve for the location of these points in the given system, the conditions for an equilibrium points are levied on the EOMs at said locations. This essentially means that velocity and acceleration of m at these locations is identically zero in the barycentric rotating reference frame. Therefore, using the previously derived EOMs and setting all dot quantities to zero we have,

$$x = \frac{(1-\mu)(x+\mu)}{p_1^3} + \frac{\mu(x-1+\mu)}{p_2^3} \tag{2.21}$$

$$y = \frac{(1-\mu)y}{p_1^3} + \frac{\mu y}{p_2^3}. \tag{2.22}$$

Note that these algebraic equations remain non-linear in (x, y) since the p_i are non-linear functions of (x, y). Combining the two equations, Euler (1765) discovered the three collinear Lagrangian Points ($y = 0$) i.e., named as L_1, L_2 and L_3. The following equation is to be solved for x,

$$x - \frac{(1-\mu)(x+\mu)}{|x+\mu|^3} + \frac{\mu(x-1+\mu)}{|x-1+\mu|^3} = 0 \tag{2.23}$$

This equation has only real roots and can be solved for numerically to locate the three collinear Lagrange points. Note that the parameter μ appears in the equation and therefore the primary-secondary pair of interest strongly dominates the location of the system equilibrium points, as is evidenced in Table 2.2. Typically, L_1 and L_2 lie on either side of the secondary while L_3 lies on the far side ("back-side") of the primary (see Figure 2.2). Note that we follow the predominantly used nomenclature for the Lagrange Points.

Table 2.2: Common systems and location of the co-linear Lagrange Points.

System	μ	L_1	L_2	L_3
Sun-Earth	3.0039×10^{-7}	0.995363	1.004637	-1.0001
Earth-Moon	1.2151×10^{-2}	0.836915	1.15568	-1.00506
Sun-Jupiter	7.1904×10^{-4}	0.938466	1.06267	-1.00030
Sun-Saturn	2.8571×10^{-4}	0.95475	1.04525	-1.00012
Saturn-Titan	2.366×10^{-4}	0.9575	1.0425	-1.0001

Lagrange in 1772 discovered the other two equilibrium points, namely, L_4 and L_5. He found them to exist at the unoccupied vertex of an equilateral triangle with the two larger bodies at two vertices. The location of L_4 is at $x = \mu - \frac{1}{2}, y = \frac{\sqrt{3}}{2}$ whereas the location of L_5 is at $x = \mu - \frac{1}{2}, y = -\frac{\sqrt{3}}{2}$.

Note that in some cases when the value of μ for the chosen primary-secondary pairs is very small like in the case of the Sun-Earth system, in non-dimensional units, the location of the Lagrange points L_1 and L_2 grow closer to the secondary compared to when μ is larger as in the case of the Earth-Moon system. In the succeeding sections, the stability of the mass m at these Lagrange points are discussed followed by the existence of periodic orbits around them in the CR3BP which pave the way for a discussion on manifold theory and the computation of *stable-unstable manifold pairs* for a particular periodic orbit.

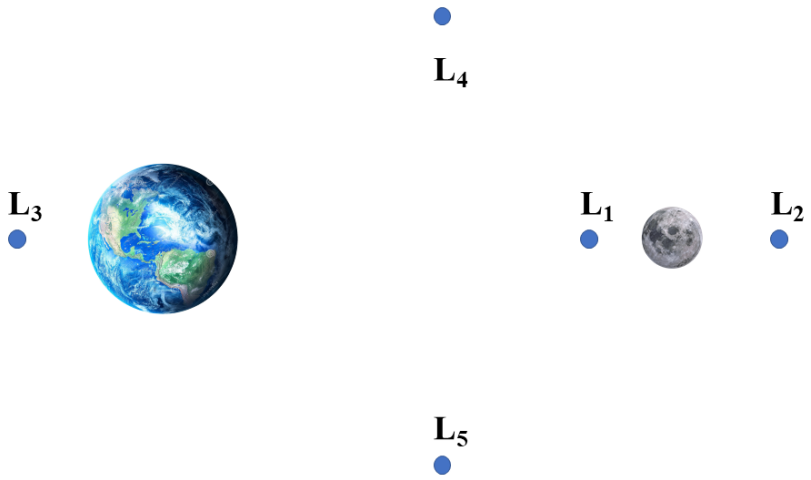

Figure 2.2: Lagrange Points Location

2.1.2.1 Stability of Lagrange Points

Since the system is Hamiltonian, according to the Kolmogorov-Arnold-Moser (KAM) theorem small perturbations from the equilibrium point will exhibit certain restrictions to their chaotic motion [80]. Thus, it is interesting to study the behavior of the flow near these equilibrium points by analyzing their stability.

In the rotating frame, the effective potential (U_{eff}) is comprised of both gravitational and centrifugal potential and can be expressed as,

$$U_{\text{eff}} = \frac{1}{2}(x^2 + y^2) + \frac{\mu_1}{p_1} + \frac{\mu_2}{p_2}. \tag{2.24}$$

Using this expression for U_{eff} and some algebraic manipulations after computing partials with respect to x and y, we have,

$$\ddot{x} - 2\dot{y} = \frac{\partial U_{\text{eff}}}{\partial x} \tag{2.25}$$

$$\ddot{y} + 2\dot{x} = \frac{\partial U_{\text{eff}}}{\partial y} \tag{2.26}$$

Stability is analyzed using a perturbation analysis as in most systems with equilibrium points. Let us think of a point close to an equilibrium point. The coordinate of such a point is,

$$x = x_{L_i} + \delta x \tag{2.27}$$

$$y = y_{L_i} + \delta y, \tag{2.28}$$

where δx and δy are small perturbations in the x and y directions respectively. x_{L_i} and y_{L_i} depict the $x-y$ coordinates of the L_i Lagrange point with $i \in \{1, 2, 3, 4, 5\}$. Using a Taylor series expansion upto second order terms for the effective potential $U_{\text{eff}}(x, y)$ about the equilibrium point, we obtain,

$$U_{\text{eff}} = U_{\text{eff}}^{L_i} + U_{\text{eff}}^{x}\delta x + U_{\text{eff}}^{y}\delta y + \frac{1}{2}U_{\text{eff}}^{xx}(\delta x)^2 + \frac{1}{2}U_{\text{eff}}^{yy}(\delta y)^2 + U_{\text{eff}}^{xy}\delta x\delta y + \mathbb{O}(3). \tag{2.29}$$

where $U_{\text{eff}}^{x}, U_{\text{eff}}^{xx}, U_{\text{eff}}^{xy}$ depict partials of the effective potential with respect to $x, \{xx\} and \{xy\}$ respectively. Due to the velocity and acceleration vanishing at the Lagrange points, U_{eff}^{x} and U_{eff}^{y} are both identically zero. Therefore,

$$U_{\text{eff}} \approx U_{\text{eff}}^{L_i} + \frac{1}{2}U_{\text{eff}}^{xx}(\delta x)^2 + \frac{1}{2}U_{\text{eff}}^{yy}(\delta y)^2 + U_{\text{eff}}^{xy}\delta x\delta y. \tag{2.30}$$

According to the linear perturbation analysis, we have $x = x_{L_i} + \delta x$ and $y = y_{L_i} + \delta y$. Thus, $\dot{x} = \dot{\delta x}$ and $\dot{y} = \dot{\delta y}$. Plugging the series expansion of the effective potential U_{eff} the perturbation equations of motion become,

$$\ddot{\delta x} = 2\dot{\delta y} - U_{\text{eff}}^{xx}\delta x - U_{\text{eff}}^{xy}\delta y \tag{2.31}$$

$$\ddot{\delta y} = -2\dot{\delta x} - U_{\text{eff}}^{yy}\delta y - U_{\text{eff}}^{xy}\delta x \tag{2.32}$$

In the matrix form, this linearized system is represented in the following manner,

$$\frac{d}{dt}\begin{pmatrix}\delta x\\ \delta y\\ \dot{\delta x}\\ \dot{\delta y}\end{pmatrix}=\begin{pmatrix}0 & 0 & 1 & 0\\ 0 & 0 & 0 & 1\\ -U^{xx}_{\text{eff}} & -U^{xy}_{\text{eff}} & 0 & 2\\ -U^{xy}_{\text{eff}} & -U^{yy}_{\text{eff}} & -2 & 0\end{pmatrix}\begin{pmatrix}\delta x\\ \delta y\\ \dot{\delta x}\\ \dot{\delta y}\end{pmatrix} \tag{2.33}$$

Eigenvalues of the coefficient matrix gives insight into stability of the different equilibrium points. These eigenvalues must be computed at all the Lagrangian Points separately. If all the eigenvalues are purely imaginary, the point is stable to small perturbations but for any other case, the point is said to be unstable. The characteristic equation of the linear system is found to be,

$$\lambda^4 + (4 + U^{xx}_{\text{eff}} + U^{yy}_{\text{eff}})\lambda^2 + (U^{xx}_{\text{eff}}U^{yy}_{\text{eff}} - (U^{xy}_{\text{eff}})^2) = 0. \tag{2.34}$$

In order to find the roots of this equation, second partials need to be computed. These partials are provided below for the reader,

$$U^{xx}_{\text{eff}} = \frac{1-\mu}{p_1^3} + \frac{\mu}{p_2^3} - \frac{3(1-\mu)(x+\mu)^2}{p_2^5} - \frac{3\mu(x-1+\mu)^2}{p_1^5} - 1 \tag{2.35}$$

$$U^{yy}_{\text{eff}} = \frac{1-\mu}{p_1^3} + \frac{\mu}{p_2^3} - 3y^2\left[\frac{1-\mu}{p_1^5} + \frac{\mu}{p_2^5}\right] - 1 \tag{2.36}$$

$$U^{xy}_{\text{eff}} = 3y\left[\frac{(1-\mu)(x+\mu)}{p_1^5} + \frac{\mu(x-1+\mu)}{p_2^5}\right] \tag{2.37}$$

Let us define $\alpha = \frac{1-\mu}{p_1^3} + \frac{\mu}{p_2^3}$ to simplify the calculation. Now for the collinear Lagrange points, $y = 0$, i.e., they lie on the x-axis. Therefore, $U^{xy}_{\text{eff}} = 0$ and $U^{yy}_{\text{eff}} = \alpha - 1$ and after some algebra, $U^{xx}_{\text{eff}} = -2\alpha - 1$. Plugging in these values in the quartic obtained above, a simple quadratic equation appears in λ^2,

$$\lambda^4 + (2-\alpha)\lambda^2 - (2\alpha+1)(\alpha-1) = 0. \tag{2.38}$$

For the roots of the equation to be purely imaginary, it is found that $\frac{8}{9} \leq \alpha \leq 1$. But this is

false for $0 < \mu \leq 0.5$ which is the case for all relevant systems in our solar system. Therefore, the Lagrange points L_1,L_2 and L_3 are unstable. For the L_4 and L_5 Lagrange points that exist at the unoccupied vertex of the unity equilateral triangle, $(p_1, p_2) = (1, 1)$. Using these values, the partials are simplified to be,

$$U_{\text{eff}}^{xx} = -\frac{3}{4}, U_{\text{eff}}^{yy} = -\frac{9}{4}, U_{\text{eff}}^{xy} = \pm\sqrt{\frac{27}{16}}(1 - 2\mu). \tag{2.39}$$

The characteristic equation relevant to the L_4 and L_5 Lagrange points then becomes,

$$\lambda^4 + \lambda^2 + \frac{27}{4}\mu(1 - \mu) \tag{2.40}$$

The roots of the equation are,

$$\lambda^2 = \frac{-1 \pm \sqrt{27\mu(1 - \mu)}}{2}. \tag{2.41}$$

Thus for purely imaginary roots, the inequality $1 > 27\mu(1 - \mu)$ must hold. Thus, for L_4 and L_5 Lagrange points to be stable,

$$\mu < 0.0385208965 \tag{2.42}$$

Note that this is true for all primary-secondary pairs of interest in the solar system as shown before in Table 2.1. It can also be shown that the stability of L_4 and L_5 is due to the presence of coriolis force.

2.1.3 Jacobi Constant and Zero Velocity Curves

From Eq. (2.25) and Eq. (2.26), multiplying the first by $\frac{dx}{dt}$ and the second by $\frac{dy}{dt}$, and then adding the two equations,

$$\frac{d^2x}{dt^2}\left(\frac{dx}{dt}\right) + \frac{d^2y}{dt^2}\left(\frac{dy}{dt}\right) = \frac{\partial U_{\text{eff}}}{\partial x}\left(\frac{dx}{dt}\right) + \frac{\partial U_{\text{eff}}}{\partial y}\left(\frac{dy}{dt}\right). \tag{2.43}$$

Since U_{eff} is purely a function on x and y. The right hand side of the equation gives $\frac{dU_{\text{eff}}}{dt}$ so that

we have,

$$\frac{d^2x}{dt^2}\left(\frac{dx}{dt}\right) + \frac{d^2y}{dt^2}\left(\frac{dy}{dt}\right) = \frac{dU_{\text{eff}}}{dt}. \tag{2.44}$$

Integrating the equations on both sides,

$$\left(\frac{dx}{dt}\right)^2 + \left(\frac{dy}{dt}\right)^2 = 2U_{\text{eff}} - C \tag{2.45}$$

where C is an arbitrary constant of integration known as the Jacobi's Constant. C is a constant of motion in the CR3BP. Also note that the left hand side of the equation depicts square of velocity, such that,

$$V^2 = 2U_{\text{eff}} - C. \tag{2.46}$$

Using this relation, curves of zero velocity can be derived in the plane of the primaries. Note that this can be easily extended to three dimensions which is trivial and not discussed here. For more details please refer advanced orbital mechanics textbooks e.g., [81]. These curves are important because they bind the motion of the third body m in the system depending on the initial energy it possesses. For instance, for a certain amount of initial total energy, the velocity of m goes to zeros it reaches a zero velocity boundary and therefore the region beyond the boundary is not accessible to the spacecraft/third body. When $V = 0$, these curves are defined as locations where,

$$2U_{\text{eff}} = C \tag{2.47}$$

$$\text{or,} \quad x^2 + y^2 + \frac{2(1-\mu)}{p_1} + \frac{2\mu}{p_2} = C. \tag{2.48}$$

Figures 2.3-2.4 depict the zero velocity curves for various values of C for the Earth-Moon system. Note how more of the region becomes accessible to the spacecraft as the total energy of the spacecraft depicted by C starts increasing i.e., starts becoming less negative.

Note that in Figure 2.3 (a), when C = -1.6725 the L_1 equilibrium point just starts becoming

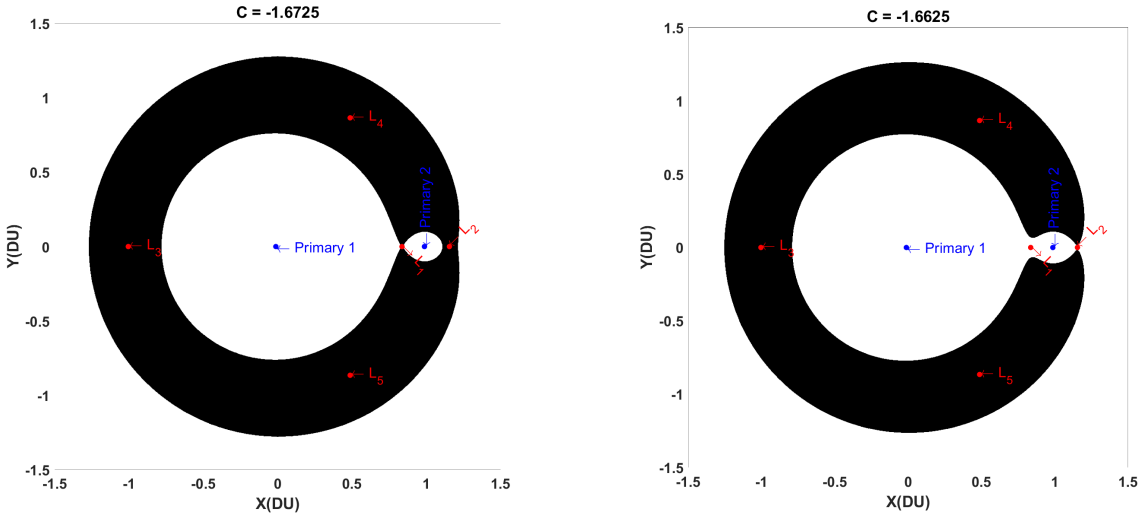

(a) L_1 Zero Velocity Contour

(b) L_2 Zero Velocity Contour

Figure 2.3: L_1 and L_2 Contours showing Forbidden Regions

accessible to the spacecraft but L_2 and L_3 are still beyond reach and lie in the forbidden region. As C increases to -1.6625 (Figure 2.3(b)), we reach the limiting case when L_2 starts becoming accessible with the second neck in the forbidden region opening up. Finally, Figure 2.4 shows the opening of the L_3 neck as it becomes available when $C \leq -1.58$. Upon increasing the Jacobi Constant further the whole region becomes available to the spacecraft.

2.1.4 Applications of CR3BP for Space Missions

Understanding the CR3BP, Lagrange Points and their stability can be used to the advantage of mission designers for complicated missions. Astronomers based on the stability observed for the L_4 and L_5 Lagrange Points discovered the Trojan Asteroids which exist in the Sun-Jupiter System [82]. Mars, Jupiter and Saturn have all had these Trojans discovered but in the Sun-Earth system, the stable Lagrange Points only have dust and debris.

For artificial applications, scientists and mission designers have placed the Solar and Heliospheric Observatory satellite (SOHO) [83] at the Sun-Earth L_1. Since this is an equilibrium point, the satellite faces towards the Sun and captures the Solar Wind effectively. Although it must be

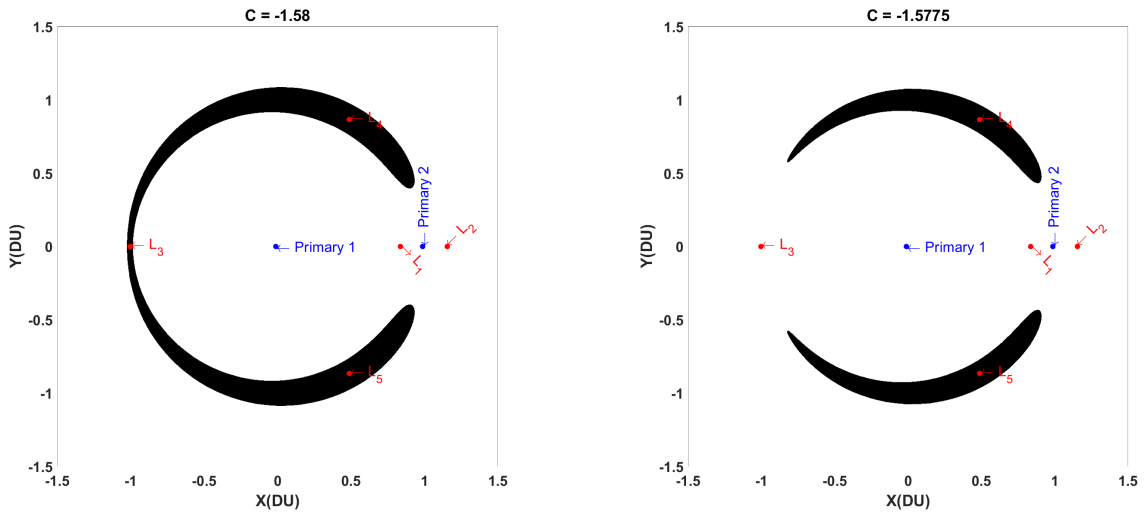

(a) Path to L_3 closed from Inside

(b) L_3 accessible form both Inside and Outside

Figure 2.4: L_3 contour : Limiting Behavior

noted here that since the collinear Lagrange Points are intrinsically unstable, any perturbation leading to departure from the equilibrium state must be counteracted by a station-keeping maneuver. We have already discussed the use of WSB trajectories which are present in the neighborhood of Lagrange Points by Belbruno for ballistic capture of the Japanese Hiten Mission [18]. Building on this concept, researchers have now started looking at the use of periodic orbits that exist around the Lagrange Points especially L_1 and L_2 and their associated invariant manifolds and leverage the ballistic nature of these space trajectories to design efficient missions, which also summarizes the context of work described in this thesis. The developments in this section are a modern paraphrase of Lagrange's late 1770s treatment but the libration points, their stability and zero velocity surfaces are intimately related to subsequent developments in this dissertation. Therefore, it is included for completeness and to establish notations.

2.2 Other Simplified Models

While, the CR3BP is the most widely used simplification of a high-fidelity model (HFM) that works well since the assumptions apply to most scenarios in the solar system up to a tolerable first-degree approximation, there are some other variations which bridge the long gap between a

HFM and the CR3BP. In this section, we briefly discuss a couple of these models.

2.2.1 Elliptical Restricted Three Body Problem (ER3BP)

Similar to the CR3BP, the ER3BP is also concerned with defining the motion of a body of negligible mass m in the presence of gravitational attraction from two larger bodies m_1 and m_2. It follows that the relative motion of m_1 and m_2 is also elliptical. This truth is frequently convenient, because a single orbit is required to describe the motion of m_2 to m_1. For the ER3BP, the primary-secondary pair is assumed to move in elliptical orbits around their barycenter rather than the circular assumption in the CR3BP. Figure 2.5 depicts a schematic describing the setting for ER3BP. All the notations as well as position of the primary and secondary are the same as in CR3BP but the TU is not defined as $T_{\text{el}}/2\pi$ where T_{el} is the time-period of the elliptical orbit. Instead of time (t), in the ER3BP the true anomaly (f) is designated as the independent variable of the system. To differentiate from the time derivatives in the CR3BP, we express derivatives with respect to f by $()'$.

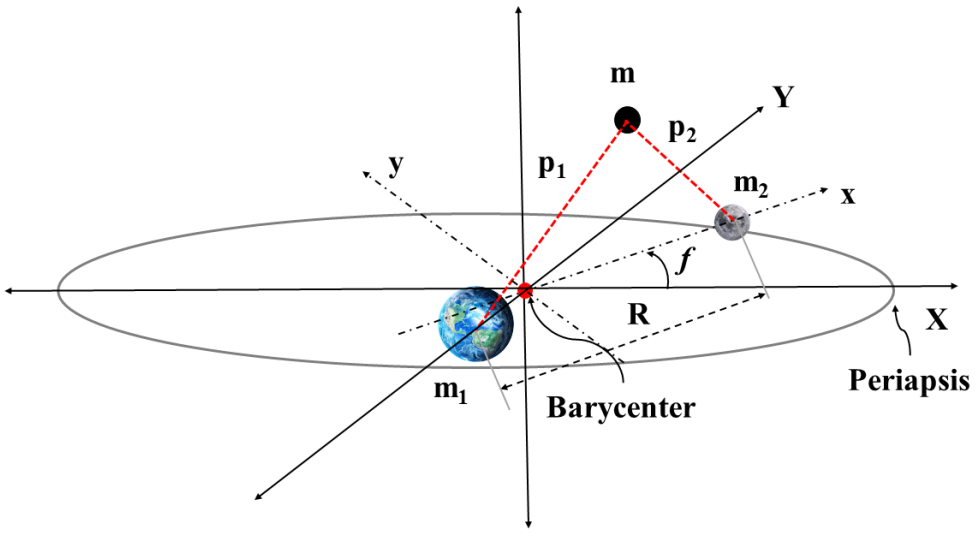

Figure 2.5: Elliptical Restricted Three Body Problem: A Schematic

Szebehely has presented the EOMs describing motion of m in the ER3BP in his paper [84].

This has been presented below,

$$x'' - 2y' = U^x_{\text{eff}} \tag{2.49}$$

$$y'' + 2x' = U^y_{\text{eff}} \tag{2.50}$$

where,

$$U_{\text{eff}} = \frac{\tilde{U}}{(1 + e\cos f)}. \tag{2.51}$$

is the effective potential of the system. e denotes the eccentricity of the elliptical orbit of m_2 around the barycenter and f is the true anomaly describing that motion. $\tilde{U}$ is mathematically expressed as,

$$\tilde{U}(x, y) = \frac{1}{2}(x^2 + y^2) + \frac{1-\mu}{p_1} + \frac{\mu}{p_2} + \frac{1}{2}\mu(1-\mu) \tag{2.52}$$

where as in the case of the CR3BP, $p_1 = \sqrt{((x+\mu)^2 + y^2)}$ and $p_2 = \sqrt{(x+\mu-1)^2 + y^2}$ are the dimensionless distances of the mass m from m_1 and m_2 respectively. While the numerical complications arising out of considerations of the ER3BP are not worth it for approximate multi-rev low-thrust trajectories, simulation of flyby trajectories with an elliptical trajectory assumption during flyby has shown significant variations from CR3BP which is typically used by mission designers [85].

2.2.2 Bi-Circular Problem (BCP)

The BCP is a cousin of the CR3BP, in such that, the Earth and the Moon are assumed to be revolving in circular orbits around their barycenter, while the barycenter itself is moving in a circular orbit around the Sun (located at the assumed inertial origin O) (see Figure 2.6).

R is the position vector from the Sun to barycenter, r is the position vector of the Moon with respect to the Earth and ρ is the position vector of the spacecraft with respect to the barycenter. A serious weakness of the BCP assumption is that all three massive bodies Earth-Moon-Sun lie

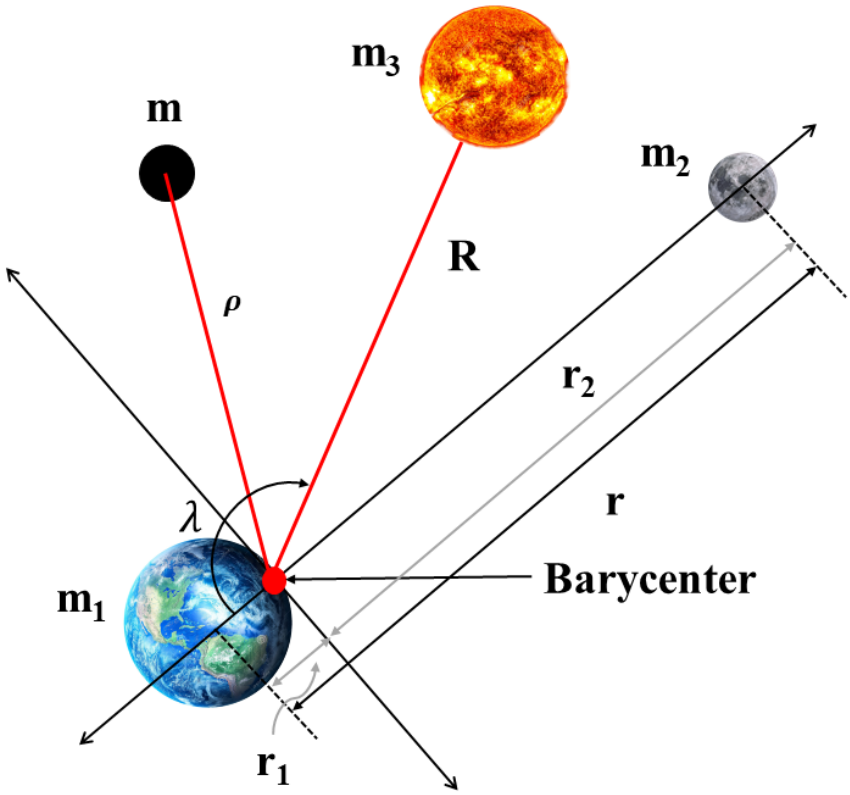

Figure 2.6: Bi-Circular Problem: A Schematic

at all times in the same plane i.e., the Ecliptic plane. In this particular instance of the BCP, the Earth-Moon orbital plane lies relatively close to the ecliptic at around 5 degrees, making this a reasonable approximation. More significant, however, is the inclination of the Earth-Moon orbital plane with respect to Earth's equatorial plane, which undergoes precession with an approximate 18.6 year period. This detail has an effect on any results in terms of plotting optimal trajectories when defining orbital inclinations with respect to the Earth's equator. If the time of flight is small compared to 18.6 yrs. of course, the effect will be small. However, a work-around is to define inclination relative to the ecliptic in order to decouple the time dependency. The further assumption that the Sun and the barycenter move in a uniform circular motion can be expected to cause a smaller but nonetheless significant modeling error. While the errors associated with these idealized approximations are important, the fidelity of the BCP is generally significantly closer to physical reality than the CR3BP, and we can anticipate that the remaining errors can be readily removed using final design iterations with a high fidelity force model.

The equations of motion (EOMs) for the spacecraft in the inertial O frame turn out to be quite complicated due to the time-dependence of the relative positions of the primary-secondary pair. It is convenient to use the Earth-Moon synodic frame instead, since it decreases the level of non-autonomy by a factor of 2. The resulting system is still a non-autonomous system and more complex than the autonomous CR3BP. A phase angle (λ) of the Sun's position vector in the synodic frame relative to the synodic x axis (see Figure 2.6) is used to describe the time dependence.

Let $\mathbf{X} = [x, y]$ be the position coordinates in the Earth-Moon Cartesian rotating frame. The EOMs for the BCP in this coordinate system can be mathematically written as,

$$\begin{aligned}\ddot{\mathbf{X}} = \mathbf{A}\dot{\mathbf{X}} + \mathbf{B}\mathbf{X} + (\mu_2 - 1)\Bigg[(1-\mu_1)\frac{\mathbf{R}-\mu_1\mathbf{r}}{|\mathbf{R}-\mu_1\mathbf{r}|^3} + \mu_1\frac{\mathbf{R}+(1-\mu_1)\mathbf{R}}{|\mathbf{R}+(1-\mu_1)\mathbf{R}|^3} - \frac{\mathbf{R}+\boldsymbol{\rho}}{|\mathbf{R}+\boldsymbol{\rho}|^3}\Bigg] \\ - (1-\mu_1)\frac{\boldsymbol{\rho}+\mu_1\mathbf{r}}{|\boldsymbol{\rho}+\mu_1\mathbf{r}|^3} - \mu_1\frac{\boldsymbol{\rho}-(1-\mu_1)\mathbf{r}}{|\boldsymbol{\rho}-(1-\mu_1)\mathbf{r}|^3}\end{aligned} \tag{2.53}$$

where the matrices $\mathbf{A}$ and $\mathbf{B}$ are defined as,

$$\mathbf{A} = \begin{pmatrix} 0 & 2 & 0 \\ -2 & 0 & 0 \\ 0 & 0 & 0 \end{pmatrix} \quad , \mathbf{B} = \begin{pmatrix} 1 & 0 & 0 \\ 0 & 1 & 0 \\ 0 & 0 & 0 \end{pmatrix} \tag{2.54}$$

and $\mu_1 = \frac{m_2}{m_1+m_2}$ while $mu_2 = \frac{m_1+m_2+m_3}{m_1+m_2}$. The vectors $\mathbf{R}, \mathbf{r}$ and $\boldsymbol{\rho}$ are also described in the Earth-Moon rotating frame. Therefore, $\mathbf{R} = [R_x, R_y]$ can be parameterized using magnitude of the Sun's position vector with respect to the Earth-Moon barycenter and the phase angle (λ) with respect to the Earth-Moon line.

2.3 Periodic Orbits (POs)

Poìncare in 1892 [76] demonstrated the existence of an infinite number of periodic orbits (POs) in the three body problem. Many solutions are yet to be explored and practical applications yet to be investigated. The procedure for finding these POs are generally based on a two-step differential correction method, first used by Howell and Pernicka [86]. The problem of deriving periodic conditions in the three body problem is well studied, as evidenced by the numerous references contained in the most relevant literature [87, 88, 89, 90]. The main objective of this dissertation is not to discuss this methodology in detail but rather to provide a context for the new developments. A brief overview is presented below for the sake of completion. For further details, the reader is referred to the set of references provided above.

The 'first-level' correction ensures position continuity at intermediate points called patch-points. Velocity discontinuities are allowed in order to maintain position continuity. A minimum Euclidean norm solution to the linear variational equation is solved to obtain the velocities to be applied at each patch-point and the time at which they must be applied. At the end of this first step we have a position continuous arc with ΔV required at each patch-point. In the second step, these ΔV's are minimized by relocating the patch-points and time of impulses (again a minimum Euclidean norm solution is sought). The final solution gives a position-continuous and velocity-continuous quasi-periodic orbit. Note that the patch-points are identified from an initial guess obtained by solving a simplified set of EOMs (by not including all the non-linearities in the differ-

ential equations). See Figure 2.7 for a schematic overview of the two-level differential correction procedure.

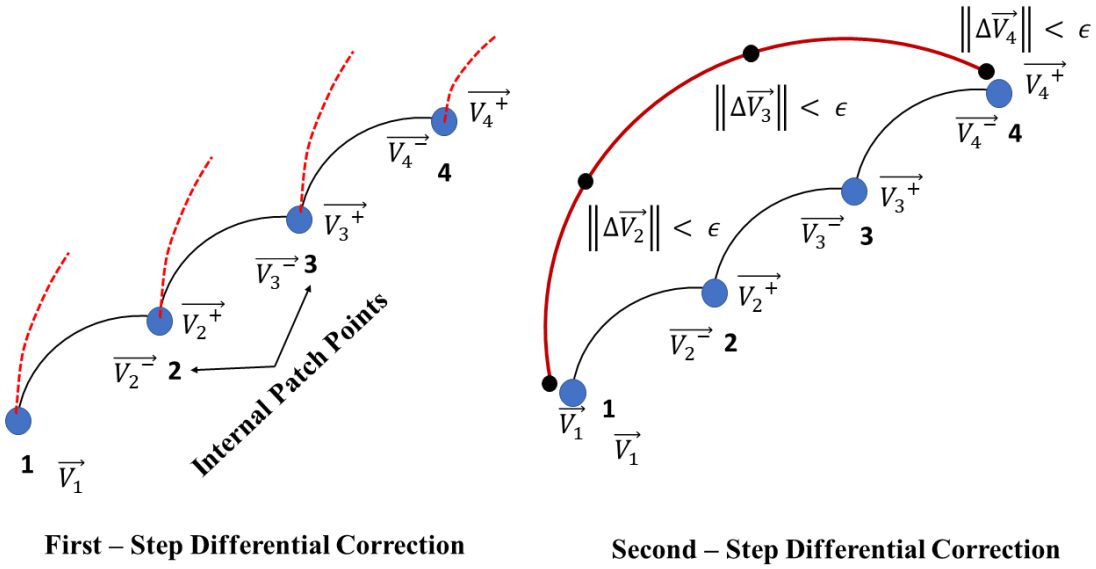

Figure 2.7: Two-Step Differential Correction to generate Periodic Orbits

The orbits are discovered by employing a differential correction method, an example of which was discussed above. Upon finding one solution from a particular family, the rest of the orbits are obtained by performing some sort of continuation, usually pseudo-arc length continuation until the solutions bifurcate and we start obtaining members of a new family. Typically the planar Lyapunov orbits bifurcate into the Halo family which in turn bifurcates into NRHO and Butterfly orbit families. Note that, some periodic orbits in the system orbit the secondary body rather than a libration point, e.g., Distance Retrograde Orbits (DROs). Some example families are depicted in the Figures 2.8 - 2.11. The system considered for the plots is the Earth-Moon system whereas the libration point orbit families orbit the L_1 Lagrange Point. Moreover Appendix A enlists the initial conditions for some relevant periodic orbits from different families for a range of Jacobi Constants (C) for the reader's perusal.

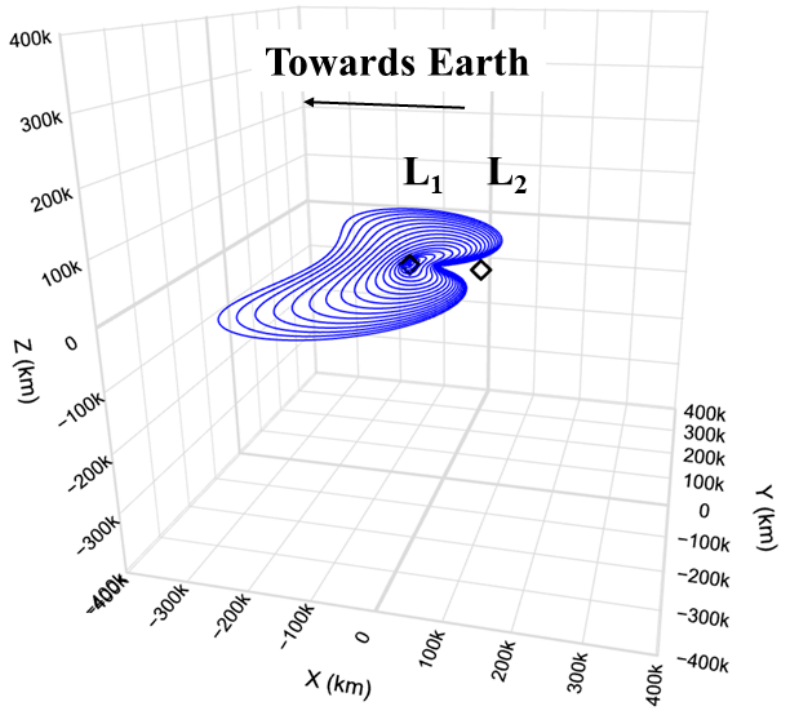

Figure 2.8: L_1 Lyapunov Orbit Family

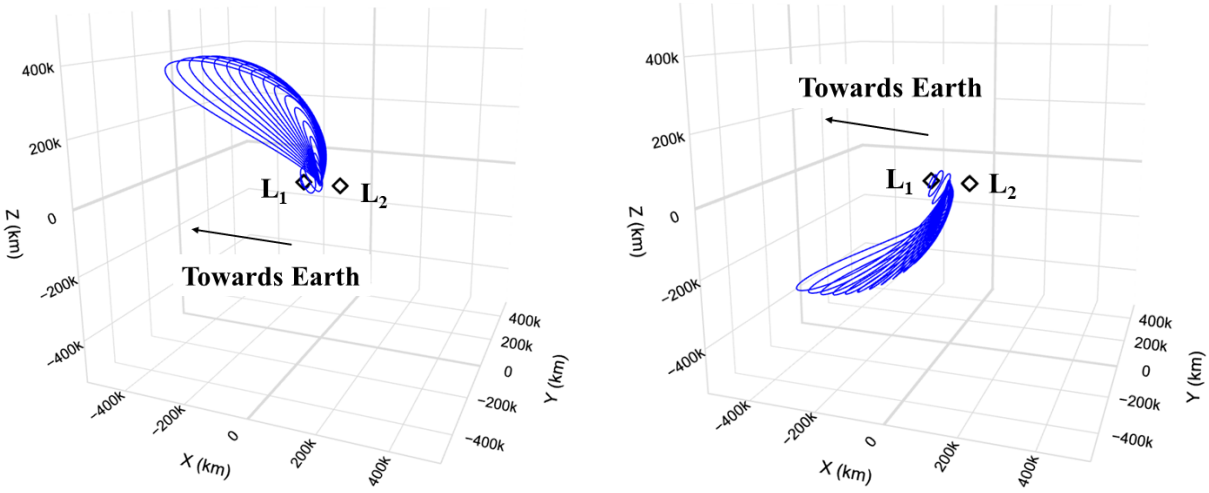

(a) Northern L_1 Halo Orbit Family

(b) Southern L_1 Halo Orbit Family

Figure 2.9: L_1 Halo Orbit families

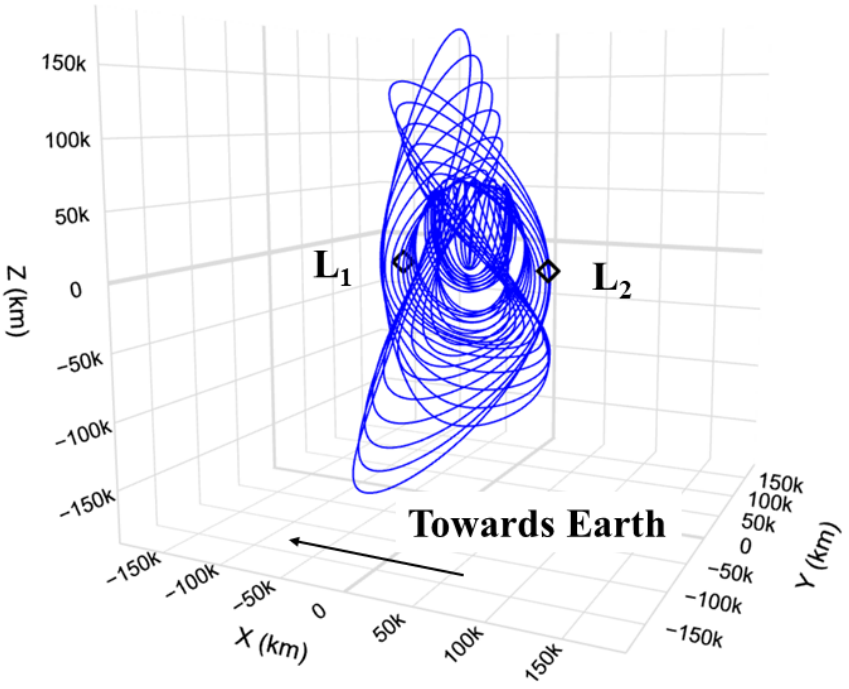

Figure 2.10: Northern Butterfly Orbit Family

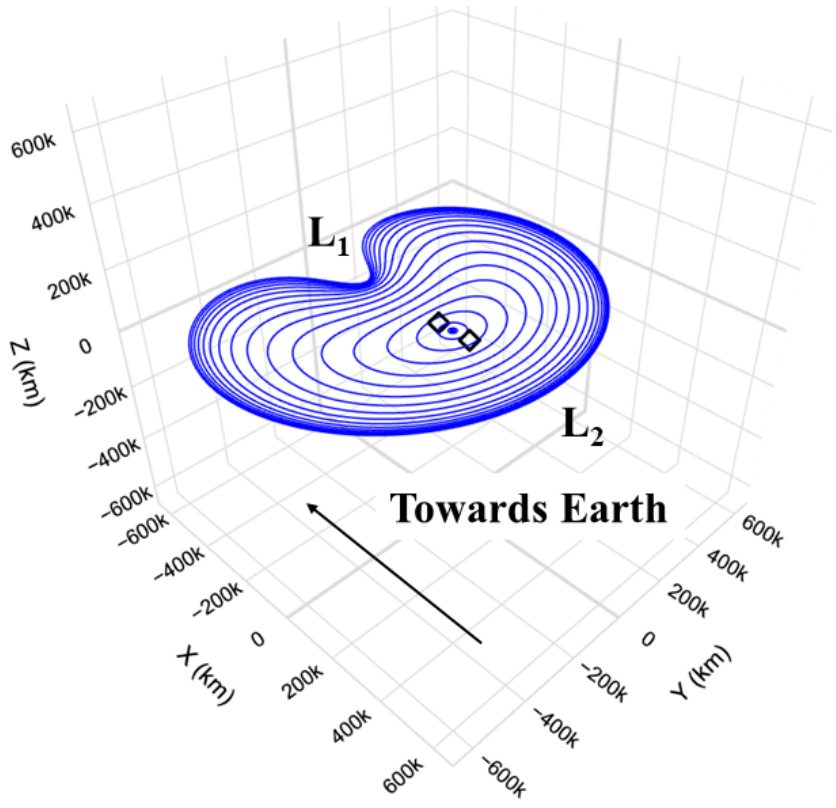

Figure 2.11: Distance Retrograde Orbit Family: A Secondary Body Centered PO

3. INVARIANT MANIFOLDS: THEORY, COMPUTATION AND APPLICATION IN TRAJECTORY DESIGN

In nature, only a small subset of dynamical systems have a linear form. While the linear forms of EOMs are especially attractive in that closed form analytical solutions can be achieved. In reality though, most systems are at least weakly non-linear and exhibit complicated motion for which no closed-form analytical expression is possible. Additionally, superposition principles do not apply to non-linear systems and the motion often chaotic. Chaotic behavior has been observed in a vast variety of fields from science and engineering, e.g., weather patterns, turbulence, planetary motion, population trends, atomic motion etc. It is important to note that chaos is exhibited even though the dynamics and initial conditions are fully deterministic and governed by the laws of classical mechanics. There is formally no uncertainty or probabilistic considerations while modeling chaotic systems. However, the essence is that such systems exhibit motion that is highly sensitive to the initial conditions. *Not all non-linear systems exhibit chaos but in order for a system to be chaotic, non-linearity must exist.*

Poincareís the first to be credited with discovering chaotic motion when studying the famous 'three-body problem'. Many researchers over the years believed in the deterministic view of nature which states that if the position and velocities of all particles are known, the future motion is predicted without ambiguity using Newtonian mechanics. Only in recent decades have scientists at large realised that knowledge of the laws of nature is insufficient to simulate deterministic systems evolution as they can be extremely sensitive to initial conditions even though they follow are technically deterministic systems. There are two high-level classifications of systems that exhibit chaos, the first includes non-dissipative Hamiltonian systems like the three-body problem while the other includes driven, damped non-linear oscillatory systems.

In the next section, a simple non-linear dynamical system that exhibits chaos is discussed as a case study. The concept of hyperbolic fixed points, linearized stability in a neighborhood of the fixed point, manifold sub-spaces and the concept of using manifolds for control of the

double-pendulum system is presented. This system and the discussed analysis is analogous to the computation and use of manifolds of periodic orbits in the CR3BP system for trajectory design and we will make that connection in this chapter.

3.1 The Double-Pendulum

A double-pendulum is an easy to understand dynamical system exhibiting non-linear behavior which is formed by two point-masses connected by massless rigid links. Both masses move in a fixed vertical plane. A constant vertical gravity field is assumed. The pivot of the first pendulum is fixed at O and all motion is frictionless.

3.1.1 Equations of Motion - Lagrangian Dynamics

Consider the double-pendulum apparatus shown in Figure 3.1. O is taken as the origin of a Cartesian 2D coordinate system, x axis in horizontal whereas y axis in vertical direction. Let θ_1 and θ_2 be the angles the first and second rods make with the vertical y axis respectively.

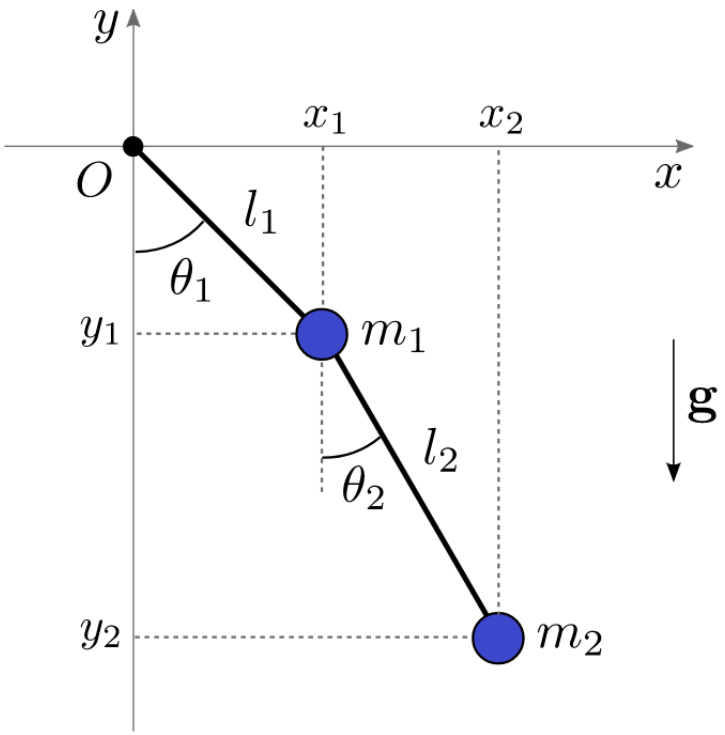

Figure 3.1: Double Pendulum: A Schematic

The Cartesian inertial positions of the two bobs m_1 and m_2 can be expressed from geometry as,

$$x_1 = l_1 \sin\theta_1, \quad y_1 = -l_1 \cos\theta_1 \tag{3.1}$$

$$x_2 = l_1 \sin\theta_1 + l_2 \sin\theta_2, \quad y_2 = -l_1 \cos\theta_1 - l_2 \cos\theta_2 \tag{3.2}$$

Differentiating these quantities with respect to time, one obtains the inertial Cartesian velocities as,

$$\dot{x_1} = l_1\dot{\theta_1} \cos\theta_1, \quad \dot{y_1} = l_1\dot{\theta_1} \cos\theta_1 \tag{3.3}$$

$$\dot{x_2} = l_1\dot{\theta_1} \cos\theta_1 + l_2\dot{\theta_2} \cos\theta_2, \quad \dot{y_2} = l_1\dot{\theta_1} \sin\theta_1 + l_2\dot{\theta_2} \sin\theta_2 \tag{3.4}$$

In the chaotic regime of the double-pendulum slight changes in the initial values of the angles (θ_1, θ_2) and angular velocities $(\dot{\theta_1}, \dot{\theta_2})$ can make the future state of the two bobs in position and velocity or angle and angular velocities be different than the original state history. The Kinetic Energy, T, of the system is mathematically expressed as,

$$T = \frac{1}{2}(m_1 v_1^2 + m_2 v_2^2) \tag{3.5}$$

$$= \frac{1}{2} m_1 (\dot{x_1}^2 + \dot{y_1}^2) + \frac{1}{2} m_2 (\dot{x_2}^2 + \dot{y_2}^2) \tag{3.6}$$

$$= \frac{1}{2} m_1 l_1^2 \dot{\theta_1}^2 + \frac{1}{2} m_2 \left[l_1^2 \dot{\theta_1}^2 + l_2^2 \dot{\theta_2}^2 + 2 l_1 l_2 \dot{\theta_1} \dot{\theta_2} \cos(\theta_1 - \theta_2) \right] \tag{3.7}$$

In the last form of Kinetic Energy, we have chosen (θ_1, θ_2) as the generalized coordinates. The Potential Energy, V, of the system on the other hand is expressed as,

$$V = m_1 g y_1 + m_2 g y_2 \tag{3.8}$$

$$= -m_1 g l_1 \cos\theta_1 - m_2 g (l_1 \cos\theta_1 + l_2 \cos\theta_2) \tag{3.9}$$

$$= -(m_1 + m_2) g l_1 \cos\theta_1 - m_2 g l_2 \cos\theta_2 \tag{3.10}$$

Thus, the system Lagrangian, $L = T - V$ can now be computed and expressed as,

$$L = \frac{1}{2}(m_1+m_2)l_1^2\dot{\theta_1}^2+\frac{1}{2}m_2l_2^2\dot{\theta_2}^2+m_2l_1l_2\dot{\theta_1}\dot{\theta_2}\cos(\theta_1-\theta_2)+(m_1+m_2)gl_1\cos\theta_1+m_2gl_2\cos\theta_2. \quad (3.11)$$

Expressing the canonical momenta, derived from the Lagrangian, L, we have,

$$p_{\theta 1} = \frac{\partial L}{\partial \dot{\theta}_1} = (m_1 + m_2)l_1^2\dot{\theta}_1 + m_2l_1l_2\dot{\theta}_2\cos(\theta_1 - \theta_2) \quad (3.12)$$

$$p_{\theta 2} = \frac{\partial L}{\partial \dot{\theta}_2} = m_2l_2^2\dot{\theta}_2 + m_2l_1l_2\dot{\theta}_1\cos(\theta_1 - \theta_2) \quad (3.13)$$

The partials of the Lagrangian with respect to the angles θ_1 and θ_2 are expressed as,

$$\frac{\partial L}{\partial \theta_1} = -m_2l_1l_2\dot{\theta}_1\dot{\theta}_2\sin(\theta_1 - \theta_2) - (m_1 + m_2)gl_1\sin\theta_1 \quad (3.14)$$

$$\frac{\partial L}{\partial \theta_2} = m_2l_1l_2\dot{\theta}_1\dot{\theta}_2\sin(\theta_1 - \theta_2) - m_2gl_2\sin\theta_2 \quad (3.15)$$

Using Equations (3.12 - 3.15) in the Euler-Lagrange equation which is mathematically written as,

$$\frac{d}{dt}\Big(\frac{\partial L}{\partial \dot{\theta}_i}\Big) - \frac{\partial L}{\partial \theta_i} = 0, \quad (3.16)$$

we obtain the EOMs governing the motion of the double pendulum,

$$\ddot{\theta_1} + \alpha\beta\ddot{\theta_2}\cos(\theta_1 - \theta_2) + \alpha\beta\dot{\theta_2}^2\sin(\theta_1 - \theta_2) + \frac{g}{l_1}\sin\theta_1 = 0 \quad (3.17)$$

$$\ddot{\theta_2} + \frac{\ddot{\theta_1}\cos(\theta_1 - \theta_2)}{\beta} - \frac{\dot{\theta_1}^2\sin(\theta_1 - \theta_2)}{\beta} + \frac{g}{l_1}\sin\theta_2 = 0, \quad (3.18)$$

where, the mass fraction, $\alpha = \frac{m_2}{m_1+m_2}$ and the length ratio, $\beta = \frac{l_2}{l_1}$.

3.1.2 Fixed/Equilibrium Points of the Double Pendulum

The state-space of the double pendulum system comprises of the angles and the angular velocities, i.e., $\mathbf{X} = [\theta_1, \theta_2, \dot{\theta}_1, \dot{\theta}_2]^T$. Let $\dot{\theta}_1$ be expressed as ω_1 and similarly $\dot{\theta}_2$ as ω_2. Then, the state space representation of the EOMs can be mathematically expressed as,

$$\frac{d}{dt}\begin{pmatrix}\theta_1\\ \theta_2\\ \omega_1\\ \omega_2\end{pmatrix} = \begin{pmatrix}\omega_1\\ \omega_2\\ g_1(\theta_1, \theta_2, \omega_1, \omega_2)\\ g_2(\theta_1, \theta_2, \omega_1, \omega_2)\end{pmatrix} \tag{3.19}$$

where g_1 and g_2 are highly non-linear functions of the state variables. There are four critical or fixed or equilibrium state-sets in the double-pendulum system. Figure 3.2 depicts these four specific equilibrium or critical state-sets.

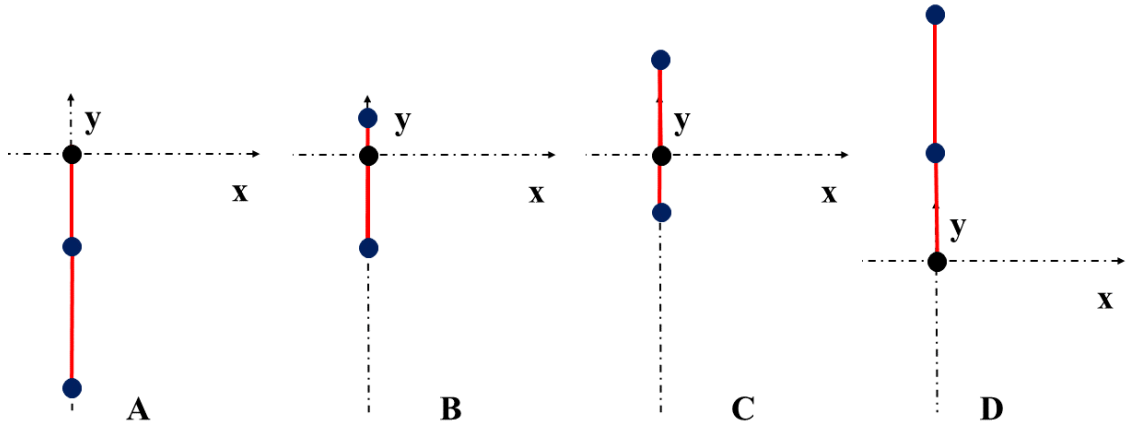

Figure 3.2: Critical Points/ Equilibrium States of the Double Pendulum System

Note that case A and D represent the 'full swing-down' and the 'full swing-up' configurations respectively. Cases B and C are two intermediate configurations with one of the two angles swung up (π) and the other swung down (0). See Table 3.1 for a full state-space representation of the four

critical points.

Table 3.1: State-Space Representation: Critical Points of the Double Pendulum.

Scenario	θ_1	θ_2	ω_1	ω_2
A	0	0	0	0
B	0	$\pm\pi$	0	0
C	$\pm\pi$	0	0	0
D	$\pm\pi$	$\pm\pi$	0	0

In the previous chapter, we saw that although closed form solutions are not available for complex non-linear systems, analysing stability of the fixed equilibrium points is an effective way to derive insights into the system. This is typically done by approximating dynamics in a small neighborhood of each critical point by a linear expansion and analysing the eigenvalues of the obtained coefficient matrix (We follow Lagrange's lead and used this approach for the Lagrange Points in a CR3BP system in the last chapter!).

The dynamical system EOMs expressed in Equation (3.19) can be compactly re-written as,

$$\dot{\mathbf{X}} = f(\mathbf{X}), \tag{3.20}$$

where $f(\mathbf{X})$ is complicated and non-linear. A solution to the set of differential equations when analyzed in phase-space is called a *trajectory*. Note that trajectories depend on the initial conditions and those emanating from a close neighborhood of some initial conditions is termed as a *flow*. As discussed before, study of fixed/critical points (i.e., all $\mathbf{X}^*$ for which $f(\mathbf{X}^*) = 0$) and their linear stability gives tremendous insights into the system and can also be used to design a control approach which includes something we will term *zero-effort* (or coast) capture based on stable and unstable manifolds emanating from a close neighborhood of these critical points. In fact, the strategy is to determine a state (or more generally, a family of states) that coast asymptotically to the equilibrium state.

Expanding the right-hand side of Equation (3.20) around a critical point and retaining only first order terms, we can write,

$$f(\mathbf{X}) = f(\mathbf{X}^*) + \mathbb{D}f(\mathbf{X}^*)(\mathbf{X} - \mathbf{X}^*) + O(2), \quad \text{where} \quad \mathbb{D}f(\mathbf{X}^*) = \frac{\partial f_i}{\partial x_j} \tag{3.21}$$

Now, for small $(\mathbf{X} - \mathbf{X}^*)$ i.e, in a sufficiently small neighborhood around the critical point, we can approximate the dynamics by,

$$f(\mathbf{X}) \approx \mathbb{D}f(\mathbf{X}^*)(\mathbf{X} - \mathbf{X}^*) = \mathbf{A}(\mathbf{X} - \mathbf{X}^*). \tag{3.22}$$

This means in the sufficiently small neighborhood around the fixed point, we have approximated the non-linear set of EOMs with a linear expansion term. Expressing this mathematically,

$$\dot{\mathbf{X}} = f(\mathbf{X}) \longrightarrow \dot{\mathbf{Y}} = \mathbf{A}\mathbf{Y}. \tag{3.23}$$

This follows straight from the *Hartman-Grobman theorem* [91, 92] which is stated below for the sake of completion. The proof of the theorem is beyond the scope of this dissertation and the reader is referred to [93] for further study.

Hartman-Grobman Theorem: *Consider a system evolving in time with state $x(t)$ in $\mathbb{R}^n$ satisfying the differential equation $\frac{dx}{dt} = f(x)$ for some smooth map $f : \mathbb{R}^n \longrightarrow \mathbb{R}^n$. Now, suppose $x^* \in \mathbb{R}^n$ is a hyperbolic equilibrium point of the system i.e, $f(x^*) = 0$ and the Jacobian Matrix $\mathbf{A} = [\frac{\partial f_i}{\partial x_j}]$ of f at x^* has no eigenvalue with real part equal to zero. Then, there exists a neighborhood $\mathbb{N}$ of x^* and a homeomorphism $h : \mathbb{N} \longrightarrow \mathbb{R}^n$, such that $h(x^*) = 0$ and in the neighborhood $\mathbb{N}$ the flow of $\frac{dx}{dt} = f(x)$ is topologically conjugate (or equivalent) to the continuous map $X = h(x)$ to the flow of its linearization $\frac{dX}{dt} = \mathbf{A}X$.*

Thus, when a non-linear system has a hyperbolic fixed point, the linearized system is basically homeomorphic to the non-linear behavior of the system in a small neighborhood of the fixed point. Additionally, the 'eigen-subspaces' of the Jacobian Matrix can be classified as follows depending upon the corresponding eigenvalues,

- *Stable eigen-subspace ($\mathbb{E}^s$):* is the subspace of $\mathbb{R}^n$ spanned by the eignvectors of $\mathbf{A}(v_i)$ such that $\text{Re}(\lambda_i) < 0$.

- *Center eigen-subspace ($\mathbb{E}^c$):* is the subspace of $\mathbb{R}^n$ spanned by the eignvectors of $\mathbf{A}(v_i)$ such that $\text{Re}(\lambda_i) = 0$.

- *Unstable eigen-subspace ($\mathbb{E}^u$):* is the subspace of $\mathbb{R}^n$ spanned by the eignvectors of $\mathbf{A}(v_i)$ such that $\text{Re}(\lambda_i) > 0$.

Qualitatively, if linearization indicates stability or instability, then these attributes apply to the non-linear motion in a finite region around the critical state-set. Before discussing the eigen-subspaces in a neighborhood around the critical point, we study the system behavior under small, medium and large deviations from a critical condition. Assuming that the system parameters are, $l_1/l_2 = 1/2$ and $m_1/m_2 = 2/1$, Table 3.2 shows the angular perturbations from the $\mathbf{X} = [0, 0, 0, 0]$ critical state for which the dynamical system behavior is plotted.

Table 3.2: Perturbation Cases for the Double Pendulum Simulation.

Perturbation	$\Delta\theta_1$	$\Delta\theta_2$	$\Delta\omega_1$	$\Delta\omega_2$
Small	2.865°	2.865°	0	0
Medium	28.65°	28.65°	0	0
Large	114.6°	114.6°	0	0

The phase plot depicted in the right sub-figure of Figure 3.3 resembles the 'Lissajous Orbits' [86] that are periodic three-dimensional orbits in the three-body system. Figures 3.4 and 3.5 depict the system behavior for the medium and large perturbations.

Notice from these figures how the phase-space plots gradually move from an ordered behavior for the trajectory for the small perturbations to a completely chaotic behavior for larger perturbations. A better understanding of the chaotic domain for this system is gained by simulating an initial condition and a neighboring condition which is 'close-enough' to the original initial condition and analyzing the respective phase-space plots. For $\Delta\theta_1 = 0.6°$ and $\Delta\theta_2 = 0.6°$ for large

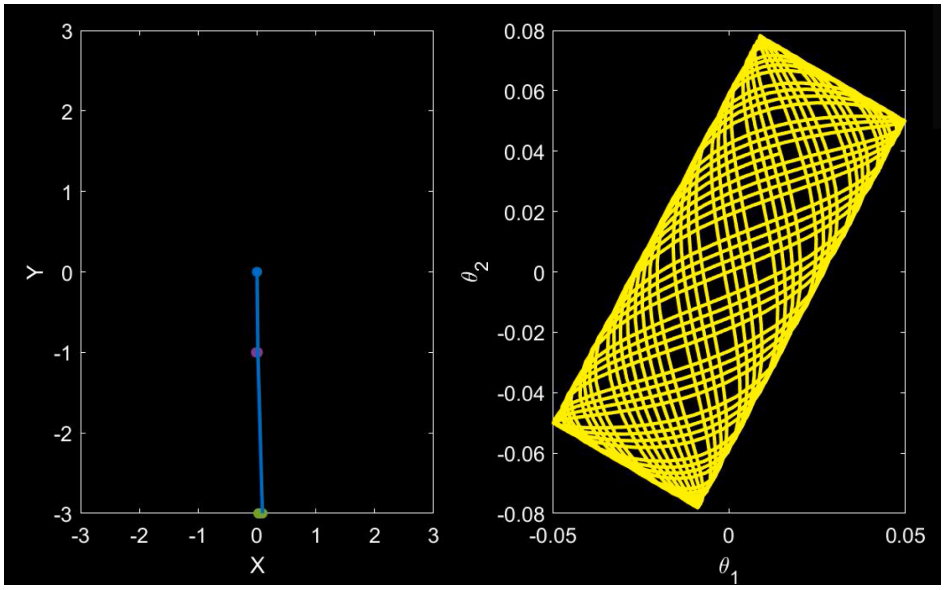

Figure 3.3: (left) Final State; (right) θ_1 vs. θ_2 evolution: Small Perturbations

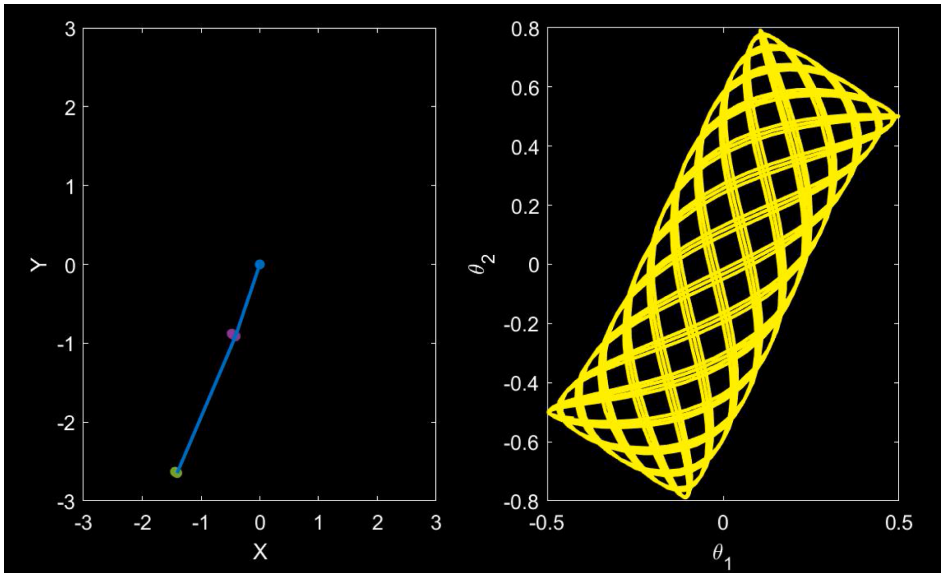

Figure 3.4: (left) Final State; (right) θ_1 vs. θ_2 evolution: Medium Perturbations

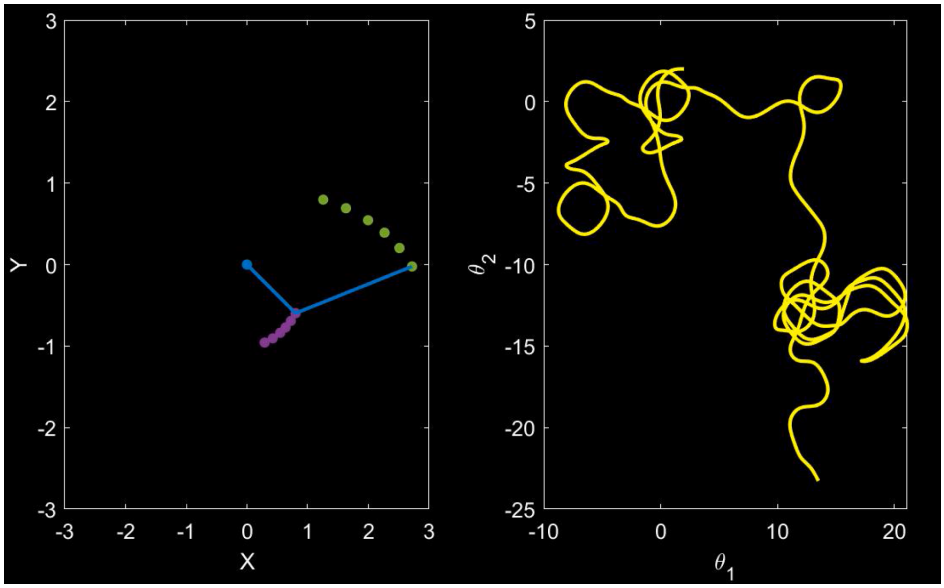

Figure 3.5: (left) Final State; (right) θ_1 vs. θ_2 evolution: Large Perturbations

perturbations around the swing-down critical state, Figures 3.6 & 3.7 depict the system behavior respectively for the original and neighboring initial conditions, propagated for the same time $\check{t}$.

Analyzing the two phase-space plots as well as the terminal states after propagating the two initial conditions for the same amount of time, it is immediately obvious that the progression of the states of the double pendulum evolve in very different ways and also end up at entirely different terminal conditions. This example clearly depicts how in the chaotic realm, conditions close together can evolve very differently despite following the same set of deterministic dynamical system EOMs. In the next section, we will look at the sub-spaces associated with all four fixed points and use the stable manifold associated with the full 'swing-up' critical state for a 'zero-effort' system control.

3.1.3 Stability of Fixed Points and Full Swing-Up using Stable Manifolds

The stable and unstable eigen sub-spaces lead to stable and unstable invariant manifolds of the double pendulum system. These trajectories get asymptotically attracted to the critical state or asymptotically depart the critical state which was used to study the linear dynamics in a neighborhood. Due to the behavior of stable manifolds getting asymptotically attracted to a state which is

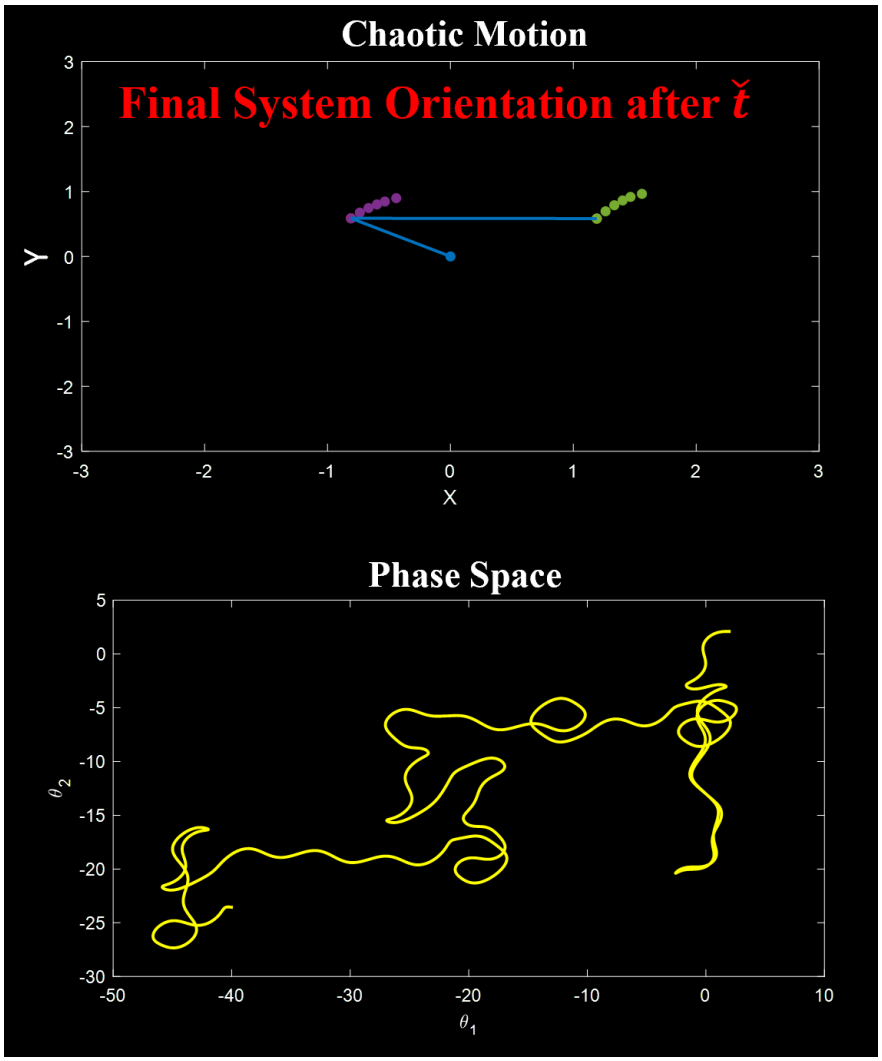

Figure 3.6: (Top) Final State; (Bot) θ_1 vs. θ_2 evolution: Original Condition

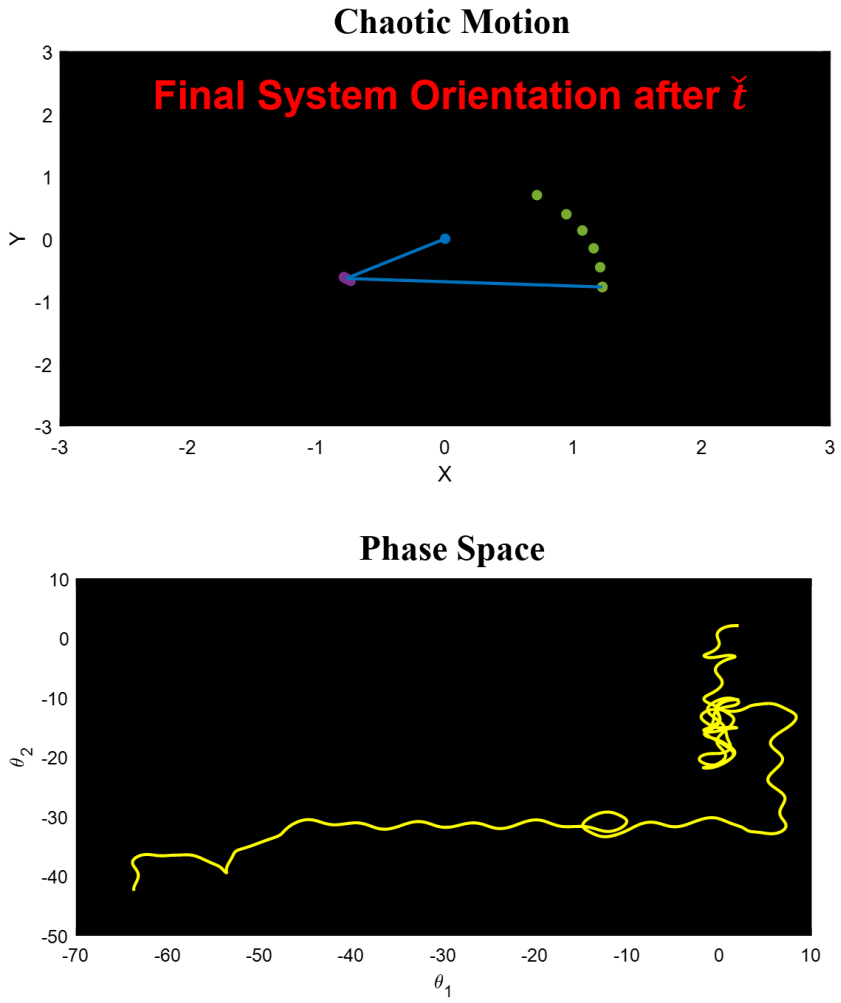

Figure 3.7: (Top) Final State; (Bot) θ_1 vs. θ_2 evolution: Neighboring Condition

'very close' to the critical state, this pre-computed trajectory can be used as a part of the control sequence by designing a control that initially drives the system to a state on the stable manifold and then switch off the control such that the system reaches the critical state in question using a 'zero-effort' control. Figure 3.9 explains this concept qualitatively using a schematic. Note that the velocities and positions of the two masses in the intermediate state must accurately match the state on the stable manifold to asymptotically approach the 'full swing-up' configuration.

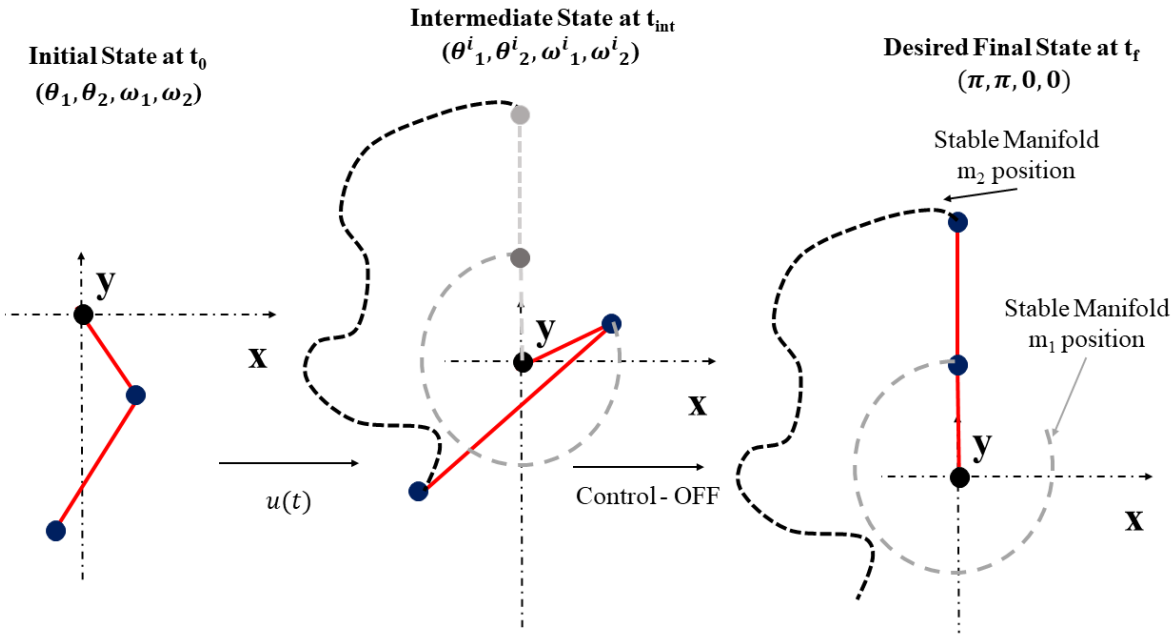

Figure 3.8: Manifold In-Loop Control for Full Swing-Up Maneuver

Using a manifold in-loop control, there are a couple of obvious advantages. Firstly, it reduces the complexity of the problem in that an end-to end optimal control problem need not be solved. The optimal control only needs to optimize the piece of trajectory till the system merges onto the manifold at a pre-computed insertion point. Secondly, it provides multiple opportunities for a re-plan of the control sequence in case some control commands are erroneous of if the control system exhibits an off-nominal performance. However, this approach does suffer from a limitation. Any

control sequence which uses a stable manifold as a part of it must pass through a neighborhood of a fixed point. Often times, when the target terminal state of the non-linear system is far away from the fixed point state, there might exist other significantly more optimal control which minimize control effort. Thus, while the concept is attractive, the results need to be validated against known end-to end results to perform a comprehensive trade-off study.

Table 3.3 shows the eigenvalues for the four critical states of the double pendulum and using them the nature of eigen-subspaces available for leveraging in each case has been deciphered and listed.

Table 3.3: Eigenvalues of Critical States of the Double Pendulum.

Critical State	λ_1	λ_2	λ_3	λ_4
$\{0, 0, 0, 0\}$	0 + 3.9317i	0 - 3.9317i	0 + 2.0352i	0 -2.0352i
$\{0, \pi, 0, 0\}$	-3.451	3.451	0 + 2.3186i	0 -2.3186i
$\{\pi, 0, 0, 0\}$	-2.3186	2.3186	0 + 3.415i	0 - 3.415i
$\{\pi, \pi, 0, 0\}$	-3.9317	-2.0352	3.9317	2.0352

Let us assume that λ_s represents the eigenvalue associated with the stable eigen-subspace and ν_s depicts the corresponding eigenvector. Then the initial condition on the stable manifold corresponding to $\{\lambda_s, \nu_s\}$ can be computed as the following,

$$\mathbf{X}^s = \mathbf{X}^* \pm \epsilon \nu_s, \tag{3.24}$$

where $\mathbf{X}^s$ depicts the initial state on the stable manifold, $\mathbf{X}^*$ denotes the corresponding critical-state condition, ϵ is a small positive multiplier which quantifies the perturbation from the critical state and should be small enough such that the linearity assumption holds. Essentially, we have perturbed the critical-state to a neighboring state using a perturbation multiplier in an eigen-direction which spans the stable region. When propagated backwards in time, a trajectory is obtained which always gets asymptotically attracted to a close neighborhood of the critical condition upon forward propagation. Figure 3.9 depicts this concept to achieve a 'Full Swing-Up' maneuver of the double

pendulum by leveraging the corresponding stable manifold.

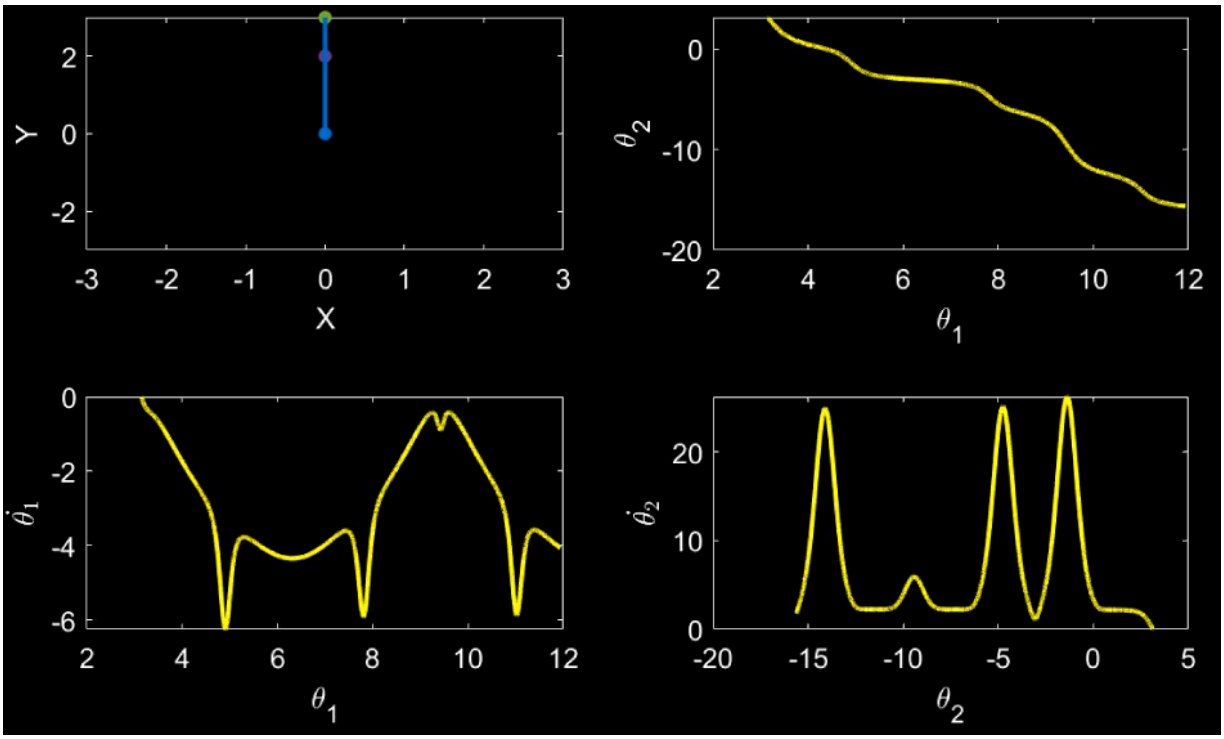

Figure 3.9: Trajectory in Phase-Space: Full Swing-Up Maneuver Leveraging Stable Manifold ($\epsilon = +1 \times 10^{-8}$)

Based on the eigenvalues listed in Table 3.3, it is clear that all critical points except the $\mathbf{X}^* = \{0, 0, 0, 0\}$ have well defined stable and unstable eigen-subspaces. Thus, stable manifolds associated with the remaining states were computed and have been plotted below in Figures 3.10 - 3.12. The manifold plots for +ve ϵ vs. $-$ve ϵ are mirror images due to the inherent symmetry in the problem. Note that the stable manifold trajectory can be propagated backwards as long as the designer deems appropriate but is typically restricted due to the trade-offs in *time vs. control effort*.

3.2 Invariant Manifolds in CR3BP

In this section, the invariant manifold theory is presented in the context of periodic orbits in the CR3BP system. In order to work with an example, Halo Orbits are the choice for periodic orbits in

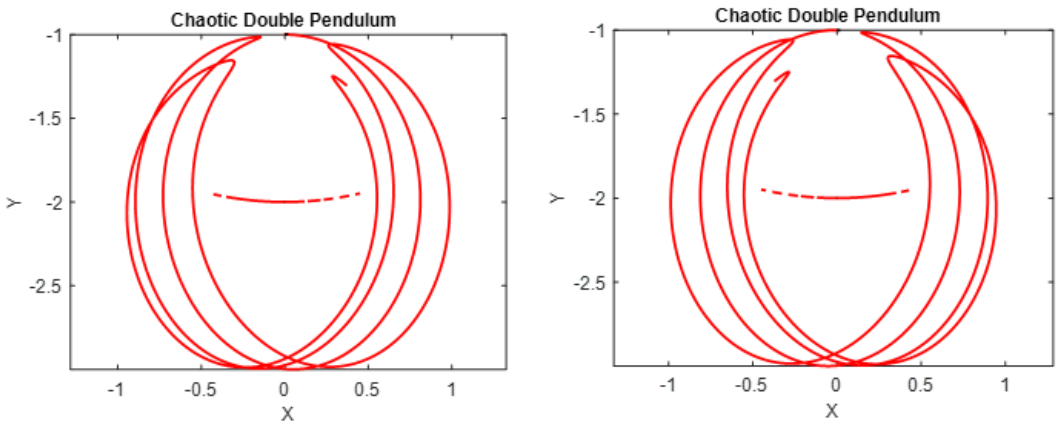

Figure 3.10: Stable Manifold for $\mathbf{X}^* = \{0, \pi, 0, 0\}$ (left) $\epsilon : +$, (right) $\epsilon : -$.

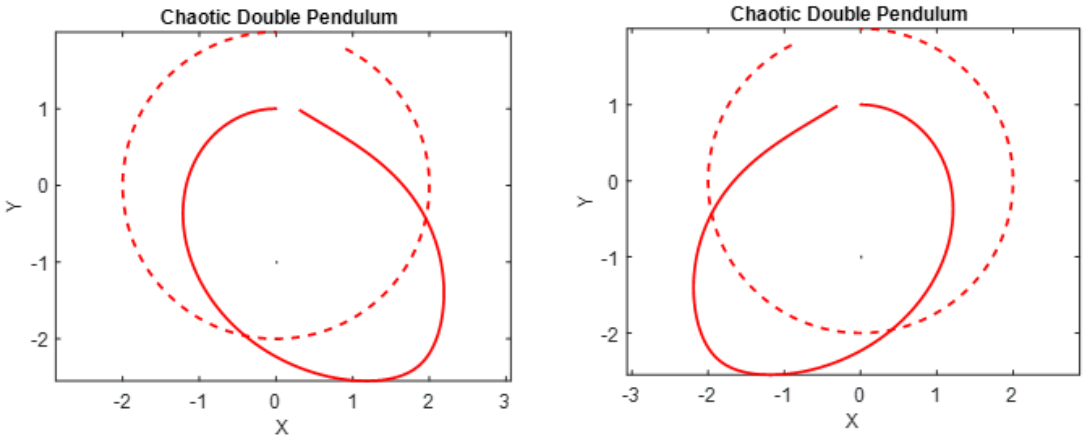

Figure 3.11: Stable Manifold for $\mathbf{X}^* = \{\pi, 0, 0, 0\}$ (left) $\epsilon : +$, (right) $\epsilon : -$.

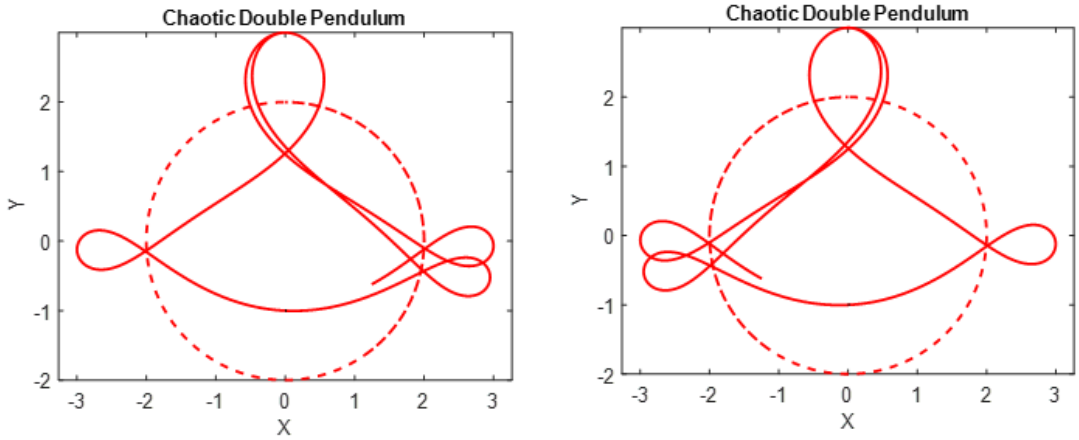

Figure 3.12: Stable Manifold for $\mathbf{X}^* = \{\pi, \pi, 0, 0\}$ (left) $\epsilon : +$, (right) $\epsilon : -$.)

this section but the approach is modular in that it works for any periodic orbit around any libration point of the system. Finally, extending the concept of leveraging invariant manifolds for control design a novel methodology is presented which utilises stable/unstable manifolds as long terminal coast arcs (LTCAs) or long originating coast arcs (LOCAs). The LTCAs are occasionally referred to as "ballistic capture" since they ideally coast into the periodic orbit.

3.2.1 Halo Orbit Computation

The procedure for computation of halo orbits and their associated manifolds are well documented in literature. However, a succinct description of the procedure is provided in the succeeding sections for the sake of completion. The Γ term in the effective potential, contains the non-linear terms, r_1 and r_2. An expansion using Legendre polynomials (P_n) [**?**] can be developed as

$$\frac{1}{\sqrt{(x-a)^2+(y-b)^2+(z-c)^2}} = \frac{1}{D}\sum_{n=0}^{\infty}\Big(\frac{\rho}{D}\Big)^n P_n\Big(\frac{ax+by+cz}{D\rho}\Big), \tag{3.25}$$

where $D^2 = a^2 + b^2 + c^2$ and $\rho^2 = x^2 + y^2 + z^2$. After some manipulations, the equations of motion can be written as

$$\begin{aligned}
\ddot{x} - 2\dot{y} - (1+2c_2)x &= \frac{\partial}{\partial x}\sum_{n\geq 3} c_n \rho^n P_n\Big(\frac{x}{\rho}\Big),\\
\ddot{y} + 2\dot{x} + (c_2-1)y &= \frac{\partial}{\partial y}\sum_{n\geq 3} c_n \rho^n P_n\Big(\frac{x}{\rho}\Big),\\
\ddot{z} + c_2 z &= \frac{\partial}{\partial z}\sum_{n\geq 3} c_n \rho^n P_n\Big(\frac{x}{\rho}\Big),
\end{aligned} \tag{3.26}$$

where the left-hand side contains the linear terms and the right-hand side contains the non-linear ones. c_2 is a positive constant and its value along with those of A, B and C depend on the primary body pair along with the libration point in question. The linearized equations of motion are obtained by setting the RHS of Eq. (3.26) to zero as follows

$$\ddot{x} - 2\dot{y} - (1+2c_2)x = 0, \qquad \ddot{y} + 2\dot{x} + (c_2-1)y = 0, \qquad \ddot{z} + c_2 z = 0. \tag{3.27}$$

The z-axis solution is independent of x and y coordinates, and can be described as a simple harmonic (note that $c_2 > 0$) motion. However, the motion in the xy-plane is coupled. The solution of the characteristic equation of the coupled xy-plane motion in Eq. (3.27) has two real and two imaginary roots $(\pm\lambda, \pm i\omega_p)$. Since the two real roots are opposite in sign, arbitrary initial conditions, in general, lead to unbounded solutions. Thus, in order to obtain bounded trajectories in the xy-plane, the initial conditions need to be restricted so that only non-divergent mode is allowed. Let $\kappa = \frac{\omega_p^2+1+2c_2}{2\omega_p}$, these solutions can be written as

$$x = -A_x \cos(\omega_p t + \phi), \qquad y = \kappa A_x \sin(\omega_p t + \phi), \qquad z = A_z \sin(\omega_v t + \psi), \tag{3.28}$$

where ω_p and ω_v denote the in-plane and out-of-plane frequencies, and A_x and A_z denote the in-plane and out-of-plane amplitude, and ϕ and ψ denote the corresponding phase difference. The linearized motion becomes quasi-periodic if the in-plane and out-of-plane frequencies are such that their ratio is irrational. The horizontal and vertical motion, in general, do not exhibit the same period. They form a 'criss-cross' or a Lissajous figure in space as viewed in the rotating frame. In the special case of identical periodicity, the resulting periodic orbit is a halo orbit. Note that there are other frequently studied periodic solutions such as Vertical Lyapunov orbits, where the vertical period is twice that of the in-plane period. Analytical approximations and the Lindstedt-Poincare method on the third-order Richardson Expansion [94] are used to compute periodic orbit families. The third-order expansion of the Legendre Polynomials in Eq. (3.26) is written as

$$\begin{aligned}
\ddot{x} - 2\dot{y} - (1 + 2c_2)x &= \frac{3c_3}{2}(2x^2 - y^2 - z^2) + 2c_4(2x^2 - 3y^2 - 3z^2) + O(4), \\
\ddot{y} + 2\dot{x} + (c_2 - 1)y &= -3c_3 xy - \frac{3}{2}c_4 y(4x^2 - y^2 - z^2) + O(4), \\
\ddot{z} + c_2 z &= -3c_3 xz - \frac{3}{2}c_4 z(4x^2 - y^2 - z^2) + O(4).
\end{aligned} \tag{3.29}$$

In order to generate a halo orbit accurate enough for mission design, the third-order approximation is used as a first guess to reliably generate accurate halo orbits (using a numerical differential corrector method). An intermediate orbit may be useful for accurate navigation and for science

payload checkout. A candidate halo orbit is used as an intermediate staging orbit for the Earth-Moon trajectories designed in this work. Since the system is symmetric about the xy-plane, and not just the linearized system, any periodic orbit has a symmetric partner. Halo orbits are usually labeled as Northern class and Southern class orbits. Using the methodology described above, several halo orbits around the Earth-Moon L_1 point were computed and characterized by their respective Jacobi constants. Figure 3.13 shows three representative L_1 halo orbits with different Jacobi constants.

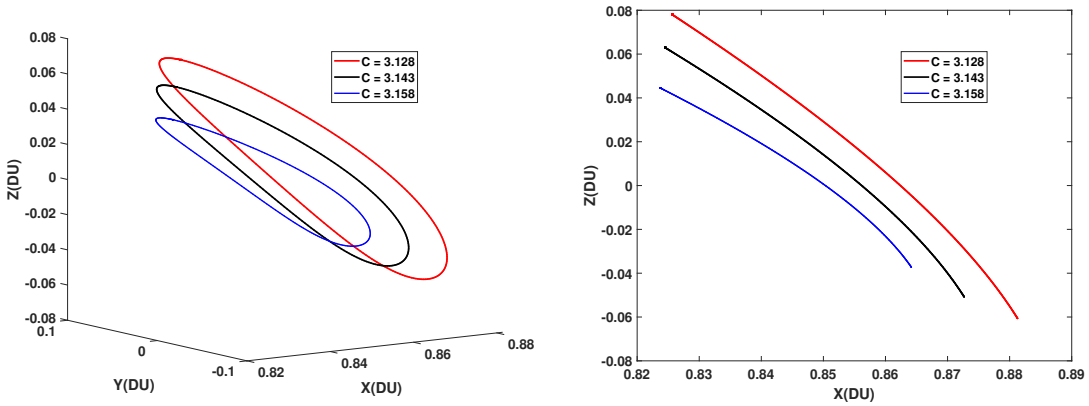

(a) 3D View (b) XZ planar view

Figure 3.13: Northern L_1 halo orbits in the Earth-Moon CR3BP with different Jacobi constants.

3.2.2 Preliminaries

The methodology for computing stable and unstable manifolds associated with a particular halo orbit is based on numerical methods. It is important to understand a few preliminaries before discussing the methodology for computation of invariant manifold trajectories.

3.2.2.1 Poincaré Maps

A Poincaré map is extremely useful for analyzing dynamical systems and is predominantly used to identify orbits and transfers between orbits in a complicated system like the CR3BP. The map is created by mapping the intersections of a trajectory in an n-dim flow defined by $\dot{\mathbf{X}} = f(\mathbf{X})$

by a $(n-1)$-dim surface, Σ. Due to this, the Poincaré mapping replaces the flow of an n^{th} order system with a discrete $(n-1)^{th}$ order system. Mathematically, a Poincaré map, P, is described as a function that maps the trajectory state at the k^{th} intersection with Σ, $\mathbf{X}_k$, to the trajectory state at the next intersection instance, $\mathbf{X}_{k+1}$

$$\mathbf{X}_{k+1} = P(\mathbf{X}_k). \tag{3.30}$$

Thus, in case a trajectory which pierces Σ at $\mathbf{X}^*$ at time t and then returns to $\mathbf{X}^*$ at time $t+T$ then it is evident that the trajectory represents a periodic orbit in the dynamical system with a period T. Researchers often consider three different kinds of Poincaré maps defined as,

- P_+ : This is a map created only from positive intersections of the trajectory with Σ. For instance, often times in the CR3BP, Σ is defined as the $Y-Z$ plane set to some x value and P_+ includes only those intersections that have a positive $\dot{X}$.
- P_- : Similarly, the map created from only negative intersections of the trajectory with Σ define P_-.
- $P_\pm$: Finally, if all intersections of the trajectory with Σ are considered, the map constitutes $P_\pm$.

While, P_+ and P_- are called one-sided maps, $P_\pm$ is called a two-sided map. Figure 3.14 depicts a schematic showing the Poincaré map for two orbits, one periodic and the other not immediately periodic.

3.2.2.2 The State Transition and Monodromy Matrices

The state transition matrix (STM), $\mathbf{\Phi}(t, t_0)$, is used to approximate the departure motion dynamics along a trajectory. It approximately quantifies the effect of a slight deviation in the state variables in the propagation of the trajectory. The first predominant use of STM in the context of periodic orbit computation lies in the differential correction approach discussed briefly in the

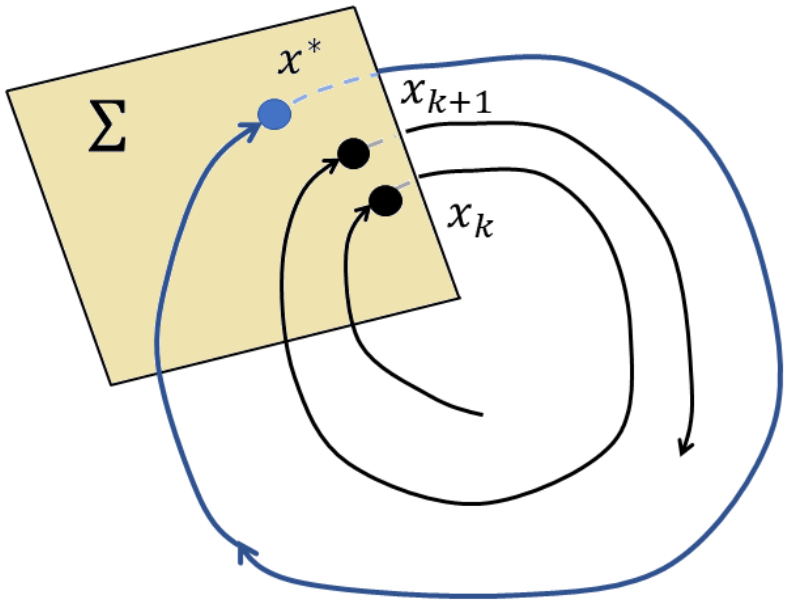

Figure 3.14: A Schematic Depicting Poincaré Map for a Periodic and a Non-Periodic Orbit

last chapter. This is because, it provides a way of adjusting initial conditions of a trajectory to arrest/correct undesired motion and it leads to periodic/quasi-periodic motion.

The second application of the STM, relevant to the discussion here, is to provide information about the stability of an orbit and help compute the orientation of eigenvectors along the orbit. In this application, a Monodromy Matrix, **M**, which is a special case of the STM along a closed periodic orbit is used. Floquet theory [95] is used to study the stability of solutions to linear periodic differential equations.

Floquet Theory: Consider a linear, first-order system defined as,

$$\dot{\mathbf{X}}(t) = \mathbf{A}(t)\mathbf{X}(t), \tag{3.31}$$

where $\mathbf{A}(t)$ is a $n \times n$ T-periodic matrix i.e.,

$$\mathbf{A}(t + T) = \mathbf{A}(t) \tag{3.32}$$

The zero-input response solution to the system described by Equation (3.31) using the STM, $\mathbf{\Phi}(t, \tau)$, is written as,

$$\mathbf{X}(t) = \mathbf{\Phi}(t, t_0)\mathbf{X}(t_0). \tag{3.33}$$

In order for $\mathbf{\Phi}(t, t_0)$ to be a fundamental solution matrix for the system, the columns must represent linearly independent solutions of the system. Therefore it satisfies,

$$\dot{\mathbf{\Phi}}(t, t_0) = \mathbf{A}(t)\mathbf{\Phi}(t, t_0) \tag{3.34}$$

and also the periodicity condition, i.e.,

$$\mathbf{\Phi}(t + T, t_0 + T) = \mathbf{\Phi}(t, t_0) \tag{3.35}$$

A general solution to Equation (3.34) can be expressed as,

$$\mathbf{\Phi}(t, t_0) = \mathbf{P}(t, t_0) \ \ e^{(t-t_0)\mathbf{Q}(t_0)}, \tag{3.36}$$

where $\mathbf{Q}(t_0)$ is a $n \times n$ matrix and $\mathbf{P}(t + T, t_0) = \mathbf{P}(t, t_0)$ is T-periodic. The fundamental matrix describes the evolution of the solutions to the linear periodic dynamical system and at some time t_0, $\mathbf{\Phi}(t_0, t_0) = \mathbb{I}$. Also, if $\mathbf{X}(t + t_0)$ is a solution then the evolution is given by,

$$\mathbf{X}(t + t_0) = \mathbf{\Phi}(t, t_0)\mathbf{X}(t_0). \tag{3.37}$$

The stability of the solution is given by the eigenvalues of the so-called, Monodromy Matrix, $\mathbf{M}$, expressed as,

$$\mathbf{M}(t_0) = \mathbf{\Phi}(t_0 + T, t_0). \tag{3.38}$$

Note that $\Delta\mathbf{X}(t_0 + T) = \mathbf{M}(t_0)\Delta\mathbf{X}(t_0)$. This is why the eigenvalues of $\mathbf{M}(t_0)$ govern stability of departure dynamics from the periodic orbit. $\mathbf{M}(t_0)$ describes the evolution over one period T. $\mathbf{M}$

can also be written in the form,

$$\mathbf{M}(t_0) = e^{T\mathbf{Q}(t_0)} \tag{3.39}$$

The eigenvalues of $\mathbf{M}(t_0)$, λ_j are sometimes referred to as *Floquet Multipliers* of the solution to Equation (3.31) and the solution is said to be stable if $|\lambda_j| \leq 1 \quad \forall \quad j$. This concept applies to identifying stable and unstable eigenspaces around a point on a periodic orbit for the CR3BP system.

Let $\mathbf{X}$ denote the column state vector which includes all variables of interest in the system. For our case, $\mathbf{X}$ includes the six state variables defining motion of a spacecraft, i.e.,

$$\mathbf{X} = [x \;\; y \;\; z \;\; \dot{x} \;\; \dot{y} \;\; \dot{z}]^T. \tag{3.40}$$

The state transition matrix is a 6×6 matrix composed of partial derivatives of the state

$$\mathbf{\Phi}(t, t_0) = \frac{\partial \mathbf{X}(t)}{\partial \mathbf{X}(t_0)} \tag{3.41}$$

with initial conditions $\mathbf{\Phi}(t_0, t_0) = \mathbb{I}$ and is propagated using Equation (3.34) where $\mathbf{A}(t) = \frac{\partial \dot{\mathbf{X}}(t)}{\partial \mathbf{X}(t)}$. For the CR3BP, $\mathbf{A}(t)$ is given by,

$$\mathbf{A}(t) = \left[\begin{array}{c|c} 0 & \mathbb{I} \\ \hline U_{\mathrm{XX}} & 2\Omega \end{array}\right], \quad \text{where} \quad \Omega = \begin{bmatrix} 0 & 1 & 0 \\ -1 & 0 & 0 \\ 0 & 0 & 0 \end{bmatrix} \tag{3.42}$$

and U_{XX} is a symmetric matrix composed of the second partial derivatives of U with respect to the spacecraft's position computed along the orbit i.e.,

$$U_{\mathrm{XX}} = \begin{bmatrix} \frac{\partial \ddot{x}}{\partial x} & \frac{\partial \ddot{x}}{\partial y} & \frac{\partial \ddot{x}}{\partial z} \\ \frac{\partial \ddot{y}}{\partial x} & \frac{\partial \ddot{y}}{\partial y} & \frac{\partial \ddot{y}}{\partial z} \\ \frac{\partial \ddot{z}}{\partial x} & \frac{\partial \ddot{z}}{\partial y} & \frac{\partial \ddot{z}}{\partial z} \end{bmatrix} \tag{3.43}$$

The Monodromy Matrix, $\mathbf{M}$, exists for periodic orbits of the system and is computed by prop-

agating the STM for one complete orbit since, $\mathbf{M} = \mathbf{\Phi}(t_0 + T, t_0)$ where T is the period. Since, an analytical expression for the STM is not available, it is usually numerically computed. This means that for a particular initial condition, $\mathbf{X}_0$, the following initial value problem has to be solved,

$$\dot{\mathbf{X}} = f(\mathbf{X}), \quad \dot{\mathbf{M}} = \left[\frac{\partial \dot{\mathbf{X}}}{\partial \mathbf{X}}\right]\mathbf{M} \tag{3.44}$$

with initial conditions,

$$\mathbf{X}(0) = \mathbf{X}_0, \quad \mathbf{M}(0) = \mathbb{I}.$$

After propagation for a full orbit, the matrix contains information about every region that a spacecraft passes through along the orbit. Stability of periodic orbits are determined by analyzing the eigenvalues of $\mathbf{M}$. A perturbation in the state of a spacecraft in an unstable orbit causes the state to exponentially diverge over time. Therefore, $\mathbf{M}$ has at least one eigenvalue outside the unit circle. In the three dimensional CR3BP, $\mathbf{M}$ has six eigenvalues, λ_i for $i = 1, 2, ..., 6$ with v_i denoting the corresponding eigenvectors. Note that since $(\mathbf{M} - \lambda_i \mathbb{I})v_i = 0$ it is obvious that if v_i is an eigenvector, so it $\pm c v_i$ where c is arbitrary. Thus the sign on v_i is also arbitrary and it is worth paying attention to when MATLTAB's *eig* or any other eigenvalue routine is invoked. The eigenvalues occur in reciprocal pairs due to the symplectic nature of $\mathbf{M}$ in the CR3BP. Additionally, a pair of eigenvalues is equal to unity because of the Jacobi integral of motion in the CR3BP. Thus, the eigenvalues have the following structure,

$$\lambda_2 = \frac{1}{\lambda_1}, \quad \lambda_4 = \frac{1}{\lambda_3}, \quad \lambda_5 = \lambda_6 = 1. \tag{3.45}$$

The eigenvalues of $\mathbf{M}$ of a periodic orbit in the CR3BP are the roots of the characteristic equation. For Keplerian orbits, three pairs of eigenvalues exist and are all identically equal to 1. This signifies that after a full orbit the perturbations neither grow nor decay. On the other hand, for CR3BP, $\mathbf{M}$ may have other eigenvalue pairs, including real values not equal to 1 and pairs of complex numbers. The reciprocal nature of non-unity eigenvalues ensure existence of at least one

pair of stable and unstable eigenvalues, the eigenvectors of which depict the direction of asymptotic growth/decay. Table 3.4 depicts the future behavior of a random perturbation for a particular range of the eigenvalue.

Table 3.4: Eigenvalues and Comments on Perturbation Decay/Growth.

Range	**Comments**
Real, $\lambda_i \in$ (-1,1) $\forall\ i = 1, .., 6$	Exponential Decay
Real, $\lambda_i = 1$ OR $\lambda_i = -1 \forall\ i = 1, .., 6$	Neither Exponential Decay nor Exponential Growth
Real, $\lambda_i \in (-\infty, -1) \cap (1, \infty) \forall\ i = 1, .., 6$	Exponential Growth
Imaginary	Perturbation oscillates about original state

All periodic orbits have at-least one pair of eigenvalues that are equal to unit and it is usual to ignore when studying stability of orbits. In order to determine the eigenvalues of **M**, we consider the characteristic equation,

$$|\mathbf{M} - \lambda\mathbb{I}| = (\lambda - \lambda_1)(\lambda - \lambda_2)(\lambda - \lambda_3)(\lambda - \lambda_4)(\lambda - \lambda_5)(\lambda - \lambda_6) = 0 \tag{3.46}$$

$$= (\lambda - 1)^2(\lambda - \lambda_1)(\lambda - 1/\lambda_1)(\lambda - \lambda_3)(\lambda - 1/\lambda_3) = 0 \tag{3.47}$$

Assuming, $p = -(\lambda_1 + 1/\lambda_1)$ and $q = -(\lambda_3 + 1/\lambda_3)$ the equation can be rewritten as,

$$(\lambda - 1)^2(\lambda^2 + p\lambda + 1)(\lambda^2 + q\lambda + 1) = 0 \tag{3.48}$$

This can also be re-written as,

$$(\lambda - 1)^2(\lambda^4 + \alpha\lambda^3 + \beta\lambda^2 + \alpha\lambda + \gamma) = 0, \tag{3.49}$$

where $\alpha = p + q$, $\beta = pq + 2$ and $\gamma = 1$. Bray and Goudas [96] have derived a simple way to

compute α and β using the Monodromy Matrix,

$$\alpha = 2 - tr(\mathbf{M}), \quad \beta = \frac{\alpha^2 - tr(\mathbf{M}^2)}{2} + 1 \tag{3.50}$$

Then p and q are determined using p and q,

$$\begin{bmatrix} p \\ q \end{bmatrix} = \begin{bmatrix} \frac{\alpha + \sqrt{\alpha^2 - 4\beta + 8}}{2} \\ \frac{\alpha - \sqrt{\alpha^2 - 4\beta + 8}}{2} \end{bmatrix} \tag{3.51}$$

Using these expressions one can solve for λ_1 and λ_3 whereas the final two eigenvalues are already known as $\lambda_5 = \lambda_6 = 1$. Thus, this is an easy way to compute the eigenvalues and the eigenvectors can be computed to within a sign and scale factor in any standard way using the equation, $\mathbf{M}v_i = \lambda_i v_i \;\; \forall i = \{1, 2, ..., 6\}$. Normally, the eigenvectors v_i are normalized to have unit magnitude. Note that the stable and unstable eigenvalues, λ^S and λ^U are equal to the pair of real eigenvalues with the smallest and largest values, if they exist.

3.2.3 Manifold Computation

CR3BP dynamics allow for five fixed points called libration points and numerous periodic orbit families as discussed before. It was also proven that periodic orbits around the three collinear libration points are unstable in the Earth-Moon CR3BP. We also saw that for an unstable periodic orbit has at least one stable and one unstable eigenvalue in the CR3BP.

A spacecraft in an unstable periodic orbit around either L_1, L_2 and L_3 that experiences a perturbation in the unstable eigen-direction exponentially diverges from its nominal position on the orbit while tracing out a smooth trajectory. Similarly, a spacecraft with the "right" initial condition would follow a smooth trajectory which exponentially approaches the orbit from the stable eigen-direction. These two trajectories describe stable and unstable invariant manifolds. Therefore, an *unstable* invariant manifold (W^U) includes the set of all trajectories that a spacecraft takes if perturbed anywhere on the unstable periodic orbit in the direction of the unstable eigenvector whereas the *stable* invariant manifold (W^S) includes the set of trajectories that a spacecraft takes

to asymptotically arrive onto the orbit along the local stable eigenvector.

3.2.3.1 Invariant Manifolds of Unstable Lagrange Points

The collinear Lagrange points are unstable and therefore have associated invariant manifolds. Since, these are singular points in space, their manifolds are one-dimensional structures. First, one needs to compute eigenvalues of the Jacobian (J) of their states where $J = \frac{\partial \dot{\mathbf{X}}}{\partial \mathbf{X}}$. Using the EOMs for the CR3BP, J is expressed as,

$$J = \begin{bmatrix} 0 & 0 & 0 & 1 & 0 & 0 \\ 0 & 0 & 0 & 0 & 1 & 0 \\ 0 & 0 & 0 & 0 & 0 & 1 \\ \frac{\partial \ddot{x}}{\partial x} & \frac{\partial \ddot{x}}{\partial y} & \frac{\partial \ddot{x}}{\partial z} & 0 & 2 & 0 \\ \frac{\partial \ddot{y}}{\partial x} & \frac{\partial \ddot{y}}{\partial y} & \frac{\partial \ddot{y}}{\partial z} & -2 & 0 & 0 \\ \frac{\partial \ddot{z}}{\partial x} & \frac{\partial \ddot{z}}{\partial y} & \frac{\partial \ddot{z}}{\partial z} & 0 & 0 & 0 \end{bmatrix} \tag{3.52}$$

The eigenvalues of J for the three collinear Lagrange points include two imaginary pairs and one pair of real numbers. Table 3.5 summarizes the six eigenvalues for the collinear Lagrange points in the Earth-Moon system.

Table 3.5: Eigenvalues of the Collinear Lagrange Points: Earth-Moon System.

Eigenvalues	L_1	L_2	L_3
λ_1	-2.932056	-2.158674	-0.177875
λ_2	2.932056	2.158674	0.177875
λ_3	2.334386i	1.862646i	1.0104199i
λ_4	-2.334386i	-1.862646i	-1.0104199i
λ_5	2.268831i	1.786176i	1.00533144i
λ_6	-2.268831i	-1.786176i	-1.00533144i

The eigenvector corresponding to the larger real eigenvalue (λ_2) indicates the most unstable direction (v^U) whereas the eigenvector corresponding to the most negative real eigenvalue (λ_1) is the most stable direction (v^S). The unstable manifold, W^U, is then computed by propagating the

state $\mathbf{X}^U$ forward in time where $\mathbf{X}^U = \mathbf{X} \pm \epsilon v^U$ and ϵ is a small perturbation. Similarly, the stable manifold, W^S, is computed by propagating the state $\mathbf{X}^S$ backward in time where $\mathbf{X}^S = \mathbf{X} \pm \epsilon v^S$.

The perturbation ϵv can be applied in a positive or negative direction as discussed above to generate the "right" initial conditions for computation of stable and unstable manifolds. The Lagrange points may be visualized as a dynamical saddle point as shown in Figure 3.15. It also depicts the two halves of each manifold. Since the eigen-decomposition routine does not establish the eigenvectors uniquely, the ± sign covers both directions and either direction can be important depending on the application.

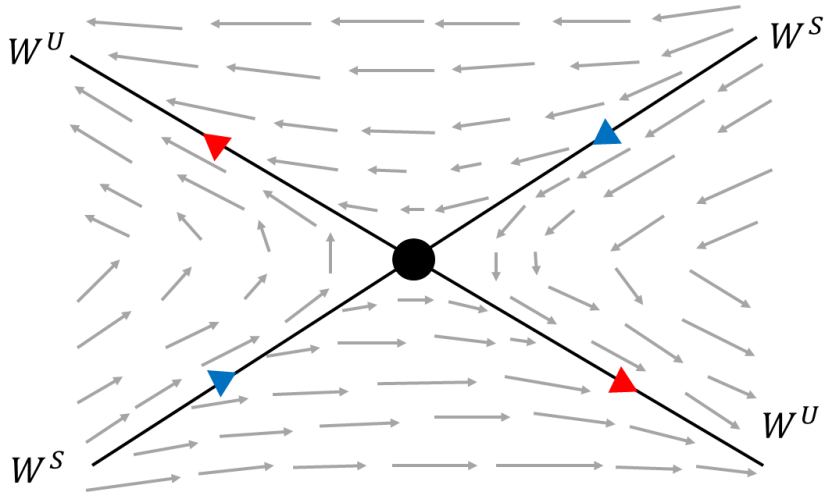

Figure 3.15: A Dynamical Saddle Point ($L_1/L_2/L_3$), Spacecraft Motion as Vector Fields

3.2.3.2 Invariant Manifolds of Unstable Periodic Orbits

Every unstable periodic orbit in the CR3BP has a set of invariant manifolds, much like the Lagrange points. Periodic orbits and Lagrange points are different in that they are one-dimensional structures whereas the Lagrange points are zero-dimensional structures. As a consequence the invariant manifolds are two-dimensional structures. They are a set of trajectories where each trajectory corresponds to one of the infinity of points along the periodic orbit. The bundle of trajectories

form a topological tube.

In order to produce invariant manifolds, one requires information about local stability characteristics of each point along the orbit. This can be done by evaluating the eigenvalues and eigenvectors of the Jacobian at each state on the orbit. However, evaluating so many eigenvalues is computationally intensive. A more efficient manner of producing invariant manifolds uses eigenvalues and eigenvectors of $\mathbf{M}$.

$\mathbf{M}$ is produced by propagating the STM around the orbit and contains information about orbit stability. In order to determine stable and unstable directions of $\mathbf{M}$ one has to propagate the stable and unstable eigenvectors of $\mathbf{M}$ about the orbit using STM. This means that the stable and unstable vectors at t_i about the orbit, v_i^S and v_i^U can be determined using stable and unstable eigenvectors of $\mathbf{M}$, v^S and v^U respectively.

$$v_i^S = \mathbf{\Phi}(t_i, t_0)v^S, \quad v_i^U = \mathbf{\Phi}(t_i, t_0)v^U \tag{3.53}$$

Following a procedure similar to the one applied for the double pendulum case and that for generating associated with the collinear Lagrange points, a small perturbation, ϵ, is then applied to the state of the orbit at that time, $\mathbf{X}_i$. Since, the STM grows exponentially along an unstable orbit, the magnitudes of the vectors v_i^S and v_i^U grow along the orbit. Therefore, it is important to perform a normalization of the vectors so that a consistent perturbation is applied to each state. The final equations to produce initial conditions for the stable and unstable manifolds at time t_i, $\mathbf{X}_i^S$ and $\mathbf{X}_i^U$ respectively are,

$$\mathbf{X}_i^S = \mathbf{X}_i \pm \epsilon\frac{v_i^S}{|v_i^S|}, \mathbf{X}_i^U = \mathbf{X}_i \pm \epsilon\frac{v_i^U}{|v_i^U|} \tag{3.54}$$

The sign of perturbation differentiates between the interior and exterior manifolds. The magnitude of perturbation, parameterized via ϵ is arbitrary but bounded. Technically, it should be small enough to be consistent with the local linearization. Theoretically, manifold trajectories asymptotically approach the orbit as time goes forward or backward. In reality, they never arrive on the orbit

in a finite amount of time and only come close to it. In order to map the manifolds, one perturbs the orbit state slightly and then propagates the state in time. It is apparent that the smaller the perturbation, the closer the approximation is to mapping the true manifolds but they require more time to depart from the orbit than larger perturbations. This trade-off becomes significant during practical mission design applications which leverage the manifolds because the designers are more interested in well behaved algorithms that are computationally swift. Another aspect is that, since a small maneuver will always be required in order to insert into the periodic orbit even though the spacecraft is flying on a manifold which was generated using very small perturbations. Being in the local small linear domain is usually sufficient for mission design applications. Therefore, flying the true manifolds does not give enough returns to warrant the computational effort required in generating them. On the other hand M serves as a local linearization and therefore the state must not be perturbed in such a significant manner that the linear assumption does not hold. Essentially, ϵ must be qualitatively a measure of the size of the linearization domain.

Furthermore, the dynamics of manifold trajectories are largely dependent on the largest eigenvalues since the motion undergoes exponential growth in those directions as compared to any other direction. Typically, perturbations of the order of 100 km in the position sub-space are used in the Earth-Moon system. Note that perturbation is applied proportionally to all six components and therefore, the velocity perturbation is computed as,

$$\epsilon = \frac{100\text{km}}{\sqrt{v_x^2 + v_y^2 + v_z^2}}. \tag{3.55}$$

Structure of manifold trajectories is influenced by the local stability characteristics of the orbit. Libration orbits are uniformly unstable and their Lyapunov exponent does not vary significantly along the orbit. This translates into smooth and well-behaved manifold trajectories. Some other periodic orbits are unstable due to a close fly-by of either the primary or secondary body and thus their local stability changes drastically in regions where the orbit approaches the massive bodies. In these cases, the manifolds are not as well behaved and uniform and they spread out quickly near

the massive bodies while the bundle thins out substantially everywhere else. Figures 3.16 and 3.17 depict the stable manifolds of a L_1 Halo orbit (C = 3.128) in the Earth-Moon CR3BP system. Note that 'Sense' denotes the ± sign of the perturbation.

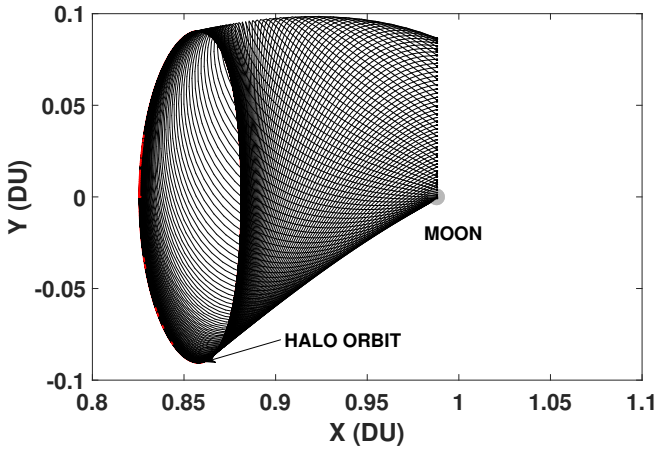

Figure 3.16: Sense: +1, Stable Manifold for L_1 Halo Orbit

Figures 3.18 and 3.19 depict the interior and exterior unstable manifolds for the same L_1 Halo Orbit.

3.2.3.3 Invariant Manifolds of Unstable Quasi-Periodic Orbits

Just like periodic orbits, unstable quasi-periodic orbits also have associated stable and unstable invariant manifolds. However, they must be thought about a bit differently. The quasi-periodic Halo orbits [97] are examples of quasi-periodic orbits that exist in the CR3BP system. Since, quasi-periodic orbits do not retrace their path, they cannot be produced in their entirety but specific segments of interest can be numerically produced. Due to a lack of periodicity, a Monodromy matrix, **M**, cannot be defined for these orbits and therefore the procedures outlined in the preceding section for periodic orbits do not apply.

Therefore, in order to produce manifolds for quasi-periodic orbits, one can compute the eigen-

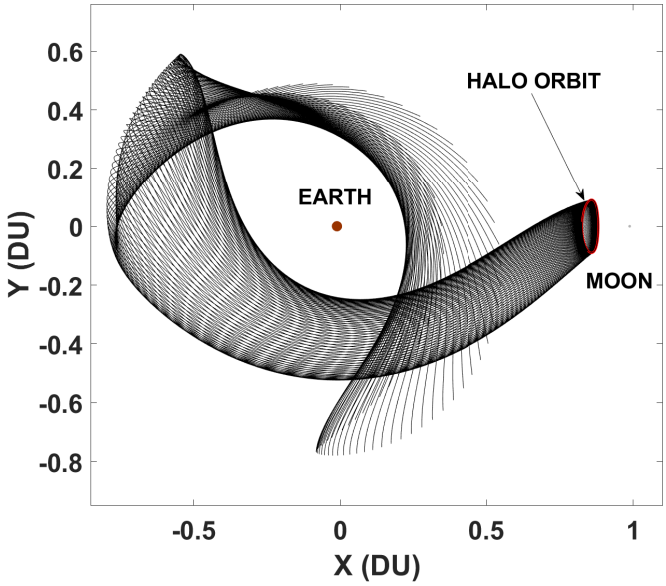

Figure 3.17: Sense: -1, Stable Manifold for L_1 Halo Orbit

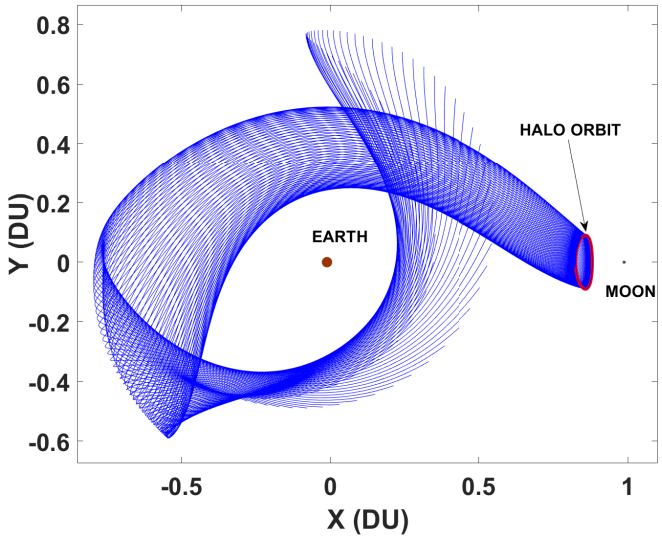

Figure 3.18: Sense: +1, Stable Manifold for L_1 Halo Orbit

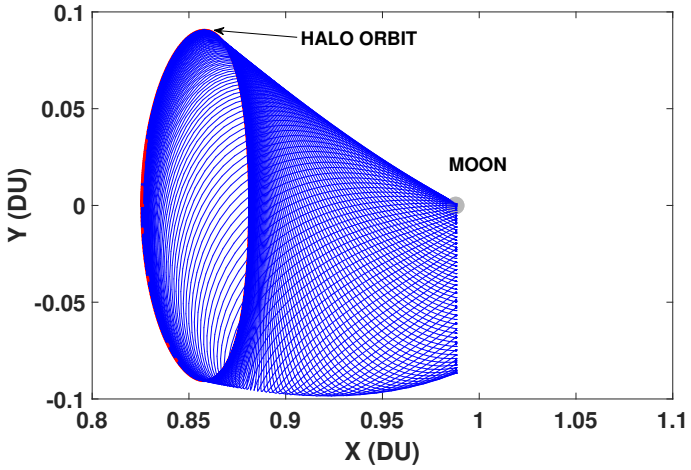

Figure 3.19: Sense: -1, Stable Manifold for L_1 Halo Orbit

vectors of the Jacobian of states at each points along the desired orbit segment but similar to our previous discussion, this method is numerically intensive. In order to reduce computational load, an approximation for the true manifold trajectories can be obtained by computing a Monodromy matrix analogue for the desired segment. This is done by propagating the STM from one $y = 0$ plane crossing to the next and use the resulting matrix ($\tilde{\mathbf{M}}$) as an approximation to $\mathbf{M}$.

Upon propagating the stable and unstable eigenvectors about the orbit segment and then follow the same process described before but now treat $\tilde{\mathbf{M}}$ as $\mathbf{M}$, one can produce approximations of the invariant manifolds of the quasi-periodic orbit. These approximations have proven to be good enough for preliminary mission design as in the case of the Genesis mission [98].

3.3 Manifold Analogues in a High-Fidelity Model[1]

Examination of states' flow near an equilibrium point in the continuous-time, autonomous , non-linear dynamical systems reveal locally stable, center and unstable sub-spaces and eventually, the corresponding global manifolds. These topological spaces constrain the natural nonlinear tra-

[1]Part of this section is reprinted with permission from "Eclipse-conscious transfer to lunar gateway using ephemeris-driven terminal coast arcs" by Singh, S., Junkins, J., Anderson, B., Taheri, E., 2021, Journal of Guidance, Control and Dynamics, 44(11), 1972-1988, Copyright ©2021 by the American Institute of Aeronautics and Astronautics, Inc.

jectories approaching and departing equilibrium solutions of the dynamical system (e.g., periodic orbits in the Circular Restricted 3-Body Problem (CR3BP)).

Quasi-periodic orbits can be computed in the CR3BP as they orbit around the periodic orbits. For instance, quasi-halo orbits orbit around a periodic Halo orbit. On the other hand, a HFM which includes third body gravitational perturbations to the 'primary-secondary' CR3BP system can also be used to differentially correct initial conditions on each revolution of the orbit and thereby produce orbits that are near-periodic in a HFM. This is important for real mission scenarios because as we discussed before, the CR3BP is only a simplified model used to make the problem more tractable. In reality, any periodic orbits produced using the CR3BP dynamics are not periodic in a HFM simulation with the same initial conditions. Due to the chaotic nature of the dynamics, the orbit diverges quickly and behaves in a very different fashion in the HFM. Therefore, although CR3BP and associated periodic orbits and manifolds are of interest for preliminary mission design, an actual mission requires consideration of other effects that were originally ignored but inclusion of these effects makes the system more realistic.

In this section, an approach for computing high-fidelity perturbed analogues for CR3BP invariant manifolds in an ephemeris-driven point-mass gravitational model ("Ephemeris Model") are highlighted. These "invariant manifold analogues" are not invariant in the strict sense, because the dynamical model is non-autonomous and therefore, does not have those ideal structures. Instead, the outputs serve as a useful qualitative approximation of CR3BP periodic orbit manifolds to design trajectories in a higher-fidelity model. Using nearly-periodic segments of orbits in a high-fidelity model and approximating them as periodic in order to compute their invariant manifold analogues has been employed with success in missions such as Genesis [98]. The advantage of this approach is that the structure of the manifolds is driven by the stability properties of the orbit in the Ephemeris Model, and the trajectories "on" the manifold satisfy the Ephemeris Model equations of motion. This method assumes the user has a "near-periodic" high-fidelity orbit solution available. An exact periodicity is highly unlikely due to the already discussed complexities of the Ephemeris Model.

3.3.1 Equations of Motion and Variational Equations

Without loss of generality, $i = 1, 2$ is chosen to represent the 'primary-secondary' pair in the CR3BP. Naturally, the chosen bodies should approximate the behavior of bodies orbiting a common barycenter. When defining the simplified rotating frame, we will choose a fixed angular rate and axis of rotation and allow this axis to define the z-axis of the frame. Thus, $\boldsymbol{\Omega} = [0, 0, \omega]^\top$ and $\dot{\omega} = 0$, where the angular rate (ω) is chosen to be the assumed constant mean motion of the primaries with the axis of rotation along the angular momentum vector at a chosen reference epoch (t^*). Considering, three basis vectors listed in Eq. (3.56), Q_0 in Eq. (3.57) is defined as the rotation matrix from the inertial frame to the rotating frame at t^*. The triad of unit vectors, with components in the Earth-Moon barycentric inertial frame are

$$\hat{\boldsymbol{e}}_{\mathbf{1}} = \frac{\boldsymbol{R}_2(t^*) - \boldsymbol{R}_1(t^*)}{|\boldsymbol{R}_2(t^*) - \boldsymbol{R}_1(t^*)|},\ \hat{\boldsymbol{e}}_{\mathbf{2}} = \hat{\boldsymbol{e}}_{\mathbf{3}} \times \hat{\boldsymbol{e}}_{\mathbf{1}},\ \hat{\boldsymbol{e}}_{\mathbf{3}} = \frac{(\boldsymbol{R}_2(t^*) - \boldsymbol{R}_1(t^*)) \times (\dot{\boldsymbol{R}}_2(t^*) - \dot{\boldsymbol{R}}_1(t^*))}{|(\boldsymbol{R}_2(t^*) - \boldsymbol{R}_1(t^*)) \times (\dot{\boldsymbol{R}}_2(t^*) - \dot{\boldsymbol{R}}_1(t^*))|}, \tag{3.56}$$

$$Q_0 = \begin{bmatrix} \hat{\boldsymbol{e}}_{\mathbf{1}}^T & \hat{\boldsymbol{e}}_{\mathbf{2}}^T & \hat{\boldsymbol{e}}_{\mathbf{3}}^T \end{bmatrix}^\top, \hat{\boldsymbol{e}}_i = \text{unit vectors with Cartesian non-rotating components} \tag{3.57}$$

Using an additional simple time-varying rotation matrix $Q_z(t)$, defined in Eq. (3.58),

$$Q_z(t) = \begin{bmatrix} \cos(\omega(t - t^*)) & \sin(\omega(t - t^*)) & 0 \\ -\sin(\omega(t - t^*)) & \cos(\omega(t - t^*)) & 0 \\ 0 & 0 & 1 \end{bmatrix}, \tag{3.58}$$

we can form the complete rotation matrix $Q(t)$ in Eq. (3.59),

$$Q(t) = Q_0 Q_z(t). \tag{3.59}$$

With this we can relate coordinates in this rotating frame to inertial coordinates using Eq. (3.60). The displacement vectors relative to the chosen center c are $\boldsymbol{\rho}_i = \boldsymbol{R}_i - \boldsymbol{R}_c$ and $\boldsymbol{\rho} = \boldsymbol{R} - \boldsymbol{R}_c$. The

relative displacement and angular velocity vectors with rotating components are

$$\begin{aligned} \boldsymbol{r}_i &= Q(t)\boldsymbol{\rho}_i, \\ \boldsymbol{r} &= Q(t)\boldsymbol{\rho}, \\ \boldsymbol{\omega} &= Q(t)\boldsymbol{\Omega}. \end{aligned} \tag{3.60}$$

The inertial point mass gravity forcing function is well known and leads to the inertial equations of motion (Eq. (3.61)),

$$\ddot{\boldsymbol{R}} = \boldsymbol{F}(t, \boldsymbol{R}) = -\sum_i \frac{\mu_i(\boldsymbol{R} - \boldsymbol{R}_i)}{|\boldsymbol{R} - \boldsymbol{R}_i|^3}, \tag{3.61}$$

where μ_i is the gravitational parameter of body i. The gravitational forcing function can alternatively be expressed as a function of the displacements relative to an accelerating center (which can serve as an idealized inertial origin), as is shown in Eq. (3.62) as

$$\boldsymbol{\phi}(t, \boldsymbol{\rho}) = -\sum_i \frac{\mu_i(\boldsymbol{\rho} - \boldsymbol{\rho}_i)}{|\boldsymbol{\rho} - \boldsymbol{\rho}_i|^3} - \sum_{i \neq c} \frac{\mu_i(\boldsymbol{\rho}_i)}{|\boldsymbol{\rho}_i|^3}. \tag{3.62}$$

Finally, the forcing function, when the time derivative of the displacement vectors are considered (relative to the rotating frame) requires additional centrifugal and Coriolis acceleration terms due to the simplified definition of the frame and is shown in Eq. (3.63) as

$$\ddot{\boldsymbol{r}} = \boldsymbol{f}(t, \boldsymbol{r}, \dot{\boldsymbol{r}}) = \underbrace{-\sum_i \frac{\mu_i(\boldsymbol{r} - \boldsymbol{r}_i)}{|\boldsymbol{r} - \boldsymbol{r}_i|^3} - \sum_{i \neq c} \frac{\mu_i(\boldsymbol{r}_i)}{|\boldsymbol{r}_i|^3}}_{\boldsymbol{f}_g(t, \boldsymbol{r}, \dot{\boldsymbol{r}})} \underbrace{-2\boldsymbol{\omega} \times \dot{\boldsymbol{r}} - \boldsymbol{\omega} \times (\boldsymbol{\omega} \times \boldsymbol{r})}_{\boldsymbol{f}_r(t, \boldsymbol{r}, \dot{\boldsymbol{r}})}, \tag{3.63}$$

which can be split into the gravitational forcing terms, $\boldsymbol{f}_g(t, \boldsymbol{r}, \dot{\boldsymbol{r}})$ and the kinematic terms due to the frame rotation, $\boldsymbol{f}_r(t, \boldsymbol{r}, \dot{\boldsymbol{r}})$. The state vector and its time derivative are defined in Eq. (3.64) as

$$\boldsymbol{x} = \begin{bmatrix} \boldsymbol{r} \\ \dot{\boldsymbol{r}} \end{bmatrix}, \quad \dot{\boldsymbol{x}} = \begin{bmatrix} \dot{\boldsymbol{r}} \\ \boldsymbol{f}(t, \boldsymbol{r}, \dot{\boldsymbol{r}}) \end{bmatrix}. \tag{3.64}$$

In order to compute the variational equations, we require the Jacobian of Eq. (3.64), expressed with simplified 3x3 blocks in Eq. (3.65).

$$J(t, \boldsymbol{r}, \dot{\boldsymbol{r}}) \equiv \frac{\partial \dot{\boldsymbol{x}}}{\partial \boldsymbol{x}} = \left[\begin{array}{c|c} 0_{3x3} & I_{3x3} \\ \hline \frac{\partial f}{\partial \boldsymbol{r}} & \frac{\partial f}{\partial \dot{\boldsymbol{r}}} \end{array}\right]. \tag{3.65}$$

The indicated position and velocity partials of the acceleration terms due to frame rotation are expressed in Eq. (3.66).

$$\frac{\partial \boldsymbol{f}_r}{\partial \boldsymbol{r}} = \begin{bmatrix} \omega^2 & 0 & 0 \\ 0 & \omega^2 & 0 \\ 0 & 0 & 0 \end{bmatrix}, \quad \frac{\partial \boldsymbol{f}_r}{\partial \dot{\boldsymbol{r}}} = \begin{bmatrix} 0 & 2\omega & 0 \\ -2\omega & 0 & 0 \\ 0 & 0 & 0 \end{bmatrix}. \tag{3.66}$$

Note:

$$\frac{\partial \boldsymbol{f}}{\partial r} = \frac{\partial \boldsymbol{f_r}}{\partial r} + \frac{\partial \boldsymbol{f_g}}{\partial r}, \tag{3.67}$$

where partials of the gravity forcing terms with respect to position upon exploiting symmetry reduce to 6 instead of 9 differential equations for the distinct elements and can be expressed as shown in Eq. (3.68),

$$\frac{\partial \boldsymbol{f}_g}{\partial \boldsymbol{r}} = \begin{bmatrix} \frac{\partial \ddot{x}}{\partial x} & \frac{\partial \ddot{x}}{\partial y} & \frac{\partial \ddot{x}}{\partial z} \\ \frac{\partial \ddot{y}}{\partial x} & \frac{\partial \ddot{y}}{\partial y} & \frac{\partial \ddot{y}}{\partial z} \\ \frac{\partial \ddot{z}}{\partial x} & \frac{\partial \ddot{z}}{\partial y} & \frac{\partial \ddot{z}}{\partial z} \end{bmatrix} = \begin{bmatrix} \frac{\partial \ddot{x}}{\partial x} & \frac{\partial \ddot{x}}{\partial y} & \frac{\partial \ddot{x}}{\partial z} \\ \frac{\partial \ddot{x}}{\partial y} & \frac{\partial \ddot{y}}{\partial y} & \frac{\partial \ddot{y}}{\partial z} \\ \frac{\partial \ddot{x}}{\partial z} & \frac{\partial \ddot{y}}{\partial z} & \frac{\partial \ddot{z}}{\partial z} \end{bmatrix}, \text{and} \tag{3.68}$$

$$\begin{aligned}
\frac{\partial \ddot{x}}{\partial x} &= -\sum_i \frac{\mu_i}{|\boldsymbol{r} - \boldsymbol{r}_i|^3}\left(1 + 3\frac{(x - x_i)^2}{|\boldsymbol{r} - \boldsymbol{r}_i|^2}\right), & \frac{\partial \ddot{y}}{\partial y} &= -\sum_i \frac{\mu_i}{|\boldsymbol{r} - \boldsymbol{r}_i|^3}\left(1 + 3\frac{(y - y_i)^2}{|\boldsymbol{r} - \boldsymbol{r}_i|^2}\right), \\
\frac{\partial \ddot{z}}{\partial z} &= -\sum_i \frac{\mu_i}{|\boldsymbol{r} - \boldsymbol{r}_i|^3}\left(1 + 3\frac{(z - z_i)^2}{|\boldsymbol{r} - \boldsymbol{r}_i|^2}\right), & \frac{\partial \ddot{x}}{\partial y} &= -\sum_i \frac{\mu_i}{|\boldsymbol{r} - \boldsymbol{r}_i|^3}\left(3\frac{(x - x_i)(y - y_i)}{|\boldsymbol{r} - \boldsymbol{r}_i|^2}\right), \\
\frac{\partial \ddot{x}}{\partial z} &= -\sum_i \frac{\mu_i}{|\boldsymbol{r} - \boldsymbol{r}_i|^3}\left(3\frac{(x - x_i)(z - z_i)}{|\boldsymbol{r} - \boldsymbol{r}_i|^2}\right), & \frac{\partial \ddot{y}}{\partial z} &= -\sum_i \frac{\mu_i}{|\boldsymbol{r} - \boldsymbol{r}_i|^3}\left(3\frac{(z - z_i)(y - y_i)}{|\boldsymbol{r} - \boldsymbol{r}_i|^2}\right).
\end{aligned}$$

Finally, the variational equations in the form of the well-known State Transition Matrix differ-

ential equation, Eq. (3.69), are used for propagation blueto perform an eigenanalysis of the locally linearized flow around a "fixed point", with the initial value problem initialized with $\mathbf{\Phi}(t_0, t_0)$ as a 6×6 identity matrix.

$$\dot{\mathbf{\Phi}}(t, t_0) = J(t, \boldsymbol{r}, \dot{\boldsymbol{r}})\mathbf{\Phi}(t, t_0). \tag{3.69}$$

While the fixed rotation rate and axis of the frame chosen can be seen as a simplifying assumption, it is a simplification that should only affect the frame, not the underlying physical dynamics. Propagation in an inertial ephemeris model and the fixed rotating ephemeris model defined here should yield the same solutions to within the effect of numerical inaccuracies, and have done so in the authors' testing. The choice of t^* is similarly a choice that only affects the chosen frame, and should not affect the dynamics themselves.

3.3.2 Orbit Manifold Parameters

Consider a single revolution of a nearly-periodic orbit in the rotating frame defined in the preceding section. Let the orbit have a period of T_i, where i is the rev number. The flow around a "fixed point" on this rev can be characterized by studying the the Monodromy matrix $M(t_0)$, which serves as a local linearization of the flow and can be computed as

$$M(t_0) = \Phi(t_0 + T_i, t_0), \tag{3.70}$$

using Eq. (3.69). It is important to note that the period T_i can be defined in several ways, such as the time at crossing a given fixed plane or by using the apsidal period. While the Monodromy matrix, $M(t_0)$, has the same period, for all choices of t_0 on an exactly periodic orbit, the elements of the Monodromy matrix, in reality do have small variations for each choice of starting state at each t_0. In the current context, the apsidal period was chosen to define the period for each quasi-periodic revolution. Then, computing the eigenvalues of $M(t_0)$ would ideally yield the properties

$$\lambda_1 = 1/\lambda_2, \ \lambda_3 = \lambda_4 = 1, \ \lambda_5 = \lambda_6^* \tag{3.71}$$

where $|\lambda_1| > |\lambda_2|$, and λ_6^* indicates the complex conjugate of λ_6. Since the orbit is "near-periodic", the eigenvalue set only approximates these characteristics. The eigenvectors associated with the real eigenvalues $\lambda_U \equiv \lambda_1$ and $\lambda_S \equiv \lambda_2$ represent the unstable and stable eigenvectors, respectively. These are labeled as, $\boldsymbol{\xi}_{U,0} \equiv \boldsymbol{\xi}_U(t_0)$ and $\boldsymbol{\xi}_{S,0} \equiv \boldsymbol{\xi}_S(t_0)$. Initial states for the unstable or stable "invariant manifold analogue" at t_0, assuming the state of the orbit is $\boldsymbol{x}_0$ at t_0, can be generated using the following relation

$$\boldsymbol{x_U}(t_0) = \boldsymbol{x}_0 + s\epsilon\boldsymbol{\xi}_{U,0},\ \boldsymbol{x_S}(t_0) = \boldsymbol{x}_0 + s\epsilon\boldsymbol{\xi}_{S,0}, \tag{3.72}$$

where $s = \pm 1$ is the "sense" of the manifold and ϵ is the desired small offset magnitude along the manifold. Due to the option of the sense, the unstable manifold can evolve in one of two directions, as can the stable manifold. To produce an approximation of a manifold surface, it is standard practice to compute initial manifold states on several sampled times (various choices for t_0 and corresponding states $\boldsymbol{x}(t_0)$) on an orbit rev. The above process can be repeated for every desired point on the orbit, or alternatively, the state transition matrix of the orbit itself can be used to approximately propagate the stable and unstable eigenvectors from a reference state on the orbit to another state on the orbit. This is applied as

$$\boldsymbol{\xi}_U(t) \approx \frac{\Phi(t,t_0)\boldsymbol{\xi}_{U,0}}{|\Phi(t,t_0)\boldsymbol{\xi}_{U,0}|},\ \boldsymbol{\xi}_S(t) \approx \frac{\Phi(t,t_0)\boldsymbol{\xi}_{S,0}}{|\Phi(t,t_0)\boldsymbol{\xi}_{S,0}|}. \tag{3.73}$$

Once several initial states have been generated on the chosen manifold these states are then all propagated using the dynamics in Eq. (3.64), with unstable manifolds propagated forward in time, and stable manifolds backward in time.

3.3.3 Discretization of the Near-Periodic Orbit

In order to generate the manifold analogues, several points on the near-periodic rev should be analyzed to reveal the "optimal" initial boundary condition. This process was carried out by first considering a discretization of states on the selected near-periodic rev followed by generation of

the corresponding Monodromy matrix. A spectral decomposition of M, reveals the stable/unstable eigenvector directions, thereby enabling computation of the manifold analogues through the process outlined before.

An important consideration in this procedure is the discrete spacing of the points on the quasi-periodic orbit. Consider a near-periodic rev on an ephemeris-corrected, 9:2 resonant NRHO of the southern L_2 family. Let the orbital period of this rev be T_i. A simple methodology for extraction of the discrete states include discretization at uniformly spaced time intervals or uniformly spaced intervals in eccentric anomaly, E.

For N discrete points, the discretization in time follows a fairly straightforward procedure, where the states are extracted as

$$\boldsymbol{x_0}(t_{j+1}) = \boldsymbol{x_0}(t_j + \delta t) \quad \forall \quad j \in \{1, 2, 3, ..., N\}, \quad \text{where } \delta t = T_i/N. \tag{3.74}$$

Discretization in eccentric anomaly (E) can be carried out by uniformly spacing in E, where $E \in [0, 2\pi]$. While an NRHO does not strictly follow the dynamics of a keplerian orbit, the 9:2 Lunar NRHO under consideration is orbiting close enough to the Moon that it becomes an adequate approximation for more even spacing of points. A mapping from E to t occurs by first mapping it to the Mean Anomaly (M) using Kepler's equation, $M = E - e \sin E$, where e is the eccentricity. Assuming T_i as the rev period and e_i as the rev eccentricity, τ as the time for a given

apoapse/periapse passage, and t_p as the periapsis epoch for the rev, $\forall \;\; j \in \{1, 2, 3.... N\}$,

$$
\begin{aligned}
M_{j+1} = E_{j+1} - e_i \sin E_{j+1} &= \frac{2\pi}{T_i}(t_{j+1} - t_p), \\
t_{j+1} &= t_p + \frac{T_i}{2\pi}(E_{j+1} - e_i \sin E_{j+1}), \\
\text{where,} \quad E_{j+1} &= E_j + \delta E \quad \text{and} \quad \delta E = \frac{2\pi}{N}, \\
\text{For Peri-Peri rev,} \quad E_1 &= 0, \; t_p = \tau, \\
\text{For Apo-Apo rev,} \quad E_1 &= \pi, \; t_p = \tau - \frac{T_i}{2}, \\
E_1 &= \begin{cases} 0, & \text{Peri-Peri} \\ \pi, & \text{Apo-Apo} \end{cases}, \\
t_p &= \begin{cases} \tau, & \text{Peri-Peri} \\ \tau - \frac{T_i}{2}, & \text{Apo-Apo} \end{cases}.
\end{aligned}
\tag{3.75}
$$

Intuitively, a uniform spacing in time leads to a denser distribution of points near apoapse as compared to near periapse. This is not ideal for analyzing resulting manifold clusters as it is quite possible to miss some viable choices near periapsis, where the state is rapidly changing. Thus, discretization in eccentric anomaly is an alternative, which unsurprisingly leads to a more regular "arc-length" dispersion of the discrete near-periodic states and provide a comprehensive coverage of all stable/unstable manifold analogue clusters.

As an example, consider the apoapsis to apoapsis or "apo-apo" rev for the 9:2 synodic NRHO with the first apoapse passage epoch: '2025 JAN 02 20:02:28.677' with $N = 100$. Note that the 'best' case manifold conditions are considered as Earth-periapse points among the cluster of 100 trajectories whose distance from the Earth is minimum and are henceforth referred to as 'optimal' unless stated otherwise. Figures 3.20a and 3.20c depict the distribution of fixed points for time and eccentric anomaly as discretization parameters respectively, with the red markers being the orbital locations leading to Earth-periapse conditions with $r_f \leq 3.5 \times 10^5$ km. It is now apparent, that as hypothesized, discretization in time leads to a sparse scattering of points near the periapse region

which often leads to a restricted mapping of the manifold analogues. A discrete search for attractive manifold trajectories is more likely to miss favourable manifolds due to non-uniform spacing. On the other hand, a more uniform spatial scattering achieved by discretization in E leads to a more comprehensive and robust mapping in our case (Figures 3.20b and 3.20d). An alternative approach to discretization can be to employ variable-step integration methods for orbit propagation, which can provide a heuristic yet reasonable discretization based on the dynamical model sensitivity.

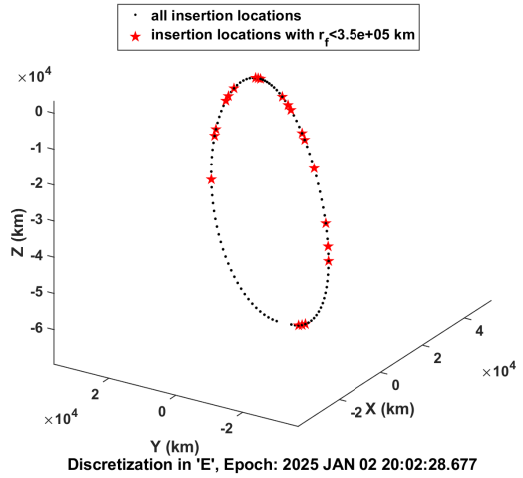

(a) Insertion Locations: E Discretization

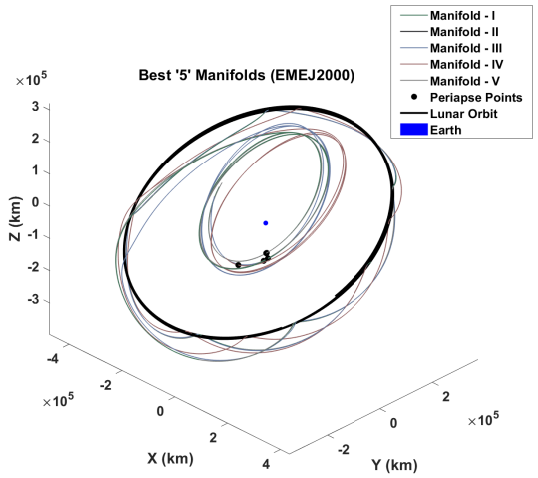

(b) '5' Best Manifolds: E Discretization

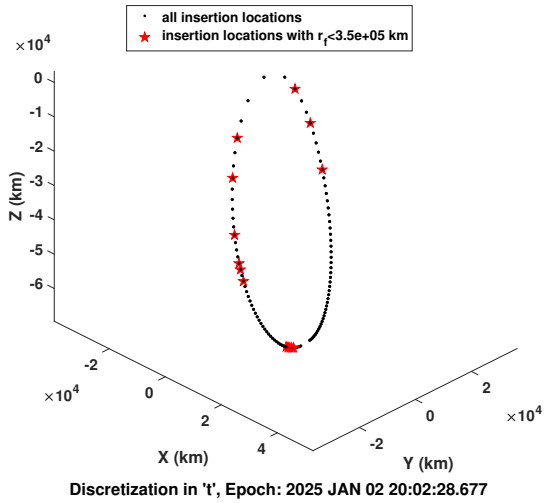

(c) Insertion Locations: t Discretization

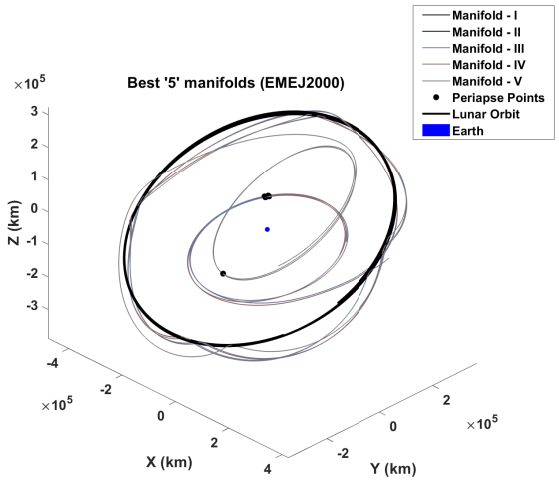

(d) '5' Best Manifolds: t Discretization

Figure 3.20: Discretization Parameter - E vs. t

3.4 Leveraging Manifolds for Trajectory Design [2]

Manifold trajectories arise out of a local linearization of the dynamics around a fixed point on a periodic orbit of a dynamical system. It was mentioned that these manifolds in the CR3BP have an asymptotic behavior as it arrives/departs the periodic orbit from the fixed point. In higher fidelity models, manifold approximation are generated in directions that provide the most exponential growth of the trajectory i.e, the most stable/unstable directions by approximating the Monodromy matrix. Due to the intrinsic ballistic nature of manifold trajectories, if a spacecraft was to merge onto any of the stable manifolds it would ballistically arrive at a state very close to the fixed point on the periodic orbit that was used to compute the manifold in the first place. Similarly, a spacecraft put on an unstable manifold of a fixed point on the periodic orbit ballistically departs the periodic orbit.

Let $\mathbf{W}_{+}^{U}$ denote the entire bundle of unstable manifold trajectories generated by applying a positive perturbation to the fixed point on a L_1 Halo orbit and $\mathbf{W}_{-}^{U}$ be the unstable manifolds computed by applying a negative perturbation. $\mathbf{W}_{+}^{S}$ and $\mathbf{W}_{+}^{S}$ are similarly defined as the stable manifold bundle counterparts (see Figure 3.21).

Mathematically the manifold bundles are expressed as,

$$\mathbf{W}_{+}^{U} = \{W_{+}^{U_i}\} \ \forall \ i \in [1, N], \quad \mathbf{W}_{-}^{U} = \{W_{-}^{U_i}\} \ \forall \ i \in [1, N], \tag{3.76}$$

$$\mathbf{W}_{+}^{S} = \{W_{+}^{S_i}\} \ \forall \ i \in [1, N], \quad \mathbf{W}_{-}^{S} = \{W_{-}^{S_i}\} \ \forall \ i \in [1, N], \tag{3.77}$$

where N is the number of discrete fixed points for which individual manifold trajectories were generated. N = 100 for Figure 3.21. Table 3.6 depicts the various mission objectives of interest in the cislunar domain and lists the manifold bundles whose trajectories can be utilised as part of the

[2] Separate parts of this section are reprinted with permissions from:
"Eclipse-conscious transfer to lunar gateway using ephemeris-driven terminal coast arcs" by Singh, S., Junkins, J., Anderson, B., Taheri, E., 2021, Journal of Guidance, Control and Dynamics, 44(11), 1972-1988, Copyright ©2021 by the American Institute of Aeronautics and Astronautics, Inc.;
"Exploiting manifolds of L1 halo orbits for end-to-end Earth–Moon low-thrust trajectory design" by Singh, S. K., Anderson, B. D., Taheri, E., Junkins, J. L., 2021, Acta Astronautica, 183, 255-272, Copyright ©2021 IAA. Published by Elsevier Ltd. All rights reserved.

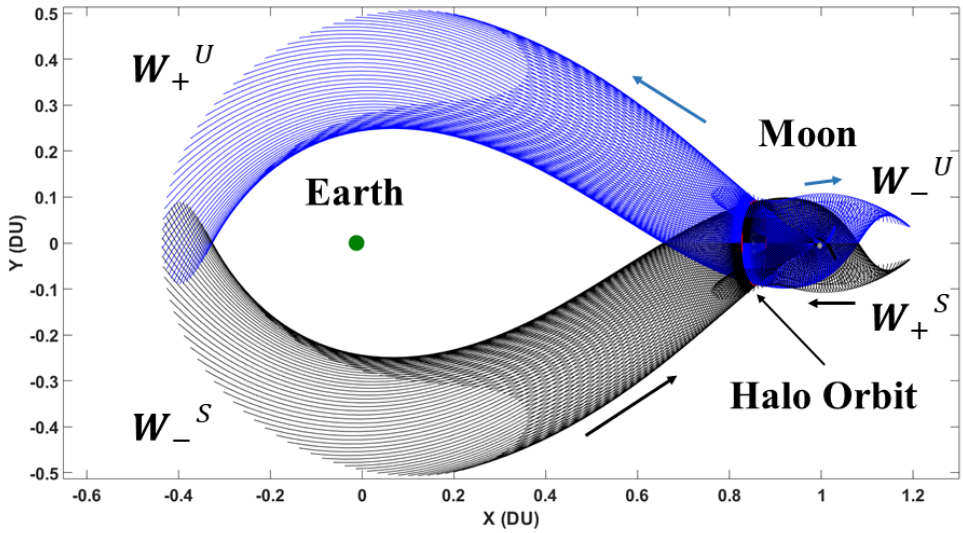

Figure 3.21: Leveraging Earth-Moon L_1 Halo Orbit Manifolds for Cislunar Trajectory Design

transfer trajectory.

Table 3.6: Manifold Bundles in the Cislunar Domain Catering to Various Mission Objectives.

Mission Objective	**Manifold Bundles of Interest**
Earth - Moon	$\{\mathbf{W}_-^S, \mathbf{W}_-^U\}$
Earth - L_1 Halo	$\mathbf{W}_-^S$
Moon - Earth	$\{\mathbf{W}_+^S, \mathbf{W}_+^U\}$
Moon - L_1 Halo	$\mathbf{W}_+^S$
Lunar Orbit - Lunar Surface	$\mathbf{W}_-^U$
Lunar Surface - Lunar Orbit	$\mathbf{W}_+^S$

Thus, leveraging the manifold trajectories for performing transfers in the cislunar domain is extremely powerful as it can serve as a LTCA or a LOCA as a part of the entire transfer trajectory. The advantage of the presence of these long coast segments are two fold:

- It splits the end-to end trajectory optimization problem into two segments where the first segment is an optimal transfer from the initial staging orbit of the spacecraft to a state on a chosen trajectory in the manifold bundle. The second segment is a pre-computed and pre-selected manifold trajectory which is entirely a coast segment i.e., no fuel is expended when

the spacecraft travels on this segment. This technique makes the OCP more amenable to numerical treatment in that even indirect single shooting methods are capable of converging to a locally optimal solution for the first segment.

- Secondly, a coast segment is highly desirable for flying an actual mission in order to cater to specific operational requirements like mission re-planning, eclipse avoidance etc. The coast segment essentially serves as a useful 'knob' which is available for tweaking during the operational segment of the mission.

3.4.1 Manifold Trajectory and Patch-Point Selection

Once the manifold trajectories have been pre-computed, the insertion points need to be characterized and the most "appropriate" manifold state selected as the final boundary condition. A TPBVP is thereafter formulated and solved to obtain the optimal trajectory for the first segment of the mission. The two approaches used to analyze and select manifold-insertion points are 1) piercing point approach and 2) periapse point approach. These approaches are briefly described in the following sections.

3.4.1.1 Piercing Point Approach

In this approach, the manifolds are propagated to intersect the planes containing the Earth and the Moon respectively to analyze stable/unstable manifold pairs which can be utilized for an Earth-Moon transfer for example. In the barycentric synodic frame, the Earth lies in the $x = -\mu$ plane whereas the Moon lies in the $x = (1 - \mu)$ plane. Figure 3.22 depicts the $\mathbf{W}_{-}^{S}$ and $\mathbf{W}_{-}^{U}$ pairs generated for N = 100 distinct fixed points on the L_1 Halo orbit with $C = 3.128$ and propagated until the trajectories in the respective bundles intersect the Earth and the Moon plane respectively.

There are two major criteria for selection of "appropriate" patch point conditions. Typically, the fidelity of discretization of the periodic orbit translates directly into the number of candidate insertion points available for selection. These criteria, largely governed by heuristic insights into the cause for excessive fuel consumption, can be described as:

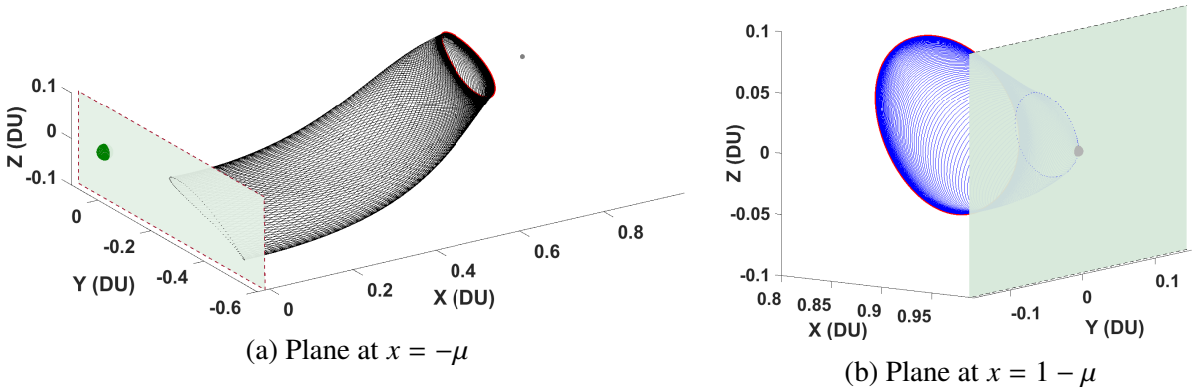

(a) Plane at $x = -\mu$

(b) Plane at $x = 1 - \mu$

Figure 3.22: Piercing Point Approach.

- Fuel is consumed when maneuvers aimed at increasing the periapse and apoapse distances for elliptical orbits and radius for circular orbits are performed. Typically, for low-thrust trajectories, this requires multiple spirals en-route to the final boundary condition which in this case is the manifold insertion point. Thus points that are closer to the initial Earth Parking Orbit (EPO) are more attractive because of the heuristic truth that a shorter path can be traversed by consuming lesser amount of fuel.

- Similarly, plane change maneuvers of any kind are expensive and require multiple spirals to achieve. The costs are further exacerbated if the maneuvers are performed in the gravity well of a primary (e.g., GTO - GEO transfer). Therefore, it is advisable to pick patch-points that have an orbital inclination that is close to the initial EPO conditions. Note that changing RAAN (Ω) is also a plane-change maneuver, whereas changing the AoP (ω) is an orbit rotation. Since both are expensive maneuvers, the same heuristic insights apply here as well.

Thus, the optimization problem statement is mathematically stated as,

$$\min_{n} \quad J = W_r \delta r + W_i \delta i + W_\omega \delta \omega + W_\Omega \delta \Omega \tag{3.78}$$

where all δx's are deviations of the corresponding 'x'-element of the candidate patch-point with

the respective initial EPO states and W_x's are some weights which can be tuned. This problem is almost impossible to solve numerically due to the underlying non-linearity in the map from manifold trajectories to the respective deviations. A more heuristic approach is therefore adopted. This approach entails conversion of the Cartesian candidate-patch states to COEs and then creating phase plots that help graphically analyze the trade-offs of interest.

3.4.1.2 Periapse Point Approach

The second approach searches for all periapse conditions on each manifold trajectory from the bundle and then analyze them using the same phase-space plots as discussed in the 'piercing point approach'. As an example, a spatial plot for the candidate lunar periapse points is given in Figure 3.23 for trajectories in the $\mathbf{W}_{-}^{U}$ bundle. The red markers depict three distinct conditions, which could serve as 'favorable' candidates for the seleno-centeric final leg of a trajectory from the periodic orbit to a Lunar Polar Orbit. Among the three marked conditions, one has an inertial inclination of 88.278° and thus provides the case with the least out-of plane maneuver required.

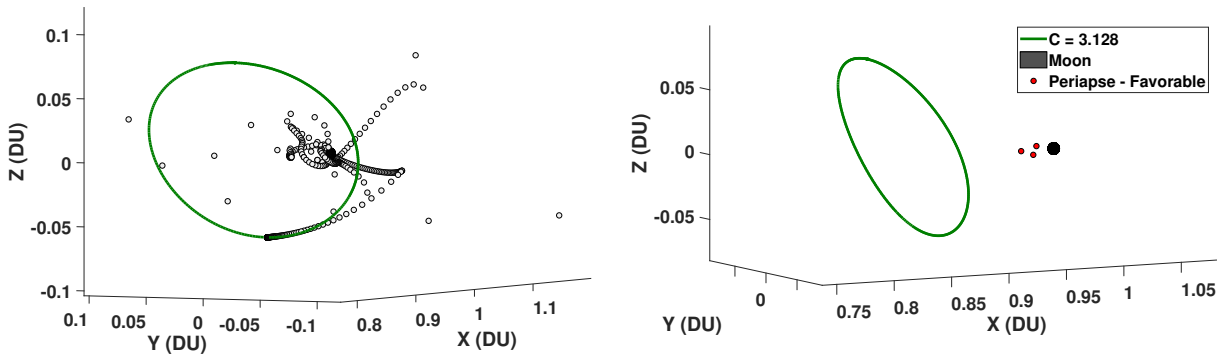

(a) Spatial Periselene Map - Moon Leg (b) Favorable Conditions - Moon Leg

Figure 3.23: Spatial Periselene Map of Manifold FCs - Moon Leg.

Note that periapse radius is another important consideration and with our heuristic choice we need to be careful to pay attention to both inclination and periapse radius. For instance, to transfer to a seleno-centric polar orbit, a periapse condition could have an inclination $\approx 90°$ but could be

very far away from the desired final periapse radius. Thus, the advantage of a small plane-change maneuver may be overshadowed by the fuel spent in spiralling down from a high altitude to the lower desired altitude in the final polar orbit. It is also important to note that circularising an orbit is also a very expensive maneuver and therefore, if possible, δe must also be as small as possible for the chosen patch-condition.

4. PROBLEM FORMULATION AND NUMERICAL TECHNIQUES [1]

In this chapter, the state-of the art novel numerical techniques utilised in generating converged optimal trajectories for the examples presented in the next chapter are discussed. Formulation of the OCP for fuel- and time- optimal trajectories is also presented. The concept of Composite Smoothing Control (CSC) is introduced which has been utilised to include shadow modelling as a part of the indirect formulation of the TPBVP. Finally, a hybrid optimization scheme is discussed which is able to solve an end-to end problem leveraging manifolds in a HFM where the trajectories are also eclipse conscious.

4.1 Homotopy and Arc-length Continuation

Homotopy methods are used to ease the solution process for complex problems. They work by first solving a simple problem and then deforming this problem into the original complex problem. During this deformation, the solution successively solves a more complex problem at each homotopy step and follows a path from solutions to the simple problem to solutions to the complicated problem. The importance of developing homotopy methods lies in the fact that other iterative solution methods like Newton's method work locally, i.e. the solution converges if the initial guess is in a close neighborhood of the actual solution. Homotopy methods do not require prior knowledge about the solution and are therefore significantly more robust.

4.1.1 The Generic Homotopy Method

With a focus on trajectory optimization problems, generally speaking, a solution to a system of non-linear equations is sought. For instance solution to the following system is desired where $\mathbf{F}$ is non-linear,

$$\mathbf{F}(\mathbf{X}) = \mathbf{0} \tag{4.1}$$

[1] Parts of this chapter have been reprinted with permission from "Eclipse-conscious transfer to lunar gateway using ephemeris-driven terminal coast arcs" by Singh, S., Junkins, J., Anderson, B., Taheri, E., 2021, Journal of Guidance, Control and Dynamics, 44(11), 1972-1988, Copyright ©2021 by the American Institute of Aeronautics and Astronautics, Inc.

Assuming a good approximation to the zero ($\mathbf{X}^*$) of $\mathbf{F}$, $\mathbf{X}_0$ is available, Newton-type algorithms are reasonably successful and widely used to obtain the solution through an iterative procedure. Typically though, $\mathbf{X}^*$ is not known a priori for most problems and any Newton-type algorithm tends to diverge due to a poor initial guess. This is where homotopy methods come in to alleviate the convergence issues for problems where a good initial guess of the solution is not known. The homotopy function $\mathbf{H} : [0, 1] \times \mathbb{R}^n \to \mathbb{R}^n$ is defined as,

$$\mathbf{H}(0, \mathbf{X}) = \mathbf{G}(\mathbf{X}), \quad \mathbf{H}(1, \mathbf{X}) = \mathbf{F}(\mathbf{X}) \tag{4.2}$$

where $\mathbf{G} : \mathbb{R}^n \to \mathbb{R}^n$ is a smooth function which has easy-to find solutions. Typically, a linear homotopy can be used,

$$\mathbf{H}(\kappa, \mathbf{X}) = \kappa\, \mathbf{F}(\mathbf{X}) + (1 - \kappa)\, \mathbf{G}(\mathbf{X}) = \mathbf{0} \tag{4.3}$$

where κ is a homotopic parameter. The zero set of $\mathbf{H}$ is written as,

$$\mathbf{H}^{-1}(\mathbf{0}) = \{(\kappa, \mathbf{X}) \in [0, 1] \times \mathbb{R}^n \mid \mathbf{H}(\kappa, \mathbf{X}) = \mathbf{0}\} \tag{4.4}$$

It is apparent that $\mathbf{H}^{-1}(\mathbf{0})|_{\kappa=0}$ coincides with the zero of $\mathbf{G}$ whereas $\mathbf{H}^{-1}(\mathbf{0})|_{\kappa=1}$ coincides with the zero of $\mathbf{F}$. The curves that belong to the set $\mathbf{H}^{-1}(\mathbf{0})$ starting from $\kappa = 0$ to $\kappa = 1$ gives a solution to $\mathbf{F}(\mathbf{X}) = \mathbf{0}$. While this method gives a systematic approach to finding solutions to a non-linear system, existence of a smooth curve in the set $\mathbf{H}^{-1}(\mathbf{0})$ from $\kappa = 0$ to $\kappa = 1$ is not guaranteed by any means. According to the implicit function theorem, the 'solution' curve in $\mathbf{H}^{-1}(\mathbf{0})$ is homeomorphic to either the real line of to the unit circle S^1. Therefore, the homotopy curves may be different geometrically and may be broadly classified as (see Figure 4.1),

- c_1: Unbounded curves without endpoints, homeomorphic to $(0, 1) \times \mathbb{R}^n$.
- c_2: Smooth curves with both end-points at boundary of $\{0\} \times \mathbb{R}^n$.
- c_3 and c_4: Smooth curves with one end point at $\{0\} \times \mathbb{R}^n$ and other at $\{1\} \times \mathbb{R}^n$.

- c_5 and c_7: Unbounded curves with only one end point at boundary of $(0,1) \times \mathbb{R}^n$.
- c_6: Bounded closed curves with no end-point and homeomorphic to the unit circle.
- c_8: Smooth curves with both end-points at boundary of $\{1\} \times \mathbb{R}^n$.

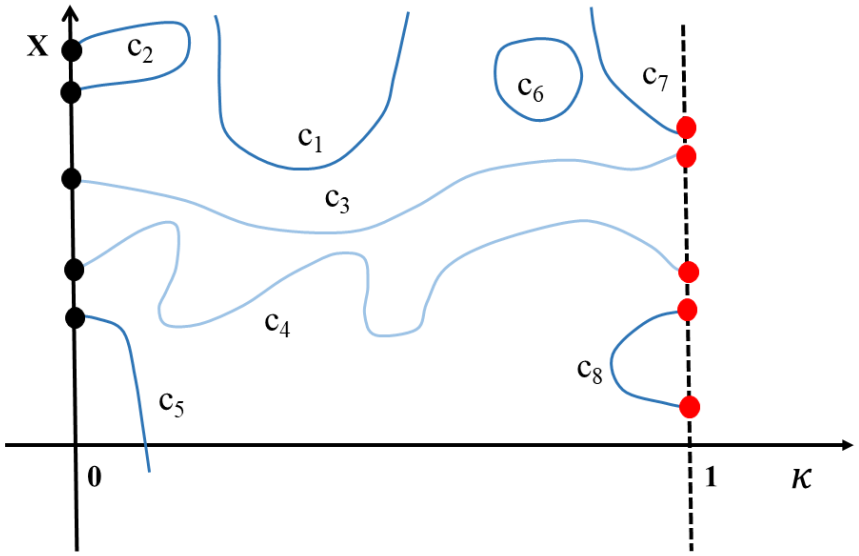

Figure 4.1: Different possibilities of Homotopy Curves

The success of a homotopy approach is highly contingent on the curve the algorithm is tracking. For instance, it is clear that if the initial solution for $\mathbf{H}(0, \mathbf{X}) = 0$ lies on the curves c_3 or c_4, then the homotopy approach will progress as planned towards the final solution. On the other hand, the curves c_1, c_2, c_6, c_5 and c_8 will face problems in progressing primarily due to finding a local solution which at initial or some intermediate step of κ lies on one of the aforementioned curves. In such cases, the most logical step is to search for a different local solution which lies on the curve c_3 or c_4 (*connection curves*). Note that there is no way of knowing if the local solution obtained does lie on the 'connection' curves and therefore the entire homotopy process cannot be completely automated. Manual intervention is essential intermittently to monitor the satisfactory progress of the algorithm.

4.1.2 Arc-length Continuation

The homotopy algorithm requires continuation of the homotopy parameter κ sequentially from 0 to 1 such that solution of the complex problem is achieved eventually. In doing so, often times a linear continuation fails to navigate turning points in the solution curves effectively since the solution to the next iterative step is much further away than predicted. The step size for a linear continuation iteration is expressed as,

$$\delta\kappa = \frac{(\kappa_f - \kappa_i)}{m}, \tag{4.5}$$

where κ_i and κ_f are the initial and final bounds on the homotopy parameter κ and m denotes the number of steps and is selected on the discretion of the programmer. Figure 4.2 depicts a turning point in the homotopy curve that needs to be tracked.

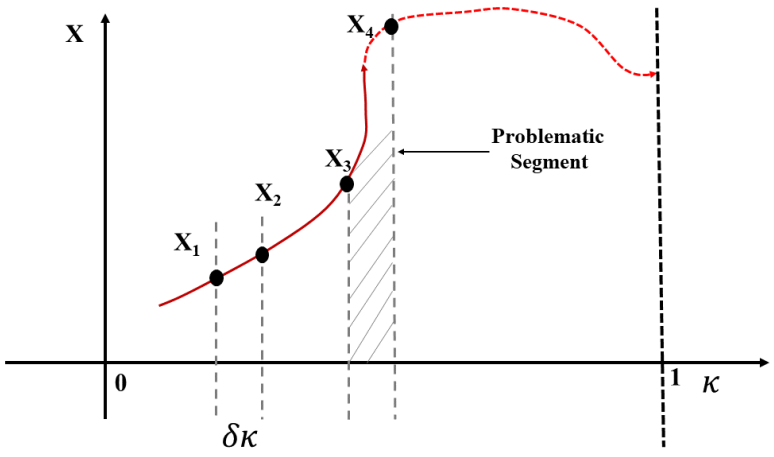

Figure 4.2: Problem with Linear Continuation around Turning Points

As is evident from the figure, the solutions $\mathbf{X}_1$ and $\mathbf{X}_2$ which lie on the homotopy curve before it encounters the turning point are close to each other and the solution $\mathbf{X}_1$ for the problem $\kappa_1\mathbf{F}(\mathbf{X}) + (1-\kappa_1)\mathbf{G}(\mathbf{X}) = \mathbf{0}$ may be continued to the obtain the solution for $\kappa = \kappa_2$. On the other hand, the solutions $\mathbf{X}_3$ and $\mathbf{X}_4$ on the homotopy curve are much further away as it passes through a turning

point. In this case, linear continuation fails to make progress to the next step due to the solutions being so far apart in the solution-space. Therefore, the algorithm would be better served in tracking the homotopy curve by taking steps along the curve rather than by taking equal steps in κ. This is essentially the idea behind arc-length continuation. Figure 4.3 depicts the arc-length continuation scheme as a schematic. For further reading, the references [99, 59] provide a comprehensive discussion.

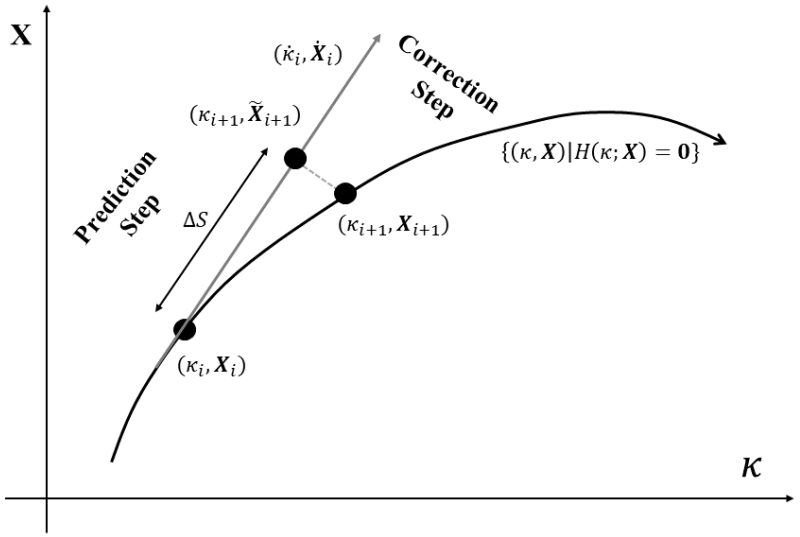

Figure 4.3: Pseudo-Arc Length Continuation: A Predictor-Corrector Method

4.1.3 Homotopy On Boundary Conditions: A Novel Trajectory Design Homotopy Method

Numerical solution to low-thrust trajectory optimization problems is not straightforward. The optimal trajectories are usually characterized by large values of the number of revolutions around the primaries, N_{rev}, and achieving convergence using a single-shooting method frequently proves to be challenging. Solving an optimal control problem (OCP) using indirect methods involves guessing an initial condition for the unknown costates and then propagating the set of state-costate differential equations with the control obtained from Pontryagin's Minimum Principle. Convergence is achieved when, for a particular set of costates, the terminal boundary conditions are satisfied.

The complication in solving an OCP arises from the need of a good guess for the initial costates. However, homotopy and/or continuation methods are often used to improve convergence while solving optimal trajectory design problems. The main idea in homotopy/continuation methods is the same as discussed before and begins by finding a solution to an easier problem. The converged costates for this initial solution are then used as an initial guess to solve the next problem (with a marginally increased level of complexity). This process is continued till a solution for the desired problem is achieved. The overall procedure is known as continuation and involves a continuation parameter (say η), which is used to impact the problem complexity. η is swept, generally in the range $[0, 1]$, where $\eta = 1$ corresponds to the actual problem. There are multiple approaches to sweeping the value of η. Since, the solution domain versus η might consist of irregularities like discontinuous solution arcs, turning points or bifurcation points, a standard numerical continuation strategy might not suffice [100]. A more robust pseudo-arc length continuation which was previously discussed is often used for these complicated problems, where the prediction of the next iteration is made by taking a step in the tangent direction of the increasing arc-length at the current iteration instead of η. This enables avoidance of the most common problem of "turning points" where the homotopy path is not a single valued function of η, but is a single valued function of arc length under much more general circumstances.

A novel method is hereby presented, where a homotopy sweep is performed on the final boundary conditions. An initial problem is first solved, where the transfer occurs between the initial point and a point close to it on a nearby orbit. This problem is frequently easier to solve or, in some cases, a solution to the neighboring problem is available from some previous design study. The next step is a 'predictor' step where the set of costates and homotopy parameter for the next iteration are predicted by moving in the direction of the arc-length (defined in the context of homotopy zero-curve). Finally, a Newton-based corrector gives a solution for the current step. The process continues until

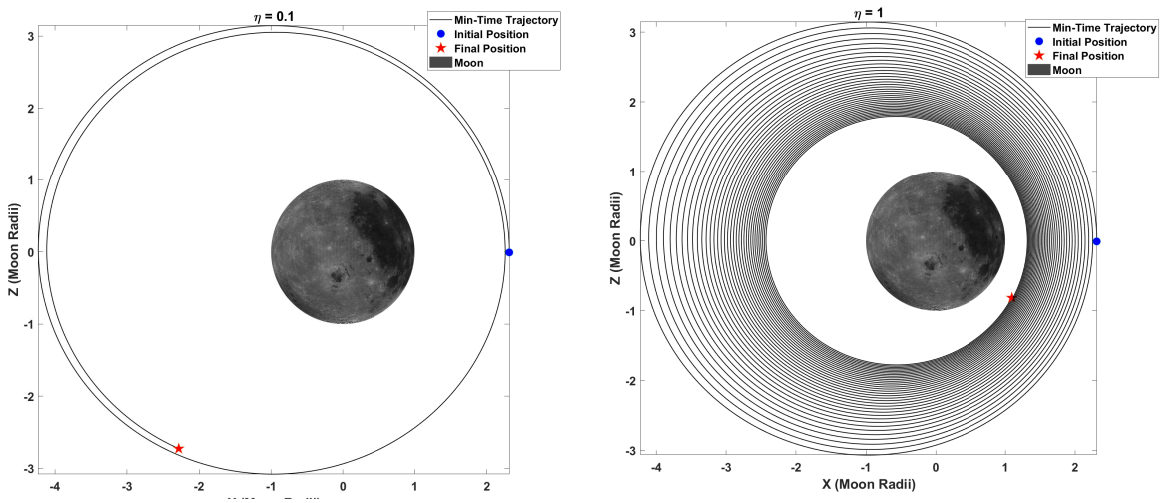

(a) $\eta = 0.01$ (b) $\eta = 1$

Figure 4.4: Converged solution using boundary condition homotopy - Equatorial to Polar Orbit.

we reach the desired final condition. The homotopy method can be defined as follows

$$\mathbf{e}_\eta = \eta\, \mathbf{e}_f + (1 - \eta)\, \mathbf{e}_0, \tag{4.6}$$

$$\mathbf{e}_0 = \mathbf{e}_\mathrm{I} + \nu\, \mathbf{e}_\mathrm{I}, \tag{4.7}$$

where $\mathbf{e}_\mathrm{I}$ is the initial boundary condition, $\mathbf{e}_0$ is a perturbed terminal boundary condition obtained via a small multiplier ν for which a converged minimum-time solution is easy to achieve and known, $\mathbf{e}_\eta$ is the terminal boundary condition at the current homotopy parameter η and $\mathbf{e}_f$ is the desired final boundary condition. While there is no guarantee that there is a homotopy path that connects the two extremes of η, the numerical results have shown reduced sensitivities and typically reliable convergence when the above homotopy method is employed.

The irregularities in the homotopy path were circumvented by re-solving the problem for a slightly larger homotopy parameter along with a larger guess for final time than that used for the previously converged solution. The methodology was found to be extremely effective even for a continuation on the final boundary condition (see Figure 4.4). We emphasize that the solution space of minimum-time orbit transfers is shown to be replete with many minima as is shown in

[101] and finding the "best" solution is a numerically intensive process. We have found, however, if attention is constrained such that a specific number of en-route revolutions (N_{rev}) is considered (for fixed-time, fuel-optimal rendezvous-like maneuvers), then for the feasible set of N_{rev} values there is typically one local minima per N_{rev}. Using accumulated longitude as the time like variable permits direct control over N_{rev} and greatly facilitates convergence, as described in Ref. [51].

4.2 Conical Shadow-Modelling Technique

In order to consider eclipse-conscious trajectories, i.e., optimal trajectories which have enforced coast arcs as the spacecraft passes through an eclipse region, a metric defining such a condition is required. There are several shadow models considered by researchers and used effectively for various applications [66, 102, 103]. In this work, eclipse-conscious trajectories are defined as trajectories where the engine throttle is turned 'OFF' (Thrust = 0) whenever the spacecraft is in the shadow of an occulting body.

In order to optimally design such trajectories, an event-trigger handling capability is required during the numerical optimization, which implicitly constrains the admissible control when applying Pontryagin's Minimum Principle (PMP). A conical shadow [104] model has been adopted for this work for analyzing the manifold analogues as well as designing eclipse-conscious optimal trajectories. The conical shadow model assumes spherical shapes of the occulting body and the Sun as is depicted in Figure 4.5.

The two bodies are viewed as overlapping discs by the spacecraft. For the spacecraft to be in at least a partial eclipse shadow, the occulting body must block some of the angular view of the sun from the spacecraft. Defining the parameters Apparent Solar radius (ASr), Apparent Occulting Body radius (ABr) and Apparent Distance (AD) as the following,

$$\text{ASr} = \sin^{-1}\frac{R_S}{\|\boldsymbol{r}_{S/sc}\|}, \quad \text{ABr} = \sin^{-1}\frac{R_B}{\|\boldsymbol{r}_{B/sc}\|}, \quad \text{AD} = \cos^{-1}\frac{\boldsymbol{r}_{B/sc}^T\,\boldsymbol{r}_{S/sc}}{\|\boldsymbol{r}_{B/sc}\|\,\|\boldsymbol{r}_{S/sc}\|}, \tag{4.8}$$

where $\boldsymbol{r}_{S/sc} = \boldsymbol{r}_S - \boldsymbol{r}_{sc}$ and $\boldsymbol{r}_{B/sc} = \boldsymbol{r}_B - \boldsymbol{r}_{sc}$. An implicit time-varying function, $f_{ec}(\boldsymbol{r}_{S/sc}(t), \boldsymbol{r}_{B/sc}(t))$ can be defined, which determines the eclipse condition as: "*Eclipse occurs when the sum of the*

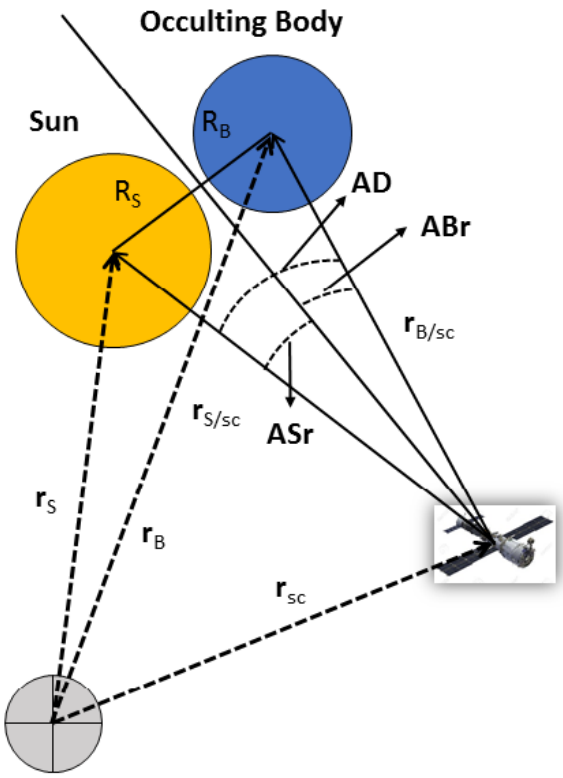

Figure 4.5: Schematic for the Conical Shadow Model.

apparent angular radii exceeds the apparent angular distance." The function f_{ec} is expressed as,

$$f_{ec}(\boldsymbol{r}_{S/sc}(t), \boldsymbol{r}_{B/sc}(t)) = AS\,r + ABr - AD. \tag{4.9}$$

This time varying function is evaluated at every time-step during state propagation and the *sign* (+ / -) triggers the onset or exit from the eclipse event (Thrust: OFF / ON). For simplicity, we do not distinguish between partial or total eclipse; we adopt the rule that the thrust should be OFF in even a partial eclipse, and ON only in "full sun". Note that additional relatively simple conditions on ASr, ABr and AD can be used to distinguish umbra, penumbra, and antumbra. We use these conditions for post processing, but they do not apply to the dynamics or optimization in our model. In this work, we only consider the Earth as the occulting body and ignore eclipses that could be caused by the Moon. This is a fair assumption, since lunar induced eclipses are more relevant for

transfers exclusively in the lunar domain, for instance a selenocentric transfer from a High Lunar Orbit (HLO) to a Low Lunar Orbit (LLO) or vice versa.

4.3 Composite Smoothing Control

It is well known that fuel-optimal trajectories require the throttling parameter of the control profile to be discontinuous. The control direction is derived from PMP while the costate differential equations arise out of first order necessary conditions. There are additional discontinuities or switches in the control profile arising due to the eclipse conditions. Typically, while solving for the switch locations, a continuation is carried out where initially the problem is solved for a smooth control function and gradually continued to the sharply switching fuel-optimal solution. Figure 4.6 depicts the transition from a smooth control to a sharply switching control using the continuation parameter 'ρ'.

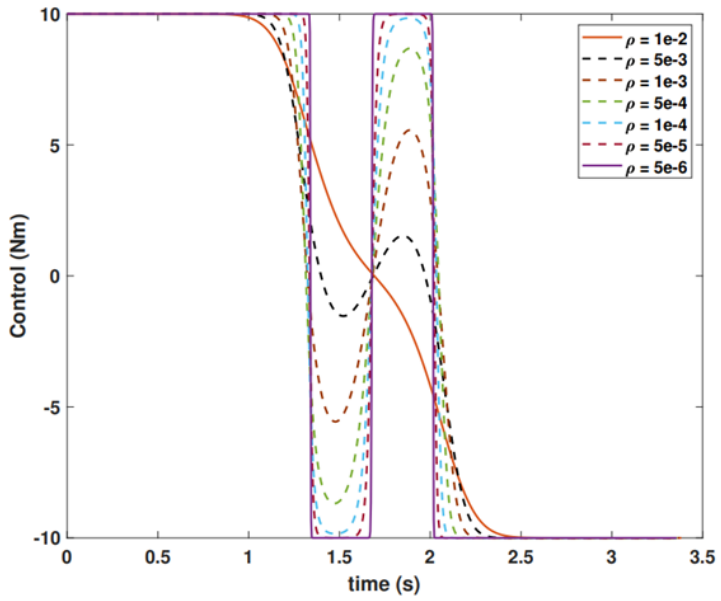

Figure 4.6: Transition from Smooth to Sharply Switching Control.

As we will see in the next section, the switches for fuel-optimal optimal trajectories are determined through a switching function. Details of how to find the analytical expression for the

function is covered later. For now, let us assume that $s_1(\mathbf{X}, \mathbf{\Lambda})$ denotes the switching function which determines the throttling parameter $\sigma \in \{0, 1\}$. Let us assume that additional conditions that force the optimal control to switch between an upper and a lower bound like the eclipse condition is governed by another switching function $s_2(\mathbf{X})$. Other effects can also be considered like engine operating modes which also contribute to additional switches. Generally speaking let S denote the set of all switching functions,

$$S = \{s_1(\mathbf{X}, \mathbf{\Lambda}), s_2(\mathbf{X}), ..., s_k(\mathbf{X})\}, \tag{4.10}$$

where k is the number of conditions considered. Usually, the switches are captured by the tangent hyperbolic function (*tanh*). Assuming $T_{\max} = 1$ and $T_{\max} = 0$ denote the bounds on the thrust, the optimal thrust magnitude governed by the switching function $s(\mathbf{X}, \mathbf{\Lambda})$ is mathematically written as,

$$\sigma^*(\mathbf{X}, \mathbf{\Lambda}, t) = \frac{1}{2}\Big(1 \pm \tanh \frac{s(\mathbf{X}, \mathbf{\Lambda})}{\rho}\Big) \tag{4.11}$$

where ρ is the continuation parameter. Usually a smaller value of ρ indicates sharper switches in the control. For the case of k switching effects governed by two distinct switching functions we have,

$$\sigma^*(\mathbf{X}, \mathbf{\Lambda}, t) = \frac{1}{2}\Big(1 \pm \tanh \frac{s_1(\mathbf{X}, \mathbf{\Lambda})}{\rho}\Big) \times \frac{1}{2}\Big(1 \pm \tanh \frac{s_2(\mathbf{X})}{\rho}\Big) \times ..... \times \frac{1}{2}\Big(1 \pm \tanh \frac{s_k(\mathbf{X})}{\rho}\Big) \tag{4.12}$$

More generally,

$$\sigma^* = \sigma_1 \times \sigma_2 \times .... \times \sigma_k. \tag{4.13}$$

Note that other combinations of the switching functions are also possible. For instance, depending on the specific problem, $\sigma^* = (\sigma_1 \times \sigma_2 \times .... \times \sigma_k) + (\sigma_{k+1} \times \sigma_{k+2} \times .... \times \sigma_m)$ can also be considered as the optimal thrust magnitude. The approach described above is known as Composite Smoothing Control (CSC) because in this process we have essentially constructed a composite

smoothing function to include the different effects contributing to the bang-off bang nature of the control.

4.4 Indirect Formulation of the Optimal Control Problem

In all the work described henceforth, indirect formalism of the optimal control problem has been used to generate low-thrust optimal solutions for trajectory design. As mentioned before, indirect optimization methods reduce the original task of minimizing (or maximizing) of a cost functional into solving TPBVPs by using PMP.

The optimal direction of the control (thrust vector) is derived from the Lawden's primer vector theory [105]. These transfers for the present discussion, are primarily classified into minimum-time and minimum-fuel transfers, with the former minimizing the time of flight for the transfer while, the latter minimizes the propellant consumption (which is equal to maximizing the final mass for a fixed dry mass).

Minimum-time transfers deal with finding the extremal thrust profile, which minimizes the time of flight to achieve specified boundary conditions. The magnitude of the thrust vector for minimum-time trajectories takes its maximum, i.e., the engine is operating at its full capacity along a minimum-time trajectory. Additionally, the set of modified equinoctial elements (MEEs) has been used due to their superiority in designing low-thrust trajectories compared to other element sets as explained in [52, 39].

For minimum-fuel transfers, optimal trajectories are characterized by 'bang-off-bang' thrust profiles [106]. In particular, an engine throttle input, σ, characterizes the thrust magnitude, which can take values between 0 and 1, denoting the coast and maximum-thrust arcs, respectively. Designing minimum-fuel trajectories are notably more difficult compared to minimum-time trajectories since: 1) the thrust magnitude undergoes multiple to-be-determined number of switches, 2) the number and time duration of thrust and coast arcs are not known a priori, and 3) theoretically optimal instantaneous changes in the engine throttle input introduce complexities in the solution procedure and reduces the domain of convergence of the resulting Hamiltonian boundary-value problems.

The difficulties associated with non-smooth control inputs are alleviated by smoothing techniques [107, 108]. The hyperbolic tangent smoothing (HTS) method has been used in the work described due to its ease of implementation as demonstrated in different capacities in [109, 49]. These smoothed extremals, via a homotopy sweep, approach the embedded discontinuous optimal controls with a high precision.

4.4.1 Time-Optimal Trajectories

The state element set is written as $\boldsymbol{X} = [P,\ e_x,\ e_y,\ h_x,\ h_y,\ L]^T$, where P is the semilatus rectum, $[e_x,\ e_y]$ is the eccentricity vector, $[h_x,\ h_y]$ is the inclination vector and L is the true longitude.

In order to scale the problem, P is normalized by R_e (the equatorial radius of the Earth), mass is normalized by m_0, while t is normalized by $\sqrt{R_e/g_0}$, m_0 is the initial mass and g_0 is 9.80665 m/s^2. Note that $T_{\max}$ is the (constant) maximum thrust provided by the spacecraft engine. With this normalization, the 3D point-mass equations of motions (with the spacecraft mass (m) also included in the state-space equations) are expressed as

$$\dot{\boldsymbol{X}} = \boldsymbol{b} + \frac{T_{\max}}{m_0\, m\, g_0}\mathbb{M}\boldsymbol{\delta_T}\sigma, \qquad\qquad \dot{m} = -\frac{T_{\max}}{m_0\, c}\sigma, \tag{4.14}$$

where $\boldsymbol{\delta_T}$ is the unit vector in the thrust direction, σ is the engine throttle input, and $c = I_{\text{sp}}/(\sqrt{\frac{R_e}{g_0^3}})$ denotes the effective exhaust velocity. The vector $\boldsymbol{b}$ and matrix $\mathbb{M}$ are defined as

$$\mathbb{M} = \sqrt{\frac{P}{\mu}}\begin{bmatrix} 0 & \frac{2P}{W} & 0 \\ \sin L & \cos L + \frac{e_x+\cos L}{W} & -\frac{Ze_y}{W} \\ -\cos L & \sin L + \frac{e_y+\sin L}{W} & \frac{Ze_x}{W} \\ 0 & 0 & \frac{C\cos L}{2W} \\ 0 & 0 & \frac{C\sin L}{2W} \\ 0 & 0 & \frac{Z}{W} \end{bmatrix}, \qquad \boldsymbol{b} = \begin{bmatrix} 0 \\ 0 \\ 0 \\ 0 \\ 0 \\ \sqrt{\mu P}\left(\frac{W}{P}\right)^2 \end{bmatrix}, \tag{4.15}$$

where the scalars $W = 1 + e_x\cos L + e_y\sin L$, $Z = h_x\sin L - h_y$ and $C = 1 + h_x^2 + h_y^2$. The performance

index for the minimum time problem is

$$J_{\mathrm{MT}} = t_f. \tag{4.16}$$

Let the augmented state vector be defined as $\mathbb{X}^T = [\boldsymbol{X}^T, m]$. Introducing the vector of costates as $\boldsymbol{\Gamma}^T = [\boldsymbol{\Lambda}^T, \lambda_m]$, where $\boldsymbol{\Lambda} = [\lambda_P, \lambda_{e_x}, \lambda_{e_y}, \lambda_{h_x}, \lambda_{h_y}, \lambda_L]^T$ and λ_m is the costate associated with mass. The Hamiltonian is defined as

$$H_{\mathrm{MT}} = \boldsymbol{\Gamma}^T \dot{\mathbb{X}}. \tag{4.17}$$

The costate dynamics are obtained using the Euler-Lagrange equation, $\dot{\boldsymbol{\Gamma}} = -[\partial H_{\mathrm{MT}}/\partial \mathbb{X}]^T$. The final time t_f is free, the initial condition is defined by the sGTO departure condition and final conditions are the fixed target orbit/patch-point conditions. The optimal thrust direction should be opposite to the direction of $\mathbb{M}^T\boldsymbol{\Lambda}$ to minimize the Hamiltonian according to the minimum principle, i.e.,

$$\boldsymbol{\delta}_{\boldsymbol{T}}^* = -\frac{\mathbb{M}^T\boldsymbol{\Lambda}}{||\mathbb{M}^T\boldsymbol{\Lambda}||}. \tag{4.18}$$

The eight unknowns for the minimum-time rendezvous TPBVP are $\boldsymbol{\Gamma}(t_0)$ and t_f. Eight final conditions must be satisfied including six state final conditions and the two transversality conditions associated with 'free final time' expressed as $1 + H_{\mathrm{MT}}(t_f) = 0$ as well as 'free final mass' expressed as $\lambda_m(t_f) = 0$.

4.4.2 Fuel-Optimal Trajectories

The cost functional for the minimum-fuel trajectory design problem is defined in terms of the propellant mass, m_{P}, and throttling input, σ, as

$$J_{\mathrm{MF}} = m_{\mathrm{P}} = m(t_0) - m(t_f) = -\int_{t_0}^{t_f} \dot{m}\, dt = \frac{T_{\max}}{m_0\, c}\int_{t_0}^{t_f} \sigma\, dt. \tag{4.19}$$

The Hamiltonian associated with the minimum-fuel problem is defined as

$$H_{\text{MF}} = \frac{T_{\max}}{m_0\, c}\sigma + \mathbf{\Gamma}^T \dot{\mathbb{X}}. \tag{4.20}$$

Substituting the value of $\dot{\mathbb{X}}$ in Eq. (4.20), with $T_{\max}$ in the minimum-time formulation replaced by $(T_{\max}\ \sigma)$ for the minimum-fuel formulation to account for engine throttling, the following is obtained for the Hamiltonian

$$H_{\text{MF}} = \frac{T_{\max}}{m_0\, c}\sigma + \mathbf{\Lambda}^T \boldsymbol{b} + \frac{T_{\max}}{m_0\, m\, g_0}\,\sigma \mathbf{\Lambda}^T \mathbb{M} \boldsymbol{\delta_T} - \lambda_m \frac{T_{\max}}{m_0\, c}\sigma. \tag{4.21}$$

Since the Hamiltonian is a bi-linear function of both controls, $\boldsymbol{\delta_T}$ and σ, the strong form of the optimality conditions, (i.e., $\partial H_{\text{MF}}/\partial \boldsymbol{\delta_T} = 0$ and $\partial H_{\text{MF}}/\partial \sigma = 0$) are not applicable. Invoking PMP, optimal control inputs can be obtained as

$$\boldsymbol{\delta}_{\boldsymbol{T}}^* = -\frac{\mathbb{M}^T \mathbf{\Lambda}}{||\mathbb{M}^T \mathbf{\Lambda}||}, \qquad\qquad \sigma^* \in \arg\min_{0\le\sigma\le 1} H_{\text{MF}}. \tag{4.22}$$

In order to obtain σ^*, upon substituting δ_T^* into the Hamiltonian, the term that is multiplied by the throttle, σ, needs to be minimized and is written as

$$-\frac{T_{\max}}{m_0\, c}\sigma\left(\frac{c\mathbf{\Lambda}^T \mathbb{M} \boldsymbol{\delta}_{\boldsymbol{T}}^*}{m} + \lambda_m - 1\right) \quad \rightarrow \quad \textbf{min}. \tag{4.23}$$

Define the term in the bracket in Eq. (4.23) as a thrust switching function (SF) as

$$\text{SF} = \frac{c\mathbf{\Lambda}^T \mathbb{M} \boldsymbol{\delta}_{\boldsymbol{T}}^*}{m} + \lambda_m - 1, \tag{4.24}$$

and assuming an absence of intermittent singular arcs (SF = 0 for finite time intervals), the optimal

value of the throttling parameter, σ^*, can be defined as a function of SF,

$$\sigma^*(\text{SF}) = \begin{cases} 1, & \text{if SF } > \ 0 \\ 0, & \text{if SF } < \ 0. \end{cases} \tag{4.25}$$

Solving optimal control problems with bang-off-bang type of engine throttling (which is a characteristic of minimum-fuel type transfers) can become difficult. In order to make the resulting TPBVPs amenable to numerical treatment, a smoothing parameter, ρ, is introduced using the HTS method [109]. The generalized hyperbolic tangent smoothing for any bounded control input is defined as [50]

$$\sigma^*(\text{SF}, \rho) = \frac{1}{2}\left[(\sigma_U + \sigma_L) + (\sigma_U - \sigma_L)\tanh\left(\frac{\text{SF} - \text{SF}_s}{\rho}\right)\right], \tag{4.26}$$

where σ_U and σ_L are the upper and lower bounds for the throttling parameter respectively and $(\sigma_L, \sigma_U) \equiv (0, 1)$. SF_s is the switching point and for the class of transfers studied in this work, $\text{SF}_s = 0$. Therefore, the smoothed throttling input becomes [50]

$$\sigma^*(\text{SF}, \rho) = \frac{1}{2}\left(1 + \tanh\left(\frac{\text{SF}}{\rho}\right)\right). \tag{4.27}$$

The costate dynamics are obtained using the Euler-Lagrange equation, $\dot{\mathbf{\Gamma}} = -[\partial H_{\text{MF}}/\partial \mathbb{X}]^T$.

4.4.3 Boundary Conditions

The TPBVP is formulated using the indirect method and a single shooting method requires an initial guess for the unknown co-states. The most relevant classification for the objective function for trajectory design problems is time-optimal and fuel-optimal trajectories which have been discussed before. The algorithm uses an initial guess of costates along with the initial states (usually known as the initial parking orbit for the spacecraft) and propagates the state-costate differential EOMs to a final time (can be known or unknown) $t = t_f$. After propagation, the boundary conditions (known as the arrival orbit state) must be met to a high degree of accuracy for the problem to converge. Additionally, some terminal states might be set free according to the nature of the

problem. For instance, considering a problem defined using MEEs, if the the spacecraft is free to enter the orbit anywhere, the final true longitude can be set as free i.e, L_f. On the other hand, in case the arrival state of the spacecraft is completely defined, the problem is a rendezvous type problem. The missing state boundary conditions due to free any final/initial states are replaced by the so called '*transversality conditions*' which are derived from first principles using calculus of variation.

There are various classes of trajectory design problems, some relevant ones have been listed in Table 4.1 below along with the associated boundary conditions.

Table 4.1: Objectives with Boundary Conditions for relevant Trajectory Design Problems.

Objective	**Type**	**Boundary Condition**
Time-Optimal	Rendezvous	$\psi\left(\mathbf{X}(t_f), t_f\right) = \left[[\mathbf{X}(t_f) - \mathbf{X}_{\mathrm{T}}]^T, \|\mathbf{\Lambda}(t_f)\| - 1\right]^T = \mathbf{0},$
Time-Optimal	Free L_f	$\psi\left(\boldsymbol{X}(t_f), t_f\right) = \left[[\mathbf{X}^*(t_f) - \mathbf{X}_{\mathrm{T}}]^T, \lambda_L(t_f), \|\mathbf{\Lambda}(t_f)\| - 1\right]^T = \mathbf{0},$
Fuel-Optimal	Rendezvous	$\psi\left(\mathbf{X}(t_f), \lambda_m, t_f\right) = \left[[\mathbf{X}(t_f) - \mathbf{X}_{\mathrm{T}}]^T, \lambda_m(t_f)\right]^T = \mathbf{0},$
Fuel-Optimal	Free L_f	$\psi\left(\mathbf{X}(t_f), \lambda_m, t_f\right) = \left[[\mathbf{X}(t_f) - \mathbf{X}_{\mathrm{T}}]^T, \lambda_L(t_f), \lambda_m(t_f)\right]^T = \mathbf{0}$

4.5 Eclipse Embedded Indirect Method and the Hybrid Optimization Scheme

In this section, we present a novel hybrid optimization scheme which is essentially a culmination of all the theoretical developments described so far. This scheme is modular and can be used to design eclipse-conscious end-to end trajectories which leverage manifolds of **any** periodic orbit in **any** 'primary-secondary' system or in **any** other dynamical fidelity.

The following formulation describes the methodology followed to embed eclipses in the fuel-optimal problem solved using indirect formulation of the OCP. It is known that the set of Cartesian coordinates is not suitable for efficient convergence of indirect optimal planet-centric, many-spiral trajectories during the Earth escape/capture phases. Therefore, the set of modified equinoctial ele-

ments (MEEs) [42] is used to formulate time- and fuel-optimal low-thrust trajectory optimization problems in all the algorithms that constitute the hybrid optimization scheme.

Let $\boldsymbol{x} = [p, f, g, h, k, l]^\top$ denote the state vector associate with MEEs. Their dynamics can be written as

$$\dot{\boldsymbol{x}}(t) = \boldsymbol{A}(\boldsymbol{x}, t) + \mathbb{B}(\boldsymbol{x}, t)\boldsymbol{a}, \tag{4.28}$$

where $\boldsymbol{A} \in \mathbb{R}^{6\times1}$ denotes the unforced vector part of the dynamics and $\mathbb{B} \in \mathbb{R}^{6\times3}$ denotes the control influence matrix with their explicit forms given in [39]. The total acceleration vector, $\boldsymbol{a}$, expressed in the Local-Vertical Local-Horizontal frame attached to the spacecraft can be written as

$$\boldsymbol{a} = \boldsymbol{a}_p + \rho_p \left[\boldsymbol{a}_{\text{Sun}} + \boldsymbol{a}_{\text{Moon}}\right]. \tag{4.29}$$

where $\boldsymbol{a}_p$, $\boldsymbol{a}_{\text{Sun}}$, and $\boldsymbol{a}_{\text{Moon}}$ denote accelerations due to the propulsion system, and perturbing accelerations due to the Sun and Moon, respectively. In Eq. (4.29), $\rho_p \in [0, 1]$ denotes a continuation parameter that is used to gradually include the non-linear third-body perturbations due to the Sun, and Moon. When $\rho_p = 0$, a two-body dynamics is considered, whereas $\rho_p = 1$ corresponds to the high-fidelity model. Point-mass gravity models are used for planetary perturbations and perturbation due to solar radiation pressure is ignored. The acceleration due to the propulsion system can be written as

$$\boldsymbol{a}_p = \frac{T}{m}\delta_s\delta_o\hat{\boldsymbol{\alpha}}, \tag{4.30}$$

where $\delta_o \in [0, 1]$ is the engine throttling input, $\hat{\boldsymbol{\alpha}}$ denotes the thrust unit direction vector, and $\delta_s \in [0, 1]$ reflects eclipse events. In Eq. (4.30), T denotes the maximum thrust value and m denotes the spacecraft total instantaneous mass. The time rate of change of mass of the spacecraft can be written as

$$\dot{m} = -\frac{T}{c}\delta_s\delta_o, \tag{4.31}$$

where $c = I_{\text{sp}}g_0$ is the constant effective exhaust velocity. In this work, it is assumed that specific

impulse and the maximum thrust value of the thruster of the spacecraft remain constant during the entire maneuver. The control inputs are $(\delta, \hat{\boldsymbol{\alpha}})$.

Equation (4.30) is the total acceleration delivered by the propulsion system and δ_o and δ_s denote the combined engine throttling input due to application of the PMP and encountering of eclipse events, respectively. Since there are two sources that can lead to discontinuity in the thrust profile, the CSC methodology [47] is used to alleviate non-smoothness issues. Assuming ρ_o and ρ_s as the respective smoothing parameters, the optimal δ^* can be written as

$$\delta^* = \delta_s \delta_o, \qquad \delta_s = \frac{1}{2}\left[1 - \tanh\left(\frac{f_{ec}}{\rho_s}\right)\right], \qquad \delta_o = \frac{1}{2}\left[1 + \tanh\left(\frac{SF}{\rho_o}\right)\right], \tag{4.32}$$

where f_{ec} (see Eq. (4.9)) is treated as a "distance measure" associated with eclipse events. On the other hand, SF is the standard switching function derived from necessary optimality condition. The proposed high-fidelity, Hybrid Eclipse-Conscious Trajectory Optimization Routine (HECTOR) is summarized using two Algorithms given below.

Algorithm 1: HECTOR - TIME OPTIMAL

Result: Minimum time (t_f^*), Converged co-state vector (λ_0^{2b})

Departure States on the sGTO : $(\boldsymbol{x}_o)$, Arrival States on the LTCA : $(\tilde{\boldsymbol{x}}_d)$

while $\epsilon_{MT} \geq \epsilon^*$ **do**

Initial Guess: t_f(*Time of Flight*) & $\boldsymbol{\lambda}(t_0)$

Propagate: Eqs. (4.28), (4.31) & ***E-L*** *Equation with* $\rho_p = 0, \delta_o^* = 1, \delta_s, \hat{\boldsymbol{\alpha}}^*$;

$\epsilon_{MT} = ||\boldsymbol{\epsilon}_{MT}|| = ||\boldsymbol{x}(t_f) - \tilde{\boldsymbol{x}}_d, H_{MT}(t_f)||$;

end

In Algorithm 1 of the HECTOR, the minimum-time problem is solved. The unknown values are the initial costates and total time of flight. The value of ϵ^* is set to 1.0×10^{-12}. The resulting TPBVP is solved using a standard single-shooting method, however, the eclipses are incorporated into the formulation through the δ_s factor. Any coast arc during the minimum-time maneuver is due to (penumbral) eclipse events and for the rest of the maneuver the thruster is always ON.

The next step is to find fuel-optimal solutions as outlined in Algorithm 2 below. However, the time of flight has to be greater than the time of flight of the minimum-time solution. Thus, a scalar parameter γ is considered. The value of γ depends on the problem. Here, it is considered to lie in a range $\gamma \in [1.2, 1.4]$. In order to simplify the problem, the initial problem corresponds to restricted two-body Earth-spacecraft dynamics (denoted by superscript '2b'). As a consequence, the associated Hamiltonian, H_{MF}^{2b} takes a simpler form (since $\rho_p = 0$).

In addition, the smoothing parameter ρ_s is set to 1 to handle the eclipse transitions. The value of ρ_s is lowered to below a certain ρ_s^* value to get sharp transitions at the entry and exit of eclipse-induced coast arcs. Then, a step is initiated to decrease the value of ρ_o below a certain threshold, ρ_o^* in order to obtain bang-off-bang thrust profiles. The value of ρ_o^* in our simulations is set to 1.0×10^{-6}. The final step is to introduce perturbations through ρ_p. When, ρ_p is equal to one, the solution associated with the high-fidelity model is obtained. While the value of ρ_p is increased, it is ensured that the final solution corresponds to $\rho_p = 1$. It is emphasized that the Hamiltonian is updated according to the considered dynamics to take into account the contribution of the perturbing accelerations. Thus, the costate differential equations are updated accordingly [47]. Please note that a time-fixed, fuel-optimal problem is solved. In fact, time-free, fuel-optimal problems are not well-defined problems since for such maneuvers the time of maneuver increases to infinity.

Convergence robustness of indirect optimization methods are known to be inferior to direct optimization methods if the initial guesses are not "close" to those that correspond to an extremal solution. In addition, there are many local extremal solutions. There are actually four issues that impact convergence robustness of indirect optimization methods: 1) the choice of coordinates, 2) non-smoothness of certain events (e.g., throttle switches and eclipse entry and exist conditions), 3) the adopted homotopy/continuation method, and 4) proper scaling of states [110]. All items can play important roles in solve challenging optimal control problems. Our experience indicates that appropriate choice of coordinates (i.e., item 1) has enormous impact on the convergence robustness of indirect methods when it comes to solving many-revolution low-thrust trajectories. In addition, the idea of smoothing (item 2) enlarges the domain of convergence of the resulting boundary-value

problems to an extent that random initialization of the missing initial costate values is sufficient to obtain convergence.

Random initialization of the costates is used to find the solution of the first member of the family of optimal control problems. The limit of achievable number of orbital revolutions depends on many factors such as the strength of disturbances and the choice of solution methodology (e.g., single-shooting vs. collocation-based method). Ref [111], for instance, provides cases with up to 500 revolutions using a single-shooting method and using MATLAB's *fsolve* and *ode45* built-in functions and using the set of modified equinoctial elements. In this work, the same methodology (and solvers) was used, but a principled continuation methodology is followed and is described in the proposed Algorithms. We have been able to achieve convergence without using the state transition matrix. The default finite-difference method (of *fsolve*) is used to calculate the sensitivity of the constraints with respect to the design variables.

Algorithm 2: HECTOR - FUEL OPTIMAL

Result: Eclipse-Conscious Fuel-Optimal Transfer Trajectory in the HFM

Fuel-optimal: $t_f^{\mathrm{MF}} = \gamma\, t_f^* \;\; \forall \;\; \gamma > 1$; *Initial Guess*: $\boldsymbol{\lambda}_0^{\mathrm{2b}}(\rho_s = 1)$

while $\rho_s \geq \rho_s^*$ **do**

  while $\epsilon_{MF}^{2b} \geq \epsilon^*$ **do**

    Propagate: Eqs. (4.28), (4.31) & **E-L** Equation with $\delta^*, \hat{\boldsymbol{\alpha}}^*$;

    $\epsilon_{\mathrm{MF}}^{2b} = \|\boldsymbol{\epsilon}_{\mathrm{MF}}^{\mathrm{2b}}\| = \|\boldsymbol{x}(t_f^{\mathrm{MF}}) - \tilde{\boldsymbol{x}}_d, \lambda_m(t_f^{\mathrm{MF}})\|$

  end

  $\boldsymbol{\lambda}_0^{\mathrm{2b}} = \boldsymbol{\lambda}^{\mathrm{2b}*}$(Converged Value), $\rho_s = 0.9\rho_s$;

end

Initial Guess : $\boldsymbol{\lambda}_0^{\mathrm{2bS}} = \boldsymbol{\lambda}^{\mathrm{2b}*}\Big|_{\rho_s=\rho_s^*}$

while $\rho_o \geq \rho_o^*$ **do**

  while $\epsilon_{MF}^{2bS} \geq \epsilon^*$ **do**

    Propagate: Eqs. (4.28), (4.31) & **E-L** Equation with $\delta^*, \hat{\boldsymbol{\alpha}}^*$;

    $\epsilon_{\mathrm{MF}}^{\mathrm{2bS}} = \|\boldsymbol{\epsilon}_{\mathrm{MF}}^{\mathrm{2bS}}\| = \|\boldsymbol{x}(t_f^{\mathrm{MF}}) - \tilde{\boldsymbol{x}}_d, \lambda_m(t_f^{\mathrm{MF}})\|$

  end

  $\boldsymbol{\lambda}_0^{\mathrm{2bS}} = \boldsymbol{\lambda}^{\mathrm{2bS}*}$(Converged Value), $\rho_o = 0.9\rho_o$;

  Initial Guess : $\boldsymbol{\lambda}_0^{\mathrm{hfS}} = \boldsymbol{\lambda}^{\mathrm{2bS}*}|_{\rho_o=\rho_o^*;\, \rho_s=\rho_s^*}$

  while $\rho_p \leq 1$ **do**

    while $\epsilon_{MF}^{hfS} \geq \epsilon^*$ **do**

      Propagate: Eqs. (4.28), (4.31) & **E-L** Equation with

      $\boldsymbol{a} = \boldsymbol{a}_p^*(\delta_s^*, \delta_o^*, \hat{\boldsymbol{\alpha}}^*) + \rho_p(\boldsymbol{a}_{\mathrm{Sun}} + \boldsymbol{a}_{\mathrm{Moon}})$;

      $\epsilon_{\mathrm{MF}}^{\mathrm{hfS}} = \|\boldsymbol{\epsilon}_{\mathrm{MF}}^{\mathrm{hfS}}\| = \|\boldsymbol{x}(t_f^{\mathrm{MF}}) - \tilde{\boldsymbol{x}}_d, \lambda_m(t_f^{\mathrm{MF}})\|$

    end

    $\boldsymbol{\lambda}_0^{\mathrm{hfS}} = \boldsymbol{\lambda}^{\mathrm{hfS}*}$(Converged Value), $\rho_p = 1.1\rho_p$;

  end

  A final fuel-optimal TPBVP is solved with $\rho_p = 1$.

end

The inherent flexibility, robustness and computational ease that leveraging manifolds provide, make the optimization scheme presented herein an extremely powerful tool for mission designers. Moreover, the ability to include the knowledge of eclipses increases the accuracy of the resulting trajectory which can mimic the mission-ready nominal trajectory that the spacecraft flies to a high degree. Furthermore, the optimization scheme has the ability to include gravitational effects from any SSB. Note that this is a sequential scheme and the numerical optimization steps are kick-started by the converged solution from the previous step.

5. EARTH TO MOON TRANSFERS USING DIFFERENT MODEL FIDELITY: RESULTS AS CASE STUDIES [1]

In this chapter, case studies are presented for various transfer scenarios in the cislunar space. The transfers considered in the chapter are comprehensive and provide a complete spectrum of cases where the dynamical systems considered for each case range from the simple CR3BP to the complex HFM. Additionally, manifolds of different periodic orbits have been leveraged for the various cases discussed below. Table 5.1 depicts the salient features of the three cases presented.

Table 5.1: Case Studies in the Cislunar Space.

Case ID	**Periodic Orbit**	**Dynamical System**	**Origin-Target**
A	L_1 Halo	CR3BP, BCP	GTO - LLO
B	9:2 Southern L_2 NRHO	HFM	sGTO - NRHO
C	9:2 Southern L_2 NRHO	HFM	sGTO - NRHO

5.1 Case A

Case A describes a transfer in the cislunar space which leverages manifolds of an orbit from the L_1 Halo Family. Both the CR3BP and BCP dynamical systems are considered for the work that follows.

[1] Parts of this chapter have been reprinted with permissions from:
"Eclipse-conscious transfer to lunar gateway using ephemeris-driven terminal coast arcs" by Singh, S., Junkins, J., Anderson, B., Taheri, E., 2021, Journal of Guidance, Control and Dynamics, 44(11), 1972-1988, Copyright ©2021 by the American Institute of Aeronautics and Astronautics, Inc. ;
"Exploiting manifolds of L1 halo orbits for end-to-end Earth–Moon low-thrust trajectory design" by Singh, S. K., Anderson, B. D., Taheri, E., Junkins, J. L., 2021, Acta Astronautica, 183, 255-272, Copyright ©IAA. Published by Elsevier Ltd.
"Low-Thrust Transfers to Southern L_2 Near-Rectilinear Halo Orbits Facilitated by Invariant Manifolds by Singh, S. K., Anderson, B. D., Taheri, E., Junkins, J. L. (2021). Journal of Optimization Theory and Applications, 191(2), 517-544. Copyright ©2021, The Author(s), under exclusive licence to Springer Science Business Media, LLC, part of Springer Nature.

5.1.1 Problem Description and Mission Parameters

The Earth-Moon transfer studied in this case is assumed to initiate from a GTO and terminate in a polar orbit around the Moon. We note that GTO initial orbit is consistent with the truth that inexpensive secondary payload opportunities exist on almost every launch of large (thousands of kg) spacecraft to GEO. Secondary payloads with mass of 250kg are frequently feasible so long as the stowed launch configuration fits with a volume of typically $\sim 1m^3$. The transfer consists of multiple phases, which are listed in Table 5.2. In the table, nGEO stands for near-Geosynchronous Earth Orbit, $M_{\mathrm{E_{IC}}}$ and $M_{\mathrm{E_{FC}}}$ stand for initial and final conditions, respectively, for the stable manifolds on the Earth side, whereas, $M_{\mathrm{M_{IC}}}$ and $M_{\mathrm{M_{FC}}}$ stand for initial and final conditions, respectively, for the unstable manifolds on the Moon side.

Table 5.2: Breakdown of the transfer trajectory phases.

Phase	**Transfers**	**Type of Maneuver**
1A	GTO - nGEO	Min-Time
1B	nGEO	Coast (30 days)
$1C_A$	nGEO - $M_{\mathrm{E_{IC}}}$	Min-Time
$1C_B$	Manifold - I	Coast
$1C_C$	$M_{\mathrm{E_{FC}}}$ - Halo	Min-Time
2A	Halo - $M_{\mathrm{M_{IC}}}$	Min-Time
2B	Manifold - II	Coast
2C	$M_{\mathrm{M_{FC}}}$ - Lunar Polar Orbit	Min-Time

The GTO for this mission is an elliptical orbit with a semi-major axis of $a = 24364.1$ km, eccentricity of $e = 0.7306$ and inclination of $i = 27^\circ$. The nGEO is also an elliptical orbit with a semi-major axis of $a = 41673.5$ km, eccentricity of $e = 0.5932$ and inclination of $i = 27^\circ$. The nGEO orbit was selected based on a preliminary mission planning study. This coast orbit is useful for navigation, SSA and evaluation of the actual performance of the spacecraft before proceeding with the mission. The terminal selenocentric orbit is a circular lunar polar orbit with a radius of 2738 km (altitude is 1000 km).

Phase 1A corresponds to an increase in the semi-major axis and a reduction in the orbit eccentricity. Phase 1B corresponds to a 30-day coast in the nGEO, where the spacecraft will perform a number of SSA tasks. The coast duration for nGEO is assumed to be 30 days, whereas the remaining coast duration depends on the choice of manifold. Phase $1C_A$ is a minimum-time transfer from the nGEO to the stable manifold initial condition, whereas Phase 2C is a minimum-time transfer from the unstable manifold final condition to the Lunar Polar Orbit (Lunar Capture). The spacecraft coasts on the stable and unstable manifolds in Phases $1C_B$ and 2B. Finally, Phases $1C_C$ and 2A are minimum-time transfers to and from the halo orbit respectively from the respective manifold conditions. All transfer segments are to be designed as minimum-time trajectories with continuous thrust except for the phases where the spacecraft is coasting.

The spacecraft is of the mini satellite / smallsat classification. The following values are used for spacecraft parameters: Initial mass, $m_0 = 240$ kg, Constant Specific Impulse, $I_{\text{sp}} = 1250$ s, and Maximum Thrust, $T_M = 0.096$ N.

5.1.2 Manifold Patch-Conditions

Since the target orbit is a Lunar Polar Orbit, the out-of-plane motion achieved by riding the manifold off the halo-orbit, needs to be leveraged in order to save fuel. This essentially means replacing a minimum-time/minimum-fuel trajectory from the halo orbit to the Lunar Polar Orbit by three separate phases - a maneuver to get on the manifold, coasting to the final condition and a maneuver to get off the manifold and insert into the terminal orbit. Another important factor is that the boundaries of the manifolds should pass 'close' to the respective primaries. Thus, a mapping of the inertial inclination of the points in Figures 5.1a and 5.1b against the magnitude of the respective position vector / periapse radius is required to qualitatively pick the 'best' patching condition set for our mission, among the considered candidate points.

5.1.2.1 Inertial inclination versus radius

The piercing points in Figure 5.1a were plotted in an 'inertial inclination' versus radius plot with respect to the Earth - Moon orbital plane and the Earth's center as the origin, whereas the

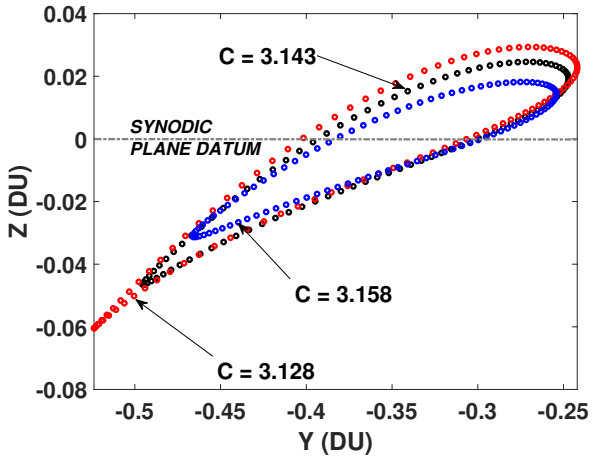

(a) YZ piercing plane $x = -\mu$ (IC - Earth Leg)

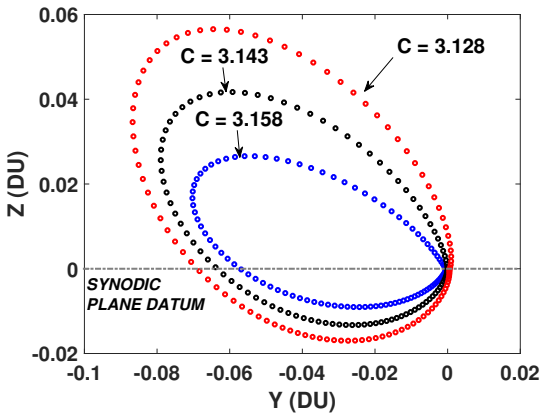

(b) YZ piercing plane $x = 1 - \mu$ (FC - Moon Leg)

Figure 5.1: Piercing plane maps.

points in Figure 5.1b were plotted with respect to the same plane and origin at the Moon's center. The radius, r, is the position vector magnitude relative to the respective center. Mapping of the inclination helps ascertain the 'best' patching condition in a close vicinity of the inclination of the nGEO for the 'Earth-Leg' and the Lunar Polar Orbit for the 'Moon-Leg'. Approximately matching inclinations are heuristically attractive because the truth that plane changes are known to be very expensive, especially when seeking to change planes close to either of the primaries.

The piercing points for the 'Earth-Leg' shown in Figure 5.2 are easy to analyze. The maximum inertial inclination achieved by the piercing manifolds from the candidate halo orbits is 8.406°, corresponding to the halo orbit with $C = 3.128$. This point is picked as the target patch-condition for trajectory design for Phase $1C_A$ due to the smallest inclination difference relative to the nGEO coast orbit plane. Note that a velocity-type analysis is also important and may lead to better patching conditions. In this work, we used relative inclination difference as our selection criterion. The portion of the graph to the left of the magenta line is the 'forbidden' region defined by the extent of the Earth's atmosphere. Since the choice of halo orbits need to be one and the same for both legs (unless we want to transfer between halo orbits, which is not considered for this paper), the red markers in Figure 5.3 constitute the possible set of final conditions (FCs) where the unstable

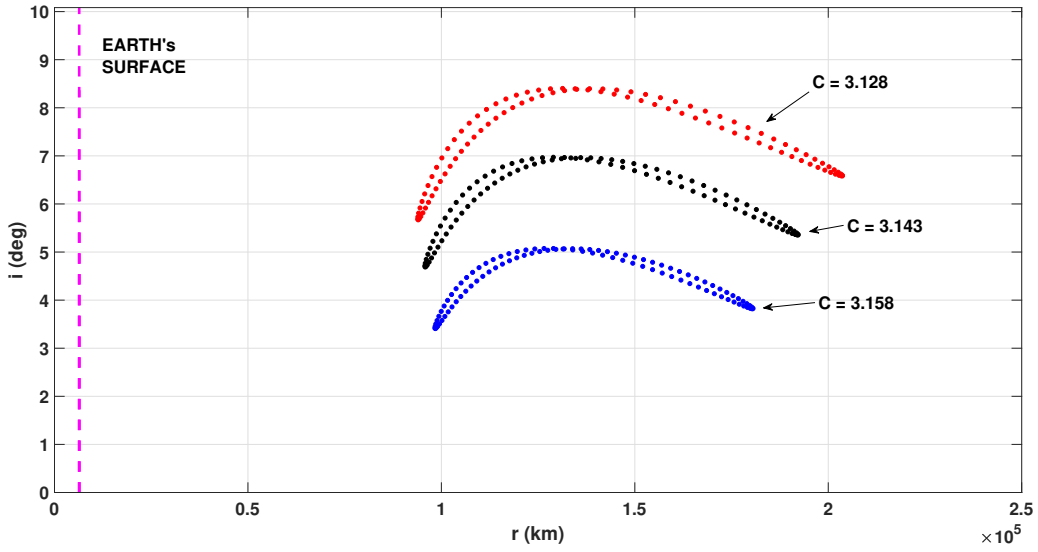

Figure 5.2: *i* vs. *r* for candidate conditions - Earth-Leg trajectory.

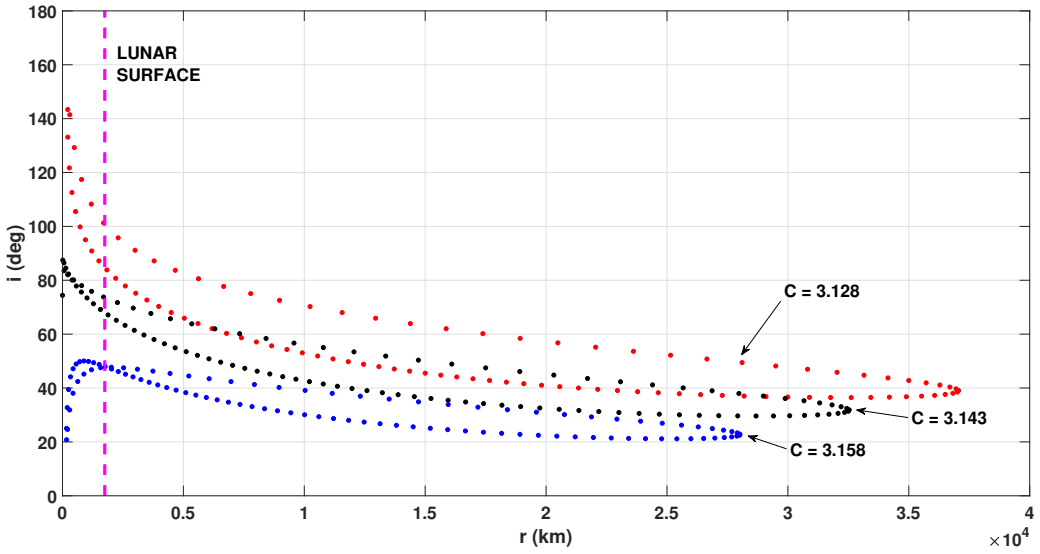

Figure 5.3: *i* vs. *r* for candidate conditions - Moon-Leg trajectory.

manifolds pierce the $x = 1 - \mu$ plane.

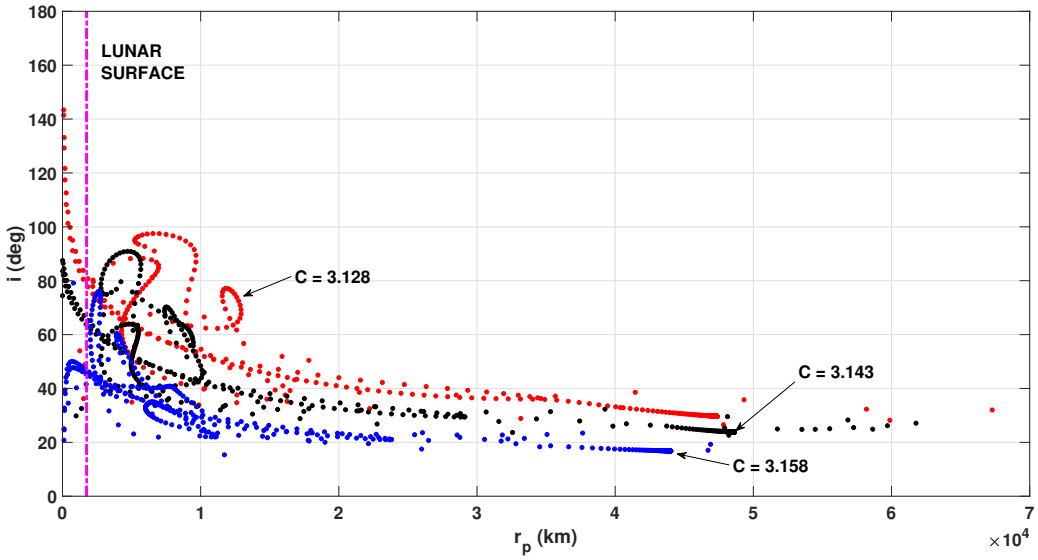

Figure 5.4: i vs. r_p for candidate conditions - Moon-Leg trajectory

However, the conditions corresponding to the piercing points generally have parabolic velocities, making a capture in such a scenario more expensive than points on the manifolds that correspond to an elliptical orbit. Thus, a Poincaré map (see Figure 5.4) of points of periapse passage on the manifolds was plotted in an 'i vs r_p' plot, where r_p is the periapse radius with respect to the Moon. This was done by propagating the EOMs for initial conditions on the halo orbit and by checking for a negative to positive sign change in the radial velocity during a zero-crossing condition. For our mission, the condition closest to polar inclination was selected as the manifold patch-condition for the 'Moon-Leg'.

The manifold patch conditions for the 'Earth-Leg' and 'Moon-Leg' selected for the mission (expressed in the normalized barycentric synodic frame) is given in the Table 5.3.

5.1.3 CR3BP Manifolds in the BCP

The invariant manifolds exist only as companions to fixed points, periodic or quasi-periodic orbits in a dynamical system, in our case halo orbits in the CR3BP. The assumptions become

Table 5.3: Chosen CR3BP manifold target states.

LEG	x (DU)	y (DU)	z (DU)	v_x (VU)	v_y (VU)	v_z (VU)
Earth (IC)	-0.0122	-0.3394	0.0199	1.6559	-0.0619	0.2742
Moon (FC)	0.9761	0.0017	0.0045	0.4163	-0.0939	1.2441

invalid once the effect of the Sun is introduced in the dynamics, therefore, adding a perturbation to any trajectory designed in the CR3BP. In addition, the dynamical system is no longer autonomous. As a consequence, a key contribution of the current study is to study the effect of Sun's perturbation on the selected manifold conditions, and to do so across several relative orientations of the Sun, Earth and Moon. While there are many ways to perform this analysis, we chose to study how the initial phase-angle of the Sun with respect to the synodic X axis effects the manifolds used as an initial guess for the optimization. Note that we define the initial phase angle, λ_0 (see Fig. 2.6), as the Sun's phase angle when the spacecraft is at the FC of the Earth-Leg manifold. Implicitly, we will find which phase angles offer advantages, and see that the perhaps though to be undesirable solar perturbation can in fact be advantageous with regard to maneuver time and/or fuel consumption.

For this analysis, we assume that the Sun at $t = 0$ is along the negative X axis of the Cartesian synodic Earth-Moon CR3B frame. The stable manifold FC on the Earth-Leg manifold as well as the unstable manifold IC on the Moon-Leg manifold are picked as respective initial states for propagation. These states are propagated backwards and forwards in time, respectively, in the presence of the BCP dynamics.

By choosing to define the time $t = 0$ as a reference angular position of the Sun, propagating trajectories with different initial Sun phase angles is equivalent to changing the initial time of that propagation. Then, as the initial phase angle (λ_0) changes, the initial time for the stable manifold FC becomes

$$t'_{s_0} = t_{s_0} + \frac{\lambda_0}{\nu_0}, \tag{5.1}$$

where $'$ denotes parameters in the BCP dynamics, t_{s_0} denotes the time corresponding to stable manifold FC in the CR3BP, λ_0 is the current Sun's phase angle and $\nu_0 = N_1 - N_2$ is the mean

motion of the Sun in the synodic frame (N_1 being the mean motion of the Earth-Moon barycenter about the Sun, and N_2 being the mean motion of the Moon about the Earth). Following similar developments,

$$\begin{aligned} t_{u_0}^{'} &= t_{u_0} + \frac{\lambda_0}{\nu_0}, \\ t_{s_f}^{'} &= t_{s_f} + \frac{\lambda_0}{\nu_0}, \\ t_{h_0}^{'} &= t_{h_0} + \frac{\lambda_0}{\nu_0}, \\ t_{h_f}^{'} &= t_{h_f} + \frac{\lambda_0}{\nu_0}, \end{aligned} \tag{5.2}$$

where $t_{u_0}^{'}, t_{s_f}^{'}, t_{h_0}^{'}$ and $t_{h_f}^{'}$ denote the time corresponding to unstable manifold IC, stable manifold IC, halo orbit IC and halo orbit FC in the BCP dynamics, respectively. The unprimed parameters denote the same quantities in the CR3BP dynamics. Using the initial conditions, respective dynamics and phase angle dependent initial and final propagation time, the EOMs were numerically propagated to study the new behaviour of the chosen manifolds. The purpose of this study is to identify a beneficial epoch for this trajectory, such that the perturbed manifolds behave similarly to the unperturbed ones, and still yield a high inclination final condition at the Moon. It is possible to make a more exhaustive study to find a better optimal solution by studying all possible manifolds at all possible Sun phase angles. However, we are for this study interested in identifying the impact of the Sun's perturbation on a trajectory similar to the one designed in the unperturbed model. That is why we chose the approach of using the previously chosen CR3BP manifolds.

5.1.3.1 Moon-Leg Manifold in the BCP

In this section, results elucidating the effect of phase angle on the manifolds used for the Moon-Leg of the mission are provided. Since the target orbit is a polar orbit around the Moon and the current work leverages the 'free' out-of-plane maneuver provided by the CR3BP manifolds, it makes the leg more critical. Therefore, we study their behaviour in the presence of the Sun and subsequently evaluate the effect of 'best' candidate phase-angles on the Earth-Leg manifold.

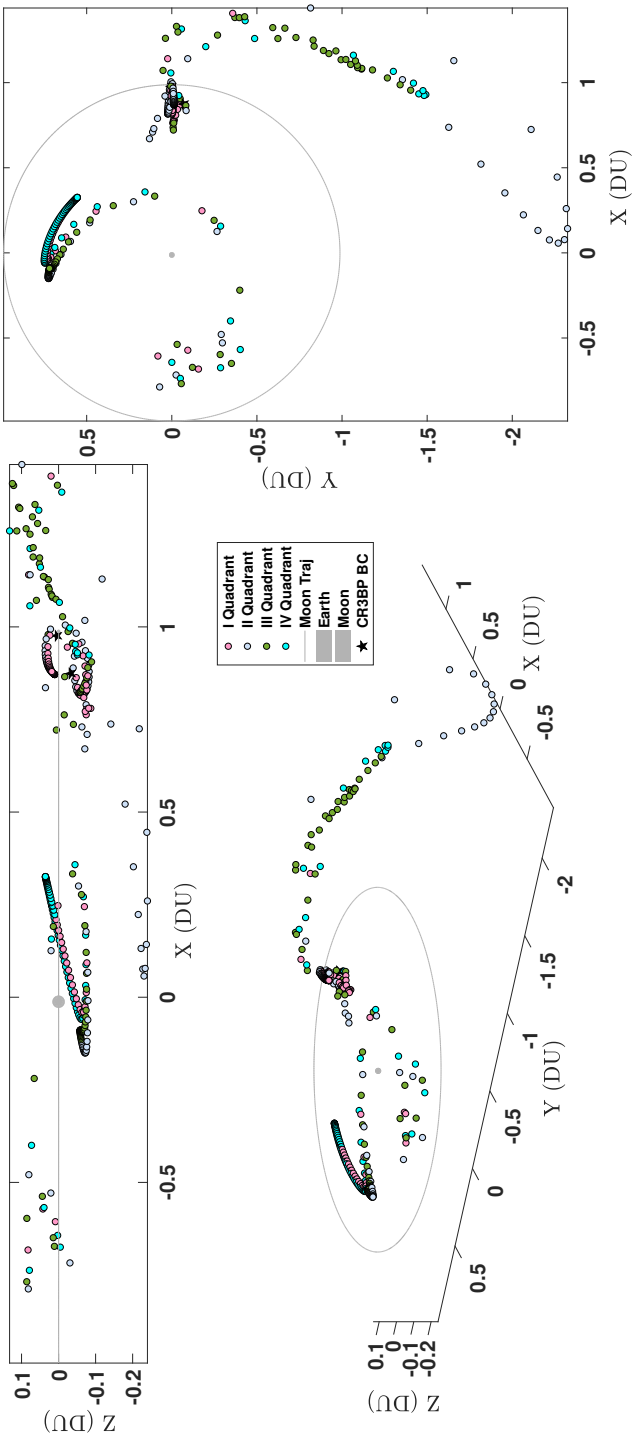

Figure 5.5: Spatial Map of the Unstable Manifold FC in the BCP, Propagation time: 29.618 days.

Figure 5.5 shows the spatial map of the Unstable Manifold FC emanating from the respective CR3BP IC (propagated for the same time as the CR3BP manifold). The effect of the initial solar phase angle is highlighted by the amount of dispersion of the points in the plot. The importance of an ideal 'phase' is quite evident due to the significant perturbation of the CR3BP manifold. As mentioned before, our criterion for selection of the 'ideal initial phase' is also driven by the periapse radius and inertial inclination of the unstable manifold FC wrt. the Moon. After generating these manifolds, a search for identifying the state closest to the CR3BP in terms of periapse radius and inertial inclination was carried out.

Figure 5.6 shows the absolute variation in these quantities from the respective CR3BP values (nominal) plotted against the initial solar phase angle. Four distinct choices, having the least variation in the new inertial inclination from the nominal value, were selected for further investigation. The manifold dynamics unsurprisingly, was found to be faster with the Sun perturbing the dynamics as compared to the CR3BP case. The halo Orbit dynamics are affected to the point that it visibly does not close (loses periodicity). The impact on stability of the fixed points previously obtained as well as the associated manifolds depends on the solar phase angle. The stable manifold associated with these four cases, were studied next to pick the 'best' case for generating end-to-end trajectories.

A phase plot (see Figure 5.7), allows the mission designer to pick the 'best' condition on the chosen manifold for the appropriate solar phase angle. A larger difference in eccentricity between the osculating condition on the manifold state and the target orbit obviously is more expensive to bridge than the respective difference in inclination, especially for circular and near-circular target orbits.

5.1.3.2 Earth-Leg Manifold in the BCP

In this section, results elucidating the effect of phase angle on the manifolds used for the Earth-Leg are provided. The four candidate cases obtained from the study of the Moon-Leg manifolds are paid close attention to. The respective stable manifolds are studied and truncated to the best ICs (closest to the CR3BP stable manifold IC). For the sake of completion, the spatial map for the

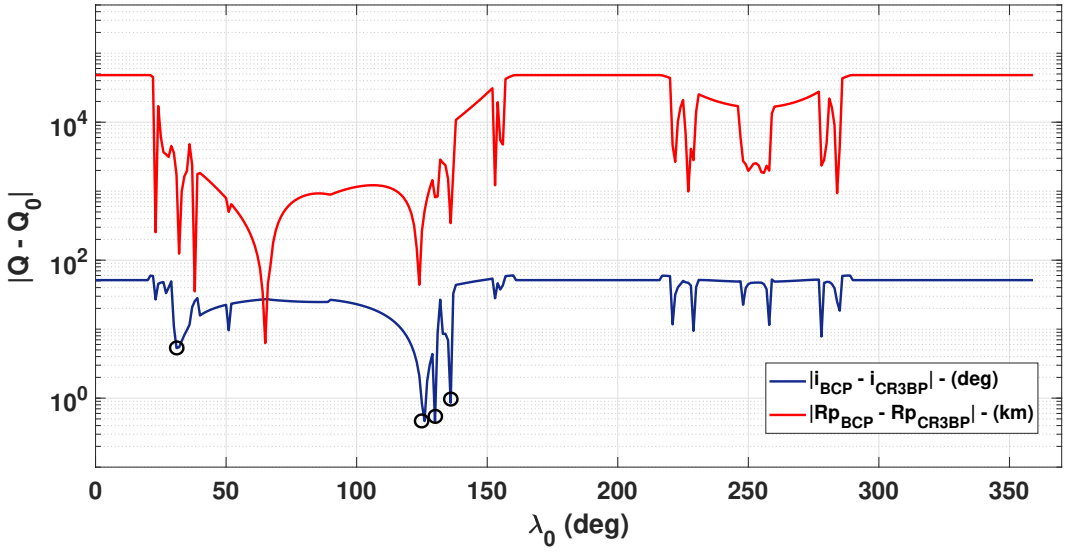

Figure 5.6: Variation in periapse radius and inertial inclination - Moon Leg.

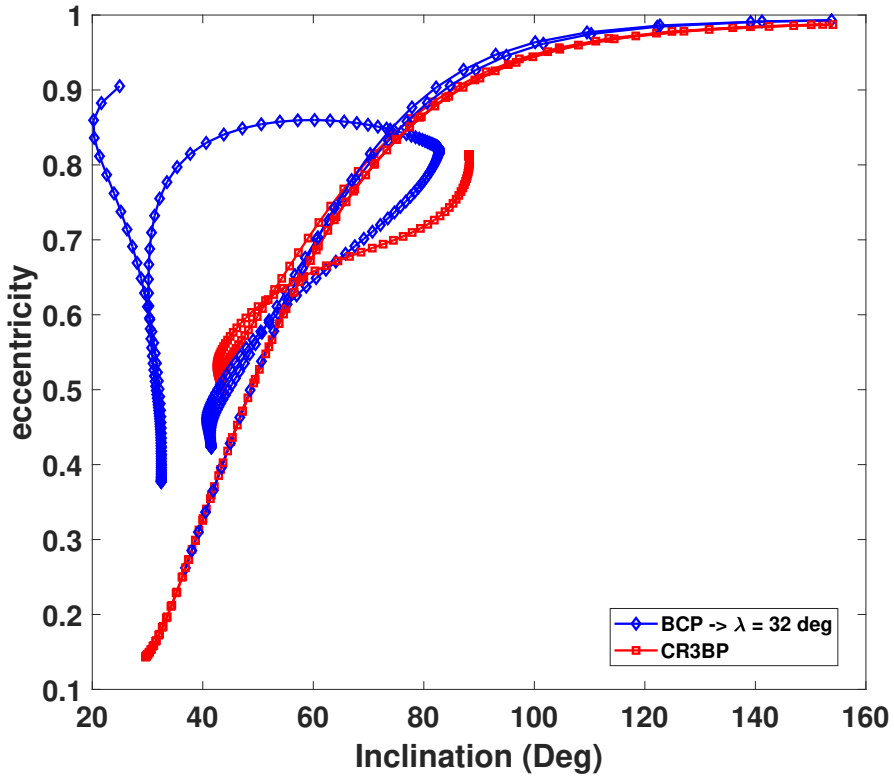

Figure 5.7: e vs. i (MCI) - Unstable Manifold.

stable manifold for varying initial solar phase angle is provided in Figure 5.8. Figure 5.9 shows the absolute difference in inertial inclination and semi-major axis plotted against initial solar phase angle. The points highlighted depict the corresponding values for the candidate cases discussed in the previous section.

5.1.3.3 Summary - CR3BP manifolds in the BCP

In this section, a summary of the behavior of the chosen invariant manifolds of the CR3BP, for the four candidate initial solar phase angles are provided. Table 5.4 lists the respective time of flight on each of the manifold pairs corresponding to these phase angles, to reach the 'best' state on the manifold (defined by the variation from CR3BP states). The first row provides the time of flight on either manifold in the CR3BP, for the sake of comparison.

Table 5.4: Time of Flight (TOF) - Manifolds in BCP.

λ_0	**TOF$_S$** (days)	**TOF$_U$** (days)	**TOTAL** (days)
-	26.10	29.62	55.72
32°	13.90	17.35	31.25
126°	22.59	14.04	36.63
130°	23.13	27.19	50.32
136°	24.35	18.43	42.78

Figure 5.10 shows the behavior of the respective manifolds listed in Table 5.4. All four candidates are viable and can be used for trajectory design. The cases with $\lambda_0 = \{126°, 130°, 136°\}$ have either the stable manifold looping around the Moon before turning back to Earth or the unstable manifold making multiple turns in the vicinity of the Moon before reaching the desired state. For this work the case with the initial solar phase angle $\lambda_0 = 32°$ was chosen because it most closely mimics the shape of the manifold from the CR3BP, as well as maintains a high inclination and similar inclination when arriving at the Moon. Remarkably, the manifold associated with a phase angle of 32° also provides very substantial time savings of 24.47 days compared to a phase angle of zero.

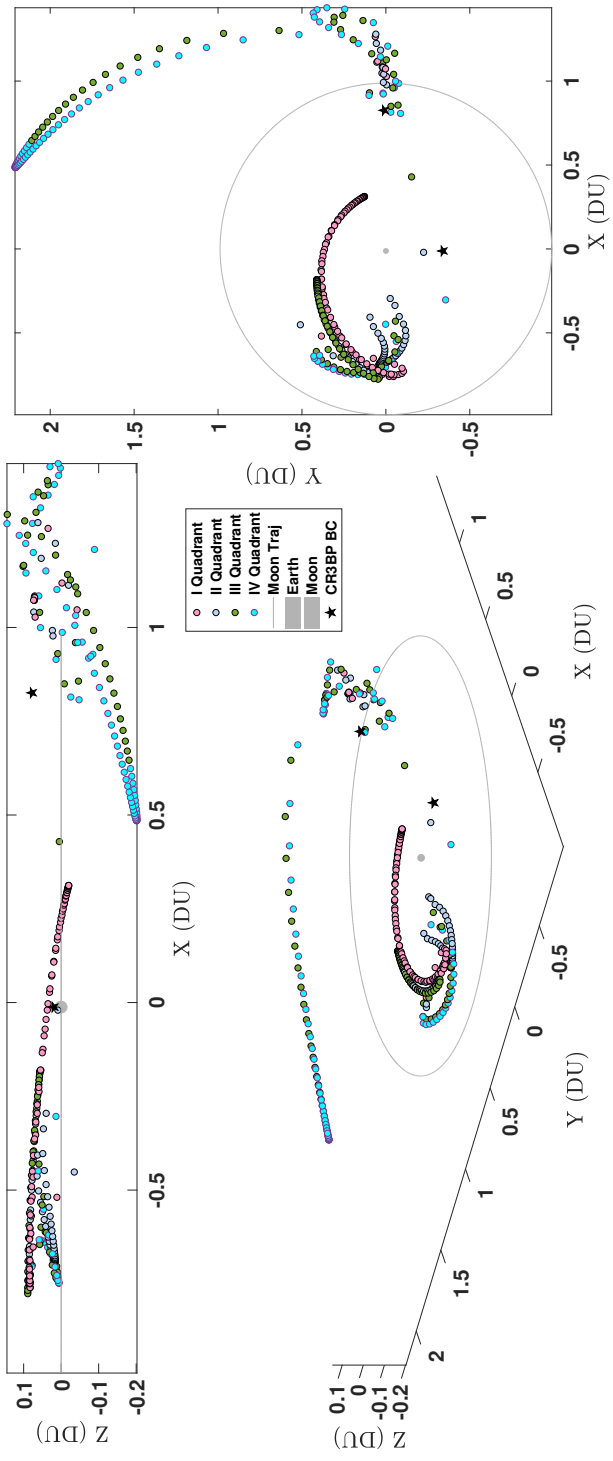

Figure 5.8: Spatial Map of the Stable Manifold IC in the BCP, Propagation time: 26.098 days

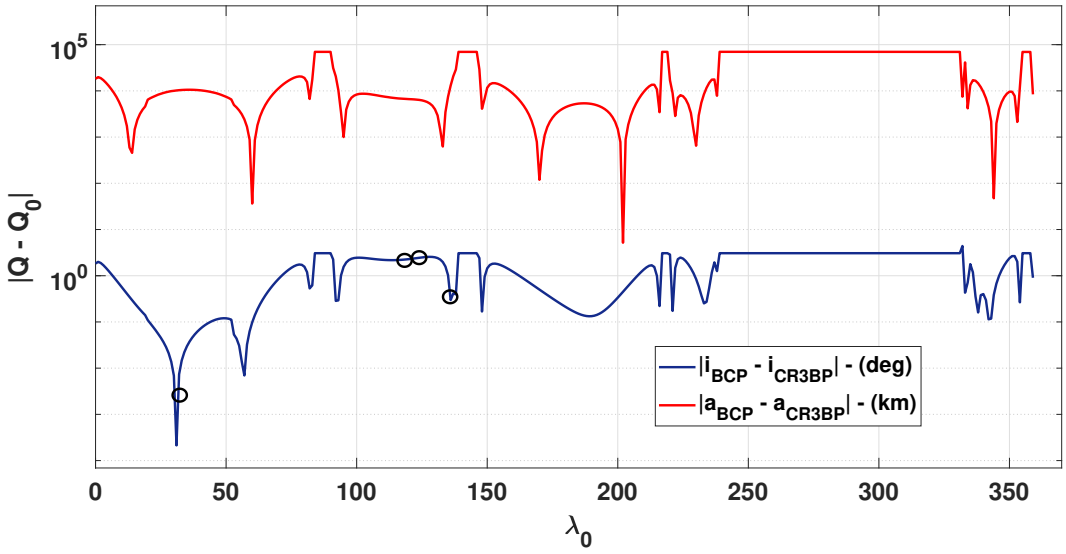

Figure 5.9: Variation in semi-major axis and inertial inclination - Earth Leg

The new manifold IC-FC to be targeted for trajectory design during the Earth-Leg and the Moon-Leg are given in Table 5.5.

Table 5.5: Chosen BCP perturbed manifold target states.

LEG	x (DU)	y (DU)	z (DU)	v_x (VU)	v_y (VU)	v_z (VU)
Earth (IC)	-0.0138	-0.3331	0.0218	1.6878	-0.0797	0.2709
Moon (FC)	0.9759	0.0009	0.0033	0.3687	-0.1333	1.2710

5.1.4 Results - End to End transfer

In this section, results for the full transfer are presented. The first subsection deals with Phase 1 or the 'Earth-Leg' of the transfer while the next subsection has results for Phase 2 or the 'Moon-Leg' of the mission. Note that for the CR3BP manifold conditions, optimal control formulation and solution includes the presence of the Moon as a third body, whereas, for the BCP manifold conditions, formulation and solution also includes the presence of the Sun along with the Moon as third bodies. A comparison of the important results for all phases have been tabulated in this

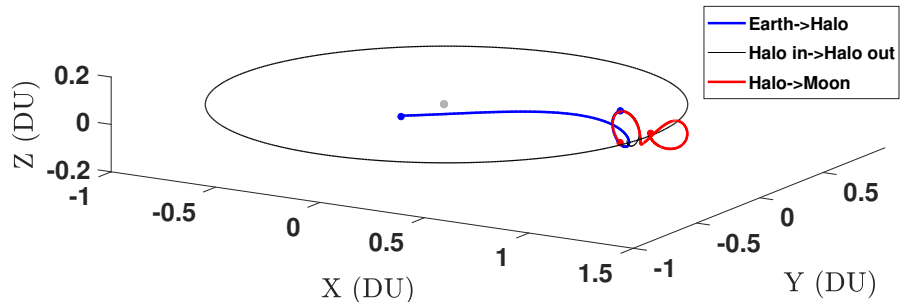

(a) $\lambda_0 = 32\ ^\circ$

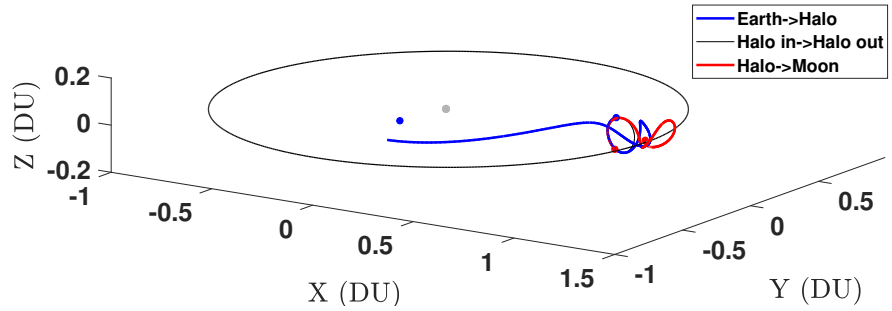

(b) $\lambda_0 = 126\ ^\circ$

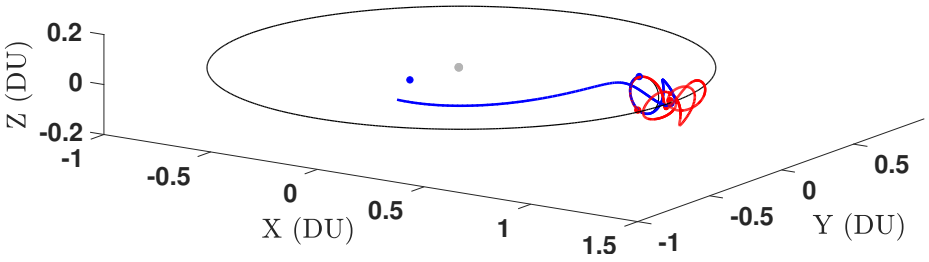

(c) $\lambda_0 = 130\ ^\circ$

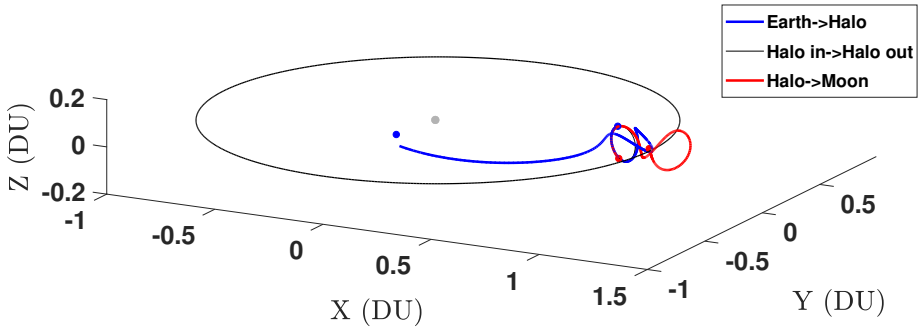

(d) $\lambda_0 = 136\ ^\circ$

Figure 5.10: Stable and Unstable manifold behavior in BCP - Candidate Cases.

section.

5.1.4.1 Earth-Leg

The 'Earth-Leg' of the mission consists of the following intermediate phases. This phase is referred to as Phase 1 (see Table. 5.2 1A to $1C_C$). Table 5.15 gives the orbital parameters for the various intermediate orbits used in mission design, where a is the semi-major axis, e is eccentricity, i is inclination, ω is the argument of periapse, Ω is the right-ascension and ν is the true anomaly.

Table 5.6: Classical Orbital Elements of the waypoint Orbits.

Orbit	a (km)	e	i (rad)	ω (rad)	Ω (rad)	ν (rad)	Center
GTO	24364	0.7306	0.4712	0	3.1415	-	Earth
nGEO	41673.5	0.5932	0.4712	0	3.1415	-	Earth
Lunar Polar Orbit	2738	0	1.5700	3.6374	5.8039	-	Moon

Phase 1A: The important results of this leg are given in Table 5.7. Note that the final true longitude is set as a free variable in the problem formulation. The minimum-time transfer problem was formulated and solved using MEEs as the choice of element set. Figure 5.11 shows the transfer trajectory for the 'Earth-Moon' case, plotted in 3D space with respect to an Earth-Centered Inertial (ECI) frame. The trajectory consists of more than 48 revolutions around the Earth.

Table 5.7: Results - Phase 1A.

Parameter	**Earth-Moon**	**Earth-Moon-Sun**
Final Mass (m_f^{1A})	219.72 kg	219.72 kg
Time of Flight (t_f^{1A})	29.9787 days	29.9787 days
ΔV	1082.042 m/s	1082.042 m/s

Phase 1B: This is a coasting phase where the spacecraft would be involved in a range of activities like orbit estimation experiments, high altitude SSA and calibration of solar electric propulsion

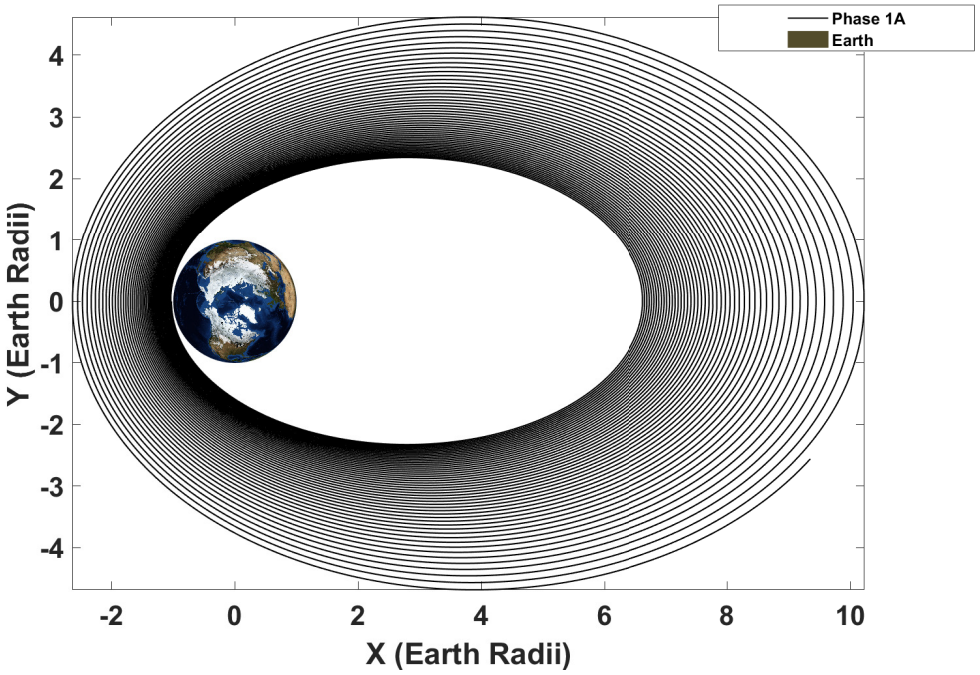

Figure 5.11: Phase 1A - Minimum-time Trajectory - ECI frame.

performance during Phase 1A. For this paper, the spacecraft is allocated a 30 day coast in nGEO. Final mass is $m_f^{1B} = 219.72$ kg, where no propellant burns are performed in nGEO.

Phase $1C_A$: The transfer in this phase was split into two separate sub-phases. The first being a minimum-time, free final longitude transfer from the nGEO to a circular orbit with a radius equal to 0.9 times the radius of the manifold patch-condition, whereas the second sub-phase is a transfer from an appropriate point on the trajectory of the first phase to the 'Earth-Leg' manifold patch-condition. The formulation for the first sub-phase was similar to Phase 1A while the second phase was formulated and solved as a CR3BP in a barycentric synodic frame. The combined results for Phase $1C_A$ are given in Table 5.8.

Figure 5.12 shows a 3D plot of both sub-phases of the transfer in Phase $1C_A$ for the 'Earth-Moon' case. Sub-phase 1 is a 33.241 day long spiral out to the selected point on the transfer to an intermediate circular orbit whereas sub-phase 2 is a 18.414 day transfer.

Table 5.8: Results - Phase 1C$_A$.

Parameter	**Earth-Moon**	**Earth-Moon-Sun**
Final Mass ($m_f^{1C_A}$)	184.763 kg	185.074 kg
Time of Flight ($t_f^{1C_A}$)	51.655 days	51.195 days
ΔV	2123.99 m/s	2103.22 m/s

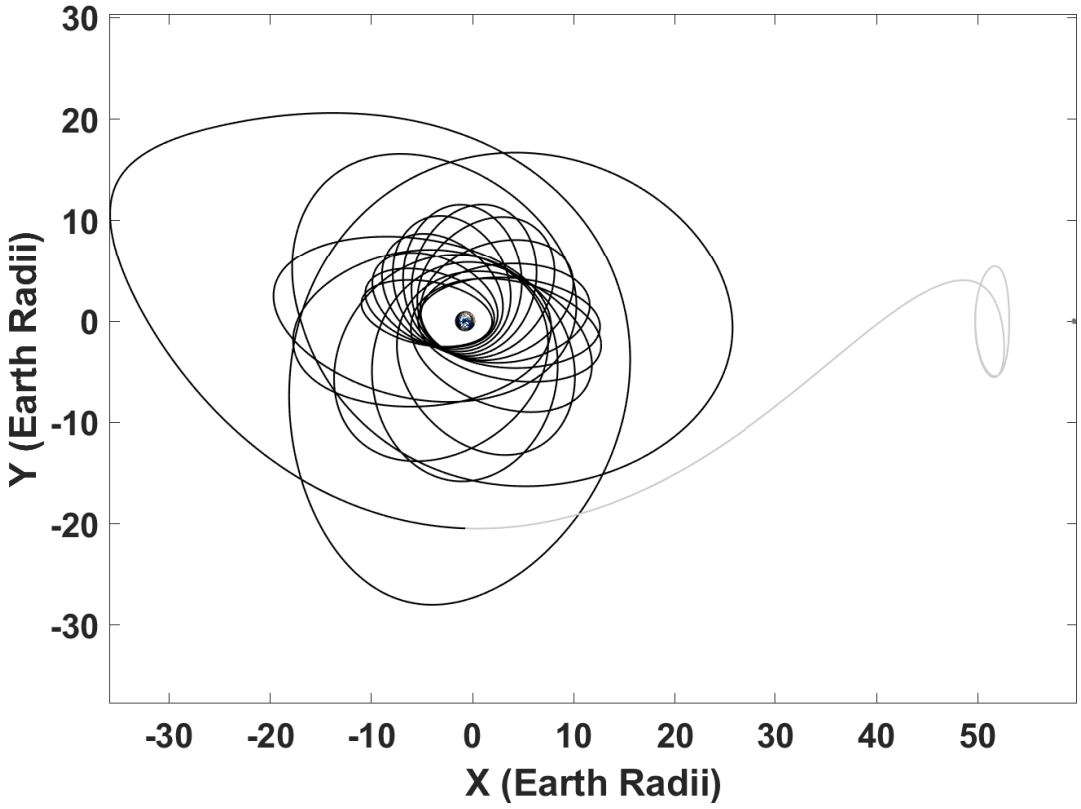

Figure 5.12: Phase 1C_A - Minimum-time Trajectory - Synodic frame.

Phase $1C_B$: This is the second coasting phase of the mission. In this phase, the spacecraft coasts on the selected stable manifold of the halo orbit. The manifold transitions the spacecraft to a state in a close vicinity of a point on the particular halo orbit. The results for this phase are provided in Table 5.9. The red curve in Figure 5.13 shows the coasting trajectory of Phase $1C_B$ for the 'Earth-

Table 5.9: Results - Phase $1C_B$.

Parameter	**Earth-Moon**	**Earth-Moon-Sun**
Final Mass ($m_f^{1C_B}$)	184.763 kg	185.074 kg
Time of Flight ($t_f^{1C_B}$)	26.098 days	13.904 days
ΔV	0 m/s	0 m/s

Moon' case (CR3BP dynamics). Since the manifold has been generated by introducing a small perturbation to a fixed-point on the halo orbit, the manifold slowly winds onto the halo orbit. For the 'Earth-Moon-Sun' case, the dynamics are faster as periodicity has been lost due to the added perturbation from the Sun and therefore reduces the coast-time while at the same time replicating the CR3BP manifold patch-condition.

Phase $1C_C$: A minimum-time transfer from the manifold final condition to the left-most point (as seen from Earth) on the halo Orbit is solved in this phase. The formulation, similar to Phase $1C_A$, is in the cislunar space. It is a relatively quick transfer. The results are provided in Table 5.12. The black curve in Figure 5.14 depicts the min-time trajectory of Phase $1C_C$ for the 'Earth-Moon' case.

Table 5.10: Results - Phase $1C_C$.

Parameter	**Earth-Moon**	**Earth-Moon-Sun**
Final Mass (m_f^{2A})	182.886 kg	183.198 kg
Time of Flight (t_f^{2A})	2.774 days	2.772 days
ΔV	125.183 m/s	124.876 m/s

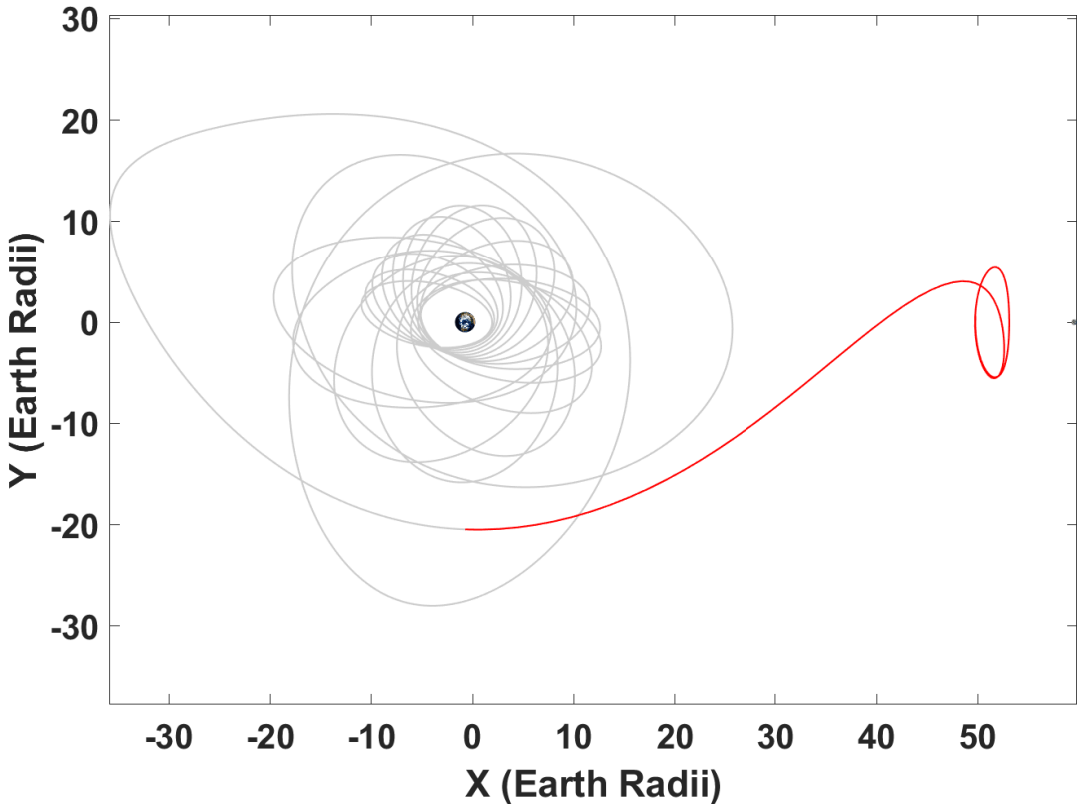

Figure 5.13: Phase 1C_B - Minimum-time Trajectory - Synodic frame

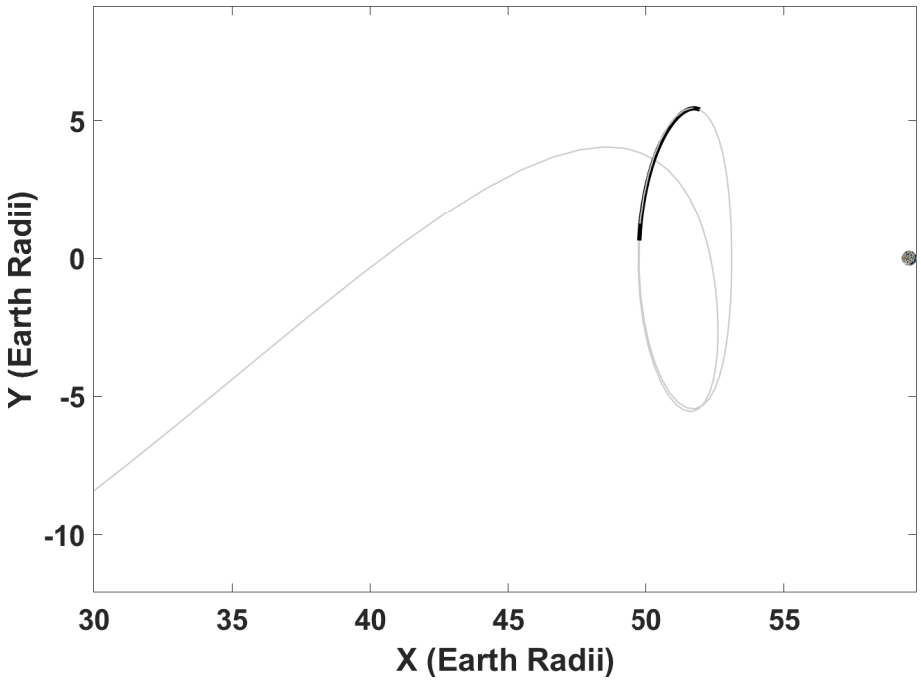

Figure 5.14: Phase 1C_C - Minimum-time Trajectory - Synodic frame.

5.1.4.2 Summary - Earth Leg

Table 5.11 summarizes Phase 1 of the mission referred to as the 'Earth-Leg' in this paper. The entire phase provides a piece-wise minimum-time transfer trajectory from a point on the GTO to the left-most point on the selected halo orbit.

Table 5.11: Summary - Phase 1, Earth Leg.

Parameter	**Earth-Moon**	**Earth-Moon-Sun**
Initial Mass (m_0^1)	240 kg	240 kg
Final Mass (m_f^1)	182.886 kg	183.198 kg
Total Time of Flight (t_f^1)	140.506 days	127.849 days
Total Coast time (t_C^1)	56.098 days	43.904 days
Total Thrusting time (t_P^1)	83.598 days	83.945 days
Total ΔV	3331.215 m/s	3310.138 m/s

5.1.4.3 Moon-Leg

The 'Moon-Leg' of the mission is referred to as Phase 2 (see 2A to 2C in Table 5.2).

Phase 2A: Results for Phase 2A give a time-optimal transfer from the top-most point of the halo orbit to the initial condition defined in Table 5.3. The results are tabulated in Table 5.12. The solid black curve in Figure 5.15 depicts the min-time trajectory for Phase 2A.

Table 5.12: Results - Phase 2A.

Parameter	**Earth-Moon**	**Earth-Moon-Sun**
Final Mass (m_f^{2A})	180.526 kg	180.798 kg
Time of Flight (t_f^{2A})	3.487 days	3.547 days
ΔV	159.196 m/s	161.673 m/s

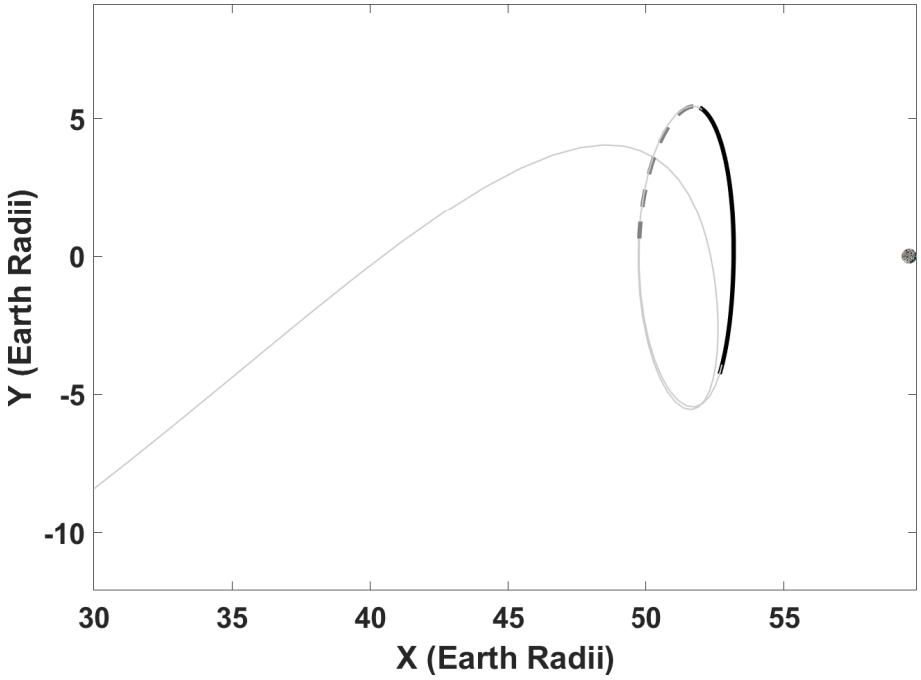

Figure 5.15: Phase 2A - Minimum-time Trajectory - Synodic frame.

Phase 2B: This phase includes coasting on the 'Moon-Leg' manifold up to the final condition defined before. Results are presented in Table 5.13. The solid red curve is the coast trajectory Phase 2B, while the dashed grey curve depicts the previous Phase 2*A* in Figure 5.16.

Table 5.13: Results - Phase 2B.

Parameter	**Earth-Moon**	**Earth-Moon-Sun**
Final Mass (m_f^{2B})	180.526 kg	180.798 kg
Time of Flight (t_f^{2B})	29.616 days	17.3524 days
ΔV	0 m/s	0 m/s

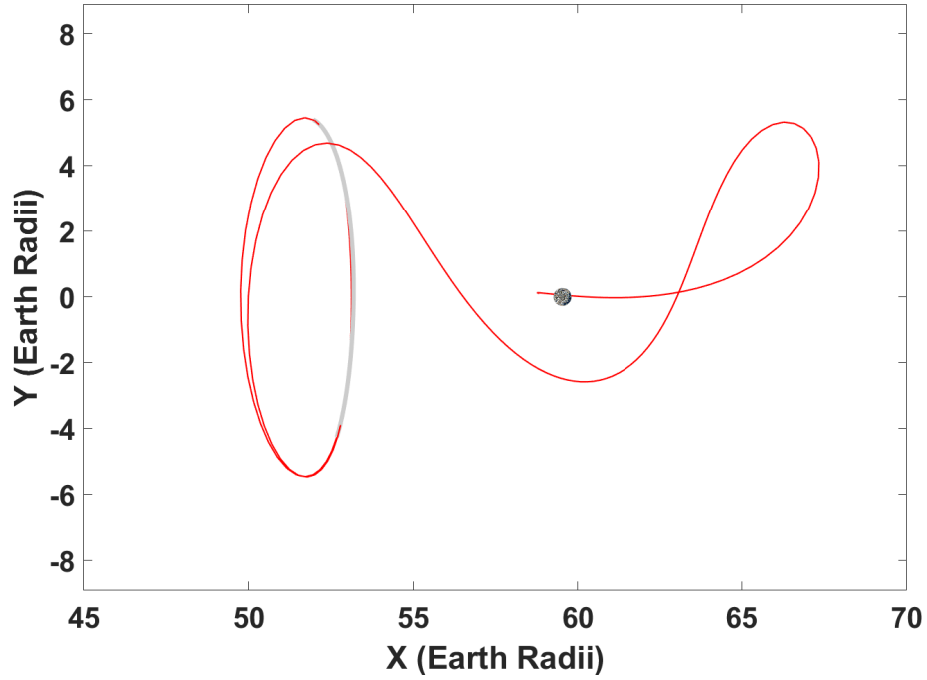

Figure 5.16: Phase 2B - Minimum-time Trajectory - Synodic frame.

Phase 2C: The final phase of the mission is a powered phase, which takes the spacecraft from the

manifold FC and inserts it into a circular Lunar Polar Orbit of 1000 km altitude. The TPBVP was formulated and solved in a Moon Centered Inertial (MCI) frame using the set of MEEs. Results of this phase are provided in Table 5.14. The transfer trajectory for the final phase is plotted in MCI frame and Barycentric Synodic frame. (see Figure 5.17 & 5.18 respectively). In Figure 5.18, the grey curve denotes the unstable manifold whereas, the black curve denotes the transfer to the Lunar Polar Orbit as seen from a BCS frame.

Table 5.14: Results - Phase 2C.

Parameter	**Earth-Moon**	**Earth-Moon-Sun**
Final Mass (m_f^{2C})	165.111 kg	165.402 kg
Time of Flight (t_f^{2C})	22.778 days	22.749 days
ΔV	1093.538 m/s	1090.860 m/s

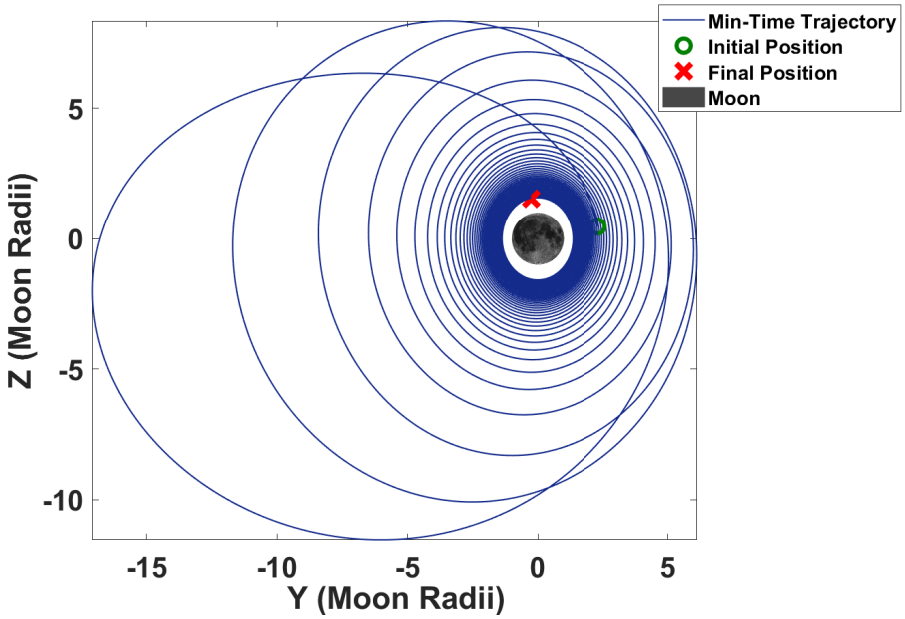

Figure 5.17: Phase 2C - Minimum-time Trajectory - MCI frame.

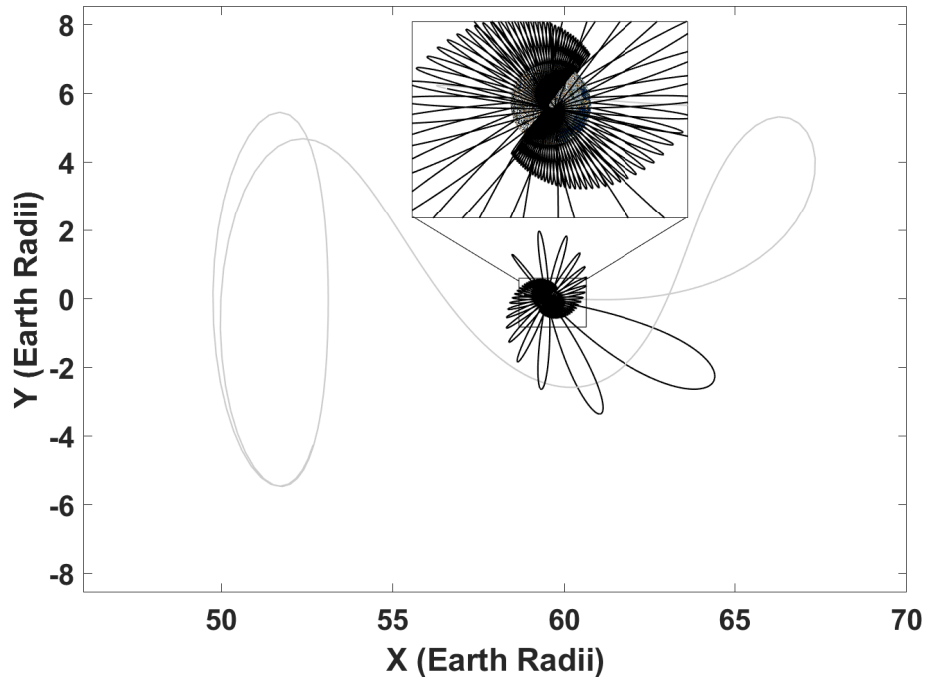

Figure 5.18: Phase 2C - Minimum-time Trajectory - Synodic frame.

5.1.4.4 End-To End Trajectory Plots

Figures 5.19 and 5.21 show the final piece-wise, minimum-time trajectory from the selected GTO to a 1000 km circular lunar polar orbit, plotted in the ECI and BCS frames respectively. Note that the red curves represent the coasting phases (nGEO and manifold legs) while the black curves denote the powered phases except the lunar capture phase which is denoted by the blue curve. EM stands for 'Earth-Moon' and describes the gravitational effects considered in the dynamics.

Figures 5.20 and 5.22 show the final piece-wise, minimum-time trajectory from the selected GTO to a 1000 km circular lunar polar orbit, plotted in the ECI and BCS frames, respectively. Similar to the previous set of plots, the red curves represent the coasting phases (nGEO and manifold legs) while the black curves denote the powered phases except the lunar capture phase which is denoted by the blue curve. EMS stands for 'Earth-Moon-Sun'.

The ECI plots elegantly captures the different behavior of the manifold dynamics in the presence of the BCP model as compared to the CR3BP assumption. It is also noticeable, that in the

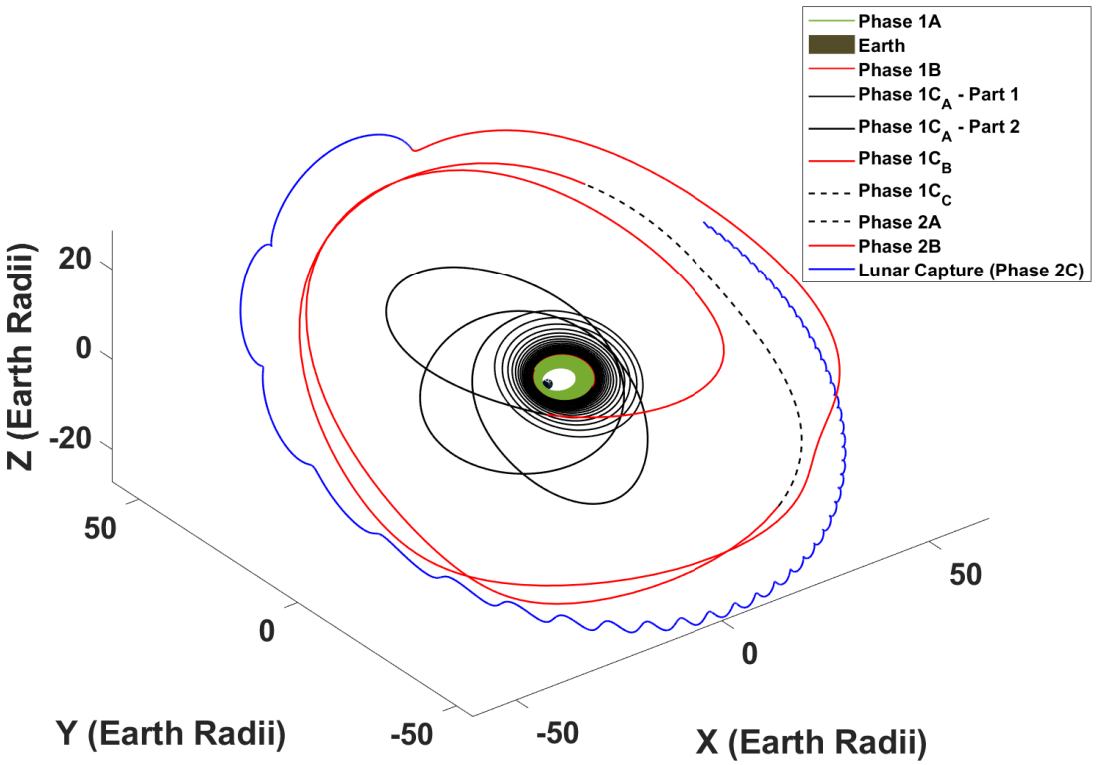

Figure 5.19: Full trajectory (EM) in the ECI frame.

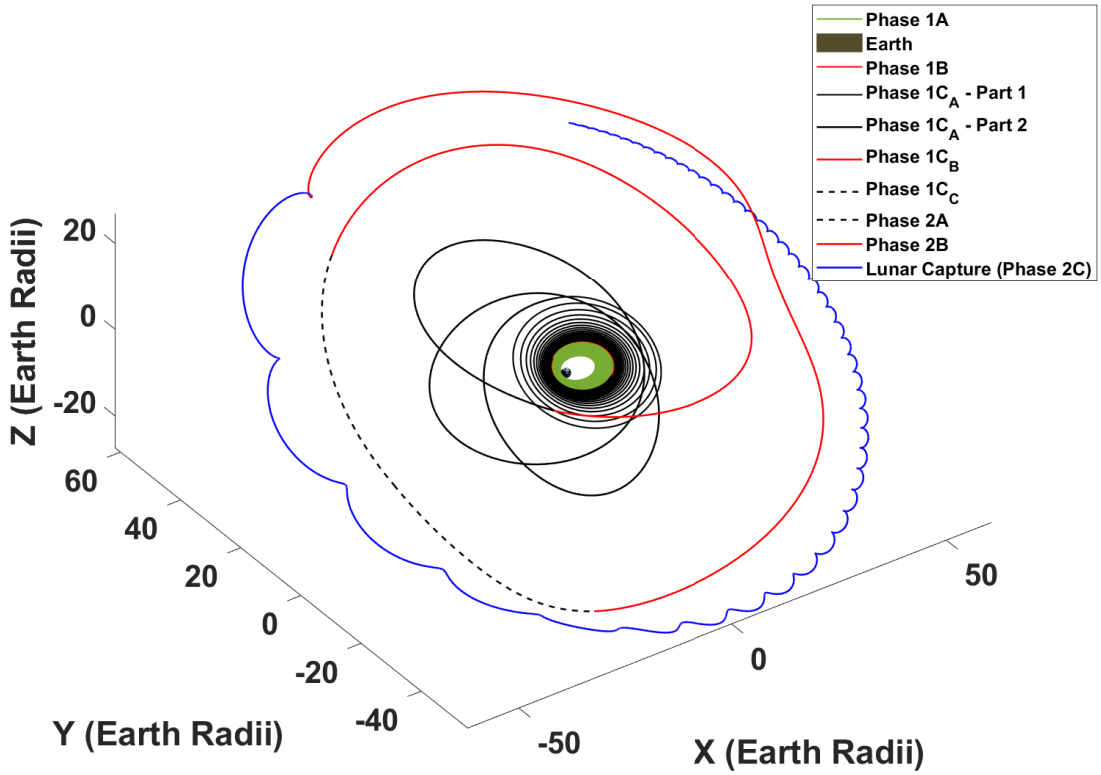

Figure 5.20: Full trajectory (EMS) in the ECI frame.

BCS plots, the manifolds of the CR3BP make multiple winding revolutions around the halo orbit before reaching the target state whereas, in the BCP dynamics the manifolds are faster and reach the target state sooner. This is attributed to the fact that the Halo orbit maintains periodicity only in the same dynamical model that was used to differentially correct the orbit to achieve periodicity in the first place.

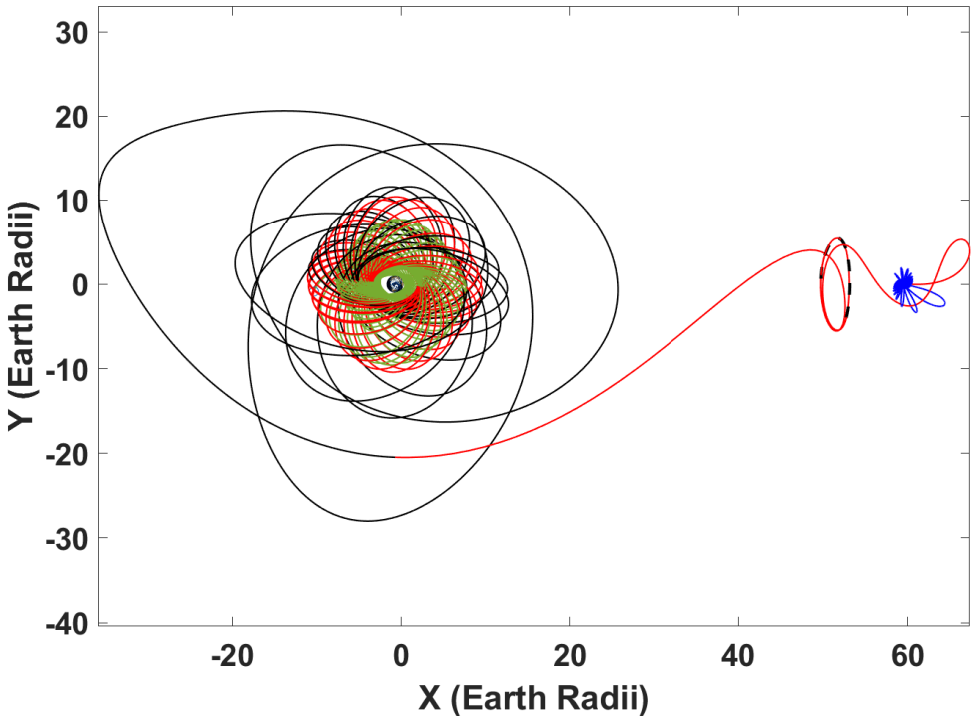

Figure 5.21: Full Trajectory (EM) in the BCS frame.

5.2 Case B

This case describes a transfer which leverages pre-computed manifolds in a HFM by propagating the initial conditions of trajectories in the manifold bundle computed in CR3BP in the presence of HFM dynamics. HFM for this case indicates that graviational effects from the Earth, Sun, Moon and Jupiter were included in the dynamics. The initial EPO is a super GTO (sGTO)

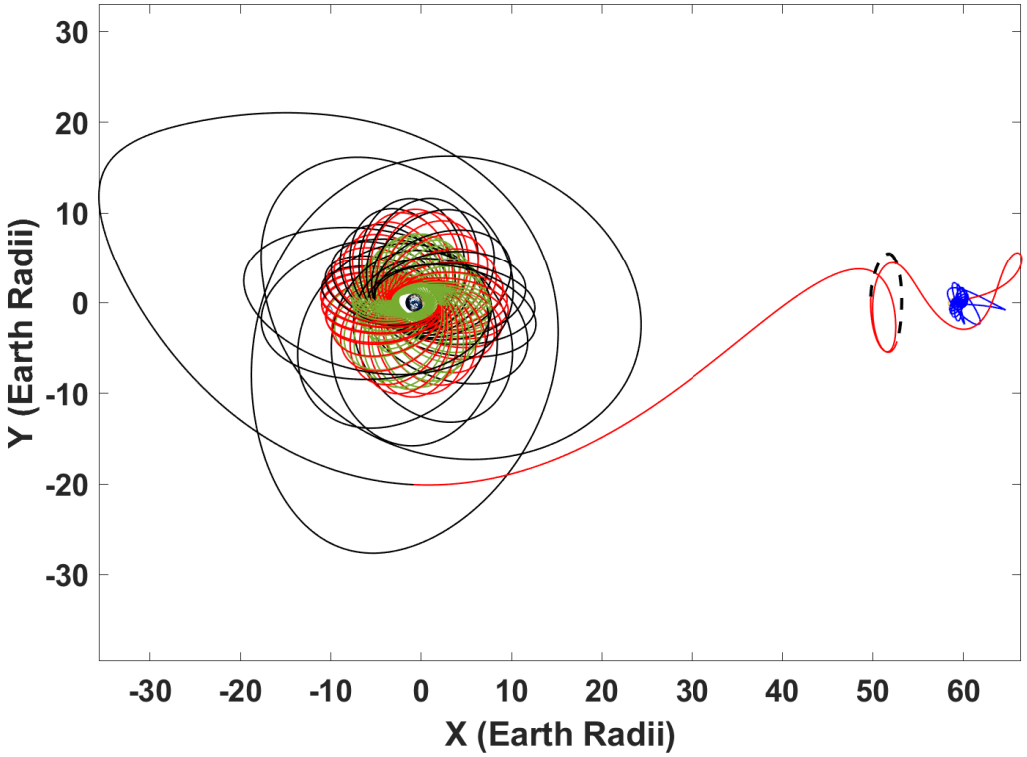

Figure 5.22: Full Trajectory (EMS) in the BCS frame.

and the terminal orbits are candidates from the Southern L_2 Near Rectilinear Halo Orbit (NRHO) in the Earth-Moon system.

5.2.1 Problem Description and Mission Parameters

The sGTO parameters (defined in Table 5.15) were selected to be representative of that class of orbit, but do not hold a very specific meaning, and the method proposed will work for other sGTOs with different parameters. First, a direct transfer from the sGTO to the NRHO was solved, followed by a solution for the analogous transfer using the selected HFM stable manifolds. This approach elucidates the advantages gained by leveraging the fuel-saving from coasting on the manifold. The considered problem falls in the class of transfers known as the minimum-time rendezvous transfers. The TPBVP was solved using a single-shooting solution scheme with MATLAB's built-in *fsolve* function. The spacecraft was assumed to have an initial mass of 1000 kg, a thruster with I_{sp} = 1500 s and maximum thrust, T_{max} = 1 N. The transfers to the 9:2 NRHO (earmarked for the Lunar

Gateway) has been treated as a benchmark, whereas transfers to the other candidate NRHOs are also tabulated for comparison.

The solutions were obtained by using the *fsolve* routine of MATLAB where the state-costate dynamics propagation was performed using *mex*-compiled version of the *ode45* propagator [52]. The Algorithm used was *Levenberg-Marquardt* with both *OptimalityTolerance* and *StepTolerance* set as 1.0×10^{-12}. Additionally, the homotopy method typically required $\approx$ 20 steps for all the solutions portrayed in the this section.

Table 5.15: Classical orbital elements of the sGTO.

Orbit	a (km)	e	i (°)	Ω (°)	ω (°)	ν (°)	Center
sGTO	44364	0.65	27	11.3044	0	0	Earth

5.2.2 CR3BP Manifolds of the NRHOs

In this section, we describe particulars about the manifolds of a NRHO in the CR3BP system. In particular, we focus on stable manifold bundles since our objective for Case B is to get captured in a NRHO after starting out in a sGTO.

5.2.2.1 Stable Manifold Bundles

In order to obtain a target state on a selected stable manifold for the NRHO-bound trajectories, the methodology followed was similar to the one in [112]. Appropriate manifold trajectories were computed and used as initial guesses for optimization of Earth-bound and NRHO-bound trajectories using the CR3BP model. Each NRHO was divided into 1000 discrete points. The stable manifold for the three candidates selected for this work are propagated until they intersect the $Y - Z$ plane of the CR3BP synodic frame at $x = -\mu$, corresponding to a plane through the Earth and henceforth called the 'Earth plane'. Figures 5.23-5.25 depict the stable manifold orbits and the respective dispersion of candidate manifold states for the three NRHOs selected for analysis.

It is hereby noted these discrete points in fact represent closed curves since they approximately lie on the manifold surface as it crosses the plane, but points were chosen to indicate the discrete trajectories that generated them, based on the approximation discussed earlier. The state markers (pentagram) represent the piercing points, i.e., the intersection of the family of separatrix trajectories with the $Y - Z$ plane containing the Earth in the CR3BP. The dispersion of piercing points are insightful towards picking initial conditions on the manifolds since they are potential target states for low-thrust trajectory design.

The piercing points intersecting the negative Y half- Earth plane in the CR3BP are more favorable due to being closer to the Earth. Such intersecting points, in general, require fewer spirals while transferring from the sGTO as compared to the piercing points in the positive Y half-plane. Other considerations include differences between eccentricity and inclination of the piercing points (when viewed as target points within an Earth-centered inertial (ECI) frame) relative to those of the sGTO or other intermediate geocentric orbit conditions.

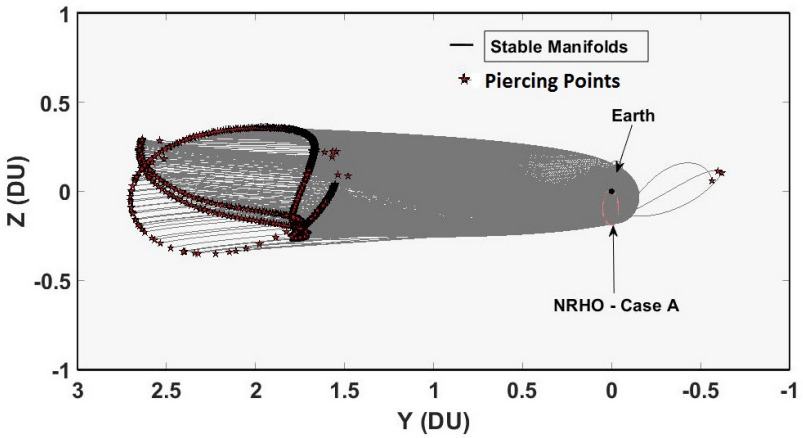

Figure 5.23: Dispersion of piercing points - 9:2 NRHO.

Various phase plots were also generated to characterize the eccentricity, inclination and radius with respect to the ECI reference frame for the manifold piercing points. In particular, the 'eccen-

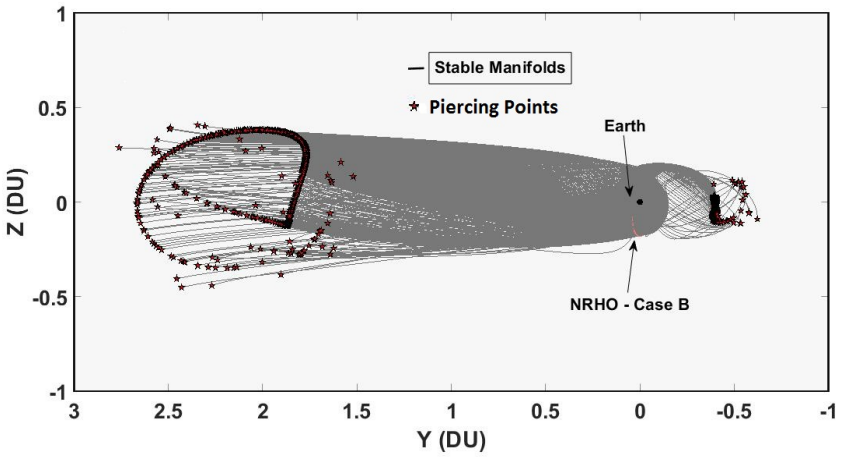

Figure 5.24: Dispersion of piercing points - 24:5 NRHO.

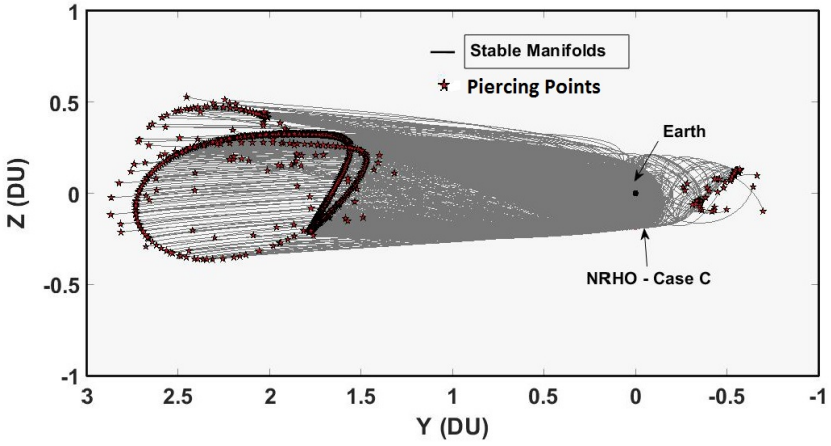

Figure 5.25: Dispersion of piercing points - 4:1 NRHO.

tricity vs. inclination (e vs. i)' and 'eccentricity vs. radius (e vs. r)' plots provide design insights into selection of the best condition depending on the intermediate geocentric orbit parameters. This enables mission designers to select a manifold trajectory that has piercing point conditions closest to those of the initial orbit, thus requiring less propellant consumption for the transfer.

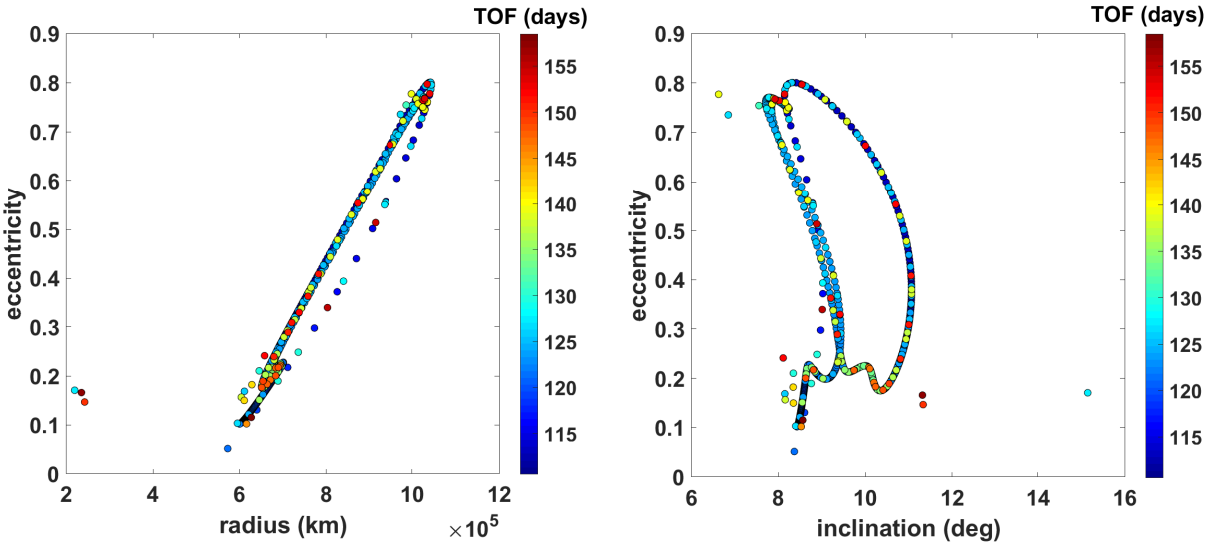

(a) e vs. r phase portrait. (b) e vs. i phase portrait

Figure 5.26: Piercing points - stable manifold phase plots - 9:2 NRHO.

Figures 5.26-5.28 depict the e vs. i and e vs. r phase portraits for the three candidate NRHOs, respectively. The color bar depicts the respective time of flight (in days) for the piercing points to the respective NRHO, i.e., the time spent on the manifold. Observe that favorable states are generally expected to have a small radius with respect to the Earth's center as well as a small absolute variation from the sGTO inclination and eccentricity. It can be deduced that the cluster of piercing points on the left-hand side of the e vs. r plots are potentially favorable.

Considering only the favorable clusters on these phase plots, certain bounds on the eccentricity and inclination can be observed. For the 9:2 resonant NRHO, favorable eccentricity belong to the range $(0, 0.2)$ and the corresponding inclinations lie between $(8, 16)°$. Similarly, the 24:5 resonant NRHO, the eccentricity of such cases lie within $(0, 0.4)$ and the corresponding inclina-

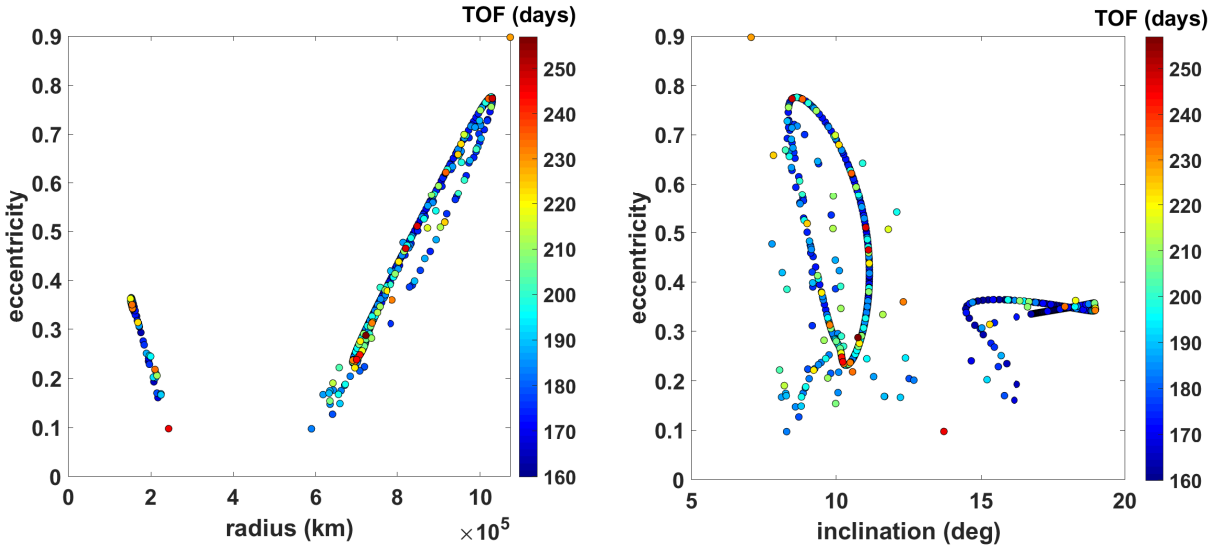

(a) e vs. r phase portrait (b) e vs. i phase portrait

Figure 5.27: Piercing points - stable manifold phase plots - 24:5 NRHO.

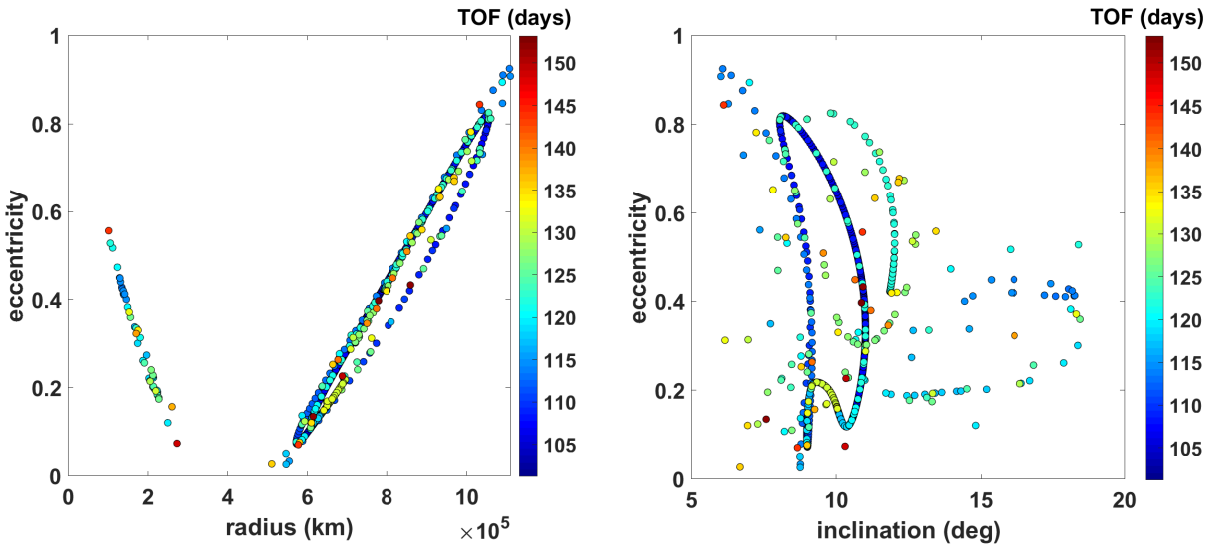

(a) e vs. r phase portrait. (b) e vs. i phase portrait.

Figure 5.28: Piercing points - stable manifold phase plots - 4:1 NRHO.

tions lie within $(6, 20)^\circ$. Finally, the 4:1 NRHO has favorable eccentricity between $(0, 0.6)$ while their corresponding inclinations lie between $(6, 20)^\circ$. Therefore, starting from an sGTO with an initial inclination of 27°, the most favorable case would be the one with the highest inertial inclination among all candidates for all three NRHOs. It is worthwhile to note that the aforementioned heuristic method of establishing favorable conditions is robust in that the cluster of piercing points correspond to a wide range of eccentricity and inclination with respect to the Earth's equatorial plane, with the choice depending on the initial departure orbit.

The transfer time is another consideration that should be taken into account. In an exact sense, trajectories on the invariant manifold take infinite time to wind off the orbit. However, the common approach of using finite offsets from the orbit along the eigenvectors has been used, which results in a finite departure time. However, due to the inherent near-stable nature of the NRHOs, the manifolds of these orbits take a long time in unwinding off the orbit starting from the reference state when compared to other Halo orbits, at least in the simplified CR3BP dynamics. The stable manifold transfer time can be on the order of multiple months. Based on the insights discussed above on the candidate NRHO stable manifold behavior, a best case piercing point was chosen for each case. These points' position and velocity, relative to the synodic frame centered at the Earth-Moon barycenter, are listed in Table 5.16. Moreover, the time of flight on the manifold is also given. Note that these coordinates become the target coordinates from the sGTO / intermediate orbit.

Table 5.16: Stable manifold ICs (CR3BP).

Case	NRHO	x (DU)	y (DU)	z (DU)	v_x (VU)	v_y (VU)	v_z (VU)	TOF (days)
A	9:2	-0.01215	-0.56415	0.05927	0.81277	0.05946	0.33727	127.5501
B	24:5	-0.01215	-0.38464	-0.06357	1.38527	0.03979	-0.51380	218.9349
C	4:1	-0.01215	-0.25881	0.03475	2.10252	-0.35388	-0.27859	144.1548

5.2.3 CR3BP Manifolds propagated in HFM

In the subsequent sections, the manifold conditions selected based on the phase-plot analysis of their behaviour in the CR3BP, have been studied in the HFM to characterize their real dynamics. Using a HFM requires the use of ephemerides to compute the position of the perturbing bodies relative to the Earth.

In this work, it was observed that the invariant manifolds of low-energy periodic orbits like the NRHOs experience a much faster dynamical behavior in the HFM, i.e., the time taken to reach the piercing plane was much lower when compared to the CR3BP. Part of this result can be attributed to a faster departure from the original orbit as a result of the additional perturbations introduced in the HFM. A state exactly on the orbit in the CR3BP would remain on the orbit indefinitely, but in a model with further perturbations will no longer remain periodic. Similarly, the initial departure of the manifolds in the CR3BP can be expected to take longer if additional perturbations were present. This faster transfer to the piercing plane makes these manifolds more interesting as long terminal coast arcs.

Unlike the CR3BP, with the introduction of ephemeris, the dynamics become non-autonomous. The purpose of this analysis is to find the best 'insertion date', which is defined by the epoch associated with the final condition on the stable manifold, such that the coast arc winds off in the Earth vicinity. Similarly, for the unstable manifold, the best 'departure date', defined by the epoch associated with the initial condition on the unstable manifold is of interest such that the coast arc winds off in the Earth vicinity.

5.2.3.1 Stable Manifolds in HFM

The selected CR3BP stable manifold conditions reported in Table 5.16 were propagated in HFM dynamics. The propagation was performed with initial epochs spaced 2 days apart for dates in the year 2022, starting Jan 1, 2022 00:00:00 in the ECI frame. The stable manifold was propagated backwards in time for 80 days starting at each epoch date. The various insertion dates were segregated based on the minimum radius that the stable manifold achieves along the trajectory.

The manifold trajectories were plotted both in the ECI and Earth-Moon barycentric synodic frame (BCS).

Figures 5.29a–5.29f show the ECI and BCS frame plots of the best cases selected for the NRHO stable manifolds. To select the best cases, they were first sorted by increasing minimum radius, and then ones with significantly higher TOF were excluded. The four best cases for the 9:2 NRHO, five best cases for the 24:5 NRHO and five best cases for the 4:1 NRHO are shown. The individual manifolds selected for designing minimum-time and minimum-fuel NRHO-bound trajectories to each NRHO orbit are summarized in Table 5.17.

Table 5.17: Selected stable manifolds (HFM).

Case	NRHO	NRHO Insertion Epoch	Manifold TOF (days)
A	9:2	August 21, 2022 00:00:00	57.726
B	24:5	May 1, 2022 00:00:00	57.422
C	4:1	September 22, 2022 00:00:00	58.862

5.2.4 Results

This section will be classified into two subsections namely, 'NRHO-bound, Time-Optimal Transfers' and 'NRHO-bound, Fuel-Optimal Transfers' where the two subsections deal with trajectories to travel from sGTO-NRHO using time- and fuel-optimal trajectories.

5.2.4.1 NRHO-bound Time-Optimal Transfers

A direct transfer from the designated sGTO to a state on the 9:2 NRHO with the most negative Z value is presented in this section. This particular choice represents the apoapsis of the NRHO, and was chosen to limit the scope of the work while still providing a reference for comparison to manifold transfers. This transfer is compared with the minimum-time solution to an NRHO state via the selected stable manifold. Figure 5.30 depicts the direct transfer in both the ECI (left subplot) and BCS (right sub-plot) frames. Figure 5.31 depicts transfer via manifold in both ECI and BCS frames.

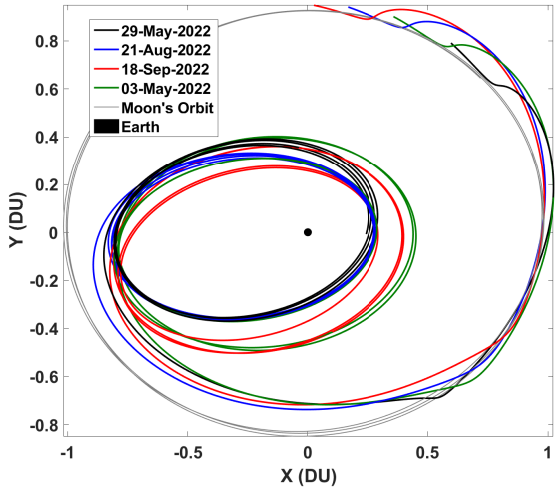

(a) 9:2 NRHO stable manifolds in ECI.

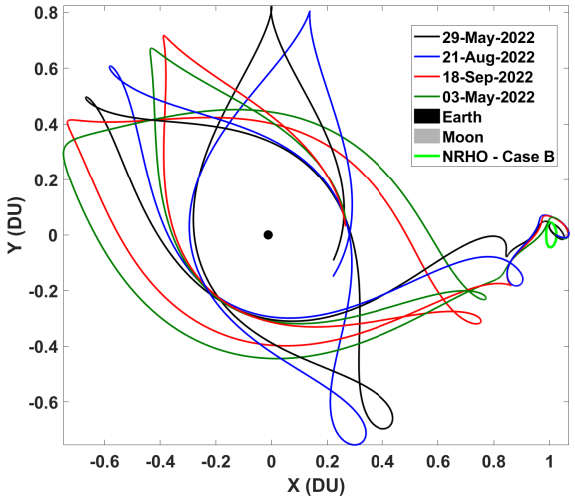

(b) 9:2 stable manifolds in BCS.

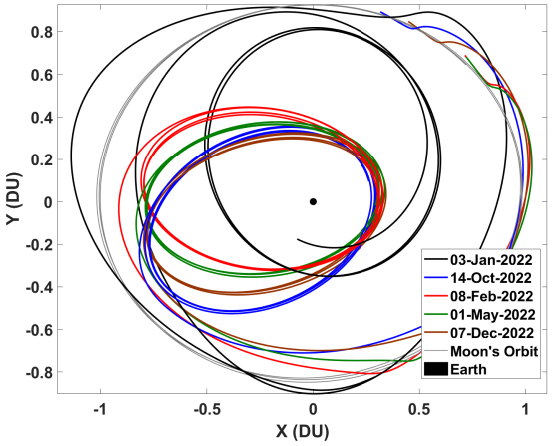

(c) 24:5 NRHO stable manifolds in ECI.

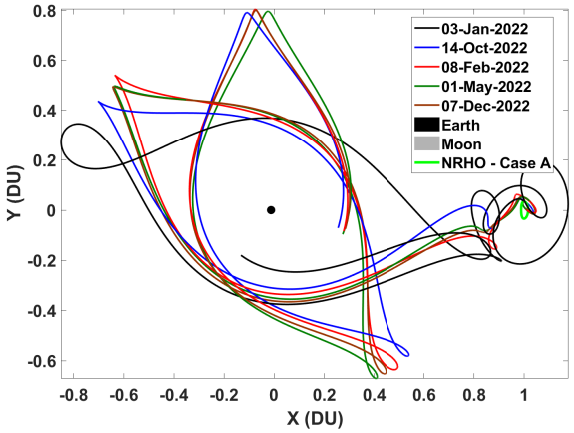

(d) 24:5 NRHO stable manifolds in BCS.

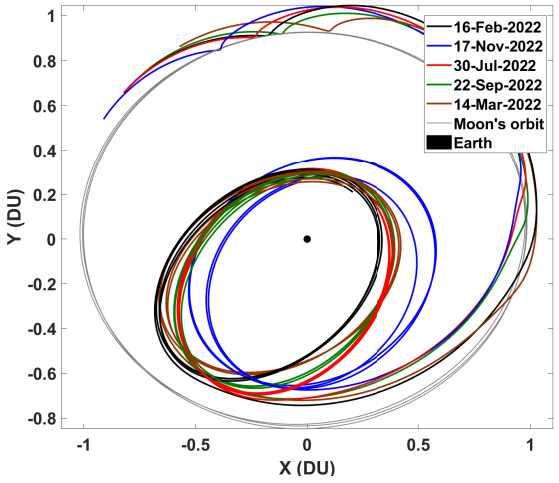

(e) 4:1 stable manifolds in ECI.

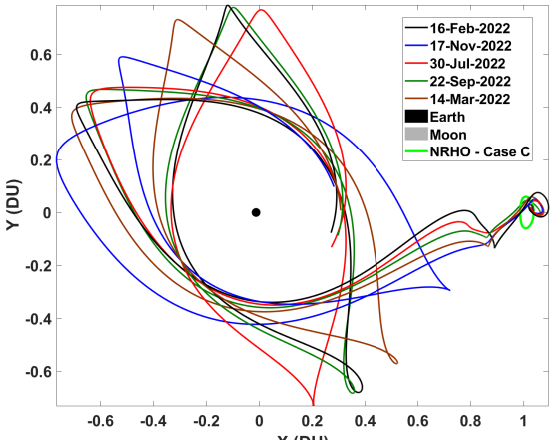

(f) 4:1 stable manifolds in BCS.

Figure 5.29: NRHO - CR3BP stable manifolds in HFM; Sense of motion is counter-clockwise from Earth-vicinity to respective NRHOs.

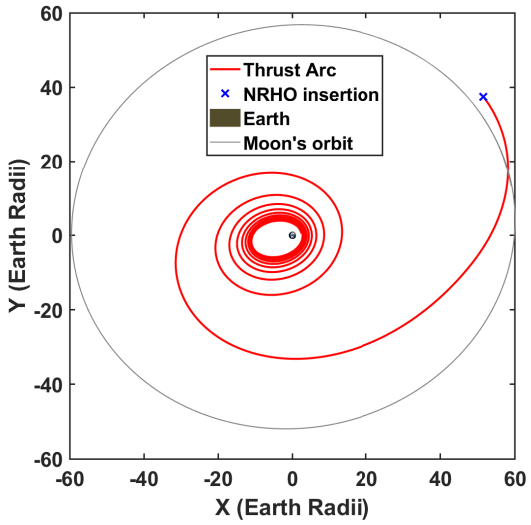

(a) Minimum-time trajectory in ECI.

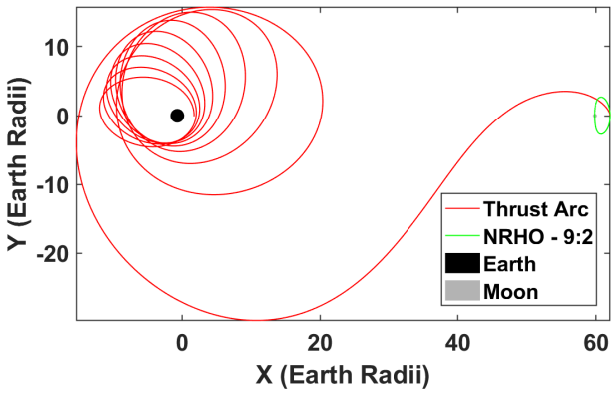

(b) Minimum-time trajectory in BCS.

Figure 5.30: sGTO - 9:2 NRHO : Minimum-time 'direct' transfer trajectories.

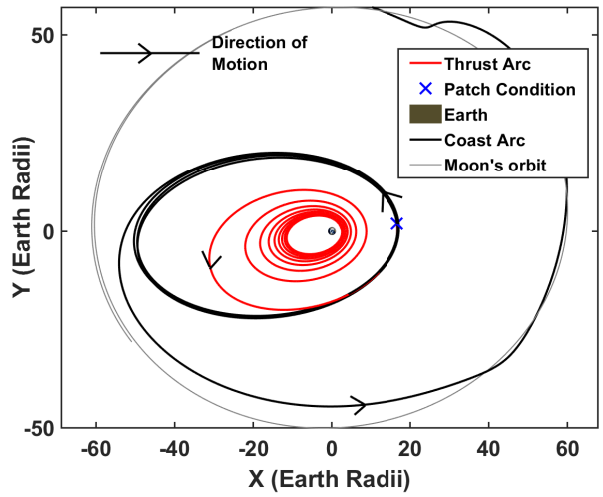

(a) Minimum-time trajectory in ECI.

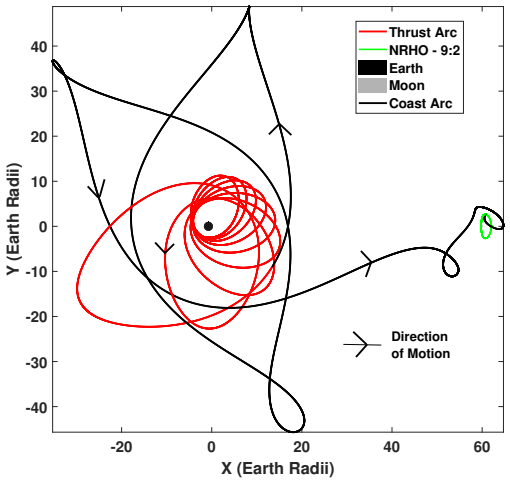

(b) Time-optimal Trajectory in BCS.

Figure 5.31: sGTO - 9:2 NRHO : Minimum-time leveraging stable manifolds.

Table 5.18 summarizes the results for all the minimum-time transfers to the candidate NRHOs, starting from the specified sGTO. The reported times denote the total time. A fuel savings of $\sim$ 586 - 860 m/s was observed by coasting on the respective stable manifold, instead of a direct flight, at the expense of a longer flight time by $\sim$ 58 days. The results clearly elucidate the fuel savings achieved by leveraging the coast phase on the respective stable manifolds. The total thrusting time (t_P) is defined as the time when the thruster is ON, while the total coast time (t_C) is the time when thruster is OFF.

The performance of the minimum-time transfers (for both direct as well as manifold-aided ones) are comparable to those found in literature. Ozimek and Howell studied low-thrust transfers from a 20,000 km circular Earth orbit to various low-energy orbits near the Moon, using engines with similar order of magnitude performance to the one considered here [113, 114]. Specifically, for a transfer to the 14-day L_2 butterfly orbit, they report the powered time $\approx$ 33 days as well as manifold coast $\approx$ 50 days.

Table 5.18: Summary - Minimum Time Transfers. D=Direct, M=Manifold.

Parameter	**9:2 D**	**9:2 M**	**24:5 D**	**24:5 M**	**4:1 D**	**4:1 M**
Initial Mass (m_0), kg	1000	1000	1000	1000	1000	1000
Final Mass (m), kg	829.49	876.63	829.85	879.97	828.89	862.58
Total TOF (t_f), days	29.026	78.728	28.964	77.854	29.127	82.254
Coast time (t_C), days	-	57.726	-	57.422	-	58.862
Thrusting time (t_P), days	29.026	21.002	28.964	20.432	29.127	23.392
Total ΔV, m/s	2749.54	1936.49	2743.08	1880.61	2760.12	2174.11

As evident in Table 5.18, even without explicitly optimizing efficiency with respect to fuel or velocity impulse, performing minimum-time transfers to the nearest point on the manifold and coasting to the target state results in substantial reductions in propellant mass. The question naturally arises: What further savings are possible if minimum-fuel transfers onto the manifold were explicitly designed? This question has been answered in the next section.

5.2.4.2 *NRHO-Bound, Fuel-Optimal Transfers*

The next step was to augment these minimum-time results by quantifying the anticipated further fuel savings by solving for minimum-fuel trajectories to the manifold patch condition, which would be followed by the coast on the manifold. In order to fix the TOF, as mentioned in section 5.3, a scalar multiplier, $\alpha > 1$ is applied to the TOF of the time-optimal solution and the resulting TPBVP is solved. A "diminishing-return" type analysis is then performed, comparing fuel-costs for different α and typically leads to a locally optimal solution for a TOF which is deemed feasible according to the mission profile. In this section, results for these trajectories and propellant requirements for each are presented. The thrust profile plots depict the time history of the switching function, SF. The engine switches ON when the value of the switching function is positive and switches OFF when the switching function is negative [50]. Similar to the discussion on the minimum-time transfers, minimum-fuel transfers for the 9:2 NRHO have been treated as benchmark and transfers to other NRHOs are tabulated for comparison.

A minimum-fuel transfer from the sGTO to the selected manifold condition (same as minimum-time solution) for the 9:2 NRHO is presented. To recap, the chosen stable manifold condition led to a arrival epoch at the NRHO of 'August 21, 2022' with a 57.726 coast time. Figure 5.32 shows the solution plotted in the ECI and BCS frames.

The total transfer time increases to 93.198 days for the minimum-fuel transfer as compared to 78.728 days of the minimum-time solution with both transfers leveraging manifolds. Figure 5.33 depicts the evolution of the switching function (SF) with time, which determines the engine 'ON-OFF' condition and therefore the optimal bang-off-bang thrust profile.

Table 5.19 summarizes the results for all the minimum-fuel transfers to the candidate NRHOs, starting from the sGTO. Additional fuel savings corresponding to a ΔV difference of $\sim$ 300-350 m/s was achieved by solving for bang-off-bang thrust profiles on the trajectory leading upto the respective stable manifold patch conditions, instead of a direct transfer, at the expense of a longer flight time by $\sim$ 12 - 15 days. Therefore, a minimum-fuel transfer leveraging manifolds can save $\sim$ 900 - 1000 m/s over the direct minimum-time transfer for the considered spacecraft parameters.

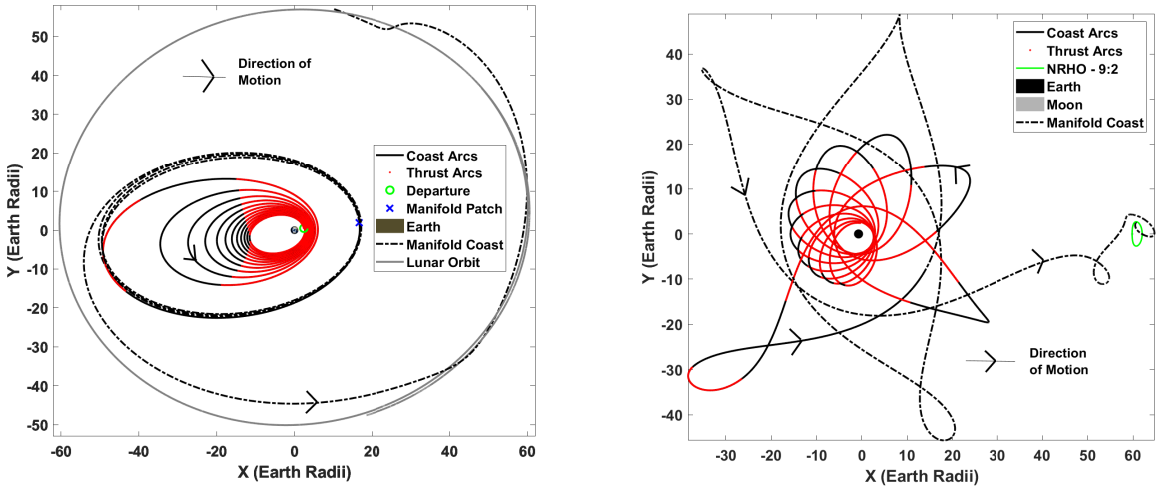

(a) Minimum-fuel trajectory in ECI.

(b) Minimum-fuel trajectory in BCS.

Figure 5.32: sGTO to 9:2 NRHO : minimum-fuel leveraging stable manifolds.

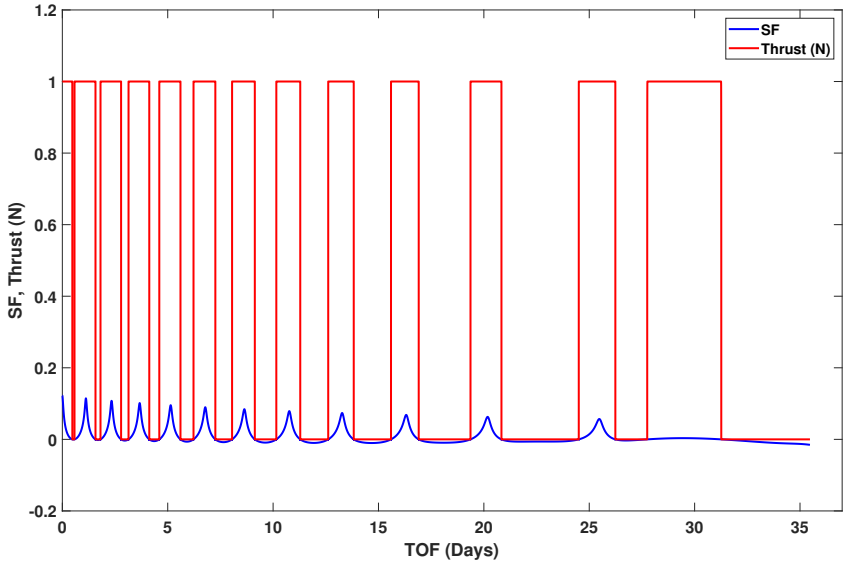

Figure 5.33: Thrust profile and SF for the minimum-fuel solution to 9:2 NRHO.

Note that $t_C = t_{C1} + t_{C2}$ and quantifies the total time for which the spacecraft coasts on the transfer trajectory and is a sum of coast-time on the selected manifold and coast arcs arising due to fuel-optimality criterion (i.e., $SF < 0$) of the 'pre-manifold' trajectory.

Table 5.19: Summary, MF_M = Minimum-Fuel via Manifold, All time parameters are in days.

Parameter	**9:2 MF_M**	**24:5 MF_M**	**4:1 MF_M**
Initial Mass (m_0), kg	1000	1000	1000
Final Mass (m_f), kg	900.51	902.65	889.59
Total Time of Flight (t_f), days	93.198	92.894	94.334
Total Coast (t_C)	75.175	74.583	75.835
Manifold Coast (t_{C1})	57.726	57.422	58.862
Pre-manifold Coast (t_{C2})	17.449	17.161	16.973
Total Thrusting time (t_P), days	18.023	18.311	18.499
Total ΔV, m/s	1540.76	1506.36	1720.69

5.3 Case C

The problem tackled in Case C includes all the complexities discussed before as it includes the class of fuel-optimal trajectories that are eclipse conscious and solved in a HFM. In particular, transfers from a sGTO to the 9:2 Southern L_2 NRHO which is differentially corrected in an ephemeris-model which is *high-fidelity* [115]. In this case, invariant manifolds in their true sense do not exist and approximate manifold bundles are generated known as 'manifold-analogues' and generated using an approximation of the Monodromy Matrix, **M**.

5.3.1 Problem Description and Mission Parameters

Geocentric sGTOs are of great commercial value. The near-circular regime of the sGTOs has perigee above the synchronous altitude, a region termed as the GEO graveyard belt [116]. These orbits find use as storage and disposal location for derelict geosynchronous satellite debris. For the current mission, we assume that the resupply spacecraft has been initially placed in a geocentric elliptical orbit of the super synchronous domain. As the name suggests, a spacecraft in this orbit would orbit the Earth at a faster angular rate than the Earth's rotation rate near perigee, and slower

at apogee. The orbits in this domain typically have a somewhat larger apogee than a GTO, as shown in Figure 5.34. Table 5.20 lists the orbital elements for the two orbits of the sGTO category selected as the initial orbits for the representative problem.

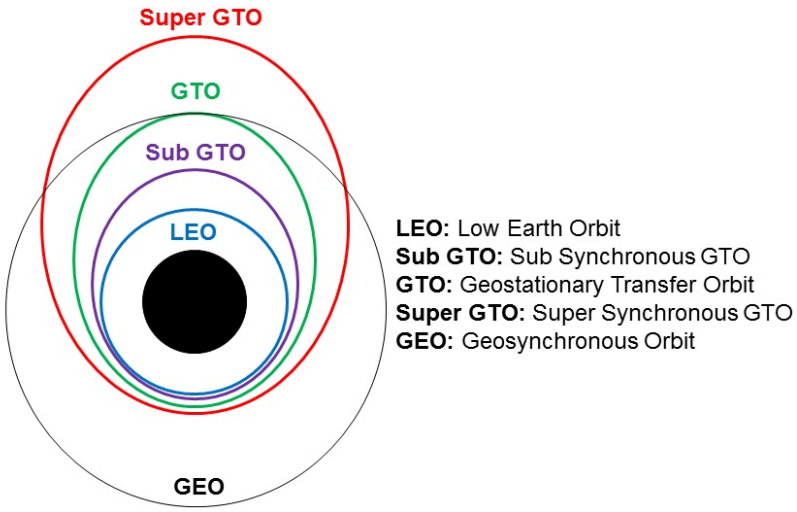

Figure 5.34: Schematic depicting the domain of Geocentric orbits.

The two starting orbits ($sGTO_1$ and $sGTO_2$) differ only in their argument of periapse as is given in the Table 5.20. The choice of sGTO with $\omega = \omega_{pp}^{\text{nom}} = 0^\circ$ or 180° was made depending on the departure epoch to enable a favorable eclipse condition and therefore an efficient transfer. Note that thrusters aboard the spacecraft are switched 'OFF' during the duration of every encountered eclipse. On the one hand, perigee is the ideal position to thrust in order to raise apogee and vice versa, while on the other, eclipses are frequently longer around apogee than the perigee, but can be more likely to occur at perigee than apogee depending on the 3D geometry and time of the year. These considerations are pertinent to designing transfers analogous to the representative problem and give rise to two competing effects, namely, efficacy of thrusting and eclipse duration. Additionally, fuel-cost for in-plane rotation of the transfer spirals is another criterion for selection of the departure orbit as discussed in the previous section. It is also worthwhile to note that a multi-objective optimization process where radiation dose is considered along with the

fuel-optimal costs, is usually characterized by several impulsive periapse raises immediately after insertion into a GTO and prior to other maneuvers in order to escape the Van Allen Belt. This solution causes a penalty in terms of fuel-optimality but is essential for mission survival [117]. In the work presented here, this factor has been ignored and fuel-optimality in conjunction with eclipses has been focused on.

Table 5.20: Classical Orbital Elements of the sGTO.

Orbit	a (km)	e	i (°)	Ω (°)	ω (°)	ν (°)	Period (hrs.)	Center
$sGTO_1$	44364	0.65	27	11.3044	180	0	25.832	Earth
$sGTO_2$	44364	0.65	27	11.3044	0	0	25.832	Earth

As discussed before, the terminal orbit for the mission is the ephemeris-corrected 9:2 resonant NRHO of the Southern L_2 family. Cartesian states for the Deep Space Gateway (DSG) platform in this orbit are available in the SPICE kernels (BODY ID '-60000') with respect to the Earth's center (BODY ID '399') [118]. The available states span 15 years from 'JAN 2, 2020' to 'FEB 11, 2035', with the trajectory being continuous in position but has repeated, small corrective velocity adjustments ($\sim$ 1.86 mm/s). The dynamical model used for differential correction was an n-body gravity model, with eclipse avoidance properties achieved by a judicious choice of initial condition. Since the orbit is quasi-periodic, every rev has a slightly different orbital period with the average being $\sim$ 6.562 days. The NRHO has been plotted in the EMEJ2000 frame between '2025 JAN 02 20:02:28.677' and '2025 DEC 23 04:37:56.003' in Figure 5.35.

Additionally, the resupply spacecraft was assumed to have an initial mass (m_0) of 1000 kg, with the engine generating a maximum thrust (T_{max}) of 0.5 N (approximately equivalent to 2 BPT-4000 Hall-thruster engines (now named XR5) operating at 4.839 kW [119]) resulting in a maximum thrust acceleration of 5.0×10^{-4} m/s with a constant specific impulse of I_{sp} = 1500 s.

Efficient transfers from $sGTO_1/sGTO_2$ to the NRHO via pre-computed stable invariant man-

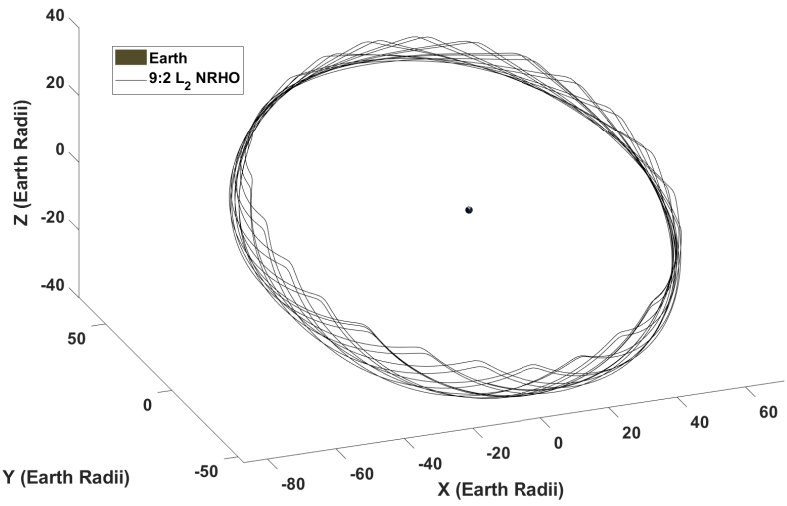

Figure 5.35: 9:2 L_2 Southern NRHO in the EMEJ2000 frame.

ifold analogues, leveraging them as LTCAs were designed for the assumed spacecraft properties. The transfer from the sGTO to the patch point was solved using the indirect formulation of the OCP, described in the previous section, in an eclipse-conscious, fuel-optimal sense. While $sGTO_1$ was the choice for departure orbit for transfers with insertion dates in January, February, March, October, November and December, for insertion dates in May, June, July, August and September, $sGTO_2$ was the departure orbit.

5.3.2 Manifold Patch Conditions in HFM

Based on the methodology discussed in the preceding chapter, stable invariant manifold analogues were generated for all "apo-apo" revs of the ephemeris-corrected 9:2 Southern L_2 NRHO. Several Earth-periapse states on the generated trajectories were extracted for further analysis to gauge viability. Figure 5.36 shows stable manifold analogues for 100 discrete points on the "apo-apo" rev starting '2025 JAN 02 20:02:28.677'.

These points were analyzed using phase portraits to pick the 'best' patch-point condition for trajectory design. The primary consideration for selecting the patch-point, and thereby the man-

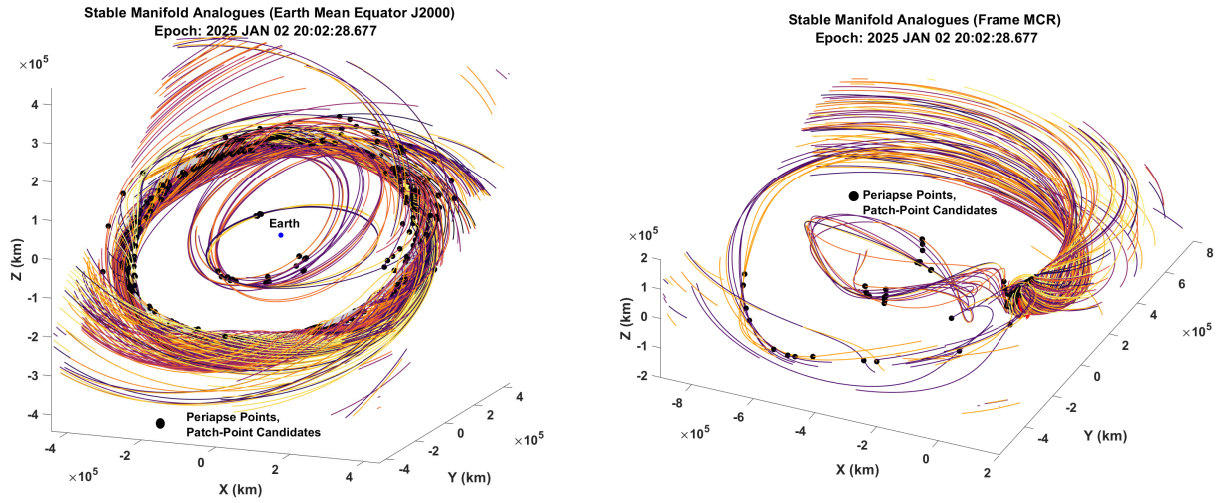

(a) Earth Mean Equator J2000 (EMEJ2000) frame.

(b) Moon-centered rotating (MCR) frame.

Figure 5.36: Patch-point candidates on stable manifold analogues.

ifold, was distance from Earth (R_d). Other considerations were maximum eclipse duration (t_{ec}) and differences in the argument of periapse ($\Delta\omega$), eccentricity (Δe), and inclination (Δi) between the geocentric departure orbit and the patch condition. While minimizing any combination of $[R_d, \Delta\omega, \Delta e, \Delta i]$, enable efficient transfers in terms of fuel consumption, t_{ec} is also an important parameter that can determine viability of the LTCAs and render otherwise valid choices impractical. Once an attractive patch-point is selected, it can either be held fixed or can be subject to further refinement in an optimization process. Also of significance, the nature of temporal and spatial behavior of manifold trajectories in a high-fidelity model implies that each subsequent state on the manifold propagates as a part of the original ballistic trajectory, enabling tracking via guidance algorithms. This provides robustness to missed thrust-arcs in the preceding phases of the converged trajectory.

Figure 5.37 depicts the maximum duration of eclipse (t_{ec}) experienced by the spacecraft while coasting on the stable manifold analogues. Five 'Best' cases in ascending order of R_d were considered for each rev in YR 2025. Note that several of the candidate LTCAs are devoid of eclipses and this knowledge enables a judicious choice of the manifold analogue and associated patch-condition

for various launch period scenarios.

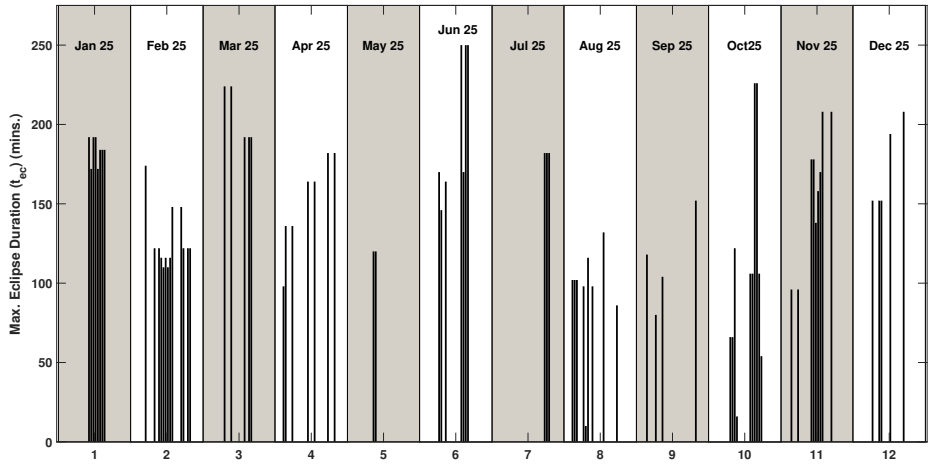

Figure 5.37: t_{ec} for stable manifold analogues in year 2025.

It is apparent that the worst case scenario in terms of eclipses occur in June 2025 with a maximum $t_{ec} = 250$ minutes. Although this includes both 'UMBRAL' (full shadow) and 'PENUMBRAL' (partial shadow) eclipse components, we are interested in the total eclipse duration to provide this essential analysis and demonstration of indirect trajectory optimization subject to eclipse constraints.

Another important consideration, as discussed above is $\Delta\omega = |\omega_0 - \omega_{\text{pp}}|$, where ω_0 and ω_{pp} are the arguments of periapse of the initial geocentric orbit and the target patch-point condition in the EMEJ2000 frame, respectively. Transfers with a minimal $\Delta\omega$ have been found to be efficient and cheaper due to minimal effort required to rotate the major axis of the osculating orbits, leading to the the final optimal osculating orbit before insertion onto the manifold coast. Typical initial geocentric departure orbits have $\omega = \omega_{pp}^{\text{nom}} = 0^\circ$ or 180°. Therefore, in order to minimize $\Delta\omega$, $\omega_{\text{pp}} \subset \{L^1, L^2\}$ where $\{L^1, L^2\} \in \mathbb{R}$ is a small neighborhood around $\omega_{\text{pp}}^{\text{nom}}$ ($\pm 30^\circ$), depending upon the value of ω_0. Figure 5.38 shows an ω_{pp} vs. R_d phase portrait of all the candidate patch-point conditions, segregated by the 'MONTH' of the year 2025 when the spacecraft gets inserted into

the NRHO. The colorbar depicts the coast-time on the LTCAs.

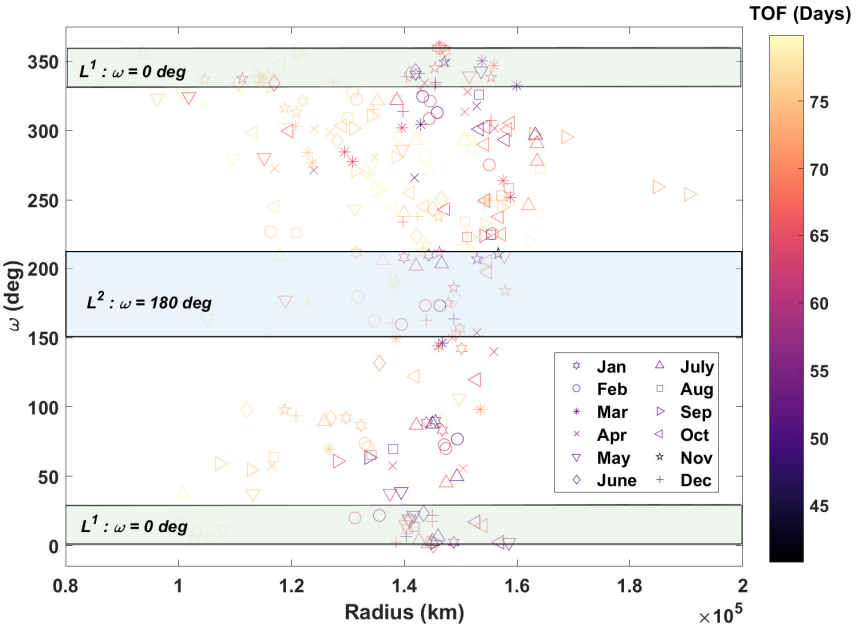

Figure 5.38: ω_{pp} vs. R_d for candidate patch-points in the YR 2025.

In addition to the primary advantage of minimizing $\Delta\omega$, analysis of the ω_{pp} vs. R_d phase portrait also introduces a flexibility in terms of mission launch window analysis and eclipse duration. In essence, it equips mission designers with multiple patch-points to choose from, depending on the departure epoch and $\omega_{\text{pp}}^{\text{nom}}$. An informed choice enables designers to circumvent many iterations of trajectory design in order to get a favorable "Spacecraft - Sun - Occulting Body" geometry.

5.3.3 Results

5.3.3.1 Eclipses not Interfering with Fuel-optimal Coasts

Eclipse-conscious transfers are mindful of all shadow encounters of the spacecraft. The formulation using CSC enables the algorithm to recognise onset and termination of eclipses on all intermediate spirals and enforces an 'OFF' condition for the engine. These eclipse regions on the transfer spirals can occur in between two consecutive thrust arcs 'THRUST - ECLIPSE - THRUST',

between a thrust and a coast arc ‘THRUST - ECLIPSE - COAST’ or between consecutive coast arcs ‘COAST - ECLIPSE - COAST’. In this section, a transfer opportunity is presented, where eclipses occurr in between consecutive coast arcs.

The spacecraft on this transfer trajectory gets inserted in the NRHO on ‘25 JAN 2025 18:39:50.103’. The total transfer time was 106.59 days with the spacecraft coasting on the LTCA for 50.59 days. The total ΔV for the transfer was 1641.867 m/s. The transfer trajectory is shown in Figure 5.39, plotted in the EMEJ2000 frame. Other important transfer events are : departure on ‘11 OCT 2024 04:17:37.145’ and patching with the LTCA on ‘06 DEC 2024 04:17:37.145’.

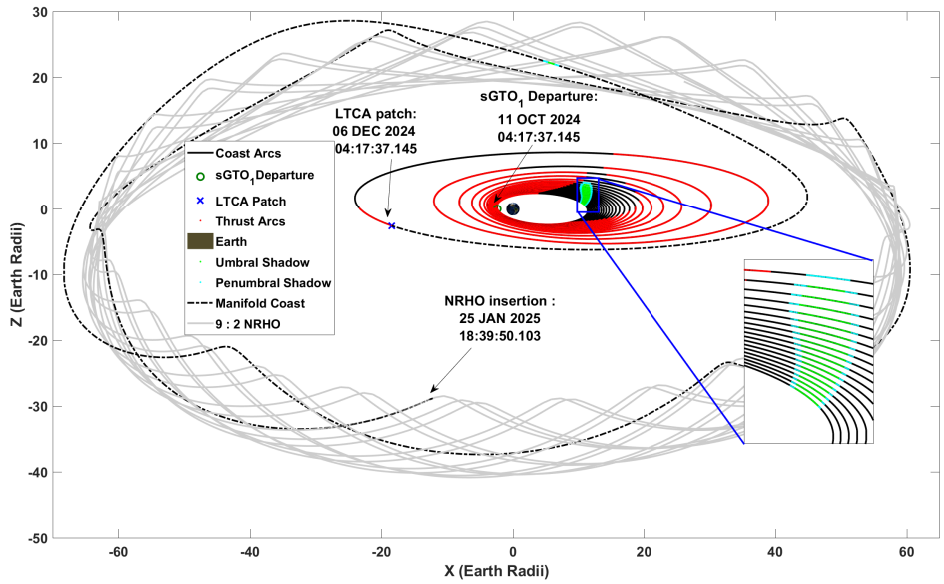

Figure 5.39: Full Transfer : $sGTO_1$ - 9:2 NRHO (EMEJ2000).

Note that highlighted ‘green’ regions of the spirals depict the part of the trajectory when the spacecraft is in Earth’s umbral shadow and the ‘cyan’ regions depict the penumbral shadow regions. Here, all the shadow regions coincide with the fuel-optimality-driven coast arcs (due to PMP). For the given departure and insertion epochs, the time-varying Sun-Earth-Spacecraft geometry results in such a favourable situation from a fuel-optimality point of view. Since, the eclipse-induced coast arcs which would have been forced coasts in the midst of neighboring thrust arcs, are on

fuel-optimal coast arcs, the optimal thrusting sequence remains intact. This efficacy would be elucidated upon comparing the ΔV cost with the former.

The bang-off-bang throttle sequence for the transfer trajectory is depicted in Figure 5.40. The 'black' colored discontinuous function represents the eclipse condition (0: No Eclipse, 1: Umbral, 2: Penumbral), whereas the 'red' plot depicts the corresponding thrust sequence. The 'blue' curve represents the switching function used for tangent hyperbolic smoothing. .

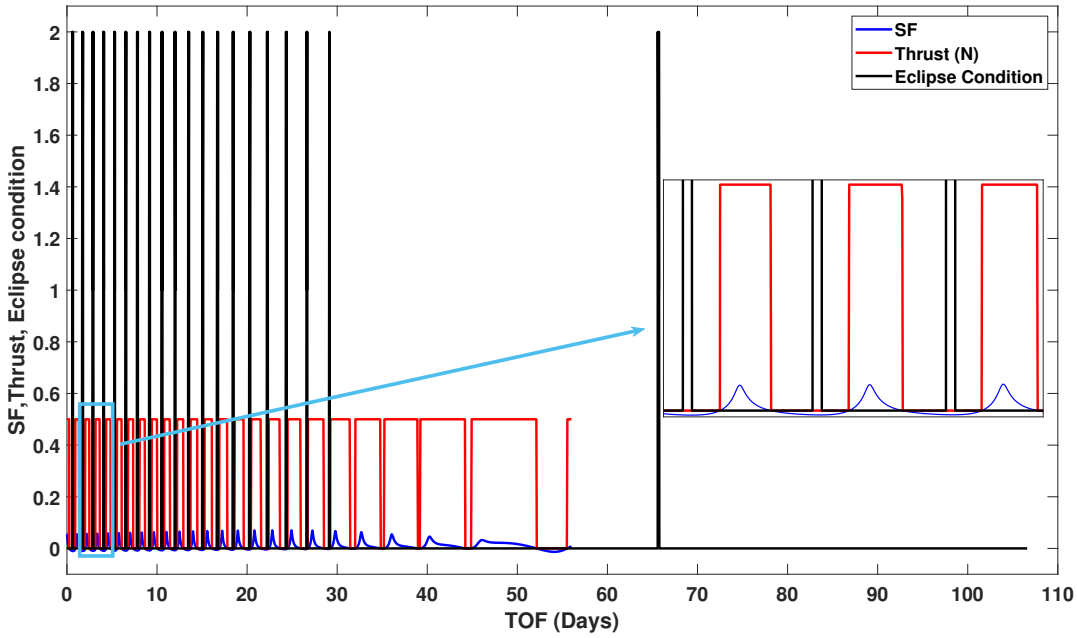

Figure 5.40: Thrusting sequence, eclipse condition, and switching function vs. time.

The blown-up image in Figure 5.40 clearly shows the eclipse arcs being out of phase with the thrust arcs, and lying on the intermediate fuel-optimal-driven coast arcs. Thus, there are no eclipse-induced coast arcs in this transfer trajectory. An eclipse on the selected LTCA is also evident from the figure, which occurs 65.46 days after departure.

Finally, as mentioned before, the frequency of eclipses is also an important parameter along with their duration. Figure 5.41 depicts this data displayed in a histogram plot with separate bins

depending on eclipse duration. The spacecraft encounters a total of 19 eclipses enroute to the

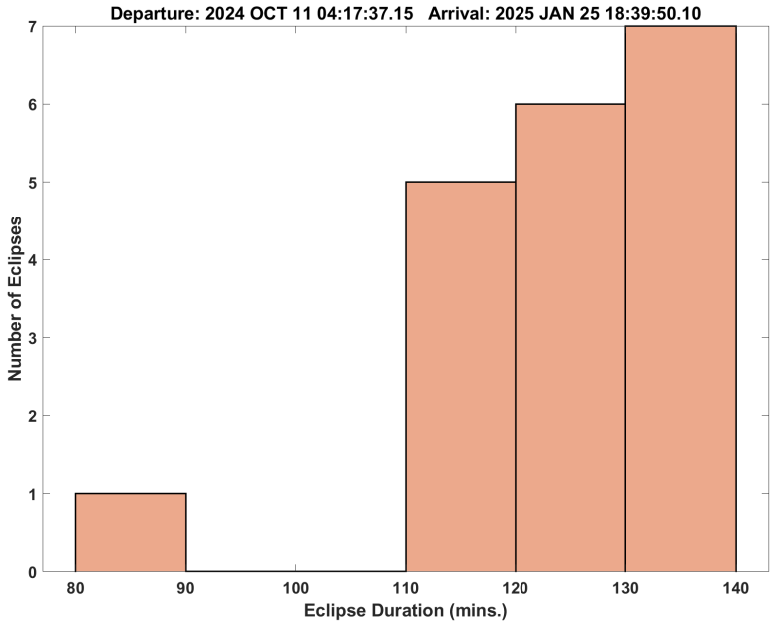

Figure 5.41: Thrusting Sequence and Eclipse Condition.

NRHO from the $sGTO_1$ for the mentioned departure and arrival epochs. It encounters 7 eclipses in the 130 - 140 mins range, 6 in the 120 - 130 mins range, 5 in the 110 - 120 mins range and 1 in the 80 - 90 mins range. The duration of the longest eclipse encountered was 136 mins.

5.3.3.2 Eclipses Interfering with Fuel-optimal Coasts

A representative transfer is presented in this section, where the eclipse arcs occur in between consecutive thrust arcs. Theoretically, eclipse-driven coast arcs result in loss of thrusting efficiency, more so, if such coast arcs appear near the periapse region of the intermediate transfer spirals, where the spacecraft velocity is high. The resulting throttling sequence represents a significant departure from the ideal fuel-optimal behavior, where the optimality conditions manifest into a regular distribution of the thrust arcs around the periapse region for maximum efficiency. This concept is elucidated in the numerical solution presented.

The spacecraft on this transfer trajectory departs from $sGTO_1$ and is inserted in the NRHO on '19 MAR 2025 01:45:00.464'. The total transfer time was 135.39 days with the spacecraft coasting on the LTCA for 79.39 days. The total ΔV for the transfer was 1991.916 m/s. The transfer trajectory is shown in Figure 5.42, plotted in the EMEJ2000 frame. Other important transfer events are : Departure on '03 NOV 2024 16:23:36.467' and Patching with the LTCA on '29 DEC 2024 16:23:36.467'.

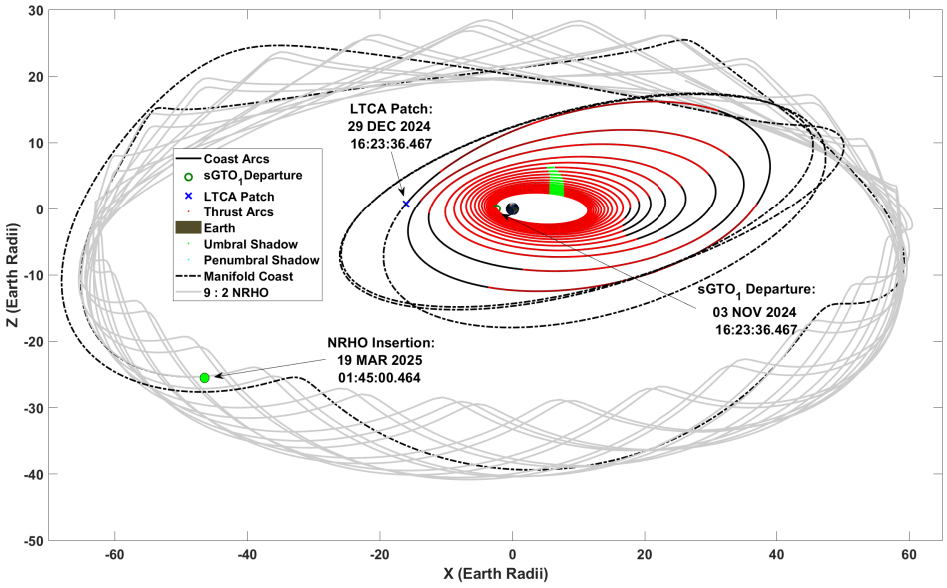

Figure 5.42: Full Transfer: $sGTO_1$ - 9:2 NRHO (EMEJ2000).

The bang-off-bang throttle sequence is depicted in Figure 5.43. Since the eclipse-driven coast arcs happen during thrust arcs, it leads to forced coasts for the eclipse duration. Comparing it with Figure 5.40, it is apparent that there are no eclipses on the selected LTCA. The blown up image in Figure 5.43 clearly depicts the switch in the throttle sequence due to the eclipse-driven coast arcs.

The frequency of 'Earth - occulted' eclipses, being an important consideration for accurate mission design, has been portrayed using a histogram plot in Figure 5.44 with separate bins depending on the eclipse duration. The spacecraft encounters 15 eclipses enroute to the NRHO from the $sGTO_1$ for the mentioned departure and arrival epochs. It encounters 1 eclipse each in the 80 -

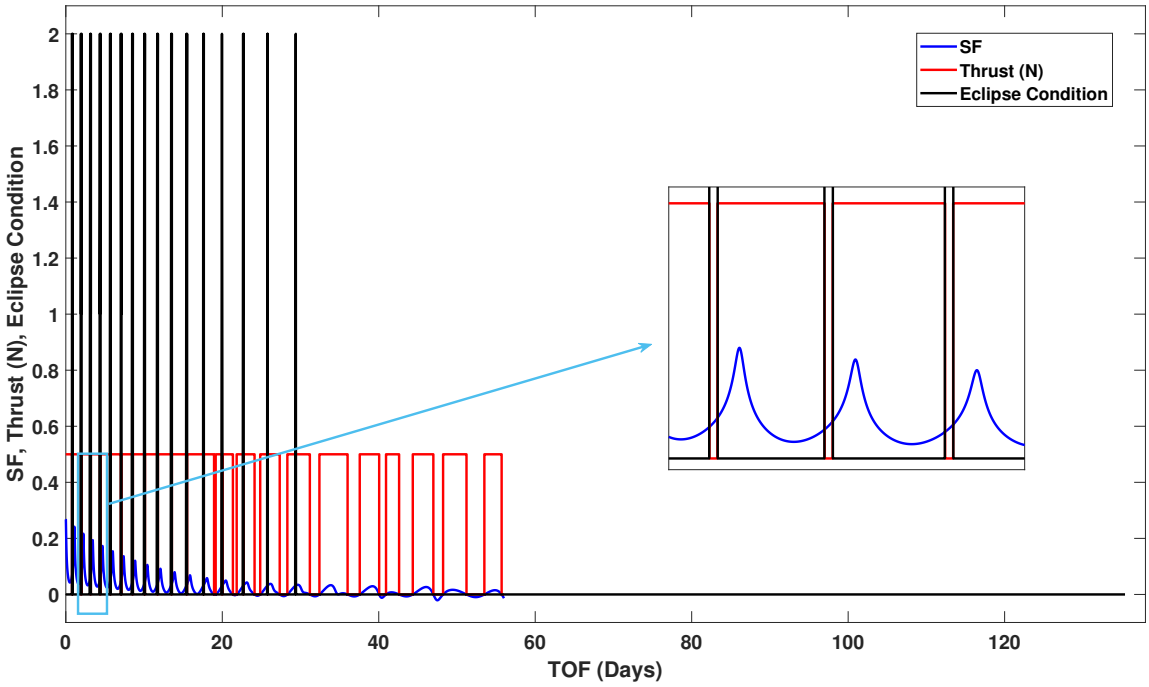

Figure 5.43: Thrusting sequence, eclipse condition, and switching function.

90 mins range and 100 - 110 mins range, 2 eclipses in the 110 - 120 mins range and 11 eclipses in the 120 - 130 mins range. The duration of the longest eclipse encountered was 126 mins.

5.3.3.3 Transfer Opportunities in 2025

In this section, opportunities for feasible and efficient transfers of a spacecraft with the assumed parameters from a sGTO to the 9:2 NRHO have been listed. The transfers were solved for one insertion opportunity every month of the year 2025. blueFigure 5.45 depicts all the spatial trajectories with respect to the Earth Mean Equator (EMEJ2000) frame. Note the counter-clockwise movement of the eclipse arcs as the insertion date is swept throughout the year. All candidate trajectories shown in blueFigure 5.45, were solved for using the same methodology with the LTCAs and associated patch-points pre-computed and identified. The 'best' LTCA for each transfer was identified by picking the one with a patch-point (periapse point) having an argument of periapse as close to the sGTO ω as possible, among the top five cases having the least radius with respect to the Earth. The nature of eclipses encountered by the spacecraft enroute has been plotted as binned

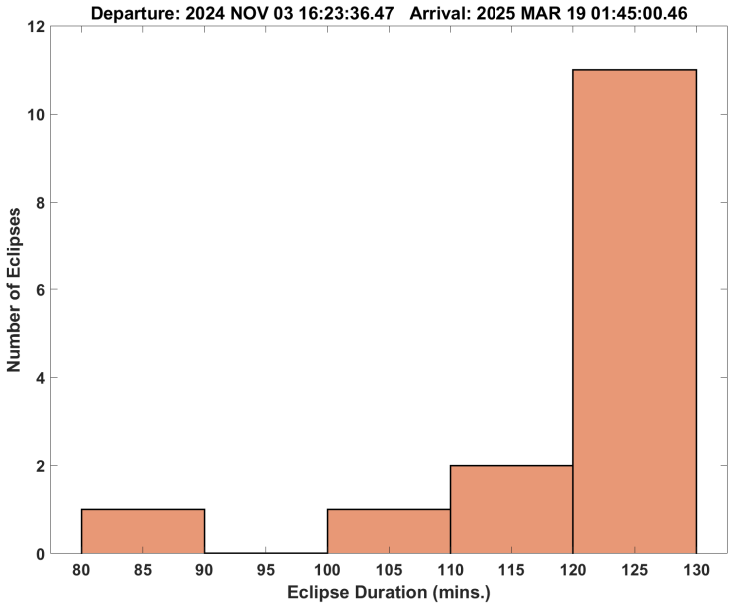

Figure 5.44: Thrusting sequence and eclipse condition.

histograms in Figure 5.46.

Table 5.21 summarizes important transfer parameters for all the mission scenarios. The duration of the longest eclipse as well as the number of eclipses encountered depend on the 'Sun-Earth-Spacecraft' geometry for the duration of the transfer. These results present mission designers with efficient eclipse-conscious trajectories for future resupply missions to the Lunar Gateway, which is beyond the scope of state-of the art trajectory design tools. The fuel cost presented is comparable to analogous results presented in [120].

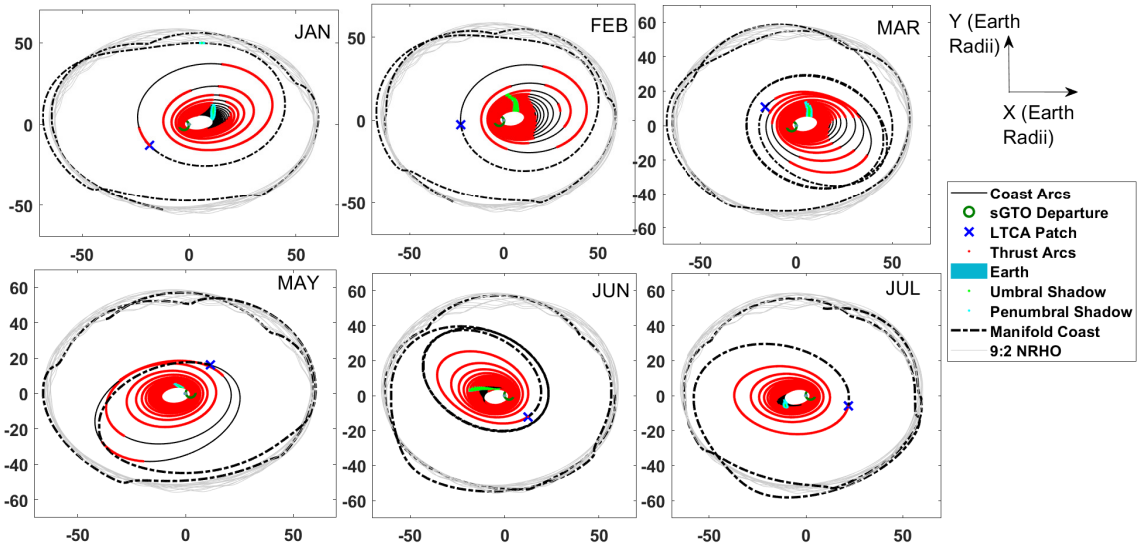

(a) Trajectories for January - July 2025.

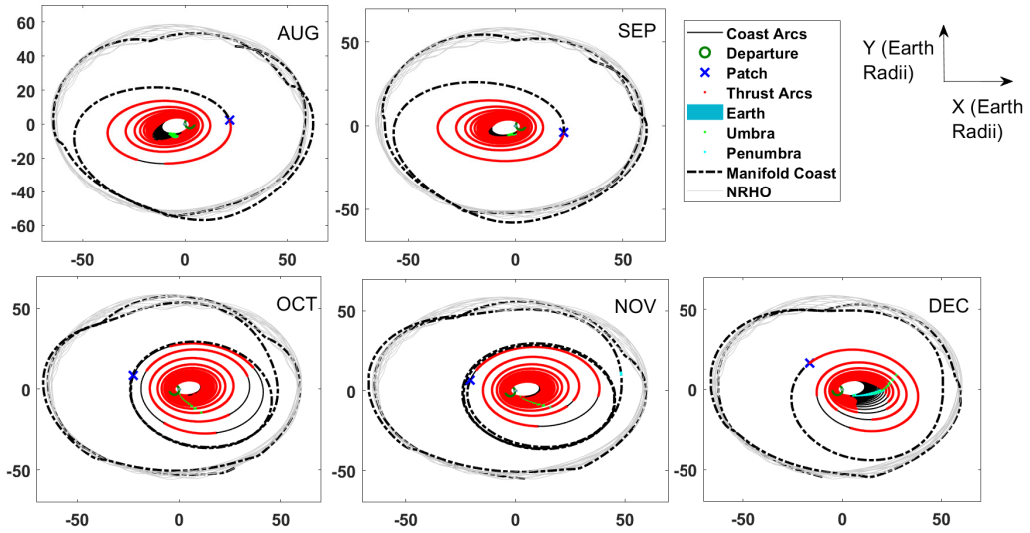

(b) Trajectories for August - December 2025.

Figure 5.45: Eclipse-conscious trajectories: YR 2025.

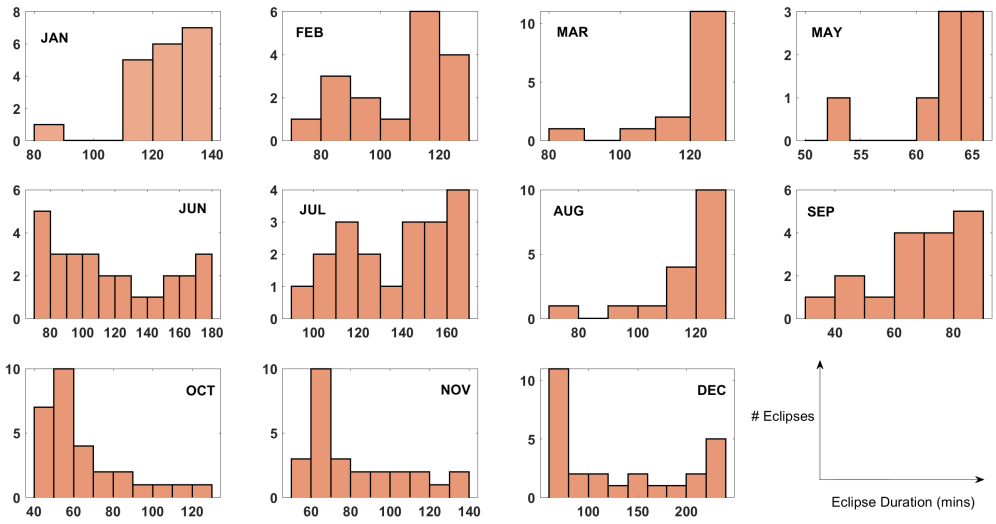

Figure 5.46: Eclipse binning for Mission Scenarios in YR 2025.

Table 5.21: Summary of departure and arrival times, ΔV, maximum eclipse duration and number of eclipses for different mission scenarios in YR 2025.

Departure Epoch	**Arrival Epoch**	ΔV (m/s)	**Duration** (mins)	**#Eclipses**
11 OCT 2024 04:17:37.15	**25 JAN 2025** 18:39:50.11	1641.867	135	19
05 OCT 2024 04:00:27.53	**21 FEB 2025** 00:19:30.41	1729.059	120	17
03 NOV 2024 16:23:36.47	**19 MAR 2025** 01:45:00.47	1991.916	126	15
16 JAN 2025 14:12:43.83	**04 MAY 2025** 00:41:05.43	1956.159	64	8
01 FEB 2025 23:50:15.69	**19 JUN 2025** 02:58:55.25	2189.803	176	27
02 APR 2025 01:36:17.10	**21 JUL 2025** 21:10:58.86	1979.373	164	19
01 MAY 2025 06:28:26.86	**17 AUG 2025** 01:44:34.07	1817.332	124	17
26 MAY 2025 23:20:11.50	**12 SEP 2025** 01:44:34.07	2054.525	86	17
15 JUN 2025 15:44:17.11	**28 OCT 2025** 17:18.58.24	2103.743	124	29
11 JUL 2025 04:23:01:44	**23 NOV 2025** 10:55:04.80	1900.061	130	27
19 AUG 2025 13:18:07.01	**19 DEC 2025** 14:58:07.03	1772.081	242	28

6. SUMMARY AND CONCLUSIONS

In this dissertation, a novel and structured methodology was presented to solve complicated optimal trajectory design problems by leveraging invariant manifold theory. In particular, the discussion focuses on missions in the cislunar domain, given the recent impetus provided by the Artemis Mission launch in the near future and many more missions internationally in the pipeline. It was successfully demonstrated that stable and unstable manifold bundles exist and can be computed for periodic orbits orbiting Lagrange Points in any primary-secondary system. The manifold bundles behave as trajectories that asymptotically grow in particular directions which are derived from an eigenanalysis of the Monodromy Matrix. The asymptotic behavior is somewhat lost with a change in dynamical system definition and alternate methods have been presented to approximate the manifolds in such systems. The choice of finding the most appropriate patch-conditions on the manifold is a multi-dimensional, non-linear optimization problem which has been graphically solved with heuristic insights derived from various phase portraits and knowledge of the initial orbit of the spacecraft.

Mission ready trajectories require consideration of an ephemeris model which sees considerable departure from the behavior observed in a simplified model like the CR3BP. It is imperative that any manifold bundles computed for a simplified system is re-computed in the ephemeris model to confirm that the departure is minimized by judiciously choices made for this new and complex epoch-driven system. Additionally, a methodology has also been presented where mission designers can embed eclipse-consciousness for generated trajectories in the well-known indirect formalism of the optimal control problem. This enables convergence to optimal trajectories that have enforced coasts when the spacecraft passes through an eclipse region and the Solar Electric Propulsion engine is unable to thrust.

The concepts presented and algorithms developed in the first four chapters were utilised to present three case studies covering the broad spectrum of different possibilities for transfer scenarios in the cislunar space where the spacecraft is required to leverage the manifold trajectories. The

results demonstrate the efficacy of the developed methodology in finding piece-wise optimal, efficient and intelligent solutions to trajectory design problems which can be readily used by mission designers. Furthermore, the long terminal coast provided by the asymptotically attracted stable manifold leads to a nominal capture scenario which is significantly more forgiving to off-nominal performance of the engine or any other untoward malfunction of the systems aboard the spacecraft as compared to a direct end-to end nominal trajectory.

6.1 Further Study

Some future research areas, building on the experience gained while working on the problems described in the dissertation are as follows:

- *Autonomous Guidance via Manifold Bundle:* A ML/AI based supervised learning process to train a regression model that selects a series of patch-states on the different trajectories in the manifold bundle based on the current spacecraft navigation state. Based on the selected patch-states, the spacecraft is autonomously, pseudo-asymptotically guided to a planetary capture condition via the manifold bundle.

- *Asteroid Mining and Spacecraft Refuelling:* A futuristic problem of establishing a mother-ship (refuelling station) in a judiciously selected Earth-Centered Distance Retrograde Orbit (DRO), equipped with a mining spacecraft as well as on-board fuel/resource-extracting labs. The idea is to fly asteroids on stable manifolds of a Sun-Earth L_1 periodic orbit (Lyapunov or Halo) and get them captured in the Sun-Earth system for cheap. Thereafter, use the manifold bundles to design to-and fro trajectories for the miner spacecraft between the mother-ship and the asteroid in the selected periodic orbit. Once, the resources mined have been converted to fuel, spacecraft for deep space missions can be designed to be significantly more light-weight which will reduce lift-off costs from the Earth. These spacecraft can then get re-fuelled on their way to deep-space destinations using the fuel on the mother-ship.

REFERENCES

[1] R. Biesbroek and G. Janin, "Ways to the moon," *ESA bulletin*, vol. 103, pp. 92–99, 2000.

[2] K. Uesugi, H. Matsuo, J. Kawaguchi, and T. Hayashi, "Japanese first double lunar swingby mission "hiten"," *Acta Astronautica*, vol. 25, no. 7, pp. 347–355, 1991.

[3] L. P. Institute, "The Moon's Influence on Us." `https://www.lpi.usra.edu/education/explore/marvelMoon/background/moon-influence/`.

[4] R. M. Canup and E. Asphaug, "Origin of the moon in a giant impact near the end of the earth's formation," *Nature*, vol. 412, no. 6848, pp. 708–712, 2001.

[5] D. L. Miller, *Earth, Sun, and Moon: Cyclic Patterns of Lunar Phases, Eclipses, and the Seasons*. Cavendish Square Publishing, LLC, 2016.

[6] N. C. Costes, W. D. Carrier III, J. K. Mitchell, and R. F. Scott, "Apollo 11: Soil mechanics results," *Journal of the Soil Mechanics and Foundations Division*, vol. 96, no. 6, pp. 2045–2080, 1970.

[7] O. L. Anderson, C. Scholz, N. Soga, N. Warren, and E. Schreiber, "Elastic properties of a micro-breccia, igneous rock and lunar fines from apollo 11 mission," *Geochimica et Cosmochimica Acta Supplement*, vol. 1, p. 1959, 1970.

[8] T. Gold, "Apollo 11 and 12 close-up photography," *Icarus*, vol. 12, no. 3, pp. 360–375, 1970.

[9] C. Yu, J. H. Hansen, and D. W. Oard, "Houston, we have a solution': A case study of the analysis of astronaut speech during nasa apollo 11 for long-term speaker modeling," in *Fifteenth Annual Conference of the International Speech Communication Association*, Citeseer, 2014.

[10] N. Hubbard, L. Nyquist, J. Rhodes, B. Bansal, H. Wiesmann, and S. Church, "Chemical features of the luna 16 regolith sample," *Earth and Planetary Science Letters*, vol. 13, no. 2, pp. 423–428, 1972.

[11] O. Eugster, N. Grögler, M. Mendia, P. Eberhardt, and J. Geiss, "Trapped solar wind noble gases and exposure age of luna 16 lunar fines," *Geochimica et Cosmochimica Acta*, vol. 37, no. 9, pp. 1991–2003, 1973.

[12] Y. Jia, Y. Zou, J. Ping, C. Xue, J. Yan, and Y. Ning, "The scientific objectives and payloads of chang'e- 4 mission," *Planetary and Space Science*, vol. 162, pp. 207–215, 2018.

[13] V. Krish, E. Belbruno, and W. Hollister, "An investigation into critical aspects of a new form of low energy lunar transfer, the belbruno-miller trajectories," in *Astrodynamics Conference*, p. 4581, 1992.

[14] E. Taheri and J. L. Junkins, "How many impulses redux," *The Journal of the Astronautical Sciences*, vol. 67, no. 2, pp. 257–334, 2020.

[15] K. Leschly, G. Sprague, and J. Rademacher, "Carrier spacecraft using ariane-5 gto piggy-back launch," *Acta astronautica*, vol. 45, no. 4-9, pp. 527–531, 1999.

[16] C. O'Quinn, "Providing maximum launchability–a guide to defined smallsat classification," *The Areospace Corporation*, 2018.

[17] I. S. R. Organisation, "PSLV-C37 Successfully Launches 104 Satellites in a Single Flight." `https://www.isro.gov.in/pslv-c37-successfully-launches-104-satellites-single-flight/`.

[18] E. Belbruno, "Lunar capture orbits, a method of constructing earth moon trajectories and the lunar gas mission," in *19th International Electric Propulsion Conference*, p. 1054, 1987.

[19] E. Belbruno and J. Carrico, "Calculation of weak stability boundary ballistic lunar transfer trajectories," in *Astrodynamics Specialist Conference*, p. 4142, 2000.

[20] E. Belbruno, "Low energy trajectories for space travel using stability transition regions," *IFAC Proceedings Volumes*, vol. 33, no. 2, pp. 7–12, 2000.

[21] F. García and G. Gómez, "A note on weak stability boundaries," *Celestial Mechanics and Dynamical Astronomy*, vol. 97, no. 2, pp. 87–100, 2007.

[22] E. A. Belbruno and J. K. Miller, "Sun-perturbed earth-to-moon transfers with ballistic capture," *Journal of Guidance, Control, and Dynamics*, vol. 16, no. 4, pp. 770–775, 1993.

[23] H. Yamakawa, J. Kawaguchi, N. Ishii, and H. Matsuo, "On earth-moon transfer trajectory with gravitational capture," in *Proceedings of the AAS/AIAA Astrodynamics Conference. Part 3 (of 3)*, pp. 397–416, Publ by Univelt Inc, 1993.

[24] W. S. Koon, M. W. Lo, J. E. Marsden, and S. D. Ross, "Heteroclinic connections between periodic orbits and resonance transitions in celestial mechanics," *Chaos: An Interdisciplinary Journal of Nonlinear Science*, vol. 10, no. 2, pp. 427–469, 2000.

[25] D. F. Lawden, "Impulsive transfer between elliptical orbits," in *Mathematics in Science and Engineering*, vol. 5, pp. 323–351, Elsevier, 1962.

[26] N. X. Vinh, S. H. Kuo, and C. Marchal, "Optimal time-free nodal transfers between elliptical orbits," *Acta Astronautica*, vol. 17, no. 8, pp. 875–880, 1988.

[27] J. E. Prussing and J.-H. Chiu, "Optimal multiple-impulse time-fixed rendezvous between circular orbits," *Journal of Guidance, Control, and Dynamics*, vol. 9, no. 1, pp. 17–22, 1986.

[28] D. J. Jezewski and H. L. Rozendaal, "An efficient method for calculating optimal free-space n-impulse trajectories.," *AIAA journal*, vol. 6, no. 11, pp. 2160–2165, 1968.

[29] O. Abdelkhalik and D. Mortari, "N-impulse orbit transfer using genetic algorithms," *Journal of Spacecraft and Rockets*, vol. 44, no. 2, pp. 456–460, 2007.

[30] A. E. Petropoulos and J. A. Sims, "A review of some exact solutions to the planar equations of motion of a thrusting spacecraft," 2002.

[31] M. S. Branicky, V. S. Borkar, and S. K. Mitter, "A unified framework for hybrid control: Model and optimal control theory," *IEEE transactions on automatic control*, vol. 43, no. 1, pp. 31–45, 1998.

[32] S. Engell, G. Frehse, and E. Schnieder, *Modelling, analysis and design of hybrid systems*, vol. 279. Springer, 2003.

[33] C. M. Chilan and B. A. Conway, "Automated design of multiphase space missions using hybrid optimal control," *Journal of Guidance, Control, and Dynamics*, vol. 36, no. 5, pp. 1410–1424, 2013.

[34] I. M. Ross and C. N. D'Souza, "Hybrid optimal control framework for mission planning," *Journal of Guidance, Control, and Dynamics*, vol. 28, no. 4, pp. 686–697, 2005.

[35] J. T. Betts, "Survey of numerical methods for trajectory optimization," *Journal of guidance, control, and dynamics*, vol. 21, no. 2, pp. 193–207, 1998.

[36] A. V. Rao, "A survey of numerical methods for optimal control," *Advances in the Astronautical Sciences*, vol. 135, no. 1, pp. 497–528, 2009.

[37] B. A. Conway, "A survey of methods available for the numerical optimization of continuous dynamic systems," *Journal of Optimization Theory and Applications*, vol. 152, no. 2, pp. 271–306, 2012.

[38] G. R. Hintz, "Survey of orbit element sets," *Journal of guidance, control, and dynamics*, vol. 31, no. 3, pp. 785–790, 2008.

[39] J. L. Junkins and E. Taheri, "Exploration of alternative state vector choices for low-thrust trajectory optimization," *Journal of Guidance, Control, and Dynamics*, vol. 42, no. 1, pp. 47–64, 2019.

[40] H. Schaub and J. L. Junkins, *Analytical mechanics of space systems*. Aiaa, 2003.

[41] D. A. Vallado, *Fundamentals of astrodynamics and applications*, vol. 12. Springer Science & Business Media, 2001.

[42] M. Walker, B. Ireland, and J. Owens, "A set modified equinoctial orbit elements," *Celestial mechanics*, vol. 36, no. 4, pp. 409–419, 1985.

[43] P. Cefola, "Equinoctial orbit elements-application to artificial satellite orbits," in *Astrodynamics Conference*, p. 937, 1972.

[44] A. E. Bryson and Y.-C. Ho, *Applied optimal control: optimization, estimation, and control*. Routledge, 2018.

[45] D. E. Kirk, *Optimal control theory: an introduction*. Courier Corporation, 2004.

[46] F. L. Lewis, D. Vrabie, and V. L. Syrmos, *Optimal control*. John Wiley & Sons, 2012.

[47] E. Taheri, J. L. Junkins, I. Kolmanovsky, and A. Girard, "A novel approach for optimal trajectory design with multiple operation modes of propulsion system, part 1," *Acta Astronautica*, vol. 172, pp. 151–165, 2020.

[48] J. Wang, H. Zhu, C. Zhang, Z. Chen, Y. Huang, W. Chen, X. Huang, and F. Wang, "Adaptive hyperbolic tangent sliding-mode control for building structural vibration systems for uncertain earthquakes," *IEEE Access*, vol. 6, pp. 74728–74736, 2018.

[49] S. Singh, E. Taheri, and J. Junkins, "A hybrid optimal control method for timeoptimal slewing maneuvers of flexible spacecraft," in *The 2018 AAS/AIAA Astrodynamics Specialist Conference, Snowbird, Utah*, 2018.

[50] E. Taheri and J. L. Junkins, "Generic smoothing for optimal bang-off-bang spacecraft maneuvers," *Journal of Guidance, Control, and Dynamics*, vol. 41, no. 11, pp. 2470–2475, 2018.

[51] S. K. Singh, E. Taheri, R. Woollands, and J. Junkins, "Mission design for close-range lunar mapping by quasi-frozen orbits," in *70th International Astronautical Congress, Washington DC, USA*, 2019.

[52] E. Taheri, I. Kolmanovsky, and E. Atkins, "Enhanced smoothing technique for indirect optimization of minimum-fuel low-thrust trajectories," *Journal of Guidance, Control, and Dynamics*, vol. 39, no. 11, pp. 2500–2511, 2016.

[53] N. Ashby, "Planetary perturbation equations based on relativistic keplerian motion," in *Symposium-International astronomical union*, vol. 114, pp. 41–52, Cambridge University Press, 1986.

[54] A. M. Atallah, A. B. Younes, R. M. Woollands, and J. L. Junkins, "Analytical radial adaptive method for spherical harmonics gravity models," in *29th AAS/AIAA Space Flight Mechanics Meeting, 2019*, pp. 1345–1356, Univelt Inc., 2019.

[55] V. Pareto, *Manuale di economia politica: con una introduzione alla scienza sociale*, vol. 13. Società editrice libraria, 1919.

[56] L. S. Pontryagin, *Mathematical theory of optimal processes*. CRC press, 1987.

[57] W. Karush, "Minima of functions of several variables with inequalities as side conditions," in *Traces and Emergence of Nonlinear Programming*, pp. 217–245, Springer, 2014.

[58] H. W. Kuhn and A. W. Tucker, "Nonlinear programming," in *Traces and emergence of nonlinear programming*, pp. 247–258, Springer, 2014.

[59] H. D. Mittelmann, "A pseudo-arclength continuation method for nonlinear eigenvalue problems," *SIAM journal on numerical analysis*, vol. 23, no. 5, pp. 1007–1016, 1986.

[60] B. Pan, P. Lu, X. Pan, and Y. Ma, "Double-homotopy method for solving optimal control problems," *Journal of Guidance, Control, and Dynamics*, vol. 39, no. 8, pp. 1706–1720, 2016.

[61] S. K. Singh, B. D. Anderson, E. Taheri, and J. L. Junkins, "Exploiting manifolds of l1 halo orbits for end-to-end earth–moon low-thrust trajectory design," *Acta Astronautica*, vol. 183, pp. 255–272, 2021.

[62] O. Von Stryk, "Numerical solution of optimal control problems by direct collocation," in *Optimal control*, pp. 129–143, Springer, 1993.

[63] S. N. Williams, "An introduction to the use of varitop, a general purpose low-thrust trajectory optimization program," *jpl d-11475, Jet Propulsion Laboratory, California Institute of Technology, CA*, 1994.

[64] L. Kos, T. Polsgrove, R. Hopkins, D. Thomas, and J. Sims, "Overview of the development for a suite of low-thrust trajectory analysis tools," in *AIAA/AAS Astrodynamics Specialist Conference and Exhibit*, p. 6743, 2006.

[65] A. Feistel and C. Ranieri, "Modeling perturbations and operational considerations when using indirect optimization with equinoctial elements," in *AAS/AIAA Space Flight Mechanics Meeting*, pp. 1737–1756, 2009.

[66] S. Geffroy and R. Epenoy, "Optimal low-thrust transfers with constraints—generalization of averaging techniques," *Acta astronautica*, vol. 41, no. 3, pp. 133–149, 1997.

[67] Y. Meng, H. Zhang, and Y. Gao, "Low-thrust minimum-fuel trajectory optimization using multiple shooting augmented by analytical derivatives," *Journal of Guidance, Control, and Dynamics*, vol. 42, no. 3, pp. 662–677, 2019.

[68] J. Olympio, "Algorithm for low-thrust optimal interplanetary transfers with escape and capture phases," in *AIAA/AAS Astrodynamics Specialist Conference and Exhibit*, p. 7363, 2008.

[69] J. Horsewood, "Program manual for astop, an arbitrary space trajectory optimization program," *NASA STI/Recon Technical Report N*, vol. 75, p. 28086, 1974.

[70] G. Johnson, S. Munoz, and J. Lehman, "Copernicus: A generalized trajectory design and optimization system," *Presentation, November*, 2003.

[71] S. P. Hughes, R. H. Qureshi, S. D. Cooley, and J. J. Parker, "Verification and validation of the general mission analysis tool (gmat)," in *AIAA/AAS astrodynamics specialist conference*, p. 4151, 2014.

[72] J. Sims, P. Finlayson, E. Rinderle, M. Vavrina, and T. Kowalkowski, "Implementation of a low-thrust trajectory optimization algorithm for preliminary design," in *AIAA/AAS Astrodynamics specialist conference and exhibit*, p. 6746, 2006.

[73] J. Schoenmaekers *et al.*, "Mantra–flight dynamics interplanetary manoeuvre optimisation software specification document," 2005.

[74] E. Gallesio, "Stk reference manual," *Université de Nice, Sophia Antipolis, julliet*, 1995.

[75] J. Barrow-Green, *Poincaré and the three body problem*. No. 11, American Mathematical Soc., 1997.

[76] A. Chenciner, "Poincaré and the three-body problem," in *Henri Poincaré, 1912–2012*, pp. 51–149, Springer, 2015.

[77] I. Newton, *Philosophiae naturalis principia mathematica*, vol. 2. typis A. et JM Duncan, 1833.

[78] A. J. Brizard, *Introduction To Lagrangian Mechanics, An*. World Scientific Publishing Company, 2014.

[79] R. Broucke, "Traveling between the lagrange points and the moon," *Journal of Guidance and Control*, vol. 2, no. 4, pp. 257–263, 1979.

[80] D. Salamon, "The kolmogorov-arnold-moser theorem," *Math. Phys. Electron. J*, vol. 10, no. 3, pp. 1–37, 2004.

[81] H. Curtis, *Orbital mechanics for engineering students*. Butterworth-Heinemann, 2013.

[82] P. R. Weissman and G. Wetherill, "Periodic trojan-type orbits in the earth-sun system," *The Astronomical Journal*, vol. 79, p. 404, 1974.

[83] V. Domingo, B. Fleck, and A. I. Poland, "The soho mission: an overview," *Solar Physics*, vol. 162, no. 1, pp. 1–37, 1995.

[84] V. Szebehely, *Theory of orbit: The restricted problem of three Bodies*. Elsevier, 2012.

[85] Y. Qi and A. de Ruiter, "Energy analysis in the elliptic restricted three-body problem," *Monthly Notices of the Royal Astronomical Society*, vol. 478, no. 1, pp. 1392–1402, 2018.

[86] K. C. Howell and H. J. Pernicka, "Numerical determination of lissajous trajectories in the restricted three-body problem," *Celestial mechanics*, vol. 41, no. 1, pp. 107–124, 1987.

[87] E. Doedel, D. Dichmann, J. Galan-Vioque, H. Keller, R. Paffenroth, and A. Vanderbauwhede, "Elemental periodic orbits of the cr3bp: A brief selection of computational results," in *EQUADIFF 2003*, pp. 163–168, World Scientific, 2005.

[88] Y. Ren and J. Shan, "A novel algorithm for generating libration point orbits about the collinear points," *Celestial Mechanics and Dynamical Astronomy*, vol. 120, no. 1, pp. 57–75, 2014.

[89] D. Guzzetti and K. C. Howell, "Natural periodic orbit-attitude behaviors for rigid bodies in three-body periodic orbits," *Acta Astronautica*, vol. 130, pp. 97–113, 2017.

[90] D. Grebow, "Generating periodic orbits in the circular restricted three-body problem with applications to lunar south pole coverage," *MSAA Thesis, School of Aeronautics and Astronautics, Purdue University*, pp. 8–14, 2006.

[91] D. M. Grobman, "Homeomorphism of systems of differential equations," *Doklady Akademii Nauk SSSR*, vol. 128, no. 5, pp. 880–881, 1959.

[92] P. Hartman, "On local homeomorphisms of euclidean spaces," *Bol. Soc. Mat. Mexicana*, vol. 5, no. 2, pp. 220–241, 1960.

[93] J. Quandt, "On the hartman-grobman theorem for maps," *Journal of differential equations*, vol. 64, no. 2, pp. 154–164, 1986.

[94] D. L. Richardson, "Halo orbit formulation for the isee-3 mission," *Journal of Guidance and Control*, vol. 3, no. 6, pp. 543–548, 1980.

[95] S. Barone, M. Narcowich, and F. Narcowich, "Floquet theory and applications," *Physical Review A*, vol. 15, no. 3, p. 1109, 1977.

[96] T. Bray and C. Gouclas, "Doubly symmetric orbits about the collinear lagrangian points," *The Astronomical Journal*, vol. 72, p. 202, 1967.

[97] G. Gómez, J. Masdemont, and C. Simó, "Quasihalo orbits associated with libration points," *The Journal of the Astronautical Sciences*, vol. 46, no. 2, pp. 135–176, 1998.

[98] M. W. Lo, B. G. Williams, W. E. Bollman, D. Han, Y. Hahn, J. L. Bell, E. A. Hirst, R. A. Corwin, P. E. Hong, K. C. Howell, *et al.*, "Genesis mission design," *The Journal of the astronautical sciences*, vol. 49, no. 1, pp. 169–184, 2001.

[99] T. F. Chan, "Newton-like pseudo-arclength methods for computing simple turning points," *SIAM journal on scientific and statistical computing*, vol. 5, no. 1, pp. 135–148, 1984.

[100] E. L. Allgower and K. Georg, *Introduction to numerical continuation methods*, vol. 45. SIAM, 2003.

[101] B. Pan, X. Pan, and P. Lu, "Finding best solution in low-thrust trajectory optimization by two-phase homotopy," *Journal of Spacecraft and Rockets*, vol. 56, no. 1, pp. 283–291, 2018.

[102] M. Cerf, "Fast solution of minimum-time low-thrust transfer with eclipses," *Proceedings of the Institution of Mechanical Engineers, Part G: Journal of Aerospace Engineering*, vol. 233, no. 7, pp. 2699–2714, 2019.

[103] R. Woollands and E. Taheri, "Optimal low-thrust gravity perturbed orbit transfers with shadow constraints," in *The 2019 AAS/AIAA Astrodynamics Specialist Conference, Portland, Maine*, 2019.

[104] J. Aziz, D. Scheeres, J. Parker, and J. Englander, "A smoothed eclipse model for solar electric propulsion trajectory optimization," *Transactions of the Japan Society for Aeronautical and Space Sciences, Aerospace Technology Japan*, pp. 17–181, 2019.

[105] D. F. Lawden, *Optimal trajectories for space navigation*, vol. 3. Butterworths, 1963.

[106] J. T. Olympio, "A continuous implementation of a second-variation optimal control method for space trajectory problems," *Journal of Optimization Theory and Applications*, vol. 158, no. 3, pp. 687–716, 2013.

[107] R. Bertrand and R. Epenoy, "New smoothing techniques for solving bang–bang optimal control problems—numerical results and statistical interpretation," *Optimal Control Applications and Methods*, vol. 23, no. 4, pp. 171–197, 2002.

[108] E. Taheri, J. L. Junkins, I. Kolmanovsky, and A. Girard, "A novel approach for optimal trajectory design with multiple operation modes of propulsion system, part 1," *Acta Astronautica*, 2020.

[109] E. Taheri and J. L. Junkins, "How many impulses redux," *The Journal of the Astronautical Sciences*, pp. 1–78, 2019.

[110] I. M. Ross, Q. Gong, and P. Sekhavat, "Low-thrust, high-accuracy trajectory optimization," *Journal of Guidance, Control, and Dynamics*, vol. 30, no. 4, pp. 921–933, 2007.

[111] E. Taheri, "Optimization of many-revolution minimum-time low-thrust trajectories using sundman transformation," in *AIAA Scitech 2021 Forum*, p. 1343, 2021.

[112] W. S. Koon, M. W. Lo, J. E. Marsden, and S. D. Ross, "Dynamical systems, the three-body problem and space mission design," in *Equadiff 99: (In 2 Volumes)*, pp. 1167–1181, World Scientific, 2000.

[113] M. T. Ozimek, *A Low-thrust transfer strategy to earth-moon collinear libration point orbits*. PhD thesis, MS Thesis, School of Aeronautics and Astronautics, Purdue University, 2006.

[114] M. Ozimek and K. Howell, "Low-thrust transfers in the earth-moon system, including applications to libration point orbits," *Journal of Guidance, Control, and Dynamics*, vol. 33, no. 2, pp. 533–549, 2010.

[115] R. J. Whitley, D. C. Davis, L. M. Burke, B. P. McCarthy, R. J. Power, M. L. McGuire, and K. C. Howell, "Earth-moon near rectilinear halo and butterfly orbits for lunar surface exploration," in *AAS/AIAA Astrodynamics Specialists Conference, Snowbird, Utah*, 2018.

[116] T. Flohrer, R. Choc, and B. Bastida, "Classification of geosynchronous objects," *GEN-DBLOG-00086-OPS-GR*, no. 14, 2012.

[117] S. L. Lorenz, C. and Guzman, "Multi-objective optimization of low thrust trajectories for propellant mass, time of flight, and radiation dose," in *Paper No. AAS 19-398, 29th AAS/AIAASpace Flight Mechanics Meeting, Ka'anapali, Hawaii, 2019*, 2019.

[118] D. E. Lee, "White paper: Gateway destination orbit model: A continuous 15 year nrho reference trajectory," in *JSC-E-DAA-TN72594*, NTRS - NASA Technical Reports Server, 2019.

[119] R. Hofer, "High-specific impulse operation of the bpt-4000 hall thruster for nasa science missions," in *46th AIAA/ASME/SAE/ASEE Joint Propulsion Conference & Exhibit*, p. 6623, 2010.

[120] S. K. Singh, B. D. Anderson, E. Taheri, and J. L. Junkins, "Low-thrust earth-moon transfers via manifolds of a halo orbit in the cis-lunar space," in *43rd Annual AAS Guidance, Navigation and Control Conference, Breckenridge*, 2020.

APPENDIX A

INITIAL CONDITIONS FOR GENERATING PERIODIC ORBITS IN THE CR3BP (EARTH-MOON)

Note that the data in the following tables are not comprehensive but provide an initial condition for further refinement in order to converge to a periodic orbit. Typically, a more condensed set of data points are necessary for efficient periodic orbit computation for a general Jacobi Constant.

Table A.1: Northern Earth-Moon L_1 Halo Orbits (see Figure A.1)

x_0(LU)	y_0(LU)	z_0(LU)	v_{x0}(VU)	v_{y0}(VU)	v_{z0}(VU)	C (LU^2/TU^2)
0.82339	0	9.8941 $\times 10^{-4}$	-2.3545 $\times 10^{-15}$	0.12634	2.2367 $\times 10^{-16}$	3.17434
0.82344	0	3.2463 $\times 10^{-2}$	3.9055 $\times 10^{-16}$	0.14215	8.8847 $\times 10^{-15}$	3.16550
0.82400	0	5.4105 $\times 10^{-2}$	1.3857 $\times 10^{-15}$	0.16423	3.6877 $\times 10^{-15}$	3.15075
0.82464	0	6.5841 $\times 10^{-2}$	-2.5303 $\times 10^{-15}$	0.17753	-1.0896 $\times 10^{-14}$	3.14036
0.82608	0	8.3403 $\times 10^{-2}$	-3.7679 $\times 10^{-16}$	0.19752	-8.2059 $\times 10^{-16}$	3.12232

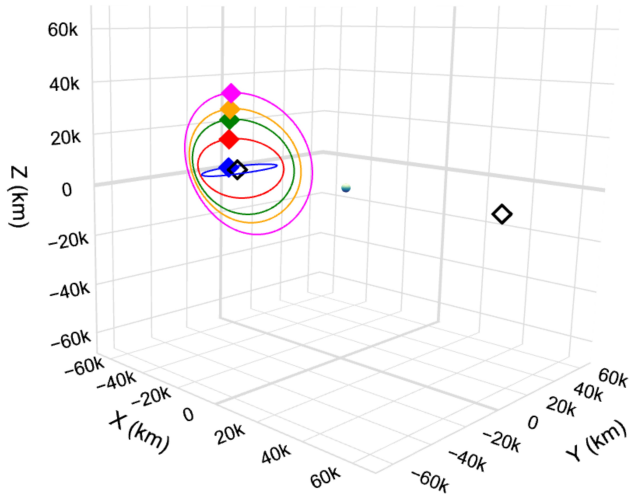

Figure A.1: Northern L_1 Halo Orbits.

Table A.2: Earth-Moon L_1 Lyapunov Orbits (see Figure **??**)

x_0(LU)	y_0(LU)	z_0(LU)	v_{x0}(VU)	v_{y0}(VU)	v_{z0}(VU)	C (LU^2/TU^2)
0.83691	0	0	6.0314 $\times 10^{-16}$	5.2232 $\times 10^{-5}$	0	3.18834
0.82630	0	0	-5.8346 $\times 10^{-16}$	9.6716 $\times 10^{-2}$	0	3.18021
0.81865	0	0	-4.4749 $\times 10^{-15}$	0.17723	0	3.16046
0.81596	0	0	-3.0339 $\times 10^{-15}$	0.20722	0	3.15001
0.81084	0	0	5.5194 $\times 10^{-16}$	0.26342	0	3.12598

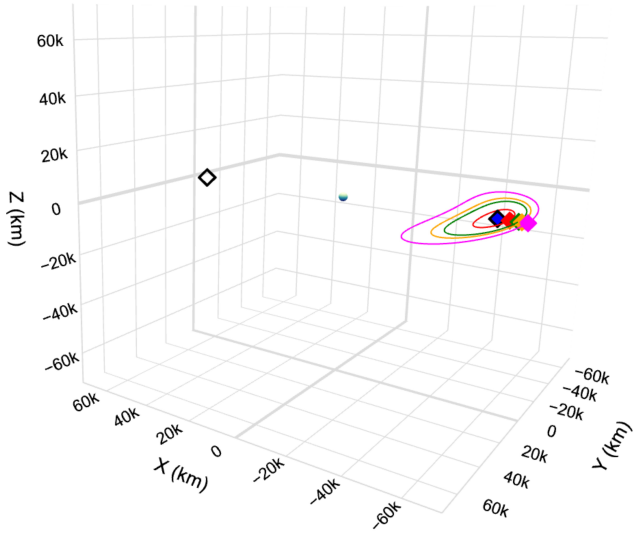

Figure A.2: Planar L_1 Lyapunov Orbits.